Microscopie non-lineaire polarimetrique dans les milieux moleculaires et biologiques

Alicja Gasecka

Université Paul Cézanne - Aix-Marseille III

THÈSE

pour obtenir le grade de **Docteur en Sciences**
de l'Université Paul Cézanne - Aix-Marseille III

Discipline : Optique photonique et traitement d'image

Polarimetric multiphoton fluorescence microscopy in molecular and biological media.

Microscopie non-linéaire polarimétrique dans les milieux moléculaires et biologiques.

soutenue publiquement le **10 Decembre 2010** par

Alicja Gąsecka

École Doctorale : Physique & Sciences de la Matičre

Rapporteurs :	Prof. Andrzej Miniewicz
	Prof. Francesco Pavone
Examinateurs :	Dr. Emmanuel Beaurepaire
Directeurs de thčse :	Dr. Sophie Brasselet
	Prof. Joseph Zyss

Institut Fresnel — CNRS UMR 6133 — Équipe MOSAIC

Abstract

Light-matter interaction in molecular and bio-molecular media can lead to complex processes where optical fields polarizations couple to an assembly of molecular transition dipoles. The manipulation of the optical fields polarization in fluorescence microscopy can in particular give access to fine changes occurring in molecular arrangements. In this PhD thesis we report a method based on a tuneable excitation polarization state complemented by a polarized read-out, applied to polarization-resolved multiphoton fluorescence microscopy. Two-photon fluorescence polarimetry allows to retrieve a quantitative information on the static molecular distribution shape and orientation in different environments such as model lipid membranes, cell membranes, and molecular inclusion compounds that can be strongly heterogeneous. Three-photon fluorescence polarimetry has been furthermore applied in bio-molecular media in order to provide a diagnostics for crystallinity in protein crystals with high sensitivity to their structure and symmetry. The experimental implementation of polarimetric multi-photon microscopy requires to quantify possible polarization distortions originating from the experimental set-up or sample itself, which are thoroughly analyzed.

Keywords : multiphoton fluorescence, polarization, microscopy, molecular distribution, membranes, zeolite L, protein crystals.

Résumé

Les interactions lumière-matičre dans les mileux moléculaires et bio-moléculaires peuvent mener ŕ des processus complexes où les polarisations des champs optiques se couplent aux assemblages de dipoles de transitions moléculaires. La manipulation des polarisations des champs optiques en microscopie de fluorescence peut en particulier donner accès à des modifications fines d'arrangements moléculaires. Dans ce travail de thèse nous introduisons une méthode basée sur la variation continue d'un état de polarisation d'excitation complémentée par une analyse polarisée, appliquée à la microscopie de fluorescence multi-photons. La fluorescence à deux photons polarimétrique permet d'accéder à une information statique quantitative sur la forme et l'orientation de la distribution orientationnelle moléculaire dans des membranes lipidiques artificielles, dans des cellules ou sur des composés molécluaires co-cristallins qui peuvent être fortement hétérogènes. La fluorescence à trois photons polarimétrique apporte de plus un diagnostique de cristallinité dans des cristaux de protéines, avec une forte sensibilité à leur structure et symétrie. L'implémentation expérimentale de cette technique requiert de quantifier les distortions de polarisation provenant du montage expérimental et de l'échantillon lui-même, qui sont finement analysés.

Mots clefs : fluorescence multi-photon, polarisation, microscopie, distribution moléculaire, membranes, zeolite L, cristaux de protéines

Acknowledgements

It is a pleasure to thank the many people who made this thesis possible.

First and foremost I offer my sincerest gratitude to Sophie Brasselet for excellent supervision, advice, and guidance. Throughout my thesis she supported me with her patience, enthusiasm, great efforts to explain things clearly and simply, and knowledge whilst allowing me to work in my own way. Above all and the most needed, she provided me unflinching encouragement by her truly scientist intuition that has made her a constant oasis of ideas and passions in science, which exceptionally inspire and enrich my growth as a student, a researcher and a scientist want to be. One simply could not wish for a better or friendlier supervisor.

I acknowledge Prof Joseph Zyss for the opportunity to do my PhD at the Institut Fresnel. I would like to thank Hervé Rigneault for his very warm welcome upon my arrival at the MOSAIC group and for his invaluable advice with presentations produced over the past three years.

Figure 1: Alicja Gąsecka in Calanques.

I would like to thank the members of the jury: Prof Andrzej Miniewicz, Prof Francesco Pavone and Dr Emmanuel Beaurepaire for their time, interest in the subject of this thesis, helpful comments and insightful questions.

I highly appreciate the collaboration with Cyril Favard for his advice, patience and help with artificial cell membranes preparation and Tsai-Jung Han for her enthusiasm and perseverance in cell membranes measurements. Special thanks for excellent cooperation on Zeolite L inclusion compounds belong to Le-Quyenh Dieu and Dominik Brühwiler from Institute of Inorganic Chemistry, University of Zürich. I would like to also thank Anita Lewit Bentley from Institut Pasteur for very fluent cooperation and fruitful discussions on protein crystallization.

My eternal gratitude goes to David Gachet who patiently answered all my questions, tracked down books and papers and generally went above and beyond in helping find any resources which might have been helpful to me.

I greatly appreciate and wish to thank all the Technical staff at Institut Fresnel for their great assistance during this project. Particular thanks go to Servane Lenne without whose support I would not be able to go through the complexity of the French bureaucracy.

The members of the MOSAIC group have contributed immensely to my personal and

professional time in Marseille. The group has been a source of friendships as well as good advice and collaboration. I would like to express my sincere thanks for all the people who have made Marseille a very special place and made all those years an unforgettable: Fabiana, Peter, Alla, David, Pascal, Pierre B. et Pierre G., Sophie Bru, Heykel, Stéphane, Jules and many others. I am grateful for time spent with them, our memorable apréos on Cours Julien and trips to the Calanques.

During these three years I have had the opportunity to participate in Nanomatch Project in the frame of Marie-Curie Research Training Network. I highly appreciated exchange of ideas and experiences during network conferences. I would like to express my special thanks to young researchers for never-ending discussions and unforgettable meetings: Krisztina, Jan, Varun, Anna, Lucas, Le-Quyenh, Mark, Agnieszka, Fabio, Arantxa, Ricarda and Julius.

I would also like to thank Gabriel, not necessarily for coming along at the right time, but for the very special person he is. And for the incredible amount of patience he had with me in the last five months.

And last but not least I would like to thank my parents for creating an environment in which following this path seemed so natural.

Contents

Introduction

Microscopy imaging, when combined with fluorescent labeling has become an essential tool in biology, biochemistry as well as medical sciences for a variety of applications from molecular and cell biology investigations to biomedical diagnostics [1, 2]. Fluorophores attached to proteins, biomolecular assemblies or lipids have made it possible to identify cells and sub-microscopic cellular components behavior with exquisite sensitivity and selectivity. Localization *in vitro* or *in vivo* of specific biomolecules (proteins, lipids) in single cells or in tissues permits the investigation of their interactions with neighboring molecules as well as environment which is a prerequisite for the understanding of their biological functions. The development of fluorescence microscopy would not have been possible without molecular engineering, that have lead to molecular and non-organic (semiconductor nanoparticles) probes able to stain biological components otherwise inaccessible for visible-range optical microscopy. These probes offer a large variety end-groups in order to target specific biological molecules attachments. They are also designed such as to cover a large range of absorption and emission wavelength ranges which makes fluorescence staining a very flexible solution. Their significant quantum yields permits to study complex biological phenomena in even delicate conditions such as tissues where autofluorescence would otherwise hamper any kind of specific imaging. Besides, the multiple fluorescence labeling that uses different probes can simultaneously identify several target molecules. A part from these synthesized probes, the discovery of fluorescent proteins has revolutionized the fluorescence microscopy imaging. Being directly expressed in cells (obtained for instance by gene manipulation) these fluorescent labels avoid difficulties of in situ chemical staining. Among other things, green fluorescent protein and its mutants, allowed comparing cancer cells with specific genotype or phenotype as well as visualizing tumor cell mobility, invasion or angiogenesis [3]. Labeling single cells in the nervous system permitted to image (determining events in) neuropathology [4]. We can thus see that the molecular imaging has a great impact on the evolution of knowledge in biology and medicine.

While fluorescence microscopy imaging has been primarily developed thanks to confo-

cal one-photon microscopy, other instrumentation developments have emerged in the last decades. Among the most successful ones, multiphoton microscopy initiated by Denk and colleagues in 1990 in a paper on two-photon laser scanning fluorescence microscopy [5, 6] brought a new opportunities to the study of biological matter. The concept of two-photon excitation was described by Maria Goeppert-Mayer in her doctoral thesis on the theory of two-photon quantum transitions in atoms in 1931 [7], and was experimentally observed after the development of laser sources, in caesium vapor in 1962 [8]. The higher order three-photon fluorescence was first demonstrated in 1964 with 20 ns pulse ruby laser [9] and high quality fluorescent images generated by three-photon excitation were then obtained in 1996 by laser-scanning microscopy [10, 11]. The interest in multiphoton microscopy comes from the fact that multiphoton excitation has intrinsic advantages relative to the one photon fluorescence process. First, the use of infrared excitation light leads to less scattering, and therefore deeper optical penetration which is crucial for tissues imaging. Secondly, the non linear nature of the excitation leads to an intrinsic spatial resolution which removes the need of confocal detection schemes. It furthermore reduces the angular photoselection and thus ameliorates the angular sensitivity of polarized measurements as will be detailed in the present work. Moreover reduction in phototoxic effects in some cases makes multiphoton excitation imaging an attractive method for imaging fluorescent probes in vivo. The combination of two and three-photon excitation finally extends the capabilities of a multiphoton imaging system since a single wavelength can provide localized excitation of a wide variety of fluorophores.

Two-photon fluorescence imaging for biology is applied to two main topics : cell membrane imaging and tissues imaging. Cell and model cell membrane studies, using about the same lipid probes as for one-photon fluorescence, have essentially focused on cell architecture imaging by probing local polarity [12] and local environment [13]. Two-photon fluorescence analysis has been completed with second harmonic generation (SHG) imaging microscopy (which is a coherent process occurring in non-centrosymmetrical media) to provide more information on molecules present in an outer leaflet of the membrane, pointing outside [14]. Tissues imaging does not necessarily require the use of exogenous stains since these studies are performed on intrinsic autofluorescence indicators such as numerous fluorescent proteins such as flavins or elastin [15, 16, 17]. Information on tissue morphology, cell behavior or diseases states is often obtained by combining different contrasts for instance multiphoton fluorescence with coherent microscopies : Second Harmonic Generation (SHG) [18, 19, 20], Third Harmonic Generation (THG) [21, 22] or Coherent Anti-Stokes Raman Scattering (CARS) [23, 24]. At last, three-photon fluores-

cence for biology has been reported in a few works that aimed to image a fixed and living biological specimens such as embryos and cells stained with fluorescent labels [25, 26]. These studies however are more delicate compared to two-photon fluorescence imaging due to the lower efficiency cross-sections of the fluorescent proteins in this regime.

An issue that has an essential importance in a large variety of biological phenomena is molecular order, or the way molecules are oriented in an ensemble. Measuring orientational information is essential to understand the molecular interactions that drive the morphology of biomolecular assemblies, from membrane proteins aggregates to biopolymers involved in signaling events [27, 28, 29], cell mechanics and adhesion [30, 31]. However imaging such organizations using optical microscopy remains a challenge, which has been essentially approached by fluorescence anisotropy measurements from molecular probes localized at adequate functional positions. This technique is based on measuring fluorescence polarization response ratio of target molecules in a sample using two excitation/detection polarization directions and can be applied for one-photon or multiphoton fluorescence. A linearly polarized incident electric field preferentially excites fluorescent target molecules with transition dipole moments aligned parallel to the incident polarization vector, therefore providing orientation sensitivity. Such a scheme has been widely used either in time-resolved [32, 33] or steady state schemes in order to answer conformational and structural questions in isotropic environments where molecules are orientationally averaged. Steady state fluorescence anisotropy can be readily implemented in imaging, in particular in membranes where fluorescent probes can be inserted. For example anisotropy analysis has been used to obtain an information on the orientation of long acyl chain fluorescent carbocyanine dye transition dipoles and on the dyes rate of rotation in a biological membrane [34], as well as local orientational distribution of actin filaments within a cell [35]. The use of fluorescent lipid probes allowed to get insight into the membrane lipid organization by studying phospholipid molecular motion [36]. It was shown that two-photon fluorescence anisotropy imaging can accurately image lipid organization in cell membranes and in ordered structures such as membrane nanotubes connecting two cells [13]. Studies on membrane ruffling of natural killer cell immune synapses have also been recently published [29]. These membrane studies have been extended to proteins order investigation, however with more difficulty since studying a protein orientation requires rigidly labeled fluorophores. Investigations on membrane protein receptors order [37] and on the averaged orientation angle of protein filaments have been nevertheless successfully implemented [38].

Fluorescence anisotropy is however limited in terms of accessible information since it only uses two parameters of information. Fluorescence anisotropy imaging has been there-

fore successful in specific cases which are limited to only geometries of the molecular angular distributions which are of cylindrical symmetry and well defined orientation [35, 13], or from which only an average molecular orientation angle is retrieved [38]. Deciphering molecular and biomolecular behaviors however generally requires dealing with complex molecular angular distributions that can strongly differ from purely cylindrical symmetry distributions. Studying molecular order would also strongly benefit from techniques that do not require the *a priori* knowledge of the mean molecular orientation. This is indeed a limitation in the current measurements in cell membranes mentioned above, in which either the contour has to be determined before any polarization resolved analysis [13] or for which studies are limited to cells of round simple shapes. For these reasons more refined polarization-dependent analysis is required. The goal of this work is to explore the capabilities of polarization-resolved two-photon fluorescence in typical studies in biology and material engineering. To do so, we follow a similar approach as in polarization resolved imaging in scattering media: using multiple states polarization analysis [39].

Recent works in polarization resolved coherent two-photon excitation microscopy (using SHG) have demonstrated that rich information is contained in polarization responses recorded from a tuning of the incident linear polarization in the sample plane in molecular media [40, 41, 42, 43]. The outcome of these studies shows that polarization tuning gives access to fine changes of a molecular distribution that would not be accessible in a traditional fluorescence anisotropy measurement, as the analysis now relies on the observation of the shape of the polarization dependence response. In particular, Second Harmonic Generation polarization resolved studies have been proposed to provide information on symmetry orders in complex orientational distributions in organized molecular organic media, for instance to distinguish specifically and locally the nature (symmetry, disorder) of molecular assemblies in molecular monolayers [42] and in crystals down to the nanometric scale [43]. Polarization-controlled contrast improvement schemes have been also applied to a variety of contrasts in nonlinear coherent imaging for biological and chemistry applications, such as Second Harmonic Generation from doped membranes under electric fields [14] and collagen [44, 45, 46, 47], Third Harmonic Generation [48, 49], and Coherent Anti-Stokes Raman Scattering in tissues [50] and in crystals [51]. The polarimetric approach opens thus a new scope of structural studies in biological and molecular media.

While a lot of work has been done in coherent nonlinear microscopy, less work exist on multiphoton fluorescence [40]. Our goal is to focus on two and three-photon fluorescence contrasts which are of great interest in microscopy imaging today. We attempt to demonstrate the feasibilities of Polarimetric Two-Photon Excitation Fluorescence Microscopy by

investigation of complex molecular organization in molecular and biological media as well as to extend the polarization resolved analysis to three-photon fluorescence microscopy to provide a new tool for microscopy structural and molecular order imaging.

Chapter 1 of this thesis recalls the principles of the multiphoton processes applied in fluorescence microscopy and describes the context of polarization resolved analysis. The basic formalism is introduced and the theoretical approach allowing for modeling fluorescence processes in ordered media is explained in details.

In order to provide relevant information on the studied system, polarimetric analysis necessitates accounting for possible polarization distortions occurring in the experimental set-up or originating from the sample itself. Chapter 2 is devoted to this issue.

Chapter 3 presents the potential of the two-photon fluorescence microscopy when probing molecular organization in biological membranes. The molecular orientation and distribution is determined in different lipid environments and compared with cell membranes.

In this introduction we have mentioned the biological context of nonlinear microscopy imaging. In chapter 4 we will show that polarization resolved fluorescence microscopy can be interesting as well for materials development such as inclusion compounds made of nanochannels doped with fluorescent molecules.

Finally, in chapter 5 the polarimetric analysis is extended to three-photon fluorescence microscopy. This new approach allows to distinguish between crystalline and isotropic structures in media of high order symmetries. We present first explorations on the polarization resolved three-photon fluorescence from molecular and protein crystals.

Chapter 1

Polarization resolved fluorescence microscopy

Polarimetric fluorescence microscopy, which is the core of this work, relies on a variation of the incident electric field polarization to read-out light matter interaction information. To understand the output of such experiment in terms of molecular order information one needs to detail the polarization resolved fluorescence process as well as define the notion of "molecular-order". In chapter 1 we will describe the properties of one-, two- and three-photon fluorescence processes, which will be used as a contrasts in the experiments performed in this work. We will also introduce a general molecular order model that will be exploited in biological and molecular samples and detail how polarization resolved experiments can reveal information on this molecular order. Finally we will analyze the range of application of the fluorescence polarization resolved technique depending on the contrast used, as well as its advantage comparing to the more traditional fluorescence anisotropy technique. Essentially, we will show how to reach higher order symmetries information with multiphoton fluorescence contrasts. The concepts introduced in this chapter will be used in all the rest of this work.

1.1 Multiphoton fluorescence processes

1.1.1 One photon fluorescence

The process by which an excited material emits light is called luminescence and among all possible excitation processes, luminescence caused by the electromagnetic radiation is called fluorescence. One of the first experiment showing the fluorescence effect was

reported by Sir J.F.W. Herschel in 1845 [52]. He observed that a solution of quinine in water illuminated with sun emits a blue color which appears stronger when observed at a right angle relative to the direction of sunlight. A few years later, in 1852, Sir G.G. Stokes published a paper where he presented the studies on the same compound reporting that the emitted light exhibits a longer wavelength than the exciting light [53]. The historical experiment presenting this fundamental property of fluorescence is shown in Fig. 1.1. G.G. Stokes showed that while the incident blue light below 400nm is absorbed by the

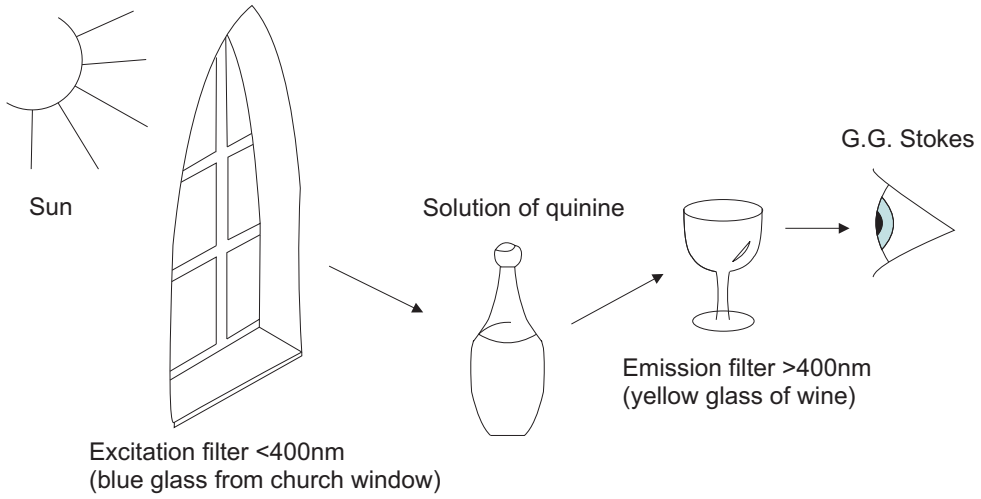

Figure 1.1: Experimental set-up used by G.G. Stokes.

quinine molecules, the emitted light is shifted to longer wavelengths (450nm), and thus can be observed by eye. The yellow (wine) filter prevents the incident radiation from reaching the observer.

The photophysical process reported by Sir J.F.W. Herschel and Sir G.G. Stokes was later understood by A. Jabłoński in 1935 in a model which is widely used today by spectroscopists [54]. In this model, supported by quantum chemistry, the molecule after absorption of a photon is able to undergo a radiative decay from a fluorescent level reached after a fast internal conversion. This is summarized in the simplified Jabłoński diagram depicted in Fig.. 1.2 a. Note that this version of the diagram does not represent all the possible non-radiative decays in the relaxation process, due to the intermolecular or intramolecular processes. In particular, intersystem crossing (form singlet to tripled states) that can result in a delayed fluorescence or phosphorescence which will not be considered in the rest of this work.

The detailed excitation/relaxation process can be summarized as follows. In the ground state $|S_0\rangle$ a molecule called fluorophore or fluorescent dye (generally poly-aromatic

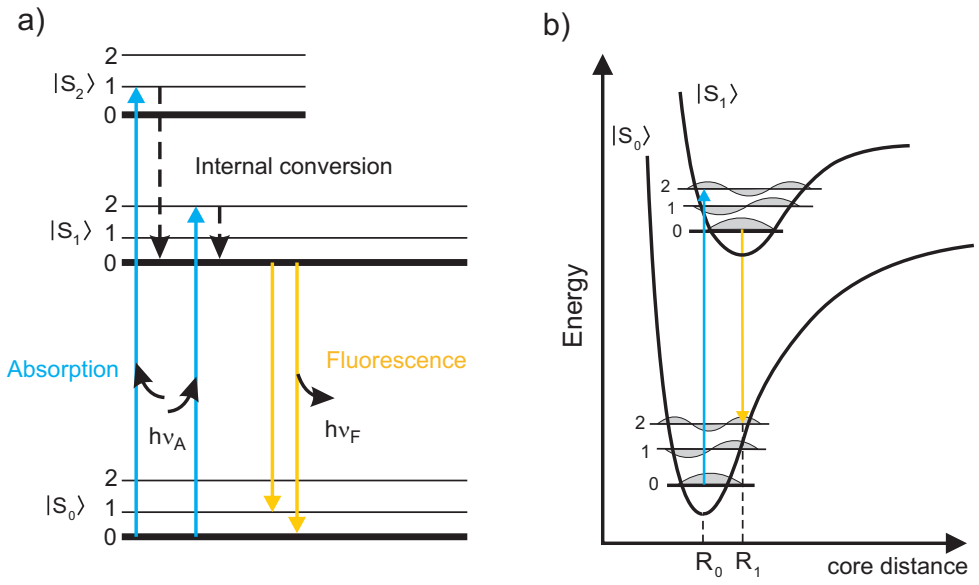

Figure 1.2: (a) Simplified Jabłoński diagram of one-photon fluorescence process. $|S_1\rangle$,$|S_2\rangle$ represent singlet electronic levels, $0, 1, 2$ are vibrational levels. (b) Illustration of the Franck-Condon principle with potential well model (molecular states as in (a)). The electronic transition is most likely to occur without changes in the positions of the nuclei (R_0, R_1 - equilibrium core distances for ground state and first excited singlet state respectively).

hydrocarbon or heterocyclic compound) lies in its lowest vibrational level 0 whereas higher vibrational levels 1 and 2 are in general not populated (less that 1% according to Boltzmann statistics). The transition to higher electronic levels occurs when this molecule absorbs a quantum of light $h\nu_A$ [55]. In general during excitation atom bonds get weaker, therefore the equilibrium distance between atom cores of the molecule in excited state is slightly larger than the one in the ground state (Fig. 1.2 b). The Franck-Condon principle states that the excitation processes are much faster ($10^{-15}s$) than the time scale of nuclear motions ($10^{-12}s$) (due to the lower mass of electrons as compared to nuclei), thus they do not displace nuclei significantly [56, 57]. Because the electronic transitions are essentially instantaneous compared with nuclear motions the fluorophore is usually excited to some higher vibrational levels of $|S_1\rangle$ (or higher energy levels $|S_2\rangle$ depending on the incident wavelength) which correspond to the minimal change of the nuclear coordinates. Hence this transitions can be drawn as a vertical line on the potential curve diagram (Fig. 1.2 b). In the next $10^{-12}s$, the molecule relaxes to the lowest vibrational level of $|S_1\rangle$ by internal conversion usually triggered by molecular relaxation influenced by solvent interactions. In the most common organic fluorophores the emission process occurs after a

few $10^{-9}s$ and originates from the lowest vibrational level of S_1 (this is the Kasha's rule which states that the emission level is the most stable one and does not depend on the excitation energy) [58]. Due to possible non-radiative relaxation processes (i.e. energy transfer, collisional quenching or intersystem crossing) the energy of the excited state is partially dissipated and not all the molecules initially excited by absorption return to the ground state $|S_0\rangle$ by fluorescence emission. This is the reason why the fluorescent efficiency quantum yields are generally below 1 (this quantum yield is defined by the ratio between the radiative and the totality of the decay rates present in the system). In the last step, the fluorophore comes back to the lowest vibrational level of the ground state directly by emission or by additional vibrational relaxation. Energy losses between excitation and emission as well as vibrational relaxations are the reason of the Stokes shift (the energy difference between the emission spectrum and the excitation wavelength).

We will detail below the calculation of the fluorescence intensity of a single molecule. To do so, we will need to separate the steps of absorption and emission since these two steps are uncorrelated in time. Therefore we will write the emitted fluorescence intensity as a product of two probabilities : the absorption between the ground and the excited state (of one, two or three photons) and the emission from the fluorescent state to the ground state (of one photon).

$$I^{n=1,2,3ph} \propto P_{abs}^{1,2,3ph} \cdot P_{em}^{1ph}. \tag{1.1}$$

The proportionality coefficient contains collection efficiencies and normalization factors. Since our analysis does not depend on these coefficients we will omit them in the future and write equals sign.

The absorption probability is calculated using quantum mechanics perturbation theory which is generally done for a one-electron atom but can be applied to a molecule [59]. We will describe here the expression for the one photon absorption probability which will be extended to two and three photons afterwards.

In the quantum mechanical picture an electromagnetic wave is considered as a perturbation $\hat{V}$ of the initial system, representing the energy of interaction of the atom/molecule with the externally applied radiation field E of a frequency ω: $\hat{V} = -\hat{\boldsymbol{\mu}} \cdot (\mathbf{E}^{\omega} + \mathbf{E}^{\omega *})$, where $\hat{\boldsymbol{\mu}} = -e\hat{\mathbf{r}}$ is the electric dipole moment operator and $-e$ is the charge of the electron at position $\hat{\mathbf{r}}$. The total Hamiltonian of the system $\hat{H}$ is thus written as :

$$\hat{H} = \hat{H}_0 + \hat{V} \tag{1.2}$$

where $\hat{H}_0$ denotes the Hamiltonian for a free system without perturbation. In order to express the excitation of the molecule as a perturbation one has to use the density matrix formalism, which permits to account for the statistical environment of the molecule. Two states of the molecule given by $|n\rangle$ and $\langle m|$ are described by the density matrix $\hat{\rho}$ elements $\rho_{nm} = |n\rangle\langle m|$. The diagonal element of this matrix ρ_{nn} gives the probability that the system is in its energy eigenstate E_n that corresponds to the statistical population of $|n\rangle$, while the out of diagonal elements ρ_{nm} quantify the coherence between levels $|n\rangle$ and $\langle m|$. The Schrödinger equation written in the density matrix formalism describes how the ρ_{nm} element evolves in time:

$$\dot{\rho}_{nm} = \frac{-i}{\hbar}[\hat{H}, \hat{\rho}]_{nm} - \gamma_{nm}(\rho_{nm} - \rho^{eq}_{nm}) \tag{1.3}$$

where γ_{nm} is a phenomenological damping term introduced to account for dissipative interactions of the molecule with its environment, which indicates that ρ_{nm} relaxes to its equilibrium value ρ^{eq}_{nm} at the rate γ_{nm}. By introducing the transition frequency $\omega_{nm} = \frac{E_n - E_m}{\hbar}$ between the $|n\rangle$ and $\langle m|$ states that correspond to the solution of the unperturbed Hamiltonian, the above equation is written:

$$\dot{\rho}_{nm} = -i\omega_{nm}\rho_{nm} - \frac{i}{\hbar}[\hat{V}, \hat{\rho}]_{nm} - \gamma_{nm}(\rho_{nm} - \rho^{eq}_{nm}) \tag{1.4}$$

$$\dot{\rho}_{nm} = -i\omega_{nm}\rho_{nm} - \frac{i}{\hbar}\sum_{\nu}(V_{n\nu}\rho_{\nu m} - V_{\nu m}\rho_{n\nu}) - \gamma_{nm}(\rho_{nm} - \rho^{eq}_{nm}) \tag{1.5}$$

where $\sum_\nu$ is a sum over all intermediate states $|\nu\rangle$. These equations cannot be solved analytically, therefore a solution has to be seek in the form of perturbation expansion performed by successive increase of the rank of V_{nm} [59]. The zero and $j > 0$ orders stationary solutions can be written :

$$\dot{\rho}^{(0)}_{nm} = -i\omega_{nm}\rho^{(0)}_{nm} - \gamma_{nm}(\rho^{(0)}_{nm} - \rho^{eq}_{nm}) \tag{1.6}$$

$$\dot{\rho}^{(j)}_{nm} = -i\omega_{nm}\rho^{(j)}_{nm} - \frac{i}{\hbar}\sum_{\nu}\left(\boldsymbol{\mu}_{n\nu}\rho^{(j-1)}_{\nu m} - \boldsymbol{\mu}_{\nu m}\rho^{(j-1)}_{n\nu}\right)\cdot(\mathbf{E}^{\omega} + \mathbf{E}^{\omega^*}) - \gamma_{nm}\rho^{(j)}_{nm}. \tag{1.7}$$

In the absence of the external field the steady state solution of equation 1.6 is:

$$\rho^{(0)}_{nm} = \rho^{eq}_{nm}. \tag{1.8}$$

At thermal equilibrium, the excited states of the system may contain populations, but coherence terms of ρ^{eq}_{nm} vanish. This is because thermal excitation (which is an incoherent process) cannot produce any coherent superposition of states:

$$\rho^{eq}_{nm} = 0 \quad \text{for} \quad n \neq m. \tag{1.9}$$

Using this zero solution in equation 1.7 leads to the first order perturbation solution :

$$\rho_{nm}^{(1)}(t) = \frac{\rho_{mm}^{eq} - \rho_{nn}^{eq}}{\hbar} \left[\frac{(\boldsymbol{\mu}_{nm} \cdot \mathbf{E}^{\omega}) e^{-i\omega t}}{(\omega_{nm} - \omega) - i\gamma_{nm}} + \frac{(\boldsymbol{\mu}_{nm} \cdot \mathbf{E}^{\omega^*}) e^{-i\omega t}}{(\omega_{nm} + \omega) - i\gamma_{nm}} \right]. \tag{1.10}$$

This term allows calculating the linear susceptibility of the molecule, using the expectation value of the induced dipole moment :

$$\langle \hat{\boldsymbol{\mu}}(t) \rangle = Tr(\hat{\rho}^{(1)} \cdot \boldsymbol{\mu}) = \sum_{n,m} \boldsymbol{\mu}_{mn} \rho_{nm}^{(1)}(t) \tag{1.11}$$

Under a single-frequency ω excitation (monochromatic wave) this dipole is a ω frequency oscillating term :

$$\langle \hat{\boldsymbol{\mu}}(t) \rangle = \boldsymbol{\mu}^{\omega} e^{-i\omega t}. \tag{1.12}$$

The linear susceptibility tensor is defined by

$$\boldsymbol{\mu}^{\omega} = \varepsilon_0 \alpha(-\omega, \omega) : \mathbf{E}^{\omega} \tag{1.13}$$

$$\alpha_{ij}(-\omega, \omega) = \sum_{n,m} \frac{\rho_{mm}^{eq} - \rho_{nn}^{eq}}{\varepsilon_0 \hbar} \frac{\mu_{mn}^{i} \mu_{nm}^{j}}{(\omega_{nm} - \omega) - i\gamma_{nm}} \tag{1.14}$$

when a molecule is initially in the ground state ($\rho_{mm}^{eq} = \delta_{m0}$) :

$$\alpha_{ij}(-\omega, \omega) = \frac{1}{\varepsilon_0 \hbar} \sum_{n} \frac{\mu_{0n}^{i} \mu_{n0}^{j}}{(\omega_{n0} - \omega) - i\gamma_{n0}}. \tag{1.15}$$

It has been shown that the absorption probability of one photon at the frequency ω can be written as [59] :

$$P_{abs}^{1ph} = Im(\alpha(-\omega, \omega)) \bullet (\mathbf{E}^{\omega} \otimes \mathbf{E}^{\omega^*}) \tag{1.16}$$

where $Im(\alpha(-\omega, \omega))$ is the imaginary part of the linear susceptibility of the molecule given by equations 1.14 and 1.15. In this expression $\otimes$ denotes the tensorial scalar product ($(\mathbf{E}^{\omega} \otimes \mathbf{E}^{\omega^*})_{ij} = E_i^{\omega} E_j^{\omega^*}$), and $\bullet$ is the tensorial product (similar to the scalar product for vectors). The demonstration of this expression requires to go to the second rank perturbation : P_{abs}^{1ph} is equal to the term $\rho_{nn}^{(2)} - \rho_{00}^{(2)}$ as an interaction of the system with the fields E^{ω} and E^{ω^*} [60].

In this work we will consider two level systems where only $n = 1$ is the dominant contribution in eq 1.15. In this case the absorption probability can be simplified in :

$$P_{abs}^{1ph} \propto \alpha_{ij} E_i^{\omega} E_j^{\omega^*} \propto \sum_{ij} \mu_{01}^{i} \mu_{01}^{j} E_i^{\omega} E_j^{\omega^*} = |\boldsymbol{\mu}_{01} \cdot \mathbf{E}^{\omega}|^2 \tag{1.17}$$

where the molecular absorption dipole $\boldsymbol{\mu}_{01}$ is the transition dipole moment from the ground state to the excited state. We also recognize here the transition rate between the $|0\rangle$ and $|1\rangle$ levels in atom optics governed by the Fermi golden rule [59] :

$$R_{01}^{1ph}(\omega) = \frac{2\pi}{\hbar^2}|\langle 0|\hat{V}|1\rangle|^2\rho_f(\omega) = \frac{2\pi}{\hbar^2}|\langle 0|\boldsymbol{\mu}\cdot\mathbf{E}^{\omega}|1\rangle|^2\rho_f(\omega) \tag{1.18}$$

where $\rho_f(\omega)$ is the density of states of the excited level measured at the vicinity of the ω_{01} transition frequency ($\rho_f(\omega)$ is the Lorentzian function of eq 1.15). The absorption cross section is defined by $R_{01}^{1ph}(\omega) = \sigma_{01}^{1ph}(\omega)I^{\omega}$ where $I = 2n\varepsilon_0 c|\mathbf{E}^{\omega}|^2$. Therefore :

$$\sigma_{01}^{1ph} = \frac{\pi}{n\varepsilon_0 c}\frac{1}{\hbar^2}|\boldsymbol{\mu}_{01}|^2\rho_f(\omega) \tag{1.19}$$

Typical values for the absorption cross sections of organic molecules are around $10^{-16}cm^2$ at the maximum of the absorption peak $\omega = \omega_{01}$ (taking $\rho_f(\omega_{01}) = \frac{1}{2\pi\gamma_{01}}$) [59]. $\boldsymbol{\mu}_{01}$ will be denoted $\boldsymbol{\mu}^{abs}$ in the rest of this work.

The emission probability along the analysis axis i, denoted $P_{em,i}^{1ph}$, corresponds to the fluorescence radiated intensity I_i^{em} :

$$P_{em,i} = I_i^{em} = |\mathbf{E}^{em}\cdot u_i|^2 \tag{1.20}$$

where u_i is a normalized vector along the direction i. The far field $\mathbf{E}^{em}$ radiated by the emission dipole $\boldsymbol{\mu}^{em}$ (which defines the transition dipole moment between the fluorescent and the ground state) in the propagation direction $\mathbf{k}$ is expressed as [60]:

$$\mathbf{E}^{em} \propto \mathbf{k}\times(\mathbf{k}\times\boldsymbol{\mu}^{em}) \tag{1.21}$$

In general $\boldsymbol{\mu}^{em}$ is different from the absorption transition dipole that we called above $\boldsymbol{\mu}^{abs}$, due to the fact that different states are involved in the absorption/emission processes. This issue will be discuss in chapter 2.

Finally the one-photon fluorescence intensity in the analyzing direction i is written:

$$I_i^{1ph} \propto |\boldsymbol{\mu}^{abs}\cdot\mathbf{E}^{\omega}|^2|\mathbf{E}^{em}\cdot u_i|^2 \tag{1.22}$$

The proportionality sign in Eq. 1.22 contains collection efficiency factors, the fluorescence quantum yield and the proportionality coefficients of the above equations.

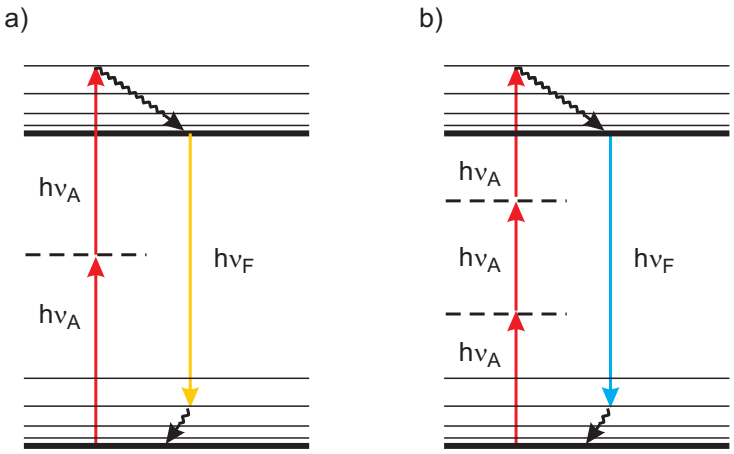

Figure 1.3: Two and three-photon fluorescence represented by a Jaboński diagram.

1.1.2 Two and three-photon fluorescence

Multiphoton Fluorescence Microscopy relies on the quasi-simultaneous absorption of two or more photons by a molecule (Fig. 1.3). The two-photon fluorescence process was predicted by M. Goeppert-Mayer in 1931 [7]. During the absorption process, an electron of the molecule is transferred to an excited-state molecular orbital. The virtual absorption of a photon of non-resonant energy lasts only for a very short period ($10^{-15} - 10^{-18} s$). During this time a second photon must be absorbed to reach an excited state. Whereas the selection rules for one and multi-photon absorption are different because of the different numbers of energy levels (virtual or not), the emission occurs from the same excited level $|S_1\rangle$. Hence the excitation spectra coming from one and multi-photon processes are not the same. This effect is clearly visible for centrosymmetric molecules where electronic levels for two-photon have generally higher energy than for one-photon excitation (indeed a two-photon absorption level has to be of different parity than a one-photon absorption level). Therefore an optimal wavelength for one-photon excitation is not necessarily equal to double of the wavelength for which two-photon excitation is maximal. The molecule in the excited state has a high probability to emit a photon during relaxation to the ground state. As in a one-photon excitation process, due to radiationless relaxation in vibrational levels, the energy of the emitted photon is lower compared to the sum of the energy of the absorbed photons.

In order to calculate the two-photon absorption probability P_{abs}^{2ph}, a similar treatment can be applied as in the previous section, using one more order of perturbation. This probability is governed by the third order nonlinear hyperpolarizability tensor $\gamma(-\omega, -\omega, \omega, \omega)$

[59]:

$$\gamma_{ijkl}(-\omega,-\omega,\omega,\omega) = \frac{1}{8\varepsilon_0\hbar^3}\sum_{n,m,\nu}\{\frac{P_{jkl}[\mu^i_{0n}\mu^j_{nm}\mu^k_{m\nu}\mu^l_{\nu 0}]}{[(\omega_{n0}-\omega)-i\gamma_{n0}][(\omega_{m0}-2\omega)-i\gamma_{m0}][(\omega_{\nu 0}-\omega)-i\gamma_{\nu 0}]} + \frac{P_{jkl}[\mu^j_{0n}\mu^i_{nm}\mu^k_{m\nu}\mu^l_{\nu 0}]}{[(\omega_{n0}-\omega)-i\gamma_{n0}][(\omega_{m0}-2\omega)-i\gamma_{m0}][(\omega_{\nu 0}-\omega)-i\gamma_{\nu 0}]}\} \quad (1.23)$$

with [60]:

$$P^{2ph}_{abs} = Im(\gamma(-\omega,\omega,\omega,-\omega)) \bullet (\mathbf{E}^{\omega^*}\otimes\mathbf{E}^{\omega}\otimes\mathbf{E}^{\omega}\otimes\mathbf{E}^{\omega^*}) \quad (1.24)$$

where $(\mathbf{E}^{\omega^*}\otimes\mathbf{E}^{\omega}\otimes\mathbf{E}^{\omega}\otimes\mathbf{E}^{\omega^*})_{ijkl} = E^{\omega^*}_i E^{\omega}_j E^{\omega}_k E^{\omega^*}_l$.
In the two level model approximation :

$$P^{2ph}_{abs} \propto \gamma_{ijkl}E^{\omega^*}_i E^{\omega}_j E^{\omega}_k E^{\omega^*}_l \propto \sum_n\sum_{ijkl}\mu^i_{0n}\mu^j_{n1}\mu^k_{1n}\mu^l_{n0}E^{\omega^*}_i E^{\omega}_j E^{\omega}_k E^{\omega^*}_l \quad (1.25)$$

the quantities $\mu_{0n} = \mu^*_{n0}$ involve additional $|n\rangle$ levels in the system.

The two-photon absorption cross section calculation can also be made using the two-photon transition rate:

$$R^{2ph}_{01}(\omega) = \frac{2\pi}{\hbar^4}\left|\sum_n \frac{\langle 0|\boldsymbol{\mu}\cdot\mathbf{E}^{\omega}|n\rangle\langle n|\boldsymbol{\mu}\cdot\mathbf{E}^{\omega}|1\rangle}{(\omega_{n0}-\omega)}\right|^2 \rho_f(2\omega) \quad (1.26)$$

Similarly as for one-photon process, the two-photon absorption cross section is defined by $R^{2ph}_{01}(\omega) = \sigma^{2ph}_{01}(\omega)\bar{I}^{\omega}$ where $\bar{I} = \frac{2n\varepsilon_0 c}{\hbar\omega}|\mathbf{E}^{\omega}|^2$ and therefore [59]:

$$\sigma^{2ph}_{01} = \frac{\omega^2}{4n^2\varepsilon_0^2c^2}\left|\sum_n \frac{1}{\hbar^2}\frac{\boldsymbol{\mu}_{0n}\boldsymbol{\mu}_{n1}}{(\omega_{n0}-\omega)}\right|^2 2\pi\rho_f(2\omega) \quad (1.27)$$

Assuming that only one of the $|n\rangle$ levels is of dominant transition dipole and that is furthermore nonresonant at ω ($\omega_{n0}-\omega \approx \omega$), σ^{2ph}_{01} can be estimated. Typical values around $10^{-55}\mathrm{m}^4\mathrm{sec/photon}^2$ can be found [11]. We can see that in the continuous excitation regime, this would lead to very low absorption efficiencies comparing to the one-photon process. This is why most of the two-photon excitation studies are performed in the pulsed regime which concentrate high energy in a short time and at high repetition rate. [61].
In the future we will mostly study one dimensional molecules in which we can assimilate $\boldsymbol{\mu}_{0n}$ and $\boldsymbol{\mu}_{n1}$ to a single vector direction $\boldsymbol{\mu}^{abs}$ along the molecular axis. This vector $\boldsymbol{\mu}^{abs}$ will allow us defining the orientation of the molecule. The two-photon absorption can thus be defined by :

$$P^{2ph}_{abs} \propto |\boldsymbol{\mu}^{abs}\cdot\mathbf{E}^{\omega}|^4 \quad (1.28)$$

Because the emission occurs from the same level as in one-photon fluorescence the two-photon fluorescence intensity along the analyzing direction i (expressed by the unit vector in that direction u_i) is written as before :

$$I_i^{2ph} \propto |\boldsymbol{\mu}^{abs} \cdot \mathbf{E}^{\omega}|^4 |\mathbf{E}^{em} \cdot u_i|^2 \tag{1.29}$$

In all future calculations we will replace the $\propto$ by $=$ since only the intensity dependance with respect to the incident polarization will be investigated.

Two-photon excitation exhibits several advantages over one photon fluorescence in microscopy. In a high peak-power pulsed laser (with mean power levels moderated to do not damage the specimen), the photon density at the point of focus is sufficiently high so that two photons can be simultaneously absorbed by the fluorophore. Eq 1.29 shows that two-photon fluorescence depends of the square of the incident intensity, therefore this process takes place only at the focus point of the microscope objective, eliminating out-of-focus excitation of a fluorophore and thereby enabling 3D optical sectioning with high spatial resolution [6]. Although the axial resolution along the propagation direction is improved, it has been shown that the lateral two-photon spatial resolution is comparable to the one-photon confocal resolution when exciting the same fluorophore [62, 63, 64]. This is due to the larger diffraction-limited spot at the longer wavelength two-photon excitation source. For a 1.25 NA objective using an excitation wavelength of 960nm the typical point spread function has an FWHM of 300nm in the lateral direction and 900nm in the axial direction (which is about half the axial resolution at one-photon) [65]. Note however that this is the resolution at the surface of the sample, but it typically degrades with depth in thick scattering samples. Another advantage over the one photon process is reduced scattering, which is a major contributor to image detioration. Indeed, because the elastic scattering of light is proportional to the inverse power of the wavelength ($1/\lambda^4$), this process is less pronounced in 2PEF and allows imaging in three times deeper regions compared to 1PEF [6]. These properties have triggered the large interest for 2PEF for bio-imaging applications.

The accessible wavelengths in widely used femtosecond Ti:Sa laser (typically 700-1000nm) allow covering a large range of either synthesized fluorophores or naturally fluorescent proteins such as flavins or elastin present in cells and tissues [6, 44, 11, 66, 67, 17].

However the majority of proteins is not maximally absorbing in the visible range but rather in the UV (250-280nm) which is the absorption range of amino-acids. Such wavelengths are not accessible by a two-photon excitation. In this work we are interested

in targeting the fluorescence from un-labeled proteins as a possible contrast for nonlinear structural imaging. For this purpose we investigated also three-photon fluorescence which is a possible way to excite such UV transitions using a Ti:Sa laser.

Three photon fluorescence process occurs in a manner similar to two-photon excitation. The difference is that three photons must be absorbed simultaneously. Following a similar approach as developed above, the three-photon absorption probability can be written using a three-photon absorption tensor :

$$P_{abs}^{3ph} \propto \sum_{ijklmn} \xi_{ijklmn} \mathbf{E}_i^{\omega^*} E_j^{\omega} \mathbf{E}_k^{\omega^*} E_l^{\omega} \mathbf{E}_m^{\omega^*} E_n^{\omega} \tag{1.30}$$

The three-photon fluorescence intensity will be defined by :

$$I_i^{3phfluo} \propto |\boldsymbol{\mu}^{abs} \cdot \mathbf{E}^{\omega}|^6 |\mathbf{E}^{em} \cdot u_i|^2. \tag{1.31}$$

Because excitation levels are dependent on the cube of the excitation power, a spatial confinement at the point of the focus is stronger, so that a higher contrast in imaging is expected. Furthermore, the resolution achieved in three-photon fluorescence microscopy is greater than for one or two-photon microscopy (200nm axial and 500nm lateral resolutions have been theoretically predicted for a 900nm excitation wavelength and a 1.35 NA objective [10]).

1.2 From one molecule to an assembly of molecules

So far we have shown the detailed analysis of fluorescence processes from a single molecule. However in a standard microscopy measurement a great number of fluorophores is present within the focal volume. Hence, in the presented section, we will extend this approach to the calculation of the fluorescence signal from an assembly of molecules and discuss orientation distribution functions defining this assembly. We will focus on two-photon fluorescence since 2PEF microscopy is applied to the major part of experiments performed in this thesis.

Let us consider the incident electric field $\mathbf{E}(\mathbf{r})$ which interacts at location $\mathbf{r}$ with the absorption dipole moment of a molecule $\boldsymbol{\mu}^{abs}(\Omega, \mathbf{r})$ whose orientation is given by the Euler set of angles $\Omega = (\theta, \phi)$ as indicated in Fig. 1.4. The far field $\mathbf{E}^{em}$ is radiated by the emission dipole in the propagation direction $\mathbf{k}$ with $\mathbf{E^{em}}(\mathbf{\Omega}, \mathbf{r}, \mathbf{k}) \propto \mathbf{k} \times (\mathbf{k} \times \boldsymbol{\mu}^{em}(\Omega, \mathbf{r}))$. The two-photon fluorescence signal detected from one molecule in the analyzing direction i and in the direction $\mathbf{k}$ can therefore be expressed :

$$I_i^{2ph}(\Omega, \mathbf{r}, \mathbf{k}) = |\boldsymbol{\mu}^{abs}(\Omega, \mathbf{r}) \cdot \mathbf{E}(\mathbf{r})|^4 |\mathbf{E}^{em}(\Omega, \mathbf{r}, \mathbf{k}) \cdot u_i|^2 \tag{1.32}$$

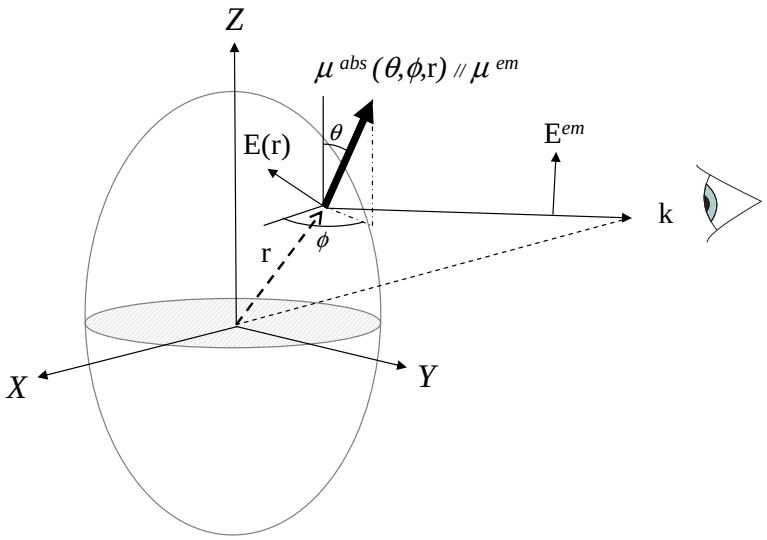

Figure 1.4: Absorption dipole moment $\boldsymbol{\mu}^{abs}$ at position $\mathbf{r}$ and orientation θ, ϕ excited by the incident field $\mathbf{E}(\mathbf{r})$ in the focal volume X, Y, Z. The far field $\mathbf{E}^{em}$ is radiated by the emission dipole $\boldsymbol{\mu}^{em}$ in the propagation direction $\mathbf{k}$.

As it was shown previously the fluorescence emission process is completely uncorrelated from the excitation process. This is because the absorption (and the subsequent internal conversion) plus the emission (after a stochastically distributed dwell time in the excited state) lead to a complete memory loss of the excitation conditions. Due to this incoherent nature of the fluorescence process, the emission of one fluorophore will be uncorrelated in time from the emission of another fluorophore. Therefore the 2PEF intensity detected from an assembly of molecules is expressed as the superposition of all its individual intensity contributions. The molecular angular distribution is described by the normalized orientation distribution function $f(\Omega)$, which is defined by the number of molecules $N(\Omega)\, d\Omega = N f(\Omega)\, d\Omega$ present in the unit solid angle $d\Omega$. Consequently :

$$I_i^{2ph} = N \int\int\int |\boldsymbol{\mu}^{abs}(\Omega, \mathbf{r}) \cdot \mathbf{E}(\mathbf{r})|^4 |\mathbf{E}^{em}(\Omega, \mathbf{r}, \mathbf{k}) \cdot u_i|^2 f(\Omega)\, d\Omega\, d\mathbf{r}\, d\mathbf{k} \tag{1.33}$$

a few remarks can be done on this expression :

- In the rigorous way the above expression (and in particular $f(\Omega)$) should be dependent on time for molecules whose orientation is fluctuating [68]. Here we will average this quantity and give a static information within the integration time of the measurements (typically >ms), which is much longer than the rotational diffusion time (ps-ns) of molecules and their excitation state life time (typically ns).

- The incident radiation is usually focused into a nonlinear medium by the high numerical aperture objective in order to increase its intensity and thereby increase the efficiency of the nonlinear optical process. Therefore $\mathbf{E}(\mathbf{r})$ exhibits a spatial dependence, which will be discussed in chapter 2. In our first analysis, we will use the planar wave approximation which is sufficient to study polarization dependencies.

- In principle $\mathbf{E}^{em}(\Omega, \mathbf{r}, \mathbf{k})$ should be integrated over all the directions $\mathbf{k}$ of the high numerical aperture detection. The effect of the strong aperture on the polarization response will be studied in chapter 2 and taken into account in all the experimental analysis presented in this work. In this section for the sake of simplicity we will consider only a planar wave approximation and omit the $\mathbf{k}$ dependence.

- We will consider a homogeneous spatial distribution of transition dipole moments therefore the $\mathbf{r}$ dependance of $\boldsymbol{\mu}^{abs}(\mathbf{r})$ will be omitted. All the possible spatial orientations will be contained in the $f(\Omega)$ function.

- The fluorescence intensity scales with the number of fluorophores in the focal volume, which is expected from the incoherent nature of this process. We will omit the N factor in the future.

- We assume in a first approximation that the absorption dipole moment of a molecule $\boldsymbol{\mu}^{abs}$ is parallel to its emission dipole moment $\boldsymbol{\mu}^{em}$ (non parallel dipoles will be studied in chapter 2).

With all the approximations mentioned above, the two-photon fluorescence signal defined in equation 1.32, measured from a molecular assembly within an orientational distribution $f(\Omega)$ and analyzed along a given polarization direction $i = X, Y$ for an incident field propagating along Z is now expressed:

$$I_i^{2ph} = \int |\boldsymbol{\mu}(\Omega) \cdot \mathbf{E}|^4 |\boldsymbol{\mu}_i(\Omega)|^2 f(\Omega)\, d\Omega. \tag{1.34}$$

where $d\Omega = \sin\theta\, d\theta\, d\phi$ and with $\theta \in [0 - \pi], \phi \in [0 - 2\pi]$. Equation 1.34 finally shows that two-photon excited fluorescence depends on both the molecular statistical orientational distribution and the excitation fields polarization. Since this field is defined in the macroscopic frame X, Y, Z, we need to express the components of the excitation/emission transition dipole moments $\boldsymbol{\mu}_i(\theta, \phi)$ in this frame. To do so, the components of $\boldsymbol{\mu}$ are given by the polar and azimuthal angles θ and ϕ in the microscopic frame (x', y', z') being defined by the symmetry axis of the molecular angular distribution function $f(\Omega)$ (see

Fig.1.5) :

$$\begin{bmatrix} \mu_{x'}(\theta,\phi) \\ \mu_{y'}(\theta,\phi) \\ \mu_{z'}(\theta,\phi) \end{bmatrix} = \begin{bmatrix} \sin\theta\cos\phi \\ \sin\theta\sin\phi \\ \cos\theta \end{bmatrix} \tag{1.35}$$

In the simple case where the distribution main symmetry axis lies in the sample plane (X,Y) the transformation matrix from the microscopic (x',y',z') to the macroscopic frame (X,Y,Z) is a rotation of an angle ρ (relative to X) around the Z axis and an out of plane angle η (relative to X,Y plane) :

$$[M]_{(x',y',z')\to(X,Y,Z)} = \begin{bmatrix} -\sin\rho & -\cos\rho\sin\eta & \cos\rho\cos\eta \\ \cos\rho & -\sin\rho\sin\eta & \sin\rho\cos\eta \\ 0 & \cos\eta & \sin\eta \end{bmatrix} \tag{1.36}$$

and therefore $\boldsymbol{\mu}$ can be expressed in the laboratory frame (X,Y,Z) as :

$$\begin{bmatrix} \mu_X(\theta,\phi,\rho,\eta) \\ \mu_Y(\theta,\phi,\rho,\eta) \\ \mu_Z(\theta,\phi,\rho,\eta) \end{bmatrix} = \begin{bmatrix} -\sin\rho\sin\theta\cos\phi - \cos\rho\sin\eta\sin\theta\sin\phi + \cos\rho\cos\eta\cos\theta \\ \cos\rho\sin\theta\cos\phi - \sin\rho\sin\eta\sin\theta\sin\phi + \sin\rho\cos\eta\cos\theta \\ \cos\eta\cos\theta + \sin\eta\cos\theta \end{bmatrix} \tag{1.37}$$

The goal of this work is to investigate how polarization tuning can provide information on the angular distribution $f(\Omega)$. This function can be written based on the molecular potential $U(\Omega)$ at thermal equilibrium T, following the Boltzmann statistics :

$$f(\Omega) \propto exp(-U(\Omega)/k_BT). \tag{1.38}$$

In many media $U(\Omega)$ is simplified (as we will see examples in next chapters). For instance in biological media where molecules undergo an orientational constraint the orientational distribution is most often defined as a cone shape with an abrupt change of the probe potential at a defined aperture angle $\theta = \Psi$ (Fig. 1.5 a) [69, 34, 68, 38] :

$$f(\theta,\phi) = \begin{cases} \frac{1}{4\pi\Psi} & \text{if} \quad |\theta| \leq \Psi \\ 0 & \text{otherwise} \end{cases} \tag{1.39}$$

In such a model fluorophores lie inside the cone aperture Ψ which depicts all their possible orientations, while their general orientation is defined by an angle ρ in the X,Y plane, which exhibits the orientation of the cone as depicted in Fig. 1.5 b, c. A more physical model that was introduced is a normalized Gaussian distribution :

$$f(\theta,\phi) = (\sqrt{\ln 2}/\Psi)\exp(-\ln 2\theta^2/\Psi^2). \tag{1.40}$$

where Ψ correspond to full width at half maximum (FWHM) and the ρ parameter is defined in the same way as in the cone model (Fig. 1.5). In those models where the distribution lies in the sample plane, the function $f(\Omega)$ is always defined by two unknown parameters Ψ (aperture of the distribution) and ρ (orientation of the distribution). Ψ is able to quantify a molecular order in the sample.

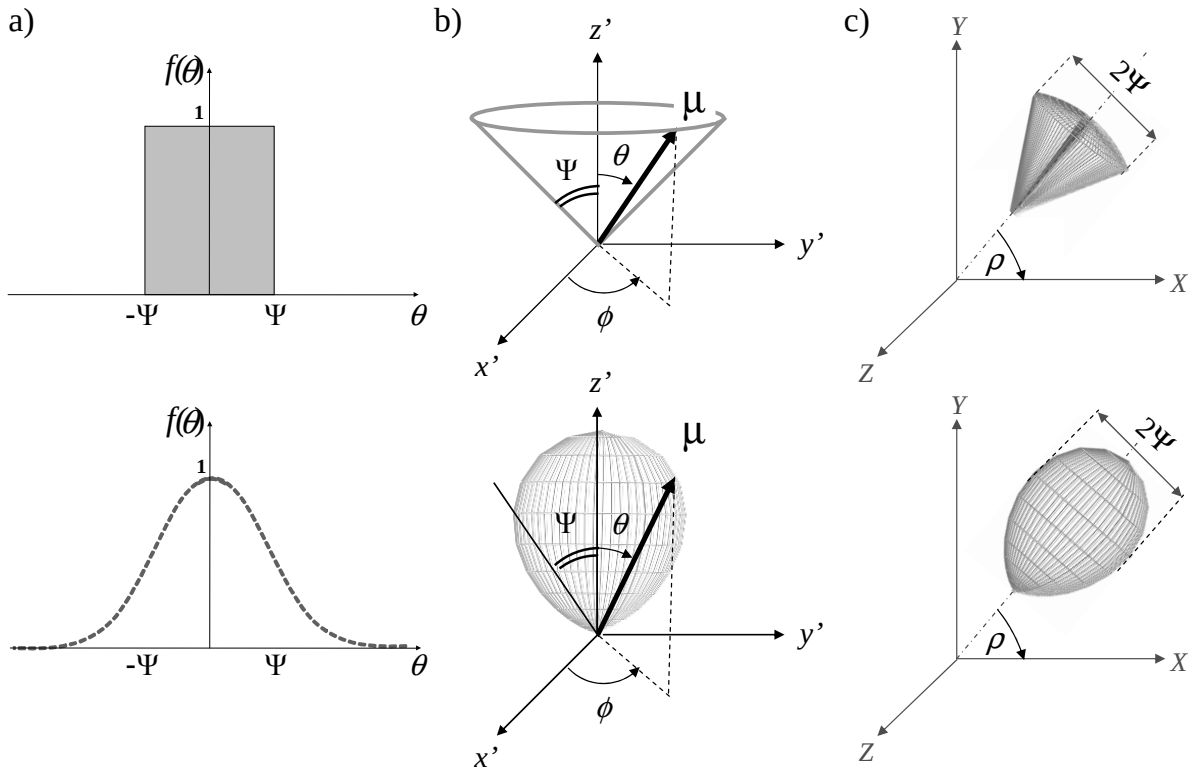

Figure 1.5: (a) FWHM of the cone and gaussian model equal to Ψ represented on the θ-dependent section (b) In the microscopic frame, the Ψ represents the cone aperture and the FWHM for the gaussian function. (θ, ϕ) defines the orientation of the molecular dipole in the cone and gaussian frame (x', y', z'). (c) In the laboratory frame (X, Y, Z), the angles ρ specifies the cone and the gaussian orientation in the plane (X, Y).

In the most general case where no *a priori* model is accessible, the distribution function can be decomposed on basis functions that are invariant upon rotation : the spherical harmonics $Y_m^{\mathbf{J}}(\theta, \phi)$. The unknown parameters are not anymore the aperture and the orientation information but the coefficients of this decomposition that carry information

on the symmetry of the distribution. $f(\theta,\phi)$ can be expressed by :

$$f(\theta,\phi) = \sum_{m,\mathbf{J}} f_m^{\mathbf{J}} \cdot Y_m^{\mathbf{J}}(\theta,\phi) \tag{1.41}$$

The $Y_m^{\mathbf{J}}(\theta,\phi)$ shape carries the symmetry of order $\mathbf{J}$, and becomes more and more complex when $\mathbf{J}$ increases. Furthermore the $\mathbf{J}$ orders are preserved upon rotation of $f(\theta,\phi)$ (a rotation of $Y_m^{\mathbf{J}}$ is just a different linear combination of $Y_{m'}^{\mathbf{J}}$ with the same $\mathbf{J}$). Therefore this decomposition is appropriate to give information on the symmetry of the distribution. In many cases $f(\theta,\phi)$ is a θ-dependent cylindrical symmetry function ($m = 0$), thus the above equation can be reduced to :

$$f(\theta) = \sum_{\mathbf{J}} f^{\mathbf{J}} \cdot P_{\mathbf{J}}(\cos\theta) \tag{1.42}$$

with $P_{\mathbf{J}}(\cos\theta)$ the $\mathbf{J}$-order Legendre polynomials defined by :

$$P_{\mathbf{J}}(\cos\theta) = \frac{1}{2_{\mathbf{J}}\mathbf{J}!}\frac{d^{\mathbf{J}}}{d(\cos\theta)^{\mathbf{J}}}(\cos^2\theta - 1)^{\mathbf{J}}. \tag{1.43}$$

a few examples are given in Fig. 1.6 showing :

$$\begin{aligned}
P_0(\cos\theta) &= 1 \\
P_2(\cos\theta) &= \frac{1}{2}(3\cos^2\theta - 1) \\
P_4(\cos\theta) &= \frac{1}{8}(35\cos^4\theta - 30\cos^2\theta + 3) \\
P_6(\cos\theta) &= \frac{1}{16}(231\cos^6\theta - 315\cos^6\theta + 105\cos^2\theta - 5).
\end{aligned} \tag{1.44}$$

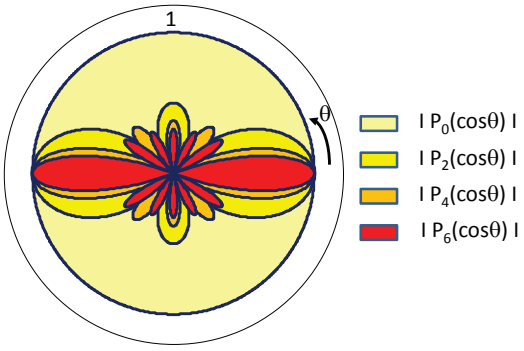

Figure 1.6: Representation of the modulus of the Legendre polynomials for $\mathbf{J} = 0, 2, 4, 6$.

It can be seen that when $\mathbf{J} = 0$ the $P_{\mathbf{J}}(\cos\theta)$ is isotropic, while when the $\mathbf{J}$ order increases the function gets narrower and more complex. The average values of the Legendre polynomials $\langle P_{\mathbf{J}}(\cos\theta)\rangle$ are called "order parameters" [70] :

$$\begin{aligned}\langle P_{\mathbf{J}}\rangle &= \langle P_{\mathbf{J}}(\cos\theta)\rangle = \int_\theta P_{\mathbf{J}}(\cos\theta)\sum_{\mathbf{J'}} f^{\mathbf{J'}}P_{\mathbf{J'}}(\cos\theta)\ \sin\theta\, d\theta \\ &= \sum_{\mathbf{J'}} f^{\mathbf{J'}}\int_\theta P_{\mathbf{J}}(\cos\theta)P_{\mathbf{J'}}(\cos\theta)\ \sin\theta\, d\theta = \sum_{\mathbf{J'}} f^{\mathbf{J'}}\delta_{\mathbf{JJ'}} = f^{\mathbf{J}} \qquad (1.45)\end{aligned}$$

using the definition :

$$\langle A\rangle = \int_0^\pi A(\theta)f(\theta)\sin\theta d\theta \qquad (1.46)$$

and the orthogonality property of the Legendre polynomials. The weighting factor $f^{\mathbf{J}}$ is therefore exactly the $\mathbf{J}$ order parameter that will be used to define the molecular order.

As we will see later in section 1.3.4 only a few orders are accessible from fluorescence measurements. Therefore the definition of the function $f(\theta)$ is truncated to a limited $\mathbf{J}_{max}$ value. In order to represent how this truncated function is deformed as compared to the initial gaussian or cone function, we calculate it using eq 1.45 and :

$$f(\theta) = \sum_{\mathbf{J}\leq\mathbf{J}_{max}} \frac{2\mathbf{J}+1}{2}\langle P_{\mathbf{J}}(\cos\theta)\rangle P_{\mathbf{J}}(\cos\theta). \qquad (1.47)$$

Fig. 1.7 represents the effects of the truncation for both the gaussian and cone functions. When we limit the composition to $\mathbf{J}_{max} = 6$ the shape is much better reconstructed for the gaussian than for the cone distribution, which is due to the smoother shape of the gaussian function. However the aperture angle Ψ is well preserved in both cases. Decreasing the decomposition to $\mathbf{J}_{max} = 4$ still keeps the qualitative information on Ψ.

1.3 Polarization resolved fluorescence analysis

1.3.1 Fluorescence anisotropy

The idea to investigate a molecular structure by a polarization resolved fluorescence method was introduced by Perrin in 1926 [71] and applied by Weber in 1953 to a structural study of the binding of small molecules and proteins [72]. This method is based on the fact that fluorophores will only absorb photons when their electric oscillations are parallel to the electronic transition dipole moment (as seen in the P_{abs} function in eq 1.28). The relationship between the polarization of the excitation beam and the subsequently emitted fluorescence is thus studied. The principle of this technique is depicted in Fig. 1.8.

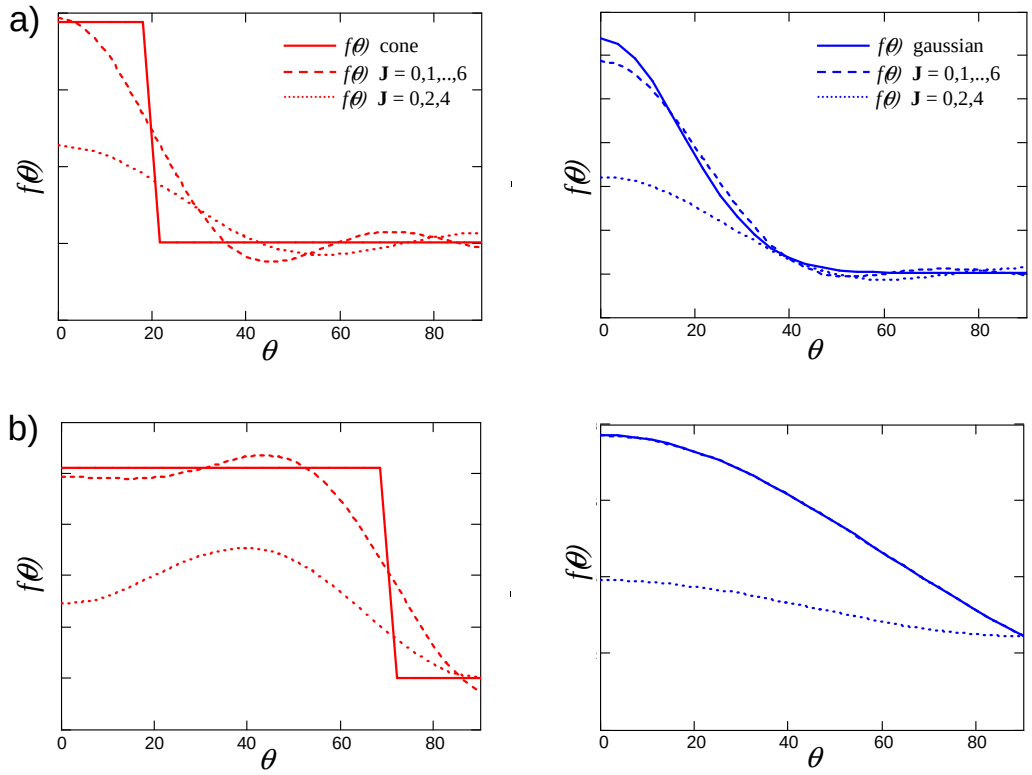

Figure 1.7: Cone and gaussian models reconstructed by using Legendre polynomials for molecular distribution parameter : (a) $\Psi = 20°$ and (b) $\Psi = 70°$ (note that the gaussian curve and the curve for $\mathbf{J} = 0, 1, 3, 4, 5, 6$ are superimposed).

The vertically polarized light (along Z direction) excites photo-selectively molecules in a cuvette containing a fluorescence solution. The fluorescence intensities measured in two perpendicular polarization directions X and Z are called $I_\perp$ and $I_{||}$ respectively. A ratiometric analysis of these two states provides information on the fluorophore orientational behavior using the "anisotropy" A:

$$A = \frac{I_{||} - I_\perp}{I_{||} + 2I_\perp}. \tag{1.48}$$

This ratiometric analysis presents the advantage to be independent from the intensity fluctuations and therefore only sensitive to variations of $I_\perp$ relative to $I_{||}$. This method permits quantitative analysis of conformational properties of macromolecules in very viscous solutions. The factor 2 in the eq 1.48 is introduced because of the perpendicular angle between the excitation and detection directions which introduces redundancies in the $I_\perp$ definition. In microscopy the fluorescence anisotropy is generally measured in the same direction as the incident excitation, which is circularly polarized to avoid any

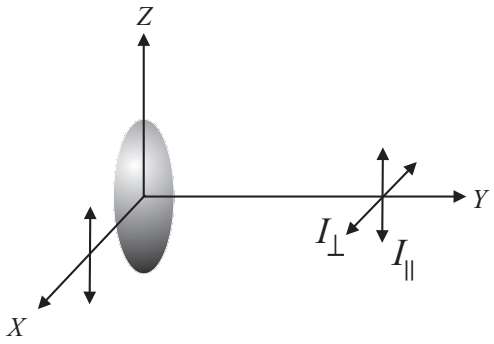

Figure 1.8: Principle of the anisotropy fluorescence analysis. The fluorescence intensities are detected for vertically $I_{||}$ and horizontally $I_\perp$ polarized emission, when the sample is excited with vertically $I_{||}$ polarized light.

angular photoselection (Fig. 1.9 a). The anisotropy is thus defined by :

$$A = \frac{I_Y - I_X}{I_Y + I_X} \tag{1.49}$$

In an ordered sample, A varies between (+1) when the fluorescence dipoles lies along Y, and (-1) when they lies along the X direction. All intermediate values will be reached if the molecular orientations are either distributed within a cone (of aperture Ψ) or globally rotated. In this scheme, since only one quantity is measured, only one unknown parameter can be retrieved. Therefore this analysis is only successful in simplified cases, for instance where molecules posses an angular distribution of cylindrical symmetry of known orientation, which reduces the amount of unknown parameters [73, 74]. An example of the anisotropy analysis is depicted in Fig. 1.9 b where a cone model of an aperture Ψ and of an orientation ρ is used. The polarization anisotropy A is calculated by using the intensities I_X and I_Y measured in two polarization detection directions (see eq 1.34), for $\rho = 0°$, $\rho = 45°$ and $\rho = 90°$ as a function of a cone aperture Ψ. It is clearly seen that knowing the molecular orientation ρ, it is possible to deduce the cone aperture Ψ and thus determinate the degree of order within the sample. However this works only when the mean orientation of the cone lies close to the major axes X, Y. As soon as ρ lies around 45° no information about molecular distribution can be obtained. Moreover the determination of Ψ requires precise information on ρ because a small change in this parameter can lead to very different results. The anisotropy analysis has therefore been applied in very specific situations :

- simplified orientational distribution function where (i) the symmetry is of cylindrical distribution and (ii) the mean orientation of the distribution can be *a priori* known [34, 68],

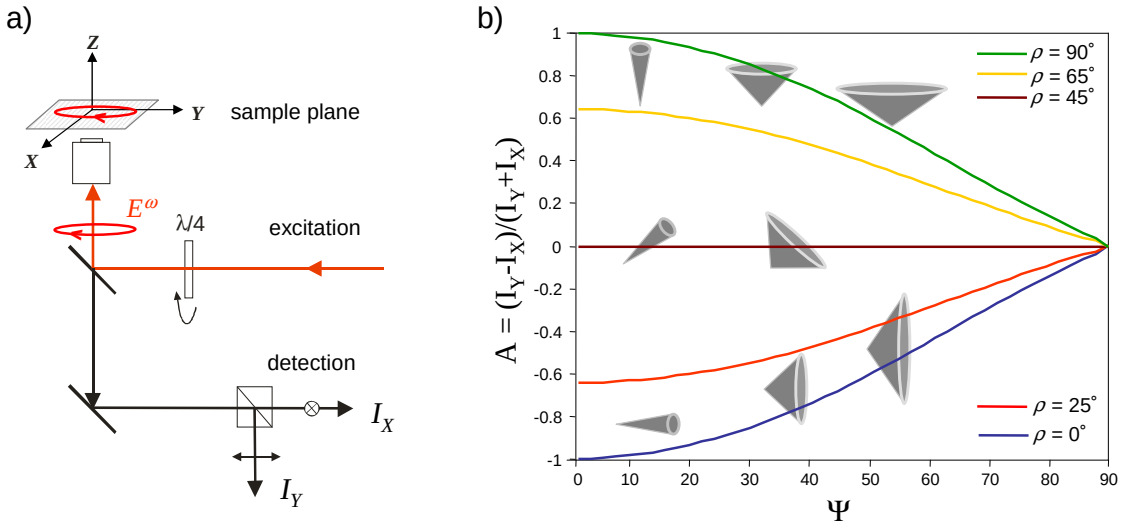

Figure 1.9: (a) Circularly polarized incident field $\mathbf{E}^{\omega}$ excites the sample, the detected intensities I_X and I_Y are measured in two orthogonal polarization directions. (b) A factor defined in the text, calculated for a cone aperture model, at different cone mean orientations ρ.

- measurements in isotropic viscous solutions in order to obtain information such as $\boldsymbol{\mu}^{abs}/\boldsymbol{\mu}^{em}$ relative angles or fluorescence resonance energy transfer (FRET) [75],
- single molecule studies, where A is directly related to the orientation of the molecule [76]. This has been recently extended to super-resolution microscopy imaging [77],
- time resolved measurements to retrieve orientational diffusion rates in isotropic media and extended further to functional contrasts in isotropic intracellular media [32, 33].

Nevertheless, the anisotropy has been largely used to address the problem of "molecular orientational order" since the seminal work of Axelrod [34], in which the orientation of long chain carbocyanine dyes in lipid membranes was determined using steady-state fluorescence polarization microscopy. In this article theoretical expressions where derived for polarized fluorescence intensity as a function of location on the membrane surface and experimental polarization ratios were measured and compared with the corresponding theoretical ratios to determine the most probable probe orientation in the membrane. This work has been later extended to model cell membranes imaging in different lipid compositions and round shape cells [68, 78, 79, 13, 80, 29]. A-part from the membrane studies the fluorescence anisotropy analysis has been applied to the determination of the

width of the angular distributions in biopolymers such as actin filaments [35] and also the mean molecular orientation angles of muscle fibers [73] and septin filaments [38].

Unfortunately many problems require the knowledge on both orientation and symmetry information which are two important components of a distribution function (see section 1.2). In general the molecular and biological media exhibit complex and heterogenous angular distributions [81] and it is clear that anisotropy imaging is limited in this context. For these reasons a more refined polarimetric analysis is required.

1.3.2 Polarimetric analysis : a tool to probe molecular angular distribution functions

In a complete polarimetric analysis the excitation of the fluorophores is controlled over a large number of polarization states due to the rotation of the incident polarization beam. Essentially the linear polarization of the incident electric field $\mathbf{E}$ is rotated in the sample plane X, Y of an angle α relative to X-axis by a half wave plate at the entrance to the microscope (Fig. 2.1). The emitted fluorescence signal is detected for two perpendicular polarization directions I_X and I_Y for an aperture distribution lying in the sample plane (X, Y), the 2PEF intensity of the ensemble of molecules expressed by equation 1.34 is thus written:

$$I_i^{2ph}(\alpha, \rho, \eta, \Psi) = \int_0^{2\pi} \int_0^{\pi} |\boldsymbol{\mu}_i(\Omega, \rho, \eta) \cdot \mathbf{E}(\alpha)|^4 |\boldsymbol{\mu}_i(\Omega, \rho, \eta)|^2 f(\rho, \eta, \Psi)\, \mathbf{d}\Omega \tag{1.50}$$

Polarization intensity is now a function of the molecular orientation ρ, the molecular distribution aperture Ψ and the polarization of the incident electric field $\mathbf{E}(\alpha)$. Polarization responses are represented as polar diagrams where each measurement point is a vector pointing from the origin with an amplitude equal to the fluorescence intensity and a tilt angle relative to X equal to α. This allows a direct visualization of the fluorescence angle dependence relative to a rotation of the excitation field polarization. The form of the polarimetric responses depends on the medium order and orientation properties. In order to get a better impression to what kind of information this analysis gives access, let us consider a few fundamental cases of molecules lying in the X, Y plane (Fig. 1.10) :

Polarimetric response from *1D crystal* of $\theta = \frac{\pi}{2}, \phi$ fixed orientation ($f(\theta, \phi) = \delta_{\theta=\pi/2,\phi}$). In such a sample all molecules point in the same direction and the transition dipole moment μ is oriented with an angle ϕ relative to X-axis. A maximum of the fluorescence intensity corresponds to the dipole orientation and thereby the tilt of the polarimetric responses indicates the macroscopic crystal orientation (Fig. 1.10).

In an *isotropic sample* ($\Psi = 90°$) where dipole moments are fixed, rotational diffusion of the fluorophore is prevented. In this case the incident electric field $\mathbf{E}(\alpha)$ always excites the fluorophores whatever the polarization angle α. Nevertheless because of the photoselection the highest fluorescent signal is obtained for polarization parallel to X and Y-axis. Therefore the polar graph shows two symmetric perpendicular patterns. The total fluorescent signal $I_X + I_Y$ is constant and as expected from an isotropic media the polarimetric pattern is circular (Fig. 1.10).

In *a solution* fluorophores move and rotate quickly, so that in the time between the absorption and the subsequent fluorescence emission they have completely changed their orientation. This results in decorrelation between absorption and emission dipole moment and circular shape of the polarimetric pattern for both I_X and I_Y. The reason of this will be explained in chapter 2.

General *statistic organization* ($\Psi < 90°$). In the case of molecular disorder, when molecules are not oriented randomly but distributed in the cone aperture Ψ, the form of the polarimetric responses gives access to more complete information on molecular orientation and distribution. This subject will be also explored in next chapters.

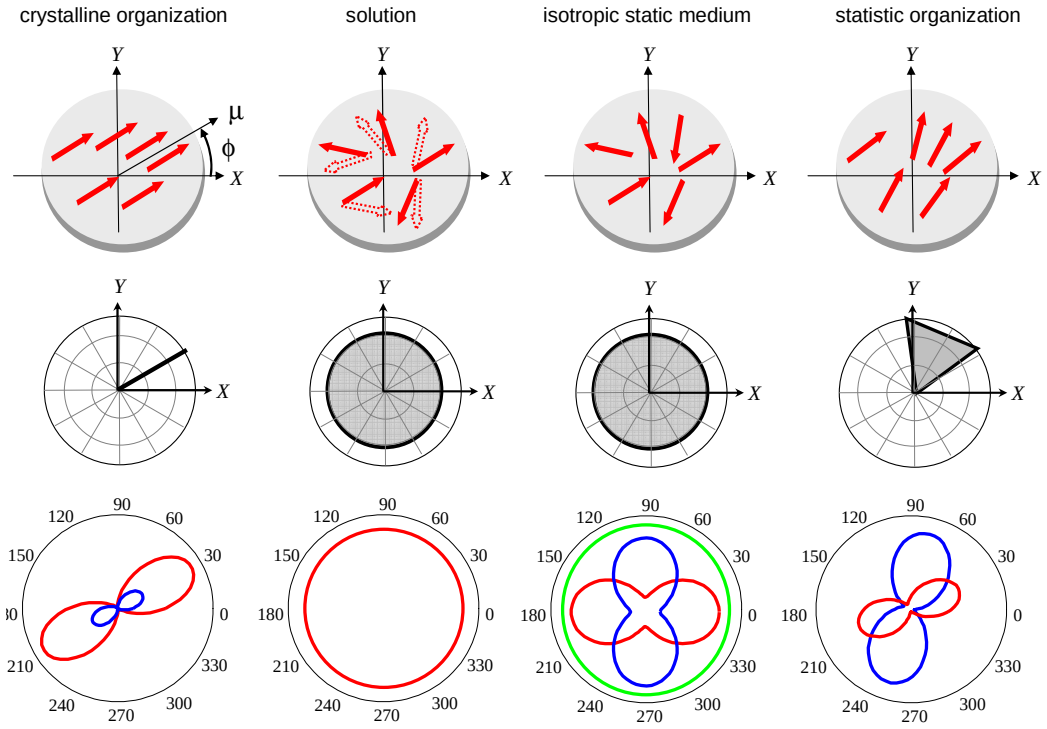

Figure 1.10: Schematic representations of the molecular organization with corresponding polarimetric responses analyzed along X (red line) and Y (blue line) polarization directions.

1.3.3 Comparison of one, two and three-photon fluorescence

In addition to a less scattering, a deeper optical penetration and an intrinsic spatial resolution, the nonlinear nature of the excitation reduces the angular photoselection and thus ameliorates the angular sensitivity of polarized measurements.

Indeed, when a linearly polarized light excites an isotropic sample (with fixed dipoles and parallel orientation of absorption and emission dipole moments), the highest probability of absorption occurs for molecules whose transition dipole moment is orientated parallel to the incident polarization. Other molecules will also be excited however with lower efficiency. Based on eq 1.17 the probability of one-photon absorption between the $|0\rangle$ and $|1\rangle$ molecular levels :

$$P_{abs}^{1ph} \propto |\boldsymbol{\mu}_{01} \cdot \mathbf{E}^{\omega}|^2 \propto \boldsymbol{\mu}_{01} \cos^2\theta I^{\omega} \tag{1.51}$$

is proportional to $\cos^2\theta$, with θ the angle between transition dipole moment $\boldsymbol{\mu}$ and the incident field polarization $\mathbf{E}^{\omega}$. This results in an excited state angular distribution function of cylindrical symmetry ("photoselection distribution") depicted in Fig. 1.11. It can bee seen that the molecules lying in the plane $\perp$ to $\mathbf{E}$ will not be excited, while the molecules strongly tilted relative to the incident field polarization direction will have a small excitation probability. For two and three-photon excitation process the absorption is proportional to $\cos^4\theta$ and $\cos^6\theta$ respectively (see eq 1.29,1.31). This results in more highly oriented excited populations and thereby a reduced photoselection (Fig. 1.11).

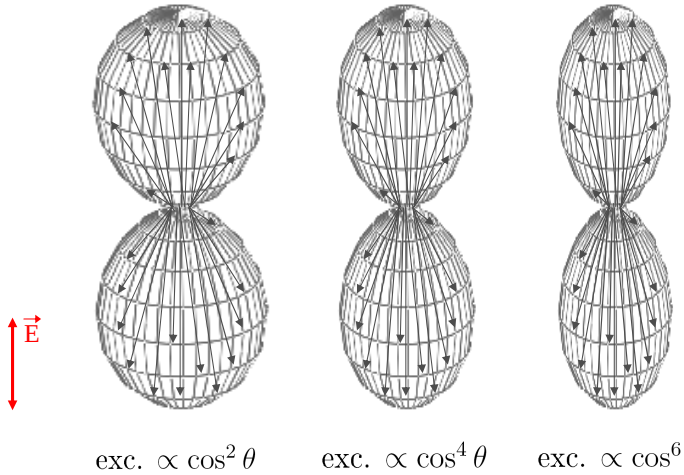

Figure 1.11: Excitation photoselection for one, two and three-photon excitations.

In order to reveal the importance of this effect let us consider the fluorescence polarimetric response of a single molecule oriented along an angle θ_m in the X, Y macroscopic

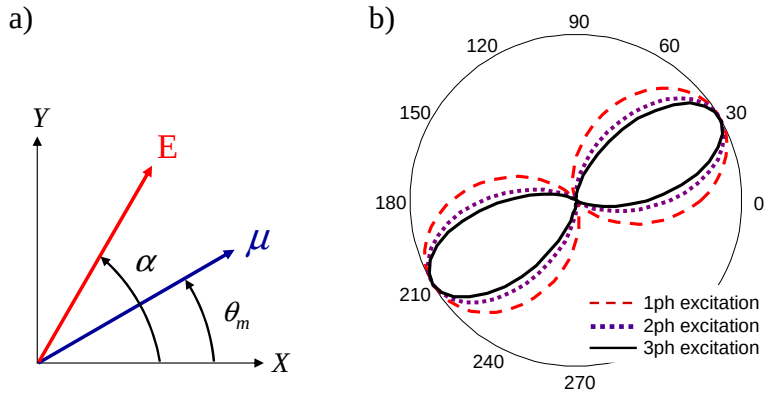

Figure 1.12: (a) The orientation of the absorption dipole moment and the rotation of the incident electric field of an angle α in XY plane. (b) Polarimetric responses I_X obtained with one-photon excitation (dashed line), two-photon excitation (dotted line) and three-photon excitation (solid line).

plane. The 1PEF, 2PEF, 3PEF polarimetric responses, depicted on Fig. 1.12b, analyzed in X polarization direction ($i = X$) depend on the dipole moment orientation and the polarization of the incident electric field $\mathbf{E}$. Precisely, while the global orientation of the lobes lies along the $\boldsymbol{\mu}$ direction ($\boldsymbol{\mu} = \boldsymbol{\mu}^{abs} = \boldsymbol{\mu}^{am}$ here), the width of the polarimetric pattern is strongly changed and decreased when increasing the order of the nonlinear excitation which the consequence of the narrower photoselection. As a results the dipole direction can be pointed with a better precision by using a higher order nonlinear excitation.

1.3.4 Read-out of a symmetry information using polarization resolved fluorescence

In this section we will explain which molecular symmetry information can be read-out by multiphoton fluorescence processes. For this we will consider two types of media : statistic distribution and crystalline symmetry, which require different approaches.

Statistic distribution

Let us consider a cylindrical geometry depicted in the Fig. 1.13 where the incident electric field $\mathbf{E}$ is parallel to X axis and the angle θ describes the transition dipole moment orientation relative to X axis (the distribution symmetry axis is along X). In the macroscopic

frame, the orientational distribution function is directly expressed by :

$$f(\theta) = \sum_{\mathbf{J}} f^{\mathbf{J}} \cdot P_{\mathbf{J}}(\cos\theta) \tag{1.52}$$

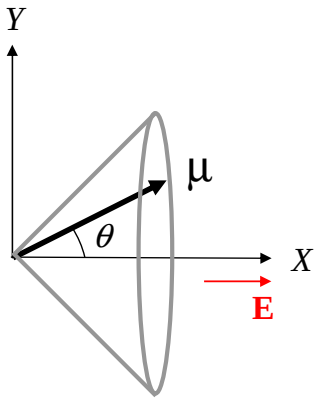

Figure 1.13: A cylindrical geometry in the macroscopic frame (X,Y,Z).

The probability of n-photon absorption in this case can be written :

$$P_{abs}^{n\,ph} = |\boldsymbol{\mu} \cdot \mathbf{E}|^{2n} = \cos^{2n}\theta(\mu^{2n} \cdot E^{2n}) \tag{1.53}$$

The n-photon fluorescence intensity without any analyzer is therefore expressed :

$$\begin{aligned} I_{tot} = I_X + I_Y &= \int_{\infty}\int_{\infty} \cos^{2n}\theta\,(\mu_X^2 + \mu_Y^2)(\theta,\phi)\,f(\theta)\,\sin\theta\,d\theta\,d\phi \\ &\propto \int \cos^{2n}\theta\mu^2 f(\theta)\,\sin\theta\,d\theta \end{aligned} \tag{1.54}$$

where $(\mu_X^2 + \mu_Y^2)(\theta,\phi) = \mu^2\cos^2\phi$. Both $\cos^{2n}\theta$ and $f(\theta)$ functions can be decomposed on the Legendre polynomials functions. In particular :

$$\cos^{2n}\theta = \sum_{p=0}^{2n} a_p P_p(\cos\theta) \tag{1.55}$$

where p is necessarily even (from the definition of Legendre polynomials). The n-photon fluorescence is thus defined by :

$$\begin{aligned} I_{tot} &= \sum_{\mathbf{J}=0}^{\infty} f^{\mathbf{J}} \sum_{p=0}^{2n} a_p \int_{\theta} P_p(\cos\theta) P_{\mathbf{J}}(\cos\theta)\sin\theta\,d\theta \\ &= \sum_{\mathbf{J}=0}^{\infty}\sum_{p=0}^{2n} a_p \delta_{p\mathbf{J}} \end{aligned} \tag{1.56}$$

Therefore **J** verifies $0 \leq \mathbf{J} \leq 2n$ and **J** : even. For this reason we can only read-out partial information of the distribution function $f(\theta)$: for the one-photon process the I_{tot} measurement leads to $\mathbf{J} \leq 2$, for the two-photon process $\mathbf{J} \leq 4$ and for three-photon process $\mathbf{J} \leq 6$. Note that projecting the detection over the X or Y directions adds two orders in the read-out information (since in this case $\mu_X^2 = \cos^2(\theta)$ or $\mu_Y^2 = \sin^2(\theta)$ will be included in eq 1.54). Overall, even though some information is lost in the molecular distribution function since the limited number of orders is accessible, we have shown in Fig. 1.7 that quantitative information on molecular order is still accessible.

Crystalline symmetry

A crystal is described by fixed orientations of molecular transition dipoles who define its

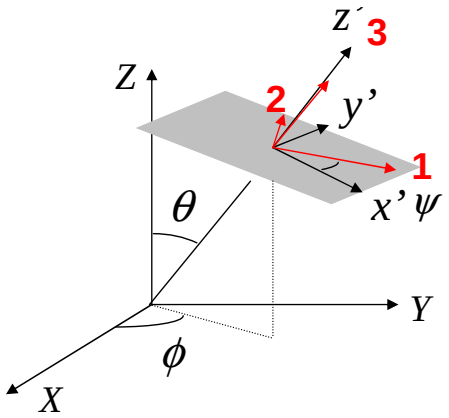

Figure 1.14: (a) Orientation of the unit cell frame (1,2,3) in the macroscopic frame (X,Y,Z). The (x',y') axes define the unit cell plane (grey rectangle) in the crystal frame (x',y',z'). (z' is the highest order symmetry axis).

unit cell symmetry. In this situation we will use a tensorial approach which is better suited to the crystal point group symmetry analysis. If the crystal point group is known one can deduce the susceptibility tensors for one, two and three-absorption process expressed previously by :

$$P_{abs}^{1ph} = \sum_{ij} \alpha_{ij} E_i E_j^* \tag{1.57}$$

$$P_{abs}^{2ph} = \sum_{ijkl} \gamma_{ijkl} E_i E_j E_k^* E_l^* \tag{1.58}$$

$$P_{abs}^{3ph} = \sum_{ijklmn} \xi_{ijklmn} E_i E_j E_k E_l^* E_m^* E_n^* \tag{1.59}$$

where the i,j,k,l,m,n indices span the unit cell frame (1,2,3).

Following the formalism introduced in equations 1.17, 1.25 and 1.30 these absorption susceptibility tensors can be reconstructed from the individual $\boldsymbol{\mu}_p$ dipoles constituting the unit cell ($p = 1, .., n$ with n the number of molecules in the unit cell) (here we assimilate $\boldsymbol{\mu}$ to the $\boldsymbol{\mu}^{abs}$ absorption dipoles of the crystal individual molecules) :

$$\alpha_{ij} = \sum_{p=1}^{n} \mu_p^i \mu_p^j \tag{1.60}$$

$$\gamma_{ijkl} = \sum_{p=1}^{n} \mu_p^i \mu_p^j \mu_p^k \mu_p^l \tag{1.61}$$

$$\xi_{ijklmn} = \sum_{p=1}^{n} \mu_p^i \mu_p^j \mu_p^k \mu_p^l \mu_p^m \mu_p^n \tag{1.62}$$

The emission probability is expressed similarly using the one-photon emission tensor α involving the $\boldsymbol{\mu}^{em}$ emission dipole in the unit cell frame. Assimilating $\boldsymbol{\mu}^{abs}$ and $\boldsymbol{\mu}^{em}$ to a single $\boldsymbol{\mu}$ direction leads to an identical expression as in eq 1.60. The 1PEF intensity along a direction of analysis q in the unit cell frame is for instance written :

$$I_q^{1ph}(\alpha) = \sum_{ij} (\alpha \otimes \alpha)_{ijqq} E_i E_j^*(\alpha) \tag{1.63}$$

with $(\alpha \otimes \alpha)_{ijqq} = \sum_{p=1}^{n} \mu_p^i \mu_p^j \mu_p^q \mu_p^q$, by extension 2PEF can be written :

$$I_q^{2ph}(\alpha) = \sum_{ijkl} (\gamma \otimes \alpha)_{ijklqq} E_i E_j E_k^* E_l^*(\alpha) \tag{1.64}$$

and 3PEF :

$$I_q^{3ph}(\alpha) = \sum_{ijklmn} (\xi \otimes \alpha)_{ijklmnqq} E_i E_j E_k E_l^* E_m^* E_n^*(\alpha) \tag{1.65}$$

The fluorescence intensity requires to express these susceptibilities in the macroscopic frame. The macroscopic coefficients $(\alpha \otimes \alpha)_{IJQQ}(\Omega)$, $(\gamma \otimes \alpha)_{IJKLQQ}(\Omega)$ and $(\xi \otimes \alpha)_{IJKLQQ}(\Omega)$ depend on both the crystal orientation defined by Ω ($\Omega = (\theta, \phi, \psi)$ being the Euler set of angles defined in Fig. 1.14) and its symmetry specified by its microscopic components α_{ij}, γ_{ijkl} and ξ_{ijklmn} :

$$(\alpha \otimes \alpha)_{IJQQ}(\Omega) = \sum_{ij} (\alpha \otimes \alpha)_{ijqq} (i \cdot I)(j \cdot J)(q \cdot Q)(q \cdot Q)(\Omega) \tag{1.66}$$

$$(\gamma \otimes \alpha)_{IJKLQQ}(\Omega) = \sum_{ijkl} (\gamma \otimes \alpha)_{ijklqq} (i \cdot I)(j \cdot J)(k \cdot K)(l \cdot L)(q \cdot Q)(q \cdot Q)(\Omega) \tag{1.67}$$

$$(\xi\otimes\alpha)_{IJKLQQ}(\Omega) = \sum_{ijklmn} (\xi\otimes\alpha)_{ijklmnqq}(i\cdot I)(j\cdot J)(k\cdot K)(l\cdot L)(m\cdot M)(n\cdot N)(q\cdot Q)(q\cdot Q)(\Omega) \tag{1.68}$$

where the $(i \cdot I)$ factors are the Ω-dependent cosine directors of the microscopic frame relative to macroscopic one. They are formed as follows :

$$\begin{bmatrix} (X.x),(X.y),(X.z) \\ (Y.x),(Y.y),(Y.z) \\ (Z.x),(Z.y),(Z.z) \end{bmatrix} \tag{1.69}$$

$$= \begin{bmatrix} \cos\phi\cos\theta\cos\psi - \sin\phi\sin\psi, \sin\phi\cos\theta\cos\psi + \cos\phi\sin\psi, -\cos\psi\sin\theta \\ \cos\phi\cos\theta\sin\psi - \sin\phi\cos\psi, -\sin\phi\cos\theta\sin\psi + \cos\phi\cos\psi, \sin\psi\sin\theta \\ \cos\phi\sin\theta \end{bmatrix}$$

The 1PEF, 2PEF, 3PEF polarimetric responses analyzed in X polarization direction can finally be expressed :

$$I_X^{1ph}(\alpha) = \sum_{IJ}(\alpha\otimes\alpha)_{IJXX}(\Omega)E_I E_J^*(\alpha) \tag{1.70}$$

$$I_X^{2ph}(\alpha) = \sum_{IJKL}(\gamma\otimes\alpha)_{IJKLXX}(\Omega)E_I E_J E_K^* E_L^*(\alpha) \tag{1.71}$$

$$I_X^{3ph}(\alpha) = \sum_{IJKLMN}(\xi\otimes\alpha)_{IJKLXX}(\Omega)E_I E_J E_K E_L^* E_M^* E_N^*(\alpha) \tag{1.72}$$

where I, J, K, L, M, N indices span the macroscopic frame (X, Y) and the E_I is the incident field polarization projections on each macroscopic axis.

Fig. 1.15 depicts the sum $I_X + I_Y$ for 1PEF, 2PEF and 3PEF polarimetric responses calculated for different set of dipoles representing different symmetries. These dipoles are positioned in the sample plane (X, Y) and of same magnitude. As expected, the polarimetric responses depend on the symmetry built by the dipoles :

- one dipole unit cell (Fig.1.12) : this situation can be studied by any order of fluorescence as it was shown in the previous section
- two dipoles unit cell (Fig.1.15 a, b) : this scheme can be studied by any order, except if they form a pure symmetry such as a four fold symmetry where $\mathbf{J} = 4$. In this situation one-photon fluorescence process becomes polarization independent since this symmetry cannot be read-out. This was demonstrated in the previous section for statistical distributions.

- three dipoles unit cell (Fig.1.15 c, d) : this scheme can be studied by any order, except if they form a pure symmetry such as a six fold symmetry where **J** = 6, which can only be read-out by three-photon fluorescence process.

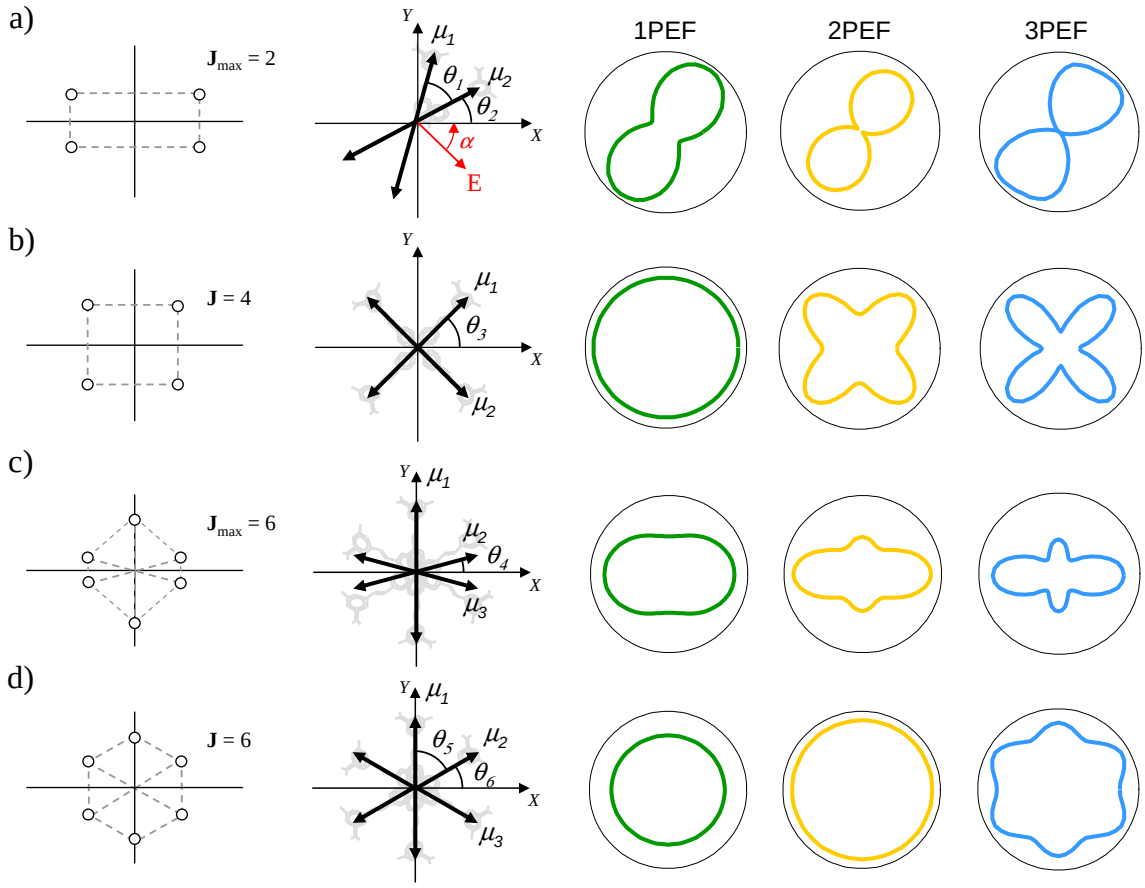

Figure 1.15: Examples of 2D symmetries built up from unit dipoles (oriented in the sample plane (X, Y) and of same magnitude) and corresponding polarization responses I_{tot} recorded for rotating electric field $E(\alpha)$. (a) Two dipoles $\theta_1 = 50°, \theta_2 = 30°$. (b) Four-fold symmetry $\theta_3 = 45°$. (c) Three dipoles $\theta_4 = 10°$. (d) Six-fold symmetry $\theta_5 = 60°, \theta_6 = 30°$.

Note that if the detected intensities are projected on the X, Y axes, these fluorescence processes become sensitive to two more orders of symmetry. This is one of the reason why we will favor this situation in the next chapters. Finally, this study show that to analyze a crystal, using multiphoton fluorescence polarimetry, different situations are possible : either the crystal symmetry and associated tensors are known (for instance from the dipoles angular positions in the unit cell) and therefore its orientation can be determined,

or the crystal orientation is known and same information on its order of symmetry can be given. We will see in the next chapters that another effect occurring in molecular crystals, energy transfer between molecules, will produce another specificity of crystalline media that can be exploited for further diagnostics in such systems.

1.4 Conclusion

In this chapter we described how polarimetric multiphoton fluorescence can unravel information on the properties of molecular orientational distributions. We showed in particular that such analysis is able to retrieve information on both the mean orientation and the aperture of a cylindrical distribution. We also demonstrated the potentiality of this technique to study the symmetry properties of both statistical and crystalline distributions. Note that the tensorial approaches introduced in this chapter can be extended to any other nonlinear contrasts such as coherent second harmonic or third harmonic generations [43].

Chapter 2

Polarization distortion effects in polarimetric multiphoton microscopy

Polarimetric studies require the control of the excitation polarization state at the focal spot of an objective, which is a delicate task : although the polarization state of the excitation beam at the entrance of the microscope is known, this beam after entering the microscope can suffer from instrumental distortions that might change its initial state. Therefore in order to obtain the relevant information from the polarimetric analysis a particular care has to be brought on these possible polarization distortions.

Multiphoton microscopy is particularly developed in epi-detection scheme where the incident and emitted signals are governed by the same objective. Therefore this configuration is used in 2PEF experiments presented in this thesis, except for three-photon detection which requires UV optics for the detection of proteins fluorescence. In such a scheme, several parameters can affect an incident polarization.

First, excitation polarization fixed at the entrance of the microscope will be affected by reflection optics (principally the dichroic beam splitter) which can induce additional phase shifts on the initial polarization states. The effect of the beam splitter is generally described by its dichroism and ellipticity factors. Second, the high numerical aperture objective will produce polarization deformation of the exciting beam in the focal plane. In particular, an extra coupling along the propagation direction appears to be non-negligible when using high aperture focusing [82]. Third, the same objective will scramble the detected polarization states of emission.

Apart from these instrumental effects, other polarization distortions can originate from the sample itself. At the molecular scale, the angle between the absorption and emission dipoles of the fluorescent probe, and the possible presence of Fluorescence Reso-

nant Energy Transfer between neighbor molecules (homo-FRET) are possible reasons for polarization fluorescence modifications. Both effects, for which excitation and emission become decorrelated, are expected to introduce a degree of depolarization of the polarimetric responses, which might lead to a misinterpretation of the polarimetric data. At last, when an excitation beam propagates through a micrometric scale depth it can be affected be the anisotropic nature of the sample itself, through the birefringence effect. Birefringence, which introduces extra phase shifts of polarization can lead to the erroneous determination of the sample properties. This effect can occur in crystalline [83] and biological samples, in particular from fibrillar structures such as collagen [84, 85].

In this chapter we will present the experimental set-up used in this work and a global analysis of experimental factors affecting polarization responses in two-photon microscopy. In particular we will describe a model accounting for the dichroism and ellipticity effect of the reflection optics and develop a calibration technique that allows for the determination of these parameters. We will use a numerical calculation of the emitted signal to quantify the contribution of polarization spatial distortions induced by the high numerical aperture focussing and collection. We will introduce the effects of distinct absorption and emission angles of the molecular transition dipoles, as well as the presence of fluorescence resonance energy transfer (homo-FRET) on the polarization resolved studies. Finally we will analyze the influence of the birefringence in polarization resolved microscopy applied to anisotropic samples and we will develop a method to measure and account for this effect.

2.1 Polarization resolved experimental set-up

2.1.1 Two-photon fluorescence microscopy set-up

The experimental setup used in 2PEF microscopy is depicted in the Fig. 2.1. The excitation light source is a tunable Ti:Sapphire laser (which characteristics are described below). The incident wavelength is set for each sample to be the maximal at two-photon excitation, with a typical averaged power of a few mWs. The laser beam is reflected by a dichroic mirror and focused on the sample by a high numerical aperture objective. The backward emitted signal is collected by the same objective and filtered by a visible bandpass filter. The fluorescence signal is directed to a visible broad band polarization beam splitter that separates the beam towards two detectors (avalanche photodiodes or Photomultipliers). Images are performed by the scanning of the sample on a piezoelectric stage, which allows precise location of polarimetric measurement points. In 2PEF polarimetric measurement

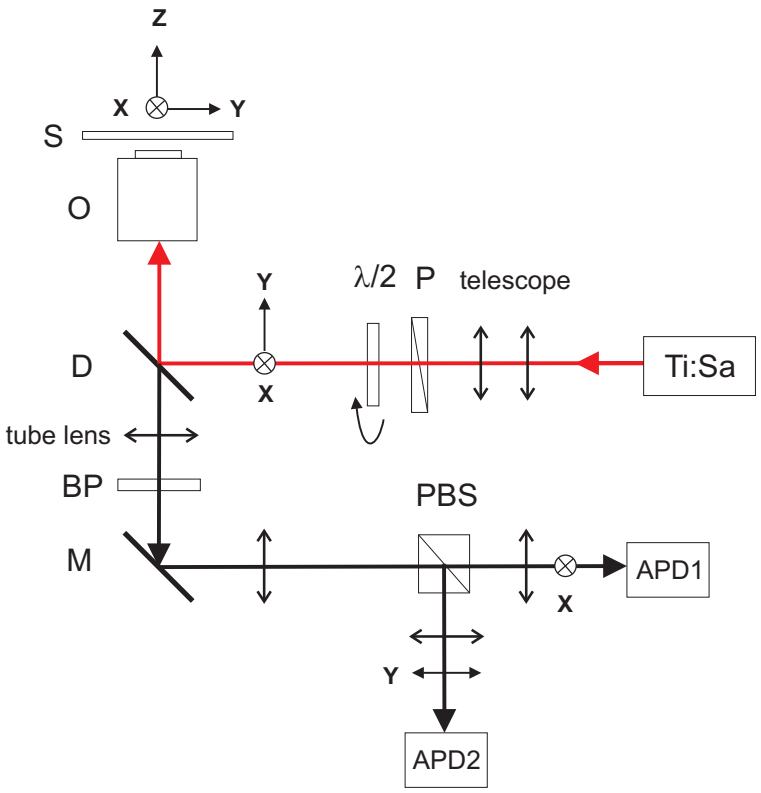

Figure 2.1: Experimental setup. Ti:Sa: tunable Ti:Sapphire laser (690nm - 1080nm); P: polarizer, $\lambda/2$: tuneable half waveplate; S: sample; D: dichroic mirror; O: objective; M: mirror; BP: VIS bandpass filter; PBS: polarization beamsplitter; APD1, APD2: avalanche photodiodes detecting respectively the I_X and I_Y components of the signal.

the linear polarization of the incident laser beam is rotated continuously in the sample plane by an achromatic half waveplate mounted on a step rotation motor at the entrance of the microscope. For each value of the polarization angle, the emitted signal is recorded for two perpendicular directions X and Y defining the sample plane (these directions also correspond to the s and p reflection directions for the dichroic beamsplitter).

Femtosecond Ti:Sa laser

The IR excitation light source is a tunable Ti:Sapphire laser (Chameleon, Coherent) which emits red and near-infrared light in the range from 680 to 1080 nanometers. The lasing medium, a crystal of sapphire (Al2O3) doped with titanium ions and pumped with 5 W diode pumped solid state laser (Verdi, Coherent), delivers 150 fs pulses at a repetition rate 80 MHz. This pulsed laser provides the peak-power sufficiently high to obtain two

and three-photon excitation processes. Typical power at the exit of the laser is around 400-500mW for the wavelength between 780-1040nm used in this work. This power is decreased, before being focused on the sample, to a few mW by optical density filter as well as half waveplate placed at the entrance of a polarizer.

Dichroic mirrors

The IR laser beam undergoes reflection on the dichroic mirror FF720-SDiO1 (Semrock) for excitation beam at 800nm and 640 DCSPXR (Chroma, AHF Analysentechnik AG, Tübingen) for 950nm (The choice of the dichroic can be governed by polarization maintaining issues, as we will describe later). These mirrors reflect the IR and transmit VIS radiation (Fig. 2.2). The two-photon fluorescence signal collected by the objective is transmitted by mirrors with an efficiency of about 90-95%.

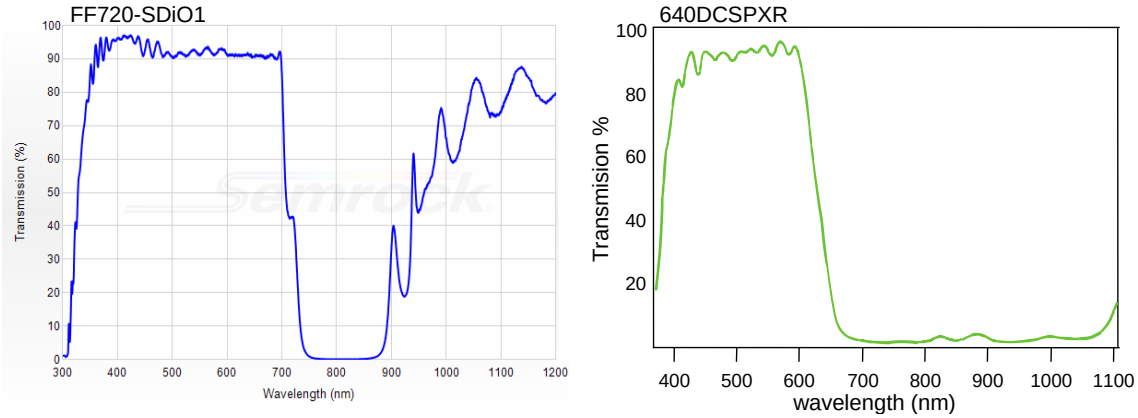

Figure 2.2: Transmission spectra of the dichroic mirrors used in this work (reproduced from Semrock and Chroma documents).

Microscope objective

The high numerical aperture (NA 1.2) water immersion objective (plan Apo Nikon) tightly focuses the laser beam on the specimen. A linear magnification of this objective is $\times 60$ and adjustable working distance (WD) between 0.15-0.21mm is optimized to work with 0.17mm microscope slides. Apochromatic design provides the highest degree of correction for spherical and chromatic aberrations. A half-angle of the maximum cone θ_{obj} of the fluorescence signal that can enter or exit the objective covered with water ($n = 1.33$):

$$NA = nsin\theta_{obj} \tag{2.1}$$

is $\theta_{obj} = 1.125$ rad, thus 64.4°.

Polarization beamsplitters

Two-photon fluorescence signal is separated by a polarization beam splitter (10FC16PB.3, Newport). The cube polarizer consists of a pair of precision right-angle prisms carefully cemented together to minimize wavefront distortion. A multilayer dielectric polarizing beamsplitter coating is optimized for a 420 to 680 nm wavelength range. The four faces of the cube are antireflection coated with this multilayer dielectric coating to minimize surface reflection losses. The emission signal is projected on two orthogonal, linearly polarized components. p polarized light is transmitted, while s polarized light is reflected. Note that p and s polarization directions correspond to the polarization of light parallel to X and Y axis respectively.

Scanning of the sample

Most part of analyses presented in this work were performed by using a Piezo-eletric scanner (P.Instrument) which enables 3D scanning of the sample in the range of 200μm in the X and Y directions and 20μm in the Z direction at variable steps from 15nm to 242nm. Typically, one image scan of this size using a 100nm sampling lasts about a few minutes, the dwell time per pixel being around 20ms. Once a position of interest has been selected, a polarimetric measurement is performed using 90 steps of incident polarization angle between 0° and 360° (180°), using an integration time per angle of 20ms to 50ms. Recently, a new technique has been developed in the laboratory based on the fast scanning of the excitation beam direction by two galvanometric mirrors placed at the entrance of the microscope. This technique allows to obtain a stack of images corresponding to multiple angles of the incident linear polarization. The polar plot is then retrieved from an arbitrary chosen place on the image stack. The advantage of this galvanometric scanning is a faster and parallel data acquisition, which is thus more adapted to *in vivo* samples investigation. The fast rotation of the scanning mirrors allows to obtain a polarimetric image stack with 150x150 pixels resolution for 90 polarization angles within a few minutes, which can be further lowered down to a few seconds by decreasing the angular resolution. The galvanometric scanning has been lately applied to the cell membrane polarimetric measurements presented in this work.

Detectors

The two-photon fluorescence signal collected by the objective is focused on the active areas (175μm size) of photon-counting modules based on silicone avalanche photodiodes (Perkin Elmer SPCM-AQR-14). The Single-Photon Counting Module (SPCM) is a self-contained photon counter which covers the wavelength range from 400nm to 1100nm (see Fig. 2.5). The photosensitive area achieves a peak photon detection efficiency of 70% at 650nm diameter and low dark-count rates (50-200 cps).
In the galvanometric scanning regime, large area (about 5mm) detectors were used due the non-descanned geometry of the detection (MP 993, Perkin Elmer).

2.1.2 Three-photon fluorescence set-up

In three-photon fluorescence microscopy, the excitation beam follows the same path as in two-photon fluorescence. However the detection part requires fused silica optics, in order to transmit UV radiation. For this reason, the 3PEF emitted signal is collected in a forward detection set-up by a UV objective (Fig. 2.3). The nonlinear signal then undergoes a reflection on a broad band mirror and is directed to a UV polarization beam splitter that separates the beam towards two UV bandpass filters. The fluorescence emission is detected simultaneously in the two perpendicular directions X and Y by two UV sensitive photomultipliers.

Microscope objectives

Three photon fluorescence signal is collected by quartz microscope objective ($\times$40, 0.6 NA, WD = 2mm, Partec) covered with UV antireflection coating 300-400nm that increases the efficiency of the transmission from 70% to 95%. The θ_{obj} aperture angle of this objective is 36.9°.

Dichroic mirrors

In forward detection set-up 3PEF signal undergoes a reflection on two dichroic mirrors FF665-DiO2 (Semrock) that reflect UV and VIS, and transmit IR radiation in order to filter the three-photon fluorescence signal. Note that in forward geometry set-up the laser beam is transmitted together with a fluorescence signal to the detectors by microscope objective. In order to get rid of the laser radiation a stronger filtering than in the epi-detection is necessary, which explains the use of two reflection steps.

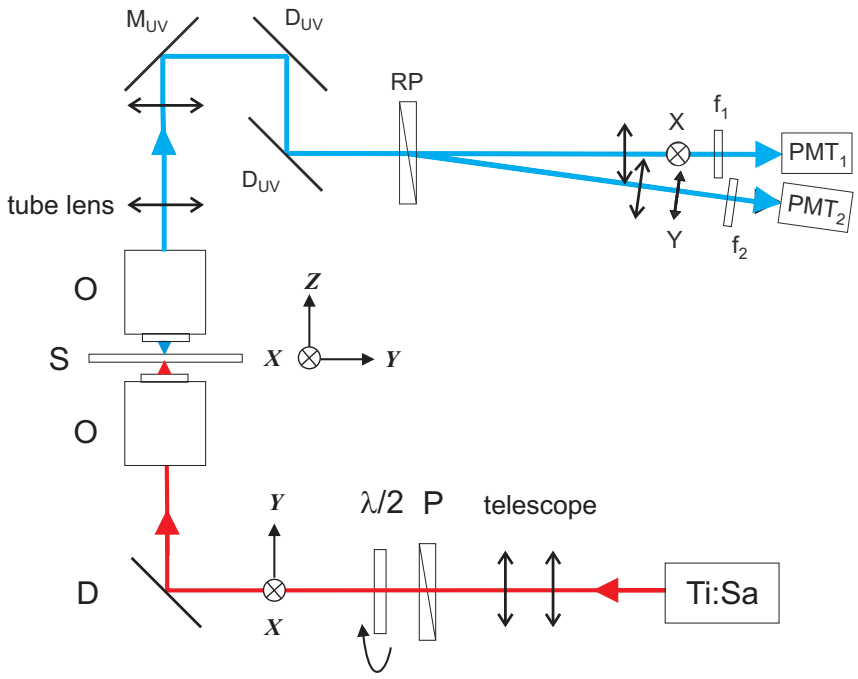

Figure 2.3: (a) Experimental setup. Ti:Sa: Ti:Sapphire laser; P: polarizer, $\lambda/2$: tuneable half waveplate; D: dichroic mirror; O: objective; S: sample; M: mirror; D_{UV}: dichroic mirrors transferring UV radiation; RP: polarization beamsplitter; PMT_1, PMT_2: photomultipliers detecting respectively the I_X and I_Y components of the signal.

Polarization beamsplitters

Three-photon fluorescence signal polarization contributions are separated by a Rochon Polarizer (PRH8010, CASIX) made of two cemented prisms by a-BBO material guaranteeing a wide transmission range 190-3500nm. Single Layer SiO2 on input and output surface of the cube makes it suitable for UV applications. The polarizer splits the fluorescence beam into components: p polarized light is transmitted, while s polarized light is deviated by 8°.

Detectors

Since in the three-photon fluorescence microscopy in proteins the specimen radiates light in the ultraviolet regime, the emitted signal is detected by two UV sensitive channel photomultipliers (MP 943, Perkin Elmer). Channel Photomultipliers operate according to the same general principles as PMTs, but is built from different materials and lack the PMT's multi-element dynode structure. Instead, the device contains a single hollow tube

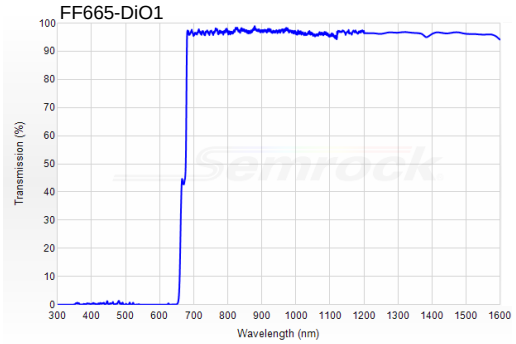

Figure 2.4: Transmission spectra of the dichroic mirror D_{UV} used in this work (reproduced from Semrock document).

internally coated with a semiconductor. Such design has several advantages: significantly less dark current is generated (10cps), photocounting is very fast (photons can be counted every 30ns in SPCM every 50ns). The fluorescence signal is focused on a photocathode of 5mm diameter and detected in the spectral range from 185 to 650 nm, with the highest sensitivity in ultraviolet and blue region (Fig. 2.5).

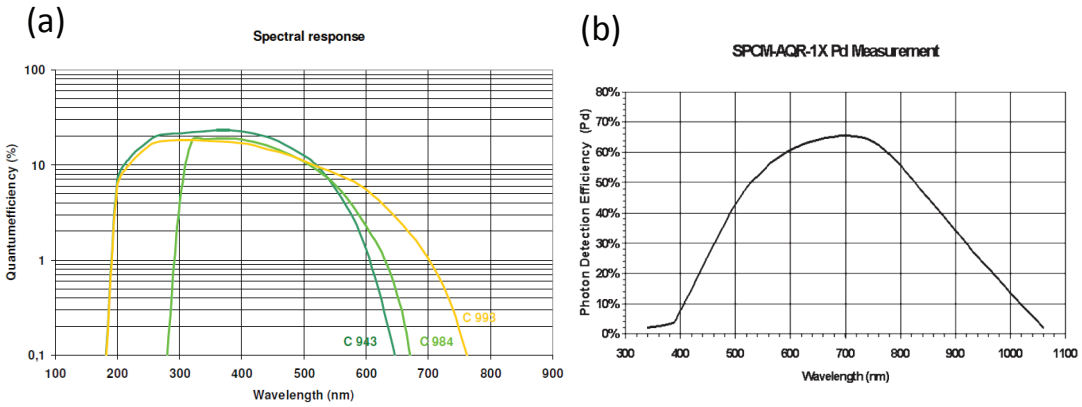

Figure 2.5: Comparison of the spectral sensitivity of the UV (a) PMT and (b) APD detectors (reproduced from Perkin Elmer document).

2.2 Polarization distortion introduced by reflection optics

2.2.1 Influence of dichroism and ellipticity on the polarization response

Upon reflection on the dichroic mirror (and possibly other optics), the incident field can be affected by a phase difference δ (ellipticity) and an amplitude factor γ (dichroism) between the two perpendicular polarization states s and p. In the geometry of the experiment, s and p also correspond to the X and Y directions defining the sample plane (Fig. 2.1). This field can be expressed as [86] :

$$\mathbf{E}(\alpha, \delta, \gamma) \propto \begin{bmatrix} \cos\alpha \\ (1-\gamma)\sin\alpha\, e^{i\delta} \\ 0 \end{bmatrix}. \tag{2.2}$$

with α the rotating polarization angle of the incident field relative to X axis. The influence of δ on the electric field is shown is Fig. 2.6. Two orthogonal polarization states

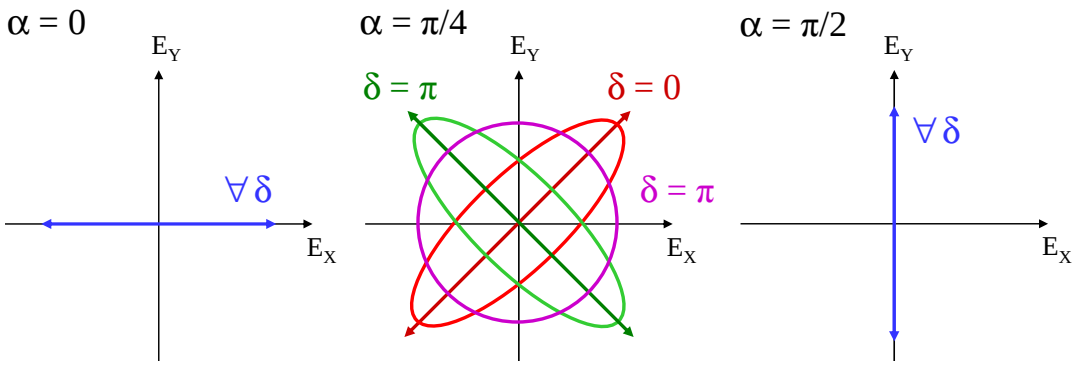

Figure 2.6: Influence of the δ ellipticity and γ dichroism on the linearly polarized electric field rotating of an angle α. When $\alpha = (0, \pi/2)$ the polarization stays linear $\forall\delta$. For intermediate direction of the incident field $\alpha = \pi/4$ the ellipticity strongly affects the linear polarization.

$\alpha = (0, \pi/2)$ are not affected by the ellipticity which is expected for the s and p directions. Likewise for $\delta = 0$, the wave stays linearly polarized whatever the rotation angle α. However when δ increase and incident fields rotates the linear polarization became more and more elliptical reaching circular polarization at $\delta = \pi/2$ and $\alpha = \pi/4$. For higher values of δ up to π the ellipticity decreases, but the ellipse switches side and is oriented

along $\pi - \alpha$. At $\delta = \pi$ the field is linear again, but along $\pi - \alpha$. γ will influence this picture by an amplitude factor on either X or Y directions.

The influence of the dichroic beamsplitter δ and γ parameters on the linear polarization has already been investigated by using a fluorescence isotropic sample made of molecules immobilized in a polymer layer [40]. The advantage of this isotropic geometry is to have polarimetric response depending on the field and not on the sample orientation. This technique permitted to retrieve the dichroism and ellipticity factors in a preliminary step before all studies, however it was limited for two reasons : first, it required the knowledge of the degree of homo-excitation energy transfer between the fluorophores, second it was influenced by a possible angle between the excitation and emission dipoles of the fluorophores [40]. These parameters are however not always available. Here, we present a simple and robust method to determine the influence of dichroic beamsplitter on the polarimetric response based on an isotropic solution in the same epi-geometry as used for future polarimetry analysis.

To start let us recall the fluorescence intensity along a given polarization direction i as defined in chapter 1 :

$$I_i(\alpha) = \int\int\int |\boldsymbol{\mu}^{abs}(\mathbf{\Omega}, \mathbf{r}) \cdot \mathbf{E}(\alpha, \mathbf{r})|^4 |\mathbf{E}^{em}(\mathbf{\Omega}, \mathbf{r}, \mathbf{k}) \cdot u_i|^2 f(\mathbf{\Omega}) \mathrm{d}\mathbf{\Omega} \mathrm{d}\mathbf{r} \mathrm{d}\mathbf{k} \tag{2.3}$$

In an aqueous solution, due to the long fluorescence lifetimes as compared to the rotational diffusion time, the orientation of the absorption dipole moment $\boldsymbol{\mu}_{abs}$ is decorrelated from that of the emission dipole moment $\boldsymbol{\mu}_{abs}$. For that reason $\boldsymbol{\mu}_{abs}(\mathbf{\Omega}, \mathbf{r})$ and $\boldsymbol{\mu}_{abs}(\mathbf{\Omega'}, \mathbf{r'})$ can be defined with two independent orientations $\mathbf{\Omega}$ and $\mathbf{\Omega'}$. Furthermore the orientation distribution function verifies $f(\Omega) = f(\Omega') = 1$. Eq. 2.3 can then be written as:

$$I_i(\alpha) \propto \int\int |\boldsymbol{\mu}^{abs}(\mathbf{\Omega}, \mathbf{r}) \cdot \mathbf{E}(\alpha, \mathbf{r})|^4 \mathrm{d}\mathbf{\Omega} \mathrm{d}\mathbf{r} \int\int\int |\mathbf{E}^{em}(\mathbf{\Omega'}, \mathbf{r'}, \mathbf{k}) \cdot u_i|^2 \mathrm{d}\mathbf{\Omega'} \mathrm{d}\mathbf{r'} \mathrm{d}\mathbf{k} \tag{2.4}$$

The emission probability (right term of this expression) is seen to not depend on the incident polarization and as a consequence contributes only as a multiplicative constant when this polarization is tuned. In addition the collection aperture has no effect on the polarimetric response of the emitted signal and will only affect its global efficiency. Hence the polarization response depends only on the absorption probability:

$$I_i(\alpha) \propto C_i \int\int |\boldsymbol{\mu}^{abs}(\mathbf{\Omega}, \mathbf{r}) \cdot \mathbf{E}(\alpha, \mathbf{r})|^4 \mathrm{d}\mathbf{\Omega} \mathrm{d}\mathbf{r} \tag{2.5}$$

where the i-independent factor C_i, containing the emitted field radiation factor, may vary for different analyzing directions due to different efficiencies along X and Y. In eq2.5

only the $\boldsymbol{\mu}^{abs}$ orientation is relevant. Therefore, the two-photon fluorescence polarimetric response from the solution does not depend on correlation-related issues such as energy transfer or angles between absorption and emission dipoles as it took a place in a polymer matrix [40]. An aqueous solution is thus adequate to sort out information on polarization distortion by reflection optics.

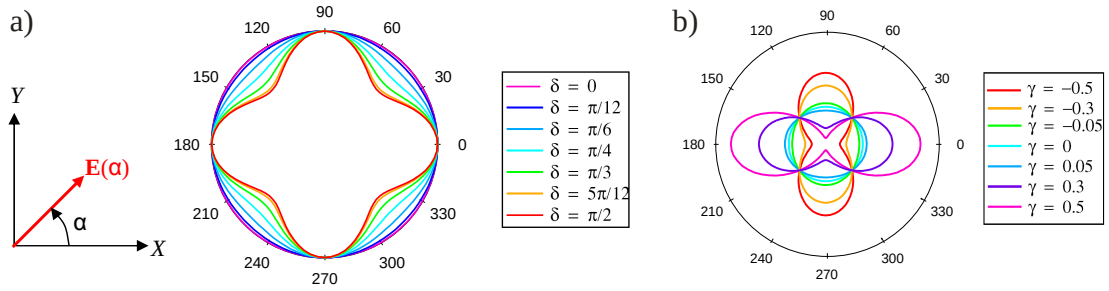

Figure 2.7: Effect of the dichroic parameters δ and γ (γ in a.u.) on the 2PEF polarization response. (a) influence of the ellipticity δ for an amplitude factor $\gamma = 0$. (b) influence of γ for $\delta = 0$.

Fig. 2.7 shows the effect of the δ and γ on the fluorescence intensity as a function of the incident polarization α in a fluorescent solution. To generate this curves we used eq.2.5 where we omit the $\mathbf{r}$ dependence of the incident field (see next section) since the medium excitation is randomized in dipoles positions and orientations. Where no ellipticity and dichroism factors arise, the 2PEF response is α-independent, as expected from an isotropic solution. Whereas when δ increase, the electric field became elliptical for intermediate angles α (Fig. 2.7a). This results in reducing the excitation efficiencies at intermediate polarization angles up to minimum at $\alpha = \frac{\pi}{4}$ modulo $\frac{\pi}{2}$. The factor γ affects the intensities in the X and Y polarization directions (Fig. 2.7b). When $\gamma > 0$ higher transmission occur for the electric field polarized along X-axis, hence the electric field E_Y is reduced. This leads to the lower 2PEF signal in Y direction. When $\gamma < 0$ the situation is opposite.

In an isotropic solution the effect of the δ factor on the fluorescence polarization response is $\pi/2$ periodical thus is only visible in the $[0 - \pi/2]$ range. For example if $\delta = 0$ the rotation of the incident polarization is clockwise whereas for $\delta = \pi$ the rotation is counter-clockwise (Fig. 2.8a). In an isotropic solution the 2PEF signal in both cases is identical, which leads to an indetermination on the range of δ. This will not take place in an anisotropic sample, which direction is known. Therefore polarization responses from non-isotropic molecular angular distribution will be able to rise the uncertainty of the $[0 - \pi/2]$ versus $[\pi/2 - \pi]$. This is illustrated in Fig. 2.8b where a fixed 1D fluorescent sample (such as a crystal made of parallel dipole molecules) is modeled with an intermediate

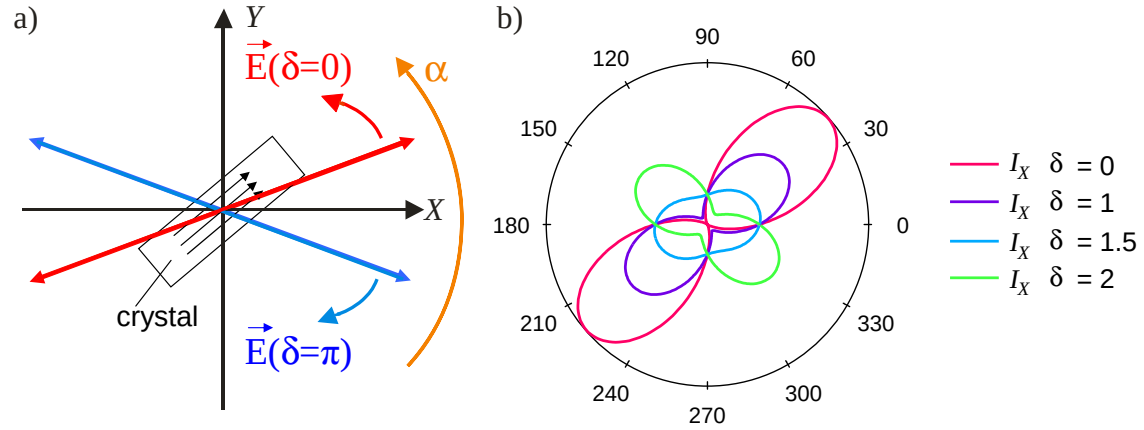

Figure 2.8: (a) Rotation direction of the linear polarization of an angle α for $\delta = 0$ and $\delta = \pi$. (b) Effect of the ellipticity on the polarization response I_X from 1D fluorescent crystal.

orientation of $2\pi/9$ relative to X. In this case $f(\mathbf{\Omega}) = \delta(\mathbf{\Omega} - \mathbf{\Omega}_0)$ with fixed dipoles within the excitation volume along the direction $\mathbf{\Omega}_0 = (\theta_0, \phi_0) = (\pi/2, 2\pi/9)$. In this situation the polarization response seems to strongly depend on the ellipticity. When $\delta = 0$, the polarization response is anisotropic in the $2\pi/9$ (40°) direction as expected from the 1D symmetry of the sample. As the ellipticity increases, the polarization response changes its direction until reaching another quadrant for $\delta > \pi/2$. Thus an easy discrimination of the range of the ellipticity is possible: a polarization response stays in the quadrant of the sample orientation for $0 < \delta < \pi/2$, whereas it reaches the next quadrant for $\pi/2 < \delta < \pi$, due to polarization rotation. This example also emphasizes the detrimental influence of in-plane polarization ellipticity when performing polarimetric measurements, the response being strongly distorted for high ellipticities.

We now explore the possibility to retrieve the (γ, δ) coefficients based on the technique described above. In a solution, the determination of these coefficients requires in fact only three measurements $I(\alpha = 0)$, $I\left(\frac{\pi}{4}\right)$, $I\left(\frac{\pi}{2}\right)$ leading to a unique solution (as seen before the analysis direction is not relevant here). Fig. 2.9 shows the cartographies of the ratios $\frac{I\left(\frac{\pi}{2}\right)}{I(0)}$ and $\frac{I\left(\frac{\pi}{4}\right)}{I(0)}$ in a (γ, δ) coordinate map. A given value of the ratio $\frac{I\left(\frac{\pi}{2}\right)}{I(0)}$ corresponds to a vertical line in the respective (γ, δ)-map (Fig. 2.9a), this ratio being independent on the ellipticity of the dichroic beamsplitter, whereas Fig. (2.9 b) indicates that a given value of the ratio $\frac{I\left(\frac{\pi}{4}\right)}{I(0)}$ corresponds to a curve that is (γ, δ)-dependent. The interception between both curves is therefore a single point in the (γ, δ)-diagram, proving that the solution (γ, δ) is unique with only three incident polarizations. Taking into account typical experimental

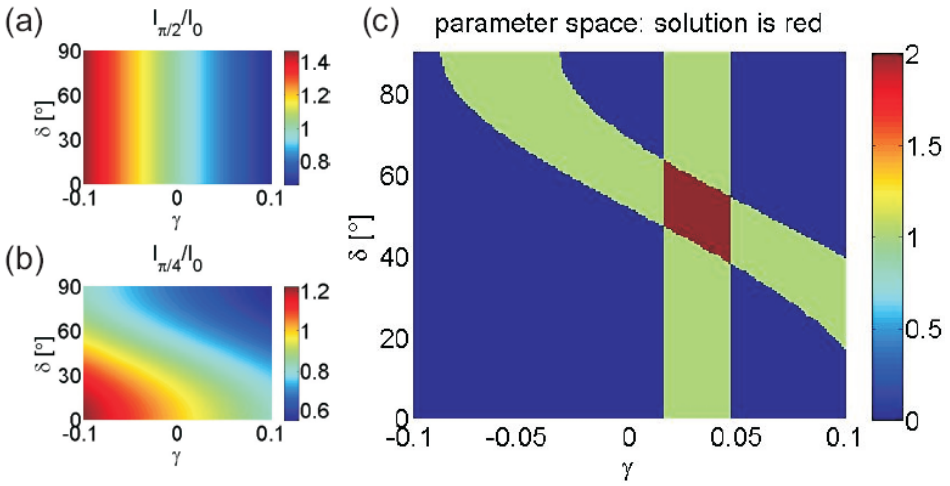

Figure 2.9: (γ, δ) cartography of the two-photon fluorescence ratios (δ in deg): (a) $\frac{I\left(\frac{\pi}{4}\right)}{I(0)}$ and (b) $\frac{I\left(\frac{\pi}{2}\right)}{I(0)}$. (c) Typical solution (red space) including experimental error margins for a three-point fit.

uncertainties, the solution space for each ratio will no longer be a single line but a band with certain error-width, as shown in Fig. (2.9 c). For a better experimental estimation we do not measure the 2PEF intensity for only three incident polarizations, but instead, we continuously rotate the incident polarization between 0° and 360°. In this case, a fit of the polarization dependent 2PEF-signal should be considered.

In order to determine the dichroic parameters δ and γ, of the 640 DCSPXR dichroic mirror used in most of this work, the theoretical curves were calculated for a large variety of δ, γ values and compared with the experimental data obtained from a solution of free Rhodamine 6G diluted in water (at about 10^{-4}mol/l concentration). The sum of mean squares (χ^2)

$$\chi^2(\gamma, \delta) = \sum_{\alpha} \left(I_{exp}(\alpha) - I_{theo}(\alpha, \gamma, \delta)\right)^2 \tag{2.6}$$

is an indication of fit quality. Fig. 2.10 a shows the dependence of χ^2 on γ and δ for a measurement at $\lambda = 900\,\text{nm}$. Only one minimum exists. This allows the use of a fitting procedure starting at any point in the (γ, δ)-space to find the global minimum by minimizing alternately both parameters until a stable χ^2 is found. On the Fig. 2.10 b an asymmetry is observed in the experimental polarimetric response, which is due to a slight misalignement of the entrance beam direction in the microscope. The consequence is a slight increase in the ellipticity error margin, which was still estimated at less than 10^{-2} rad.

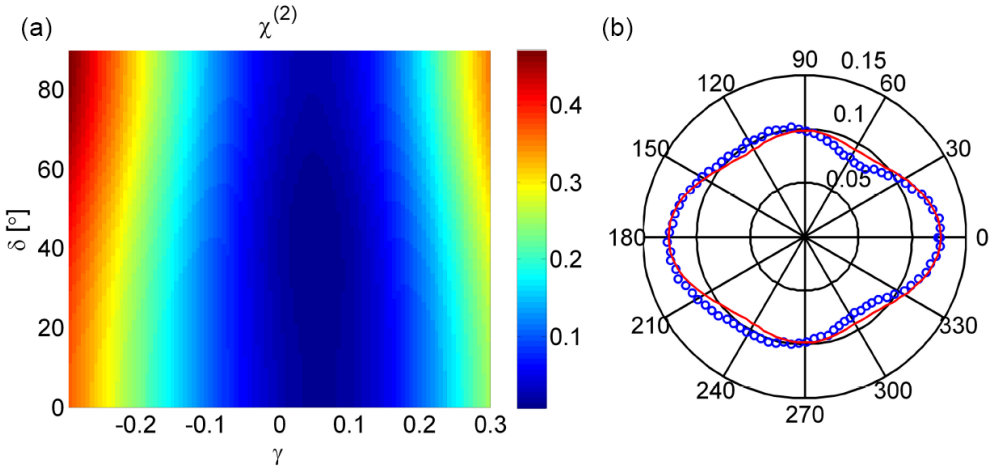

Figure 2.10: Experimental measurement of a polarimetric response from a Rh6G solution excited at 900nm: (a) χ^2 parameter represented for a range of (γ, δ). (b) experimental points (dots) and corresponding fit (continuous line). These data were measured with the 640 DCSPXR dichroic mirror.

The results of this approach for a large variety of wavelengths are shown in Fig. 2.11 together with some examples of the corresponding 2PEF signals. As stated above, the determination of the δ factor is made within a $[0 - \pi/2]$ range. In order to confirm the relevance of the retrieved parameters, we measured the expected δ and γ values from the dichroic mirror at 45° incidence by ellipsometry (GESP5 Sopra). As can be seen in Fig. 2.11, the measured parameters in two-photon fluorescence microscope are in good agreement with the ellipsometry measurement for the whole wavelength range explored. The data comparison necessitated a phase wrapping of the ellipsometric data in the $\left[0 - \frac{\pi}{2}\right]$ range. This good agreement confirms that δ and γ are almost exclusively caused by the dichroic itself and not by other optical components. It should be noted that while the dichroic factor γ is seen to lie close to 0 (which ensures the small deviation of the amplitude p/s ratio from 1), the ellipticity caused by the dichroic mirror can reach high values far above $\pi/2$. This causes an intermediate incoming polarizations to become elliptic and potentially rotated, which strongly affects polarization responses. Other two-photon excitation dichroic mirrors generally used for 2PEF microscopy were studied with the same technique and showed similar behaviors, especially close to their cut-off wavelength. The FF720-SDiO1 dichroic mirror mentioned above is however specially designed for a light quality polarization response, and therefore exhibits δ values lower than 10° over its reflection range (780-880nm).

To illustrate the dramatic changes brought by in-plane ellipticity on experimental po-

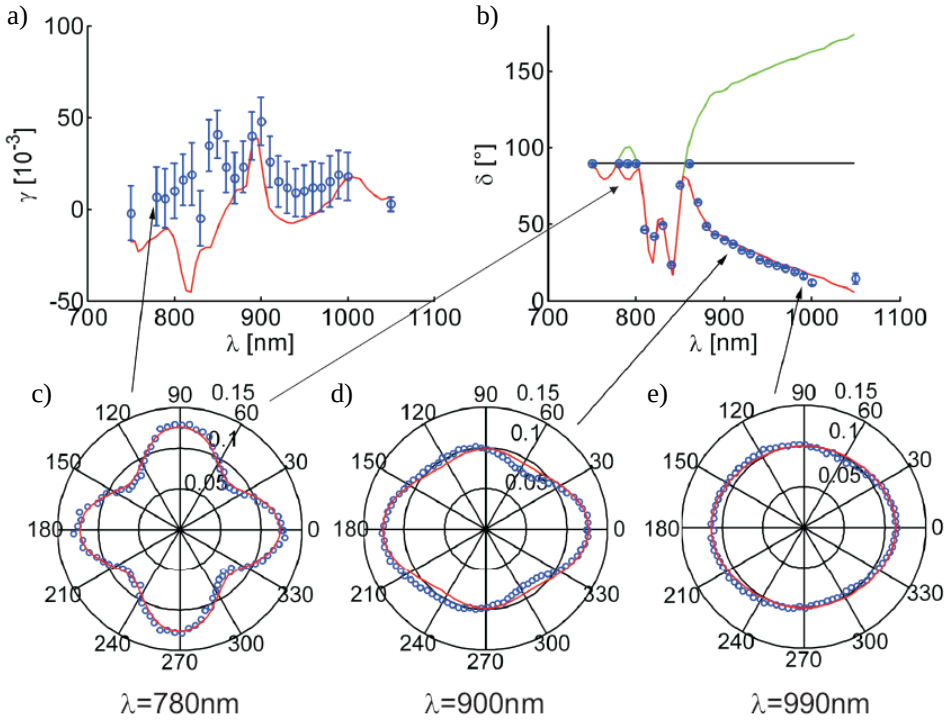

Figure 2.11: (a) δ and (b) γ parameters deduced from 2PEF polarization responses (dots) and ellipsometry data (continuous line) on the dichroic mirror used for two-photon fluorescence (640 DCSPXR), at various incident wavelengths. Each experimental point results from a series of 6 measurements. The green line in (b) corresponds to the δ ellipsometry data while the red one is wrapped in the $[0 - \pi/2]$ range for comparison with polarimetric measurements. (c-e) 2PEF polarization responses and fits (red curves) at three different wavelengths: (c) 780nm; (d) 900nm; (e) 990nm.

larization responses in anisotropic samples, we measured a 1D sample made of oriented fluorescent molecules along a macroscopic crystal axis, whose orientation can be identified visually, using 640 DCSPXR dichroic mirror. This Perhydrotriphenylene (PHTP)-4-Dimethylamino-40-nitrostilbene (DANS) co-crystal, characterized in a previous work [87], was oriented in the (X, Y)-plane at an angle close to 30° in the sample plane (Fig. 2.12). The fitting of the polarization responses by using perviously determined parameters γ and δ leads to a crystal orientation of $(\theta_0, \phi_0) = (90°, 29°)$, which is in close agreement to the initially set orientation as seen in Fig. 2.12a. This fit is therefore shown to be in excellent agreement with the expected values for the dichroic parameters. For the incident wavelengths set at 975nm, the value $\delta > \pi/2$ causes the orientation of the polarimetric response to be un-correlated with the initial crystal orientation.

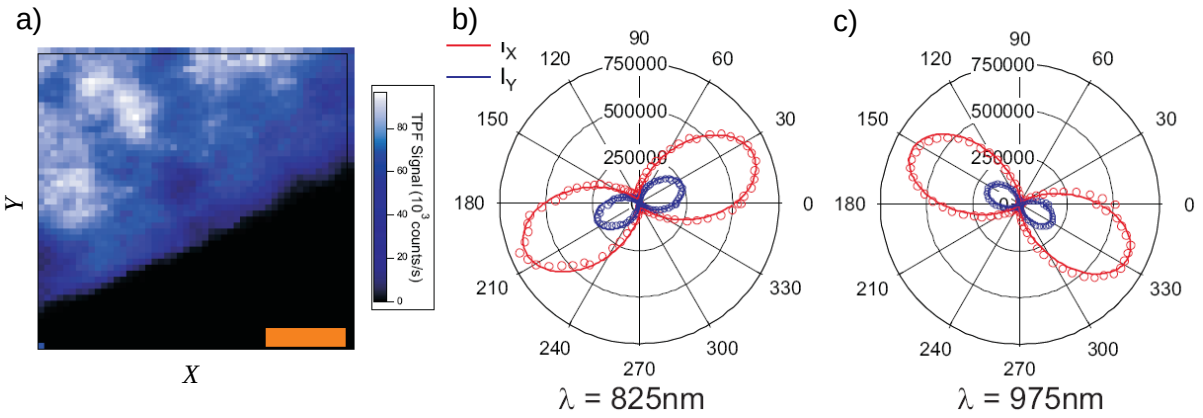

Figure 2.12: 2PEF polarization response of a 1D crystalline fluorescence sample made of DANS molecules in a PHTP crystalline host. (a) 2D scan (by a piezoelectric stage) of the sample showing the macroscopic crystal orientation (scale bar: 10μm); the heterogeneity of the intensity observed in the image is due to an imperfect surface quality. (b,c) Experimental data (dots), and corresponding fits (continuous line) at (b) 825nm excitation and (c) 975nm excitation wavelengths. The fits account for the measured dichroic parameters and for the molecular orientation $(\theta_0, \phi_0) = (90°, 29°)$.

2.2.2 Polarization distortion by high NA focussing

In the rigorous way one has to account on the $\mathbf{E}(\mathbf{r})$ dependance in eq.2.3. This is because high numerical aperture focussing modifies polarization components along the coordinate axes in the focal volume [82]. In particular a small component in the field's direction of propagation may appear when increasing the numerical aperture (Fig. 2.13). This field component can amount to up to 40% of the maximal field strength in the case of high NA objectives. It can in particular couple with the molecular excitation dipoles when they possess orientation components along the laser propagation direction. This effect has been shown by Yew *et al.* [88] in the case of second harmonic generation from objects with known symmetries. The incident beam polarization state depends thus on the space coordinates in the excitation volume. While in an isotropic liquid where the excitation process is randomized, the fluorescence polarimetric response is independent on the objective's numerical aperture, in the case of an anisotropic medium presenting out-of-plane orientation directions, a coupling in the Z direction cannot be neglected. This effect was illustrated by Peter Schön [86] in two-photon microscopy where a model system of 1D symmetry was used in the calculations of Eq. 2.3 accounting for the complete vectorial form of the spatial excitation field. Fig. 2.14 depicts the polarization TPF response of a 1D sample made of fixed dipoles with small $\left(\theta = \frac{\pi}{3}\right)$ and strong $\left(\theta = \frac{\pi}{6}\right)$ orientation

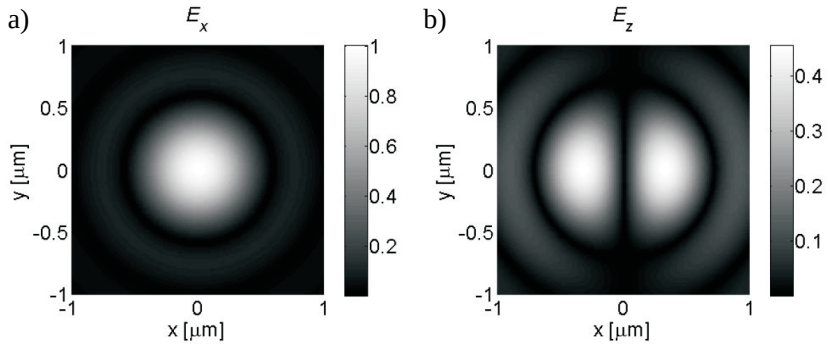

Figure 2.13: Map of the focalized incident electric field amplitude components along X and Z at the sample plane at $Z = 0$, for an incident polarization along X and focussed by an objective with NA = 1.2. (a) E_X; (b) E_Z (electric field normalized to the maximum of E_X).

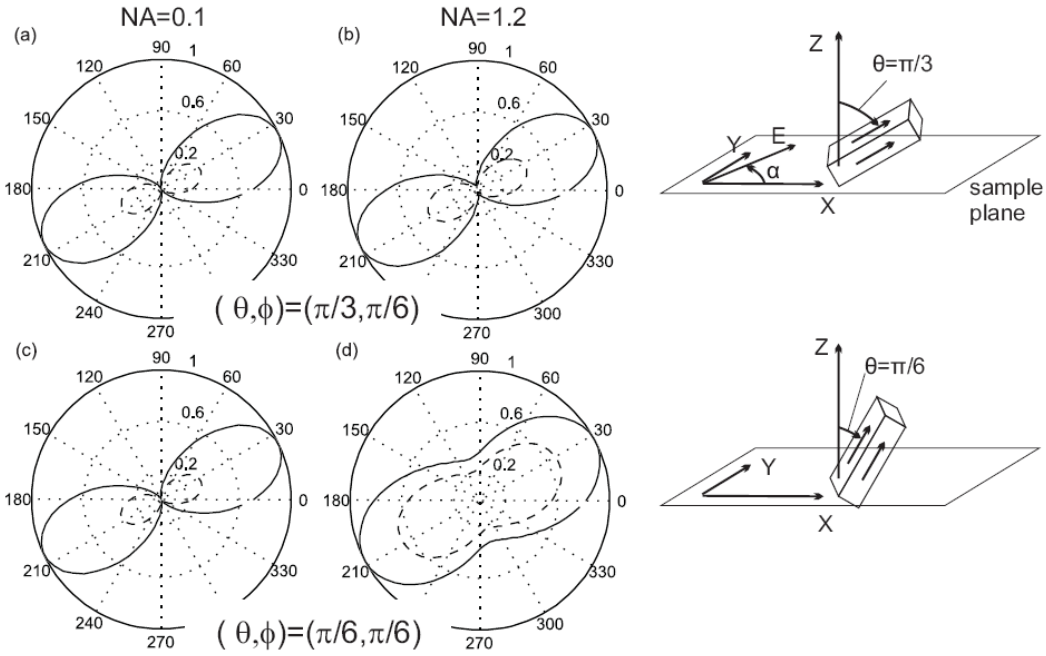

Figure 2.14: Calculated 2PEF polarization responses of a 1D fluorescence sample accounting for both reflection optics (using the parameters $\delta = \frac{\pi}{4}$, $\gamma = 0.01$) and high numerical aperture focussing. (a,c) NA = 0.1; (b,d) NA = 1.2. Sample orientation: (a,b) $(\theta, \phi) = \left(\frac{\pi}{3}, \frac{\pi}{6}\right)$; (c,d) $(\theta, \phi) = \left(\frac{\pi}{6}, \frac{\pi}{6}\right)$ - see drawings on the right. Continuous lines: I_X; dashed lines: I_Y. The polarization responses are normalized to a maximum value of 1.

components along Z. At low numerical aperture (NA = 0.1) the polarization response is only slightly deformed by an off-plane tilt. For high numerical apertures (NA = 1.2),

however, strong deformations in the polarization response appear. Such a signal could easily be misinterpreted as originating from a non-1D sample in the (X, Y)-plane because some apparent perpendicular coupling occurs. Therefore great care has to be taken when dealing with polarization responses of non-anisotropic samples especially those with out of plane orientation. Note that while the observed deformation exists even for $(\gamma, \delta) = 0$, it is enhanced with increasing ellipticities δ. In practice in the samples investigated in this thesis this contribution will not strongly affect the results due to the geometry of the investigated molecular distributions. We will therefore not include it to the data analysis, in particular when it concerns relative comparisons. However when a sample is completely unknown and qualitative analysis is required, it is safer to use a NA below 0.6 in general.

2.2.3 Polarization distortion by high NA collection

The analysis of the emission of the signal presented so far was performed for a plane wave approximation, where the collection aperture has no effect on the polarimetric response. This approximation is correct for an isotropic liquid which polarization response depends only on the absorption probability (see eq 2.5). However in the case of a static anisotropic sample were the polarimetric pattern reflects the shape of molecular distribution the high numerical aperture of the collection objective can affect the polarization radiated by the dye molecules [82]. In particular, due to high tilt angle of the emission directions, different emission polarization states will be mixed. This effect has been modeled for one-photon fluorescence [34] and then extended to two-photon processes, assuming that 2PEF emission occurs from a one-photon allowed transition, independently of the excitation pathway [40].

To express the intensity of fluorescence emitted by a single dipole set at the focal point of the microscope objective we follow an approach developed in [40] and inspired from [34]. The far field $\mathbf{E}^{em}$ is radiated by the emission dipole $\boldsymbol{\mu}(\theta, \phi)$, in the direction of wave vector $\mathbf{k}(u, v)$ with :

$$\mathbf{E}^{em} \propto \mathbf{k} \times (\mathbf{k} \times \boldsymbol{\mu}) \tag{2.7}$$

Since the orientation of the wave vector $\mathbf{k}$ depends only on the angles (u, v) (Fig. 2.15):

$$\mathbf{k}(u, v) = \begin{bmatrix} \sin u \cos v \\ \sin u \sin v \\ \cos u \end{bmatrix}, \tag{2.8}$$

the vector $\mathbf{E}^{em}$ can be expressed:

$$\mathbf{E}^{em}(u, v, \theta, \phi) = \mu_X(\theta, \phi)\mathbf{U}_1(u, v) + \mu_Y(\theta, \phi)\mathbf{U}_2(u, v) + \mu_Z(\theta, \phi)\mathbf{U}_3(u, v) \tag{2.9}$$

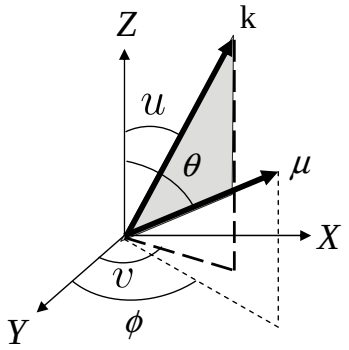

Figure 2.15: Notations introduced to account for the wide angle collection of the emitted light by a dipole, located at the origin of the (X, Y, Z) framework. The direction of the dipole is defined by the angles (θ, ϕ). The direction of the wave vector $\mathbf{k}$ corresponding to the radiated field is defined by the angles (u, v).

where $\mathbf{U}_1$, $\mathbf{U}_2$ and $\mathbf{U}_3$ are unit vectors that depend only on (u, v) :

$$\mathbf{U}_1 = \begin{bmatrix} \sin^2 u \sin^2 v + \cos^2 u \\ -\sin^2 u \cos v \sin u \\ -\sin u \cos u \cos v \end{bmatrix}, \tag{2.10}$$

$$\mathbf{U}_2 = \begin{bmatrix} -\sin^2 u \sin v \cos v \\ \sin^2 u \cos^2 v + \cos^2 u \\ -\sin u \cos u \sin v \end{bmatrix}, \tag{2.11}$$

$$\mathbf{U}_3 = \begin{bmatrix} -\sin u \cos u \cos v \\ -\sin u \cos u \sin v \\ \sin^2 u \end{bmatrix}. \tag{2.12}$$

The fluorescence radiation propagates towards the objective in the direction of the wave vector $\mathbf{k}(u, v)$ in the object space as indicated in the Fig. 2.16. The infinity-corrected objective refracts the fluorescence light in the image space into a direction parallel to the optical axis. The field transmitted by the objective can therefore be expressed as:

$$\mathbf{E}^{em,T} = [\mathscr{R}]\mathbf{E}^{em} \tag{2.13}$$

where $[\mathscr{R}]$ represents the rotation matrix simulating the infinity corrected objective refraction. $[\mathscr{R}]$ is therefore the product of three successive rotations [34] (rotation of $-v$

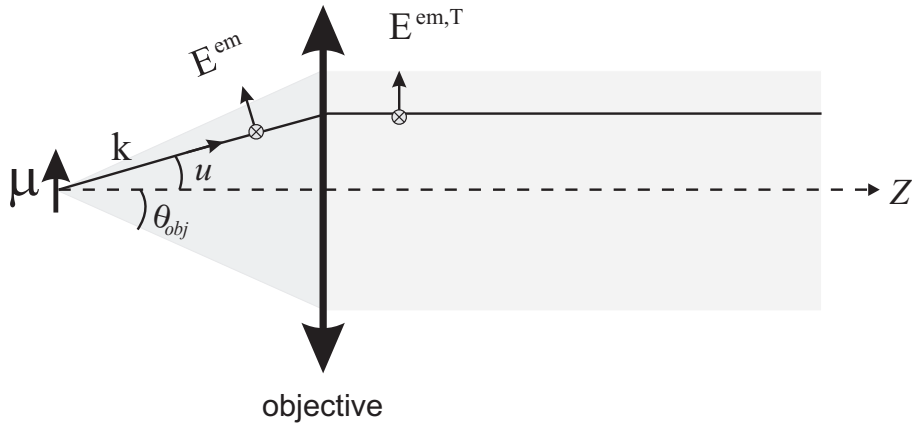

Figure 2.16: Effect of the high NA aperture on the polarized intensity emitted by a single dipole $\boldsymbol{\mu}$. The far field is $\mathbf{E}^{em}$ radiated in the direction of the wave vector $\mathbf{k}(u,v)$ (u parameter shown on the Fig. 2.15). An infinity-corrected objective refracts the fluorescence emission beam $\mathbf{E}^{em,T}$ parallel to the optical axis Z.

around Z, rotation of $-u$ around Y and rotation of v around Z) which allows to convert any input incidence on the objective into an output ray parallel to the optical axis Z :

$$[\mathscr{R}] = \begin{bmatrix} \cos u \cos^2 v + \sin^2 v & \cos v \sin v(\cos u - 1) & -\sin u \cos v \\ \cos v \sin v(\cos u - 1) & \cos u \sin^2 v + \cos^2 v & -\sin u \sin v \\ \sin u \cos v & \sin u \sin v & \cos u \end{bmatrix} \tag{2.14}$$

The vector $\mathbf{E}^{em,T}(u,v,\theta,\phi)$ of the transmitted field can then be expressed as :

$$\begin{aligned} E_X^{em,T}(u,v,\theta,\phi) &= f_X(u,v)\mu_X(\theta,\phi) + f_Y(u,v)\mu_Y(\theta,\phi) + f_Z(u,v)\mu_Z(\theta,\phi) \\ E_Y^{em,T}(u,v,\theta,\phi) &= g_X(u,v)\mu_X(\theta,\phi) + g_Y(u,v)\mu_Y(\theta,\phi) + g_Z(u,v)\mu_Z(\theta,\phi) \end{aligned} \tag{2.15}$$

where f_X,f_Y,f_Z and g_X,g_Y,g_Z are function of the (u,v) parameters.

The fluorescence light is emitted incoherently thus the emission intensities coming from the single dipole are calculated after integration of the square of each $\mathbf{E}^{em,T}$ component, over all of the angles (u,v) within the half-aperture angle θ_{obj} of the objective giving the detection probability :

$$J_{i=X,Y}(\theta,\phi) = \int_0^{2\pi} \int_0^{\theta_{obj}} |\mathbf{E}^{em,T} \cdot u_i(u,v,\theta,\phi)|^2 \sin u \, \mathrm{d}u \, \mathrm{d}v \tag{2.16}$$

After integration, the previous expression reduces to :

$$\begin{aligned} J_X(\theta,\phi) &= K_1\mu_X^2(\theta,\phi) + K_2\mu_Y^2(\theta,\phi) + K_3\mu_Z^2(\theta,\phi) \\ J_Y(\theta,\phi) &= K_2\mu_X^2(\theta,\phi) + K_1\mu_Y^2(\theta,\phi) + K_3\mu_Z^2(\theta,\phi) \end{aligned} \tag{2.17}$$

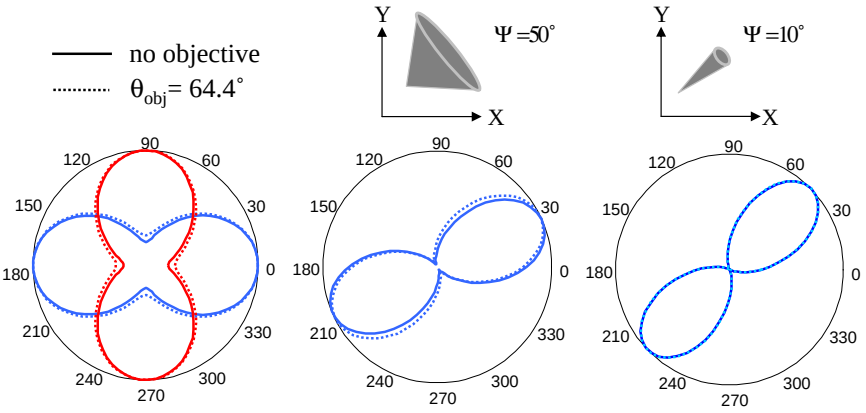

Figure 2.17: 2PEF fluorescence normalized polarimetric responses I_X (blue line) and I_Y (red line) calculated for an isotropic sample and cone distribution ($\rho = 45°$ and $\Psi = (50°, 10°)$) accounting on high N.A.=1.2 water immersion objective ($n = 1.33$) (solid line) and without objective (dotted line). (The I_Y response is not represented for the cone response as the effect is similar).

with [34] :

$$\begin{aligned} K_1 &= \frac{1}{3}(2 - 3\cos\theta_{obj} + \cos^3\theta_{obj}) \\ K_2 &= \frac{1}{12}(1 - 3\cos\theta_{obj} + 3\cos^2\theta_{obj} - \cos^3\theta_{obj}) \\ K_3 &= \frac{1}{4}(5 - 3\cos\theta_{obj} - \cos^2\theta_{obj} - \cos^3\theta_{obj}) \end{aligned} \tag{2.18}$$

The water-immersion ($n = 1.33$) objective used in this work has a numerical aperture N.A. $= 1.2$. The half-aperture angle θ_{obj} is therefore equal to 1.125rad (64.4°), leading to $K_1 = 0.86$, $K_2 = 0.015$ and $K_3 = 0.262$. Similar calculation are performed for the quartz microscope objective with low numerical aperture N.A. $= 0.6$ and the half-aperture angle θ_{obj} equal to 0.644rad (36.9°) resulting in $K_1 = 0.36$, $K_2 = 0.0006$ and $K_3 = 0.037$. K_2 and K_3 are weak in this case, as expected from the weak mixing of polarizations at low aperture.

In order to get the final fluorescence response, we directly integrate the dipole response, product of the excitation and detection probability, over all dipole orientations. Assuming that the absorption and emission dipoles of each fluorophore are parallel, the detected intensities can then be expressed as :

$$I_{i=X,Y}^{2PEF} = \int |\boldsymbol{\mu}(\Omega) \cdot \mathbf{E}|^4 J_i(\Omega) f(\Omega)\, \mathrm{d}\Omega \tag{2.19}$$

Fig. 2.17 shows the influence of the high numerical aperture of the objective on 2PEF polarimetric responses calculated for different samples. In an isotropic sample made of fixed molecules or in a cone molecular distribution the effect is negligible, however we still account on this factor in the polarimetric analysis presented in this work.

2.3 Effect of the absorption-emission dipoles relative angle on the polarimetric data

When a molecule undergoes a transition from a ground state to an excited state an orientation of its transition dipole moment can change. The difference between absorption and emission dipole moment can affect the polarimetric response.

The effect of different absorption and emission dipoles orientations is investigated by considering independent angular dependencies for both excitation and emission probabilities in the 2PEF process. While keeping the orientation of the emission dipole as defined by the angles (θ, ϕ) in the (x', y', z') local microscopic frame (defined by symmetry axes of the molecular distribution), the orientation of the excitation dipole moment is given by the respective polar and azimuthal angles ξ and φ in the (x, y, z) frame carried by the emission dipole as depicted in Fig. 2.18. Using the transformation matrix from the (x, y, z)

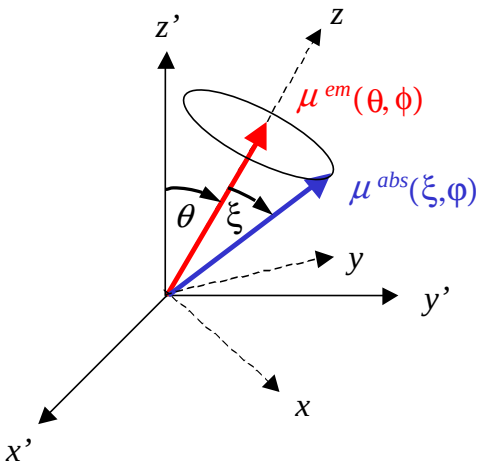

Figure 2.18: Orientation of the excitation and emission dipole moments in the microscopic (x', y', z') local frame. The emission occurs at dipole orientation (θ, ϕ) angles in the (x', y', z') frame whereas the excitation occurs at (ξ, φ) angles in the local emission dipole (x, y, z) frame. The azimuthal angles ϕ and φ are not represented.

frame to the (x', y', z') frame, the components of $\boldsymbol{\mu}^{abs}$ can be expressed as functions of

$(\theta, \phi, \xi, \varphi)$ in the local frame of the molecular distribution :

$$\begin{bmatrix} \mu_{x'}^{abs} \\ \mu_{y'}^{abs} \\ \mu_{z'}^{abs} \end{bmatrix} = \begin{bmatrix} \cos\theta\cos\phi & -\sin\phi & \sin\theta\cos\phi \\ \cos\theta\sin\phi & \cos\phi & \sin\theta\sin\phi \\ -\sin\theta & 0 & \cos\theta \end{bmatrix} . \begin{bmatrix} \sin\xi\cos\varphi \\ \sin\xi\sin\varphi \\ \cos\xi \end{bmatrix} \tag{2.20}$$

Both dipoles can be then expressed in the laboratory frame using the (ρ, η)-dependent transformation matrix from the (x', y', z') local frame to the macroscopic (X,Y,Z) frame, with ρ and η specifying the orientation of the distribution axis of symmetry (see chapter 1). The macroscopic components $\boldsymbol{\mu}^{abs}(\theta, \phi, \xi, \varphi, \rho, \eta)$ of the excitation dipole moment are therefore given by:

$$\begin{bmatrix} \mu_{X}^{abs} \\ \mu_{Y}^{abs} \\ \mu_{Z}^{abs} \end{bmatrix} = \begin{bmatrix} -\sin\rho & -\cos\rho\sin\eta & \cos\rho\cos\eta \\ \cos\rho & -\sin\rho\sin\eta & \sin\rho\cos\eta \\ 0 & \cos\eta & \sin\eta \end{bmatrix} . \begin{bmatrix} \mu_{x'}^{abs} \\ \mu_{y'}^{abs} \\ \mu_{z'}^{abs} \end{bmatrix} \tag{2.21}$$

The treatment of the emission probability is the same as detailed above. The time averaged fluorescence intensity of an ensemble of molecules within the $f(\theta, \phi)$ angular distribution, analyzed along a given polarization state i =(X,Y), can then be expressed as:

$$I_i(\rho, \eta, \alpha, \xi) = \int_0^{2\pi}\int_0^{2\pi}\int_0^{\pi} |\boldsymbol{\mu}^{abs}(\theta, \phi, \xi, \varphi, \rho, \eta) \cdot \mathbf{E}(\alpha)|^4 J_i(\theta, \phi, \rho, \eta) f(\theta, \phi) \sin\theta d\theta d\phi d\varphi$$

The integration over φ accounts for possible fast time rotation of the molecule over its emission dipole axis.

Fig. 2.19 depicts polarimetric responses in situations representative of a cone angular distribution of the molecules with different cone tilt angles ρ and cone apertures Ψ. As we can see on the polarimetric data, the effect of ξ can deform the responses, however only for $\xi > 20°$. This deformation is similar to the depolarization, as seen in the opening of the lobes.

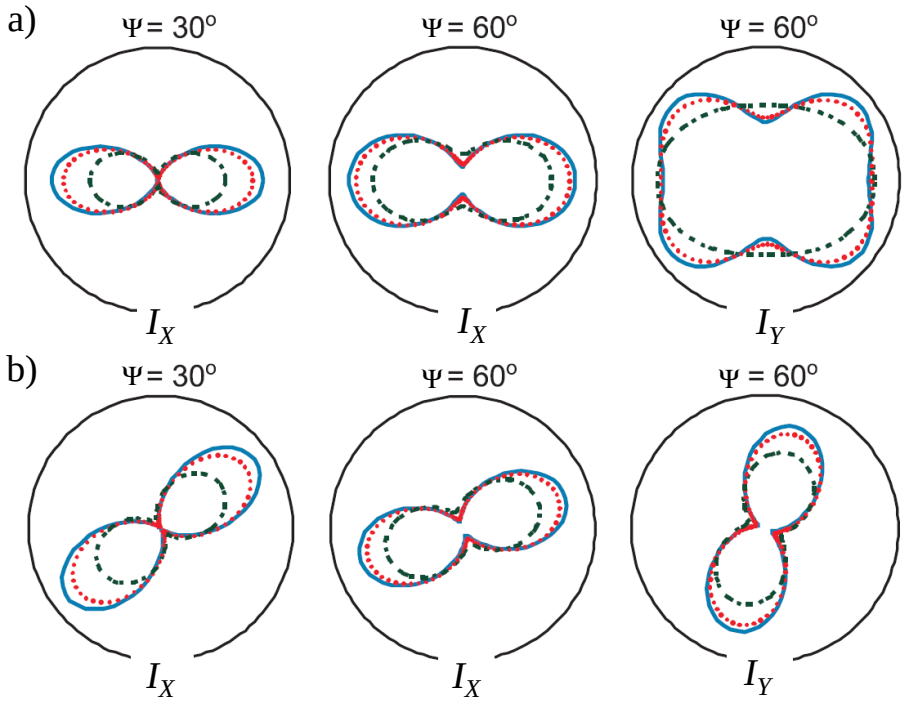

Figure 2.19: Influence of the absorption-emission dipoles relative angle ξ on polarimetric 2PEF responses for different Ψ values ($\Psi = 30°$ and $\Psi = 60°$) in the case of a cone distribution of orientation (a) $\rho = 0°$ and (b) $\rho = 45°$. Different values of the angle between excitation and emission dipole moment: $\xi = 0°$ (*solid line*), $\xi = 15°$ (*dotted line*), and $\xi = 30°$ (*dashed line*). I_Y follows a similar dependence as I_X for $\Psi = 30°$. The dichroic parameters $\delta = 0.26$rad and $\gamma = 0.005$ are used in this model (since they correspond to experimental conditions often met).

2.4 Effect of the fluorescence resonant energy transfer on the polarimetric data

Fluorescence Resonant Energy Transfer (or Förster Resonant Energy Transfer, FRET) has been studied for the first time by Förster [89]. It corresponds to a non-radiative energy transfer between a donor and an acceptor molecule through nonradiative dipole–dipole coupling, and occurs when concentration of the molecules is sufficiently high (in proximity, typically less than 10 nm). In our samples this effect is likely to occur between identical molecules (homo-FRET) in dense samples. Due to the possible decorrelation of orientations between the acceptor and the donor, we would except the polarimetric data

to be affected by a consequent depolarization. The sensibility of the 2PEF polarimetric responses to the presence of homo-FRET between the molecules is analyzed here using models previously developed [90].

We separate in what follows the case of a statistics distributions and crystals, which are defined by very specific dipoles directions.

2.4.1 Homo-FRET in statistic distributions

To account for the homo-FRET effect in the 2PEF polarimetric data, both acceptor and donor molecules have to be defined with independent orientation angles within their own molecular angular distribution. In the present model the donor molecule (1) is defined by its dipole orientation $\boldsymbol{\mu}_1(\theta_1, \phi_1)$ in the local frame (x', y', z'). The acceptor molecule position is defined by the $\mathbf{r}(\Theta, \Phi)$ vector connecting the two dipoles, and its orientation by $\boldsymbol{\mu}_2(\theta_1, \phi_1, \Theta, \Phi, \theta_2, \phi_2)$, with (θ_2, ϕ_2) the orientation of the dipole (2) in the frame defined by the $\mathbf{r}$ direction (Fig. 2.20). The acceptor coordinates in the macroscopic framework is

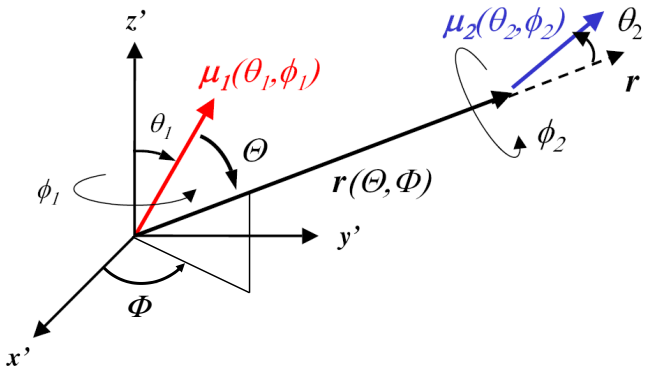

Figure 2.20: Orientation of the acceptor ($\boldsymbol{\mu}_2$) and donor ($\boldsymbol{\mu}_1$) molecular excitation-emission dipoles in the homo-FRET process, depicted in the (x', y', z') local frame. The orientation of the donor is defined by the (θ_1, ϕ_1) angles. The orientation of the unitary vector $\mathbf{r}$ along the line connecting the two fluorophores is defined by the (Θ, Φ) angles in the (θ_1, ϕ_1) framework. The orientation of the acceptor in the (Θ, Φ) framework is defined by the (θ_2, ϕ_2) angles.

written as:

$$\boldsymbol{\mu}_2(\theta_2, \phi_2, \Theta, \Phi, \theta_1, \phi_1) = [\mathcal{M}]_{(\theta_1,\phi_1)\to(X,Y,Z)}[\mathcal{M}]_{(\Theta,\Phi)\to(\theta_1,\phi_1)} \begin{bmatrix} \sin\theta_2 \cos\phi_2 \\ \sin\theta_2 \sin\phi_2 \\ \cos\theta_2 \end{bmatrix} \tag{2.22}$$

where $[\mathcal{M}]_{(\Theta,\Phi)\to(\theta_1,\phi_1)}$ is the rotation matrix from the (Θ,Φ) framework to the (θ_1,ϕ_1) framework and $[\mathcal{M}]_{(\theta_1,\phi_1)\to(X,Y,Z)}$ is the rotation matrix from the (θ_1,ϕ_1) framework to the macroscopic one. Expressions for these matrices are [40] :

$$[\mathcal{M}]_{(\Theta,\Phi)\to(\theta_1,\phi_1)} = \begin{bmatrix} \sin\Theta\cos\Phi & \cos\Theta\cos\Phi & -\sin\Phi \\ \sin\Theta\sin\Phi & \cos\Theta\sin\Phi & \cos\Phi \\ \cos\Theta & -\sin\Theta & 0 \end{bmatrix} \tag{2.23}$$

and:

$$[\mathcal{M}]_{(\theta_1,\phi_1)\to(X,Y,Z)} = \begin{bmatrix} \sin\theta_1\cos\phi_1 & \cos\theta_1\cos\phi_1 & -\sin\phi_1 \\ \sin\theta_1\sin\phi_1 & \cos\theta_1\sin\phi_1 & \cos\phi_1 \\ \cos\theta_1 & -\sin\theta_1 & 0 \end{bmatrix} \tag{2.24}$$

The fluorescence intensity emitted by the acceptor is then expressed as:

$$\begin{aligned} J_X(\Omega_1,\Omega_2,\Omega) &= K_1\,\mu_{2X}^2(\Omega_1,\Omega_2,\Omega) + K_2\,\mu_{2Y}^2(\Omega_1,\Omega_2,\Omega) \\ &+ K_3\,\mu_{2Z}^2(\Omega_1,\Omega_2,\Omega) \\ J_Y(\Omega_1,\Omega_2,\Omega) &= K_2\,\mu_{2X}^2(\Omega_1,\Omega_2,\Omega) + K_1\,\mu_{2Y}^2(\Omega_1,\Omega_2,\Omega) \\ &+ K_3\,\mu_{2Z}^2(\Omega_1,\Omega_2,\Omega) \end{aligned} \tag{2.25}$$

with $\Omega_1 = (\theta_1,\phi_1)$, $\Omega_2 = (\theta_2,\phi_2)$, $\Omega = (\Theta,\Phi)$, and the parameters K_1, K_2 and K_3 originating from the integration over the objective aperture, as defined above.

The resulting 2PEF intensity contribution to homo-FRET, accounting for both transfer rate and dipoles angular distribution f, is expressed as :

$$I_i^T(\alpha) = \int\int\int |\boldsymbol{\mu}_1(\Omega_1)\cdot\mathbf{E}(\alpha)|^4 J_i(\Omega_1,\Omega_2,\Omega)\kappa^2(\Theta,\Omega_2)f(\Omega_1)f(\Omega_2)\sin\theta d\Omega_1 d\Omega_2 d\Omega$$

with $\kappa^2(\Theta,\Omega_2)$ an interaction term related to the interaction potential between $\boldsymbol{\mu}_1$ and $\boldsymbol{\mu}_2$ dipoles [90] :

$$V_{\boldsymbol{\mu}_1\boldsymbol{\mu}_2} = |\boldsymbol{\mu}_2\cdot\mathbf{E}_1|^2 \tag{2.26}$$

with $\mathbf{E}_1$ the radiated field by the $\boldsymbol{\mu}_1$ dipole in the near field region :

$$V_{\boldsymbol{\mu}_1\boldsymbol{\mu}_2} = \frac{1}{\mathbf{r}^3}\left(\boldsymbol{\mu}_1\boldsymbol{\mu}_2 - 3(\boldsymbol{\mu}_1\cdot\mathbf{r})(\boldsymbol{\mu}_2\cdot\mathbf{r})\right) \tag{2.27}$$

κ is defined by :

$$(\frac{\boldsymbol{\mu}_1\boldsymbol{\mu}_2}{\mathbf{r}^3})^2\kappa^2 = V_{\boldsymbol{\mu}_1\boldsymbol{\mu}_2}^2 \tag{2.28}$$

therefore :

$$\kappa^2(\Theta,\Omega_2) = (2\cos\Theta\sin\theta_2\cos\phi_2 + \sin\Theta\sin\theta_2\sin\phi_2)^2 \tag{2.29}$$

In the presence of homo-FRET quantified by a transfer efficiency T, the resulting 2PEF intensity is written:

$$I_i^{homo-FRET}(\alpha) = I_i(\alpha) + \mathrm{T}.I_i^T(\alpha) \tag{2.30}$$

With $I_i(\alpha)$ the 2PEF intensity without FRET. The efficiency T depends on the inter-distance between the fluorophores, and therefore on their concentration. This coefficient is directly related to the usual FRET efficiency factor [90].

Fig. 2.21 depicts polarimetric responses in situations representative of a cone angular distribution of the molecules with different cone orientation angles ρ and cone apertures Ψ, at transfer efficiencies $\mathrm{T} = 0, 10\%, 50\%$. The dependence of the polarimetric responses as a function of the energy transfer efficiency shows that above a 10 % FRET efficiency, the depolarization effect tends to deform the polarimetric curves, especially at large cone apertures Ψ. High FRET efficiencies induce a total depolarization illustrated by almost-identical I_X and I_Y polarization dependencies.

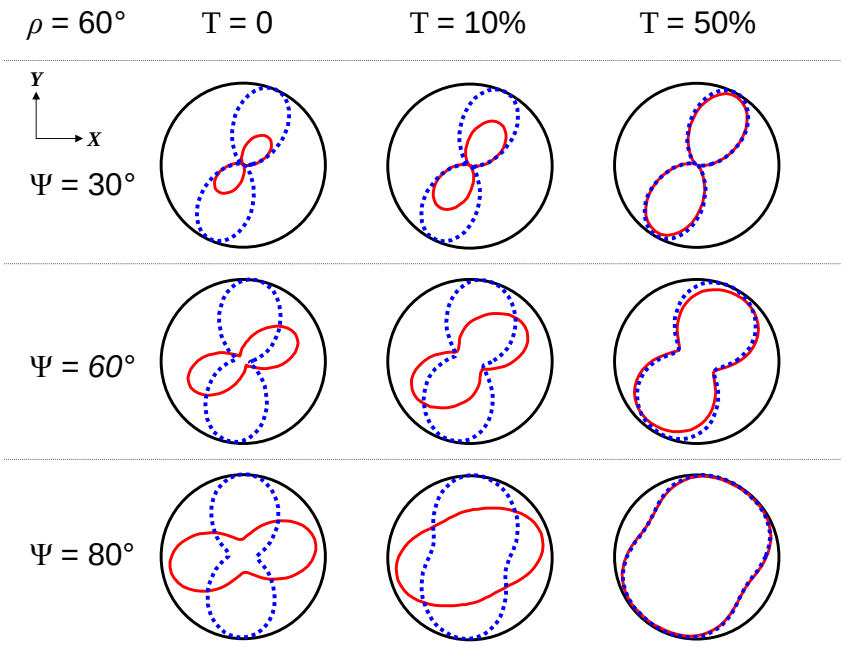

Figure 2.21: Dependence of the polarimetric 2PEF responses I_X (*solid line*) and I_Y (*dotted line*) as functions of the homo-FRET efficiency T between the fluorescent molecules in the membrane, for a cone distribution of the fluorophores with orientation angle $\rho = 60°$, at different cone apertures Ψ as indicated. The dichroic parameters $\delta = 0.26$rad and $\gamma = 0.005$ are used in this model (since they correspond to experimental conditions often met).

2.4.2 Homo-FRET in crystals

In crystalline systems, we expect the same behavior as above, except that the molecular directions are fixed. Due to the very close distance between the molecules in this case (typically below a few nm, see chapter 5) this situation is more likely to occur with very high FRET efficiencies. In the case of a crystal, eq 2.26 can be rewritten using the formalism of chapter 1 :

$$I_X^T(\alpha) = \sum_{\Omega,\Omega_a,\Omega_b} \sum_{IJKL} \gamma_{IJKL}(\Omega_a)\alpha_{XX}(\Omega_b)\kappa^2(\Omega,\Omega_a,\Omega_b) \cdot E_I E_J E_K^* E_L^*(\alpha) \tag{2.31}$$

where Ω_a, Ω_b span all the possible molecular orientations of the crystal and Ω is the angle direction between different molecules a and b (note that all angles are defined in the macroscopic frame, differently from above). In the approximation that the interaction term κ^2 is a similar constant quantity for all interacting molecular couples, which is likely to occur in a unit cell containing a few molecules, this equation can be simplified in :

$$I_X^T(\alpha) \propto \sum_{\Omega_a} \sum_{IJKL} \gamma_{IJKL}(\Omega_a) E_I E_J E_K^* E_L^* \sum_{\Omega_b} \alpha_{XX}(\Omega_b) \tag{2.32}$$

In this contribution, we can see that the polarization response will be the same whatever the analysis direction. Whereas the shape of this response is governed by the γ two-photon absorption tensor, its amplitude is driven by the α one-photon emission tensor. Note that in all the previous studies on fluorescence polarimetry in crystals this property was observed, indicating a strong energy transfer effect between molecules (Fig. 2.22). In molecular co-crystals typically 50% FRET efficiency is observed at a relative distance

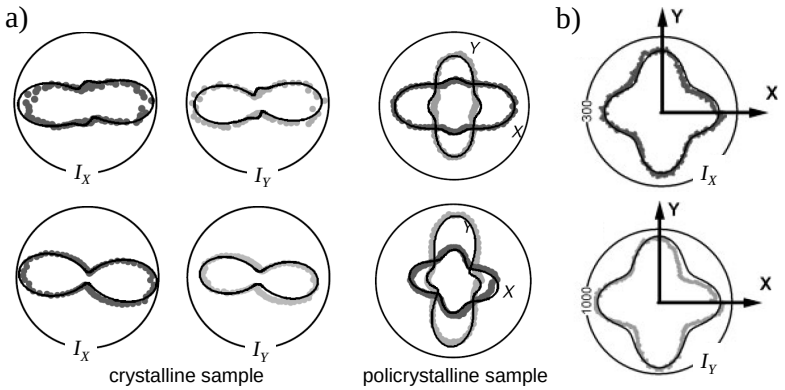

Figure 2.22: 2PEF polarization responses in (a) α-((4 prime -methoxyphenyl)methylene)-4-nitro-benzene-acetonitrile) molecule (CMONS) nanocrystals [41] (b) 1,3,5 tricyano-2,4,6-tris(p-diethylaminostyryl)benzene (TTB) macrocrystals [91].

of 35-50Å between molecules [92] or even up to 100Å [93]. Therefore in pure crystals where the distance between molecules is very small (5-10Å) one can expect close to 100% fluorescence energy transfer efficiency. Also in proteins the distance between tryptophan leads to strong homo-FRET (50%) for distance 6-12Å [94].

Since homo-FRET leads to the depolarization of polarimetric patterns which occurs in its very similar shape it could be a direct signature of a pure crystalline structure. We will extend this effect in chapter 5 to three-photon fluorescence.

2.5 Influence of birefringence on the polarimetric responses

In anisotropic samples the birefringence can introduce a phase shift in the input field polarization state between optical axes of *a priori* unknown orientations. Essentially upon rotation of the incident linear polarization, the ellipticity occurring from the sample birefringence is expected to strongly modify the polarimetric dependance of the measured signal through the whole sample thickness L (Fig. 2.23 a). In order to account on the consequent polarization distortions the electric field expressed in equation 2.3 must be re-written. In this analysis we assume that the object projection in the sample plane is uni-axial, which is consistent with a cylindrical symmetry distribution occurring in most of the systems imaged in nonlinear microscopy. Nevertheless more general distributions can be introduced accounting for the biaxial nature of the sample. Following [95], we denote Θ_b the angle between the X macroscopic axis and the fast optical axis x_b of the object, as shown in the Fig.. 2.23, and Φ_b the phase shift between its fast and slow optical axes. The new expression of the optical field polarization state at the focal depth distance d is, in the planar wave approximation:

$$\begin{bmatrix} E_X(Z=d) \\ E_Y(Z=d) \end{bmatrix} = \begin{bmatrix} \cos\Theta_b & -\sin\Theta_b \\ \sin\Theta_b & \cos\Theta_b \end{bmatrix} \cdot \cdot \begin{bmatrix} \cos\Theta_b & \sin\Theta_b \\ -\sin\Theta_b \exp(i\Phi_b(d)) & \cos\Theta_b \exp(i\Phi_b(d)) \end{bmatrix} \cdot \begin{bmatrix} E_X^0(\alpha) \\ E_Y^0(\alpha) \end{bmatrix} \quad (2.33)$$

where $E_{X,Y}^0(\alpha)$ is the optical field polarization components in the macroscopic (X,Y) frame at the sample surface $(Z=0)$ (Fig. 2.23a). The phase shift is given by $\Phi_b(d) = \frac{2\pi}{\lambda}\Delta n d$, with λ the incident wavelength and Δn the refractive index difference between the fast and slow axes of the object in the sample plane. In this expression the right matrix corresponds to the rotation of $\mathbf{E}^0(\alpha)$ in the frame of the sample optical axes. The

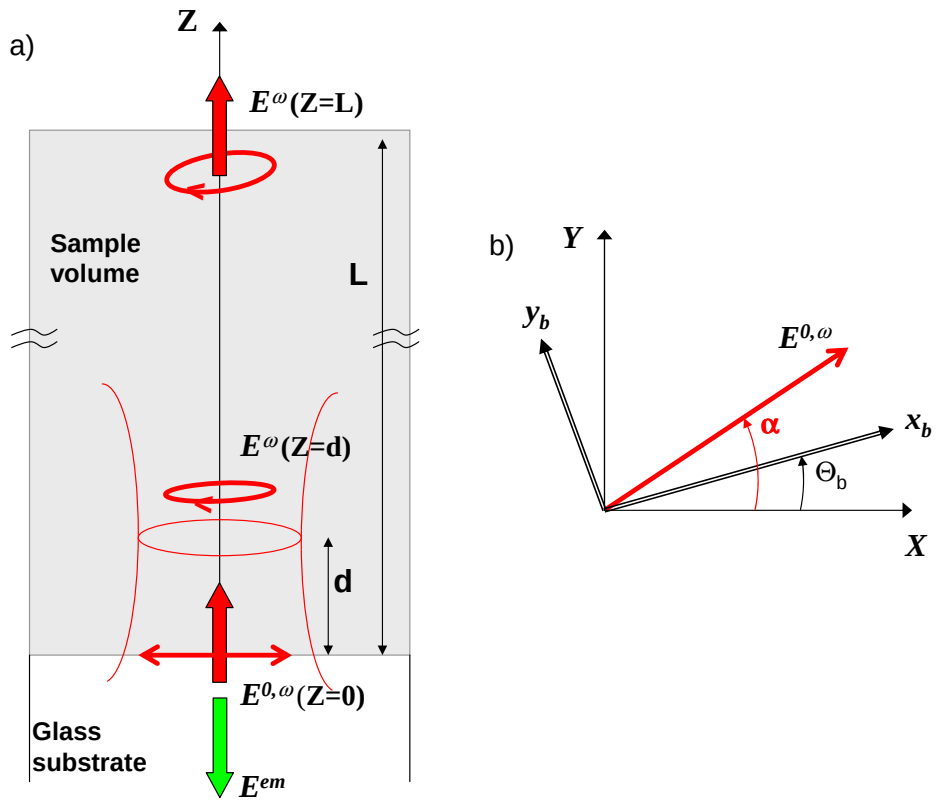

Figure 2.23: (a) Experimental configuration in the sample volume: a linearly polarized field at frequency ω is focused at a distance d from the sample bottom surface along the optical axis direction Z. The transmitted field at ω, that propagates through the whole thickness of the medium L, is elliptical if the sample is birefringent. (b) Definition of the input polarization angle α and the birefringence fast optical axis direction x_b in the macroscopic frame of the sample plane (X, Y).

left matrix contains the introduction of the phase shift along the y_b axis as well as the rotation back to the macroscopic frame.

In addition to this effect on the incident field, birefringence also affects the detected signal, which propagates back in the sample in the case of a backward detection. A similar approach as the one described above can be implemented to account for this effect, assuming that the same Δn value applies to both incident and emitted wavelengths. The relation between the macroscopic emission dipole components at the focal depth d and at the exit of the sample $(Z = 0)$ follows the same equation as in 2.33, introducing the detection wavelength in the expression of Φ_b.

2.5.1 *In situ* characterization of the sample local birefringence

In order to measure the birefringent characteristics of a sample we implemented a similar polarimetric analysis as developed for fluorescence, except that it is performed on the transmitted signal I^{ω} through the sample in a forward detection set-up (we use a similar detection set-up as in Fig. 2.3 where the ω laser frequency is measured).

The influence of the birefringence phase shift on the polarimetric response of the incident intensity I_X^{ω} passing through the birefringent sample is depicted in the Fig. 2.24. Theoretical polarimetric responses are calculated for a 1D sample, which optical axis is

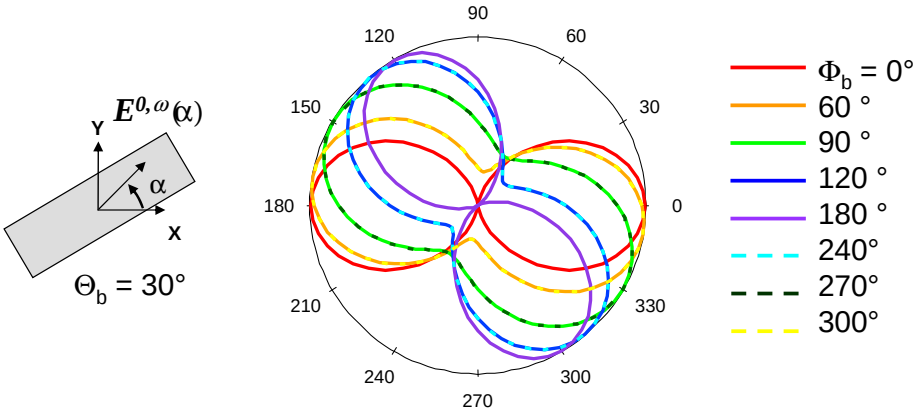

Figure 2.24: Theoretical linear polarimetric responses I_X^{ω} of the transmitted field at frequency ω detected along the X axis. The optical axis of the sample is fixed at $\Theta_b = 30°$ and the curves show the influence of the phase shift Φ_b on the polarimetric measurements.

tilted by an angle $\Theta_b = 30°$ relative to X. If no birefringence is present, the polarization response exhibits a two-lobes pattern dependent on $\cos^2\alpha$ with a maximum intensity along X and vanishing intensity along the Y axis. In the presence of birefringence, this pattern tends to open (no extinction occurring along the Y axis) and rotates progressively when Φ_b increases. A similar behavior is expected for the intensity detected along the Y axis (with I_X patterns perpendicular to I_Y patterns).

Fig. 2.25 a shows I_X^{ω} and I_Y^{ω} polarimetric theoretical responses obtained for $(\Theta_b, \Phi_b) = (44°, 97°)$ (these values have been typically measured in a 100μm thick collagen fiber oriented along 45° with respect to X axis in the sample plane). These responses are furthermore deformed accounting for the additional effect of the dichroic mirror (section 2.2), which is due to the fact that the dichroic mirror acts in the same way as a birefringence plate of optical axes along X and Y. These responses can be exploited to extract the birefringence information through the whole sample thickness. Note that knowing the depth penetration of the incident field and supposing a homogeneous medium, one can deduce

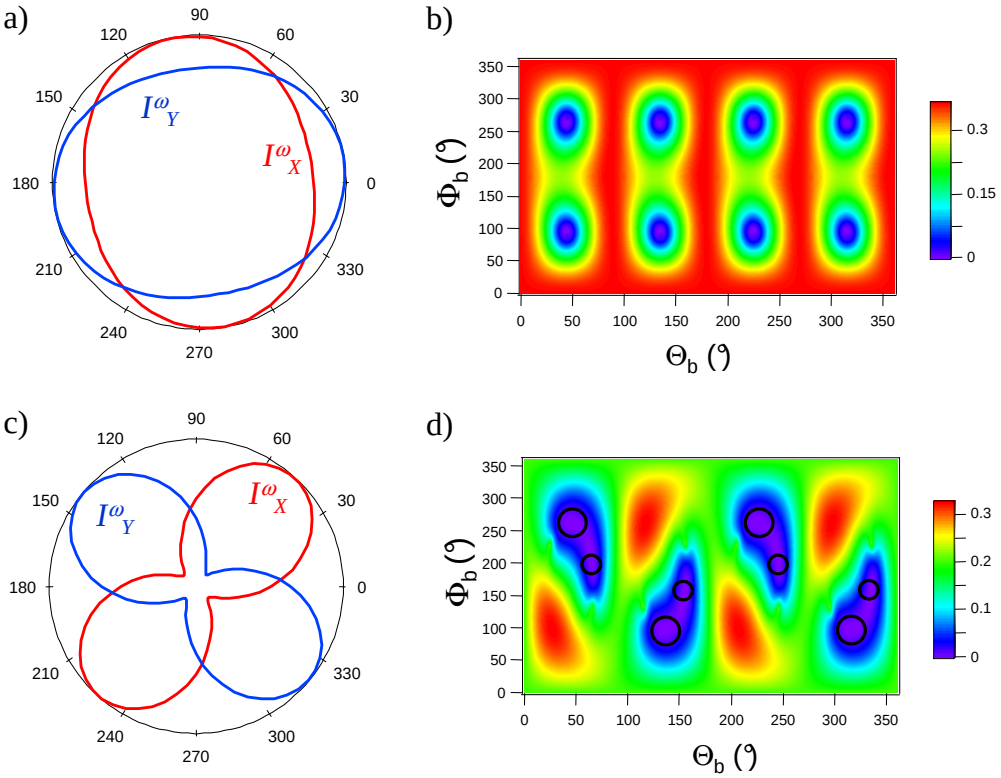

Figure 2.25: (a) Theoretical linear polarimetric responses I^{ω}_{X} calculated for $\Theta_b = 44°$ and $\Phi_b = 97°$ (b) Theoretical cartography of the mean square error as a function of the birefringence parameters (Θ_b, Φ_b) with no polarization distortions by the dichroic mirror (c) Theoretical linear polarimetric responses I^{ω}_{X} accounting on the polarization distortions ($\gamma = 0.043$ and $\delta = 55°$) and corresponding (d) map of the mean squared error. The values used here correspond to measurements performed in a collagen fiber performed by Fabiana Munhoz [95].

this birefringence information at any place in the sample and therefore use it for further 2PEF polarimetric analysis. In order to determine the validity of the method using I^{ω}_{X} and I^{ω}_{Y} to determine Θ_b and $\Phi_b(L)$, we fit theoretical data using the mean squared error (χ^2) :

$$\chi^2(\Theta_b, \Phi_b) = \sum_{\alpha} \left(I_{theo}(\Theta_b = 44°, \Phi_b = 97°) - I_{theo}(\Theta_b, \Phi_b)\right)^2 \tag{2.34}$$

χ^2 is depicted in Fig. 2.25 b, calculated for a large span of (Θ_b, Φ_b) values when no polarization distortions are introduced by the dichroic mirror. The minimum of the fitting error is unique and can be found for Θ_b with a $\pi/2$ periodicity, and two solutions for the phase shift with $\Phi_{b1}(L) + \Phi_{b2}(L) = 2\pi$ periodicity. The observed periodicity is consistent

with the fact that this technique does not discriminate the fast and slow axes of the system. Accounting for the ellipticity and dichroism introduced by the dichroic mirror (here $(\gamma, \delta) = (0.043, 55°)$), leads to a slight modification of the fit solutions (Fig. 2.23a). Precisely, introducing the polarization distortions from the reflection optics results in a new set of solutions (Θ_b, Φ_b) that is not a unique solution. This means that when performing polarimetric measurements, one has to account for the different possible solutions in the data fitting.

2.5.2 Influence of birefringence on 2PEF polarimetric responses

In the previous section we could see the influence of the sample birefringence on the polarimetric response for the ω frequency of the excitation field where the field propagates in the forward direction through the whole sample thickness.

In order to visualize the effect of birefringence on the 2PEF polarimetric response, the model described above is applied to a cone lying in the (X, Y) plane, which main orientation Θ relative to X corresponds to the optical axis of the uni-axial object. Fig. 2.26 shows the effect of birefringence on the I_X and I_Y 2PEF polarimetric responses in a system of large cone aperture. An increasing birefringence leads to a deformation of the

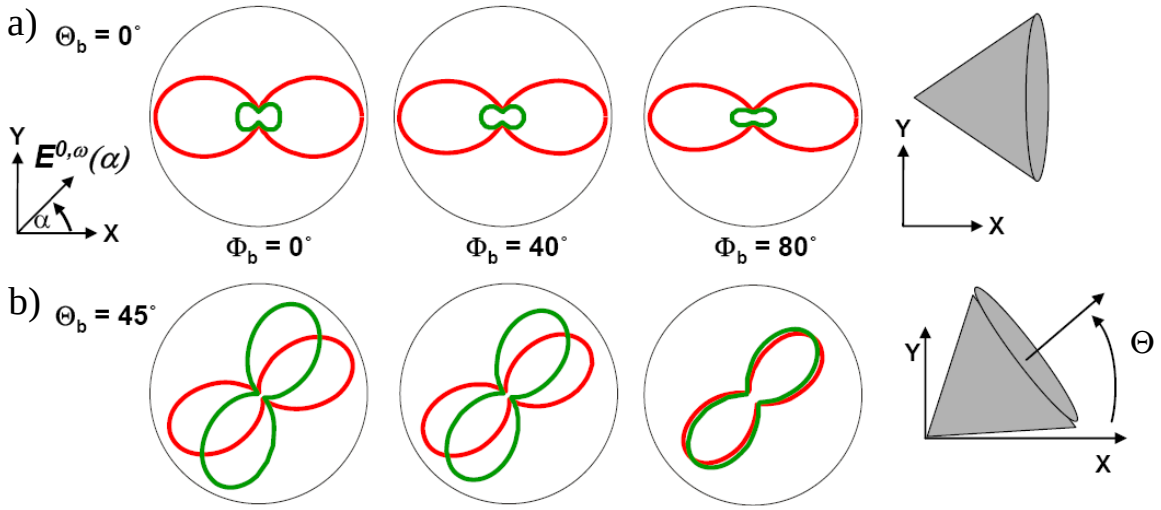

Figure 2.26: Theoretical 2PEF polarimetric responses I_X^{2PEF} (red) and I_Y^{2PEF} (green) for a molecular distribution within a large cone aperture (half angle 50°), for different orientation Θ of the cone in the (X, Y) frame (corresponding here also to optical axis orientation Θ_b). a) $\Theta = \Theta_b = 0°$ and b) $\Theta = \Theta_b = 45°$, with different values of the birefringence phase shift Φ_b.

polarimetric polar plots, in particular when the optical axis is away from the macrocscopic

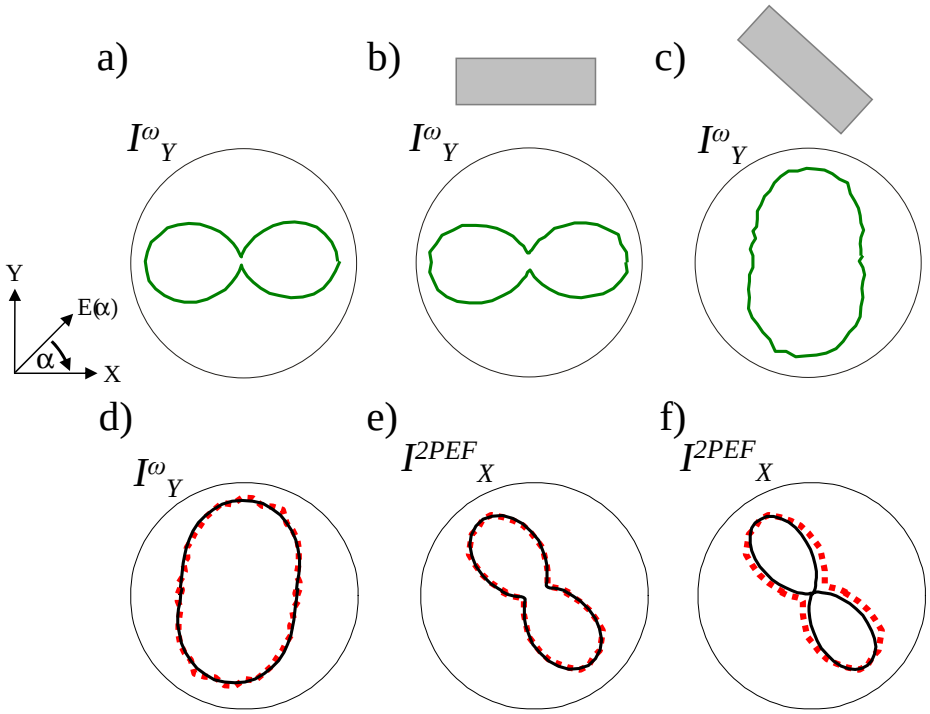

Figure 2.27: Experimental birefringence and 2PEF polarimetric measurements in PHTP-DANS 1D crystal. (a) Laser polarimetric response I_Y^{ω} of the non-birefringence glass substrate (no crystal). (b, c) Laser polarimetric response trough the crystal oriented along the (b) X axis and (c) tilted at about 135° relative to X (as sketched). (d) Fit of the laser polarimetric response (solutions : $\Theta_b = 138°, \Phi_b = 116°$). (e) Fit (continuous line) of the 2PEF I_X^{2PEF} polarimetric response (dotted line) including birefringence, at a 5μm penetration depth (solutions : $\Theta = 164°, \Theta_b = 138°, \Phi_b = 100°$). (f) Fit (continuous line) of the 2PEF polarimetric response (dotted line) with no birefringence included. All the fits include the dichroism and ellipticity parameters of the dichroic mirror (dichroism $\gamma = 0.009$, ellipticity factor $\delta = 13°$).

projection axes X or Y. This would clearly lead to a misinterpretation of the polarimetric data, even for slight birefringence phase shifts. In particular for large value of Φ_b, the polarimetric data resemble those of much smaller cone aperture than what it is actually.

Experimental TPEF polarimetric data are shown in Fig. 2.27 on a 1D macroscopic uni-axial molecular co-crystal of (PHTP-DANS) mentioned above [87]. In this crystal the birefringence is non-negligible, which is particularly visible when the crystal is tilted (Fig. 2.27 c). The birefringence phase shift $\Phi_b = 116°$ deduced from the fit of I_Y^{ω} is only indicative since a large thickness (about 500 μm) is crossed in the forward direction,

and many π phase shift periods are expected. To fit the 2PEF polarimetric data, the 1D distribution is modeled by a cone of infinitely small aperture angle (dirac function) oriented along the main axis of the crystal by an angle Θ relative to X. All angles Θ, Θ_b and Φ_b, are used as fittings parameters. The fit, which is clearly improved by accounting for birefringence (Fig. 2.27 e f), leads to values consistent with both the tilt angle of the crystal ($\Theta \approx 135°$) and a large birefringence. At a penetration depth of 5 μm, the fitted birefringence phase shift leads to $\Delta n \approx 0.04$, which is relevant in such a system where Δn value ranging between 0.001 and 0.8 have been reported in molecular crystals [83]. Note that the measured birefringence value is averaged over the excitation volume of the objective, which introduces an error margin on the penetration depth value and therefore on the Δn determination. In addition, the difference between Θ and Θ_b found when fitting I^{ω} and I^{2PEF} might be due to a slight heterogeneity of the crystal main axis orientation through its large thickness. Nevertheless, if the birefringence effect is not accounted for in the 2PEF polarimetric fit, the quality of the fit is considerably reduced (Fig. 2.27 f).

2.6 Conclusion

These studies finally show that introducing instrumental polarization distortions in the data analysis is crucial before any sample investigation. In the next chapters, each of the effects investigated here will be accounted for.

Chapter 3

Probing molecular organization in biological membranes using two-photon fluorescence imaging

In this chapter we will apply polarimetric two-photon fluorescence microscopy to the investigation of the local molecular organization in heterogeneous artificial membranes and in cell membranes doped with fluorescent probes. First we will describe the origin and the context of membrane studies. We will show examples of different lipid phases and fluorescent lipid probes. Afterwards we will demonstrate that polarimetric measurements permit a quantitative analysis of the local molecular order in different heterogeneous lipid phases and cell membranes, independently on the position investigated on the vesicle or cell contour. We introduce, in the data analysis, important parameters to account for when dealing with fluorescence polarization analysis in membranes: geometrical effects, the effects of distinct absorption and emission angles of the molecular transition dipoles, as well as the presence of fluorescence resonance energy transfer (homo-FRET) in the membrane.

3.1 The lipid membrane: an insight into cell functions

An eucaryotic cell membrane depicted schematically in Fig. 3.1 consists of an amphiphilic lipids bilayer with embedded proteins, which are involved in a variety of cellular processes such as cell adhesion, ion conductivity and cell signaling. The amphipathic lipids: phospholipids and glycolipids that make up this membrane (together with molecules such as cholesterol) have a polar, hydrophilic head and two hydrophobic hydrocarbon tails.

The entire membrane is held together via non-covalent interaction of hydrophobic tails, however the structure is quite fluid and not fixed rigidly in place. According to the

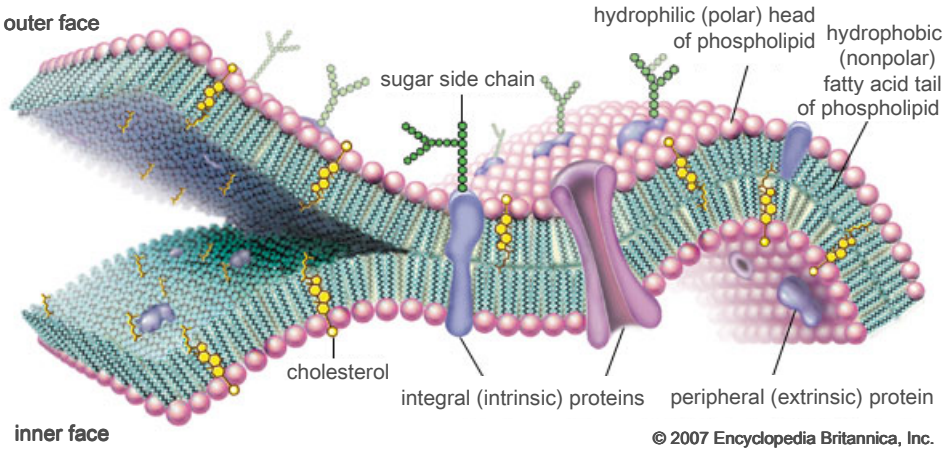

Figure 3.1: A molecular view of the cell membrane. Proteins penetrate the lipid bilayer, which is made up largely of phospholipids and cholesterol.

fluid mosaic model of S. J. Singer and G. L. Nicolson [96], the biological membranes can be considered as a two-dimensional liquid where all lipid and protein are free to diffuse and exhibit rapid lateral diffusion along the layer in which they are present. Proteins and lipids that float freely within the fluid bilayer can create dynamic assemblies that are of higher local viscosity called lipid rafts, constituted of saturated lipids, cholesterol or sphingomyelin. These assemblies are diffusing but more ordered and tightly packed than the surrounding bilayer. These membrane domains which size is below 100 nm are highly dynamic, and regulate cell membrane functions by creating an assembly of signaling molecules, influencing membrane fluidity and membrane protein trafficking or regulating neurotransmission and receptor trafficking [97, 98]. For example a raft clustering by increasing the proteins concentration can initiate a signaling cascade which occurs in allergic reactions [99], but also regulates cell growth, survival, and death [100]. Several groups of pathogens, bacteria, prions, viruses, and parasites hijack lipid rafts for their purposes [101]. Cholesterol is highly involved in the raft formation together with sphingomyelin. Epidemiologic and biochemical studies suggest that low level of cholesterol may also influence the progression of Alzheimer's disease [102]. Therefore the knowledge on how lipids, cholesterol and proteins interact in cell membranes is a key element to understand raft function in human physiology as well as in development of human diseases. For this reason large amount of work have been dedicated to the cell membrane architecture investigation in the last few years. Significant progress in research on membrane

lateral organization has been made by using membrane model systems. Essentially Giant Unilamellar Vesicle (GUV) (Fig. 3.2b) which size is similar to the size of eukaryotic cells and which one can control the molecular composition as well as the environmental conditions, allows direct visualization of the membrane organization by means of fluorescent microscopy [103, 104, 105, 78, 106, 79, 107]. The imaging of molecules in such systems and comparison with biological membranes reveals intra-and inter-cellular dynamics, as well as subcellular structure, the properties of membranes (mechanical, viscosity, elasticity...), and the molecular trafficking of proteins, nucleic acids and other molecules.

So far, imaging lipid organization has relied on the use of dedicated fluorescent probes specifically partitioning in regions of known lipid composition or local polarity [12, 108, 107]. These probes are also expected to undergo specific orientational orders detectable by fluorescence anisotropy [12, 108, 109]. However so far, no direct imaging of molecular order in heterogeneous lipid domains has been attempted probably because of the limitations of the use of anisotropy in heterogeneous systems as explained in chapter 1. In addition, studies of molecular orders in living cells has been so far very limited and restricted to rand cell shapes which all more readily exploitable by fluorescence anisotropy [13, 29]. Here we illustrate the application of TPEF polarimetry on two issues that cannot be addressed by a pure ratiometric method: (i) the investigation of the orientational organization in coexisting liquid phase with different fluid domains of micrometric sizes in GUVs, (ii) and in cell membranes of non-spherical shapes.

3.1.1 Giant Unilamellar Vesicles (model cell membrane)

GUVs studied as a model for domain formation in cellular membranes are lipid bilayers formed from a ternary mixture of different lipids. Here we will essentially study three components : 1,2-dioleoyl-sn-glycero-3-phosphocholine (DOPC), sphingomyelin from chicken egg yolk (SM), and cholesterol (Chol) [78, 106, 79, 107] (Fig. 3.2). DOPC lipids are derivatives of glycerol comprising two fatty acyl residues (nonpolar tails) and a single phosphate ester substituent (polar head group). The structural backbone of sphingolipids is the sphingosine to which a single fatty acid residue is attached via an amide linkage (Fig. 3.2a). Aggregation of lipids is a self-assembly process driven by lipid interactions such as Van Der Waals, hydrophobic, electrostatic interactions and hydrogen bonding. This lipid mixture allows formation of coexisting domains of controllable size and different fluidity phases (Fig. 3.2c). The liquid-ordered (Lo) phase is enriched in sphingomyelin and cholesterol whereas liquid-disordered (Ld) phase is mainly composed of DOPC. The difference comes from the saturation of the hydrocarbon chains in sphingolipids in the rafts

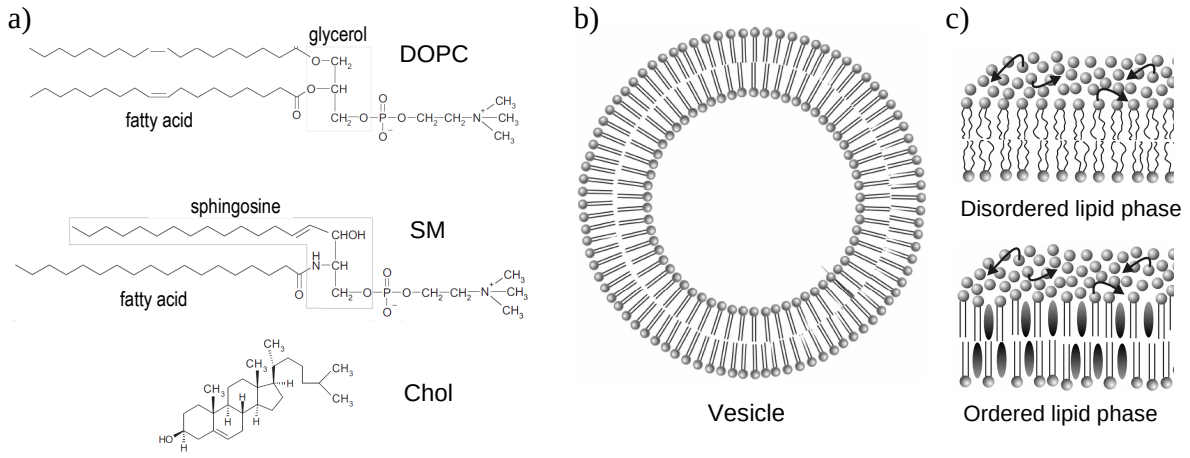

Figure 3.2: (a) Three major phospholipids. (b) Giant Unilamellar Vesicles (GUV) build of phospholipids. (b) Schematic representation of liquid disorder (Ld) and order phase (Lo). In Ld phase lipids show both lipid chain conformational and translational disorder. In Lo phase the lipid chains are ordered due to interactions with the cholesterol (depicted as ellipses), but there is translational disorder allowing for lateral diffusion.

as compared with the unsaturated state of fatty acids of DOPC in the Ld phase [110]. Cholesterol presented in Lo phase serves as a dynamic glue that keeps the rafts assembly together [111]. The rigid nature of its sterol group interacts preferentially, although not exclusively, with the phase where acyl chains of the lipids tend to be more rigid and in a less fluid state [97]. Nevertheless there is translational disorder, allowing for lateral diffusion. Ld phase is characterized both by low conformational order in the carbon chains and by low translational order [112, 113]. These two liquid phases have been characterized by measuring the diffusion of the small, lipid-like probe inside these liquid phase domains using Fluorescence Correlation Spectroscopy (FCS) Microscopy which probes the lateral diffusion dynamics of fluorescent molecules [114]. The morphology of the lipid domains and their changes at the phase transition in complex lipid mixture has been determined by two-photon fluorescence microscopy imaging using partitioning probes [115]. Finally the fluorescence imaging of two-photon linear dichroism and anisotropy analysis allowed to investigate the orientation of molecules relative to the cell membrane and show that the cholesterol plays important role in stabilization and ordering lipid tails within the membrane [13]. Moreover high resolution fluorescence imaging using two dyes preferentially labeling different phases provided correlation between domain composition and local membrane curvature [107]. Note that in living cells, similar domains exist but at a much smaller size (∼100nm). Therefore the present study in GUVs is made to provide some

lower and upper limits of angular order behavior that can be observed in cells.

Giant Unilamellar Vesicles sample preparation

The giant unilamellar vesicles were prepared according to the electroformation method developed by Angelova and Dimitrov [116] depicted schematically on the Fig. 3.3. First, 10 μL of a 6.6 mM solution of DOPC, cholesterol (Chol) and SM (1:1:1) loaded with fluorescent lipid probes (1:1000) were deposited at 40°C on two glass slides covered with indium tin oxide. This temperature is chosen to facilitate the evaporation of chloroform. The chloroform elimination was completed by drying the slides under vacuum for 1 hour. The slides were then sealed together and solvent (428 mM solution of sucrose in water) was added to the chamber and heated to the desired temperature (above the lipid mixture phase transition, 55°C for DOPC/cholesterol/SM). In the last step, the chamber was connected to an electrical generator (AC Exact, model 128; Hillsboro). A 8 Hz, 25 mV peak to peak sinusoidal voltage was applied. It was increased by 100 mV steps every 5 minutes, up to a value of 1225 mV. These conditions were maintained overnight. Next, the application of electrical square pulses of same amplitude at 4 Hz detached the GUVs from the slides.

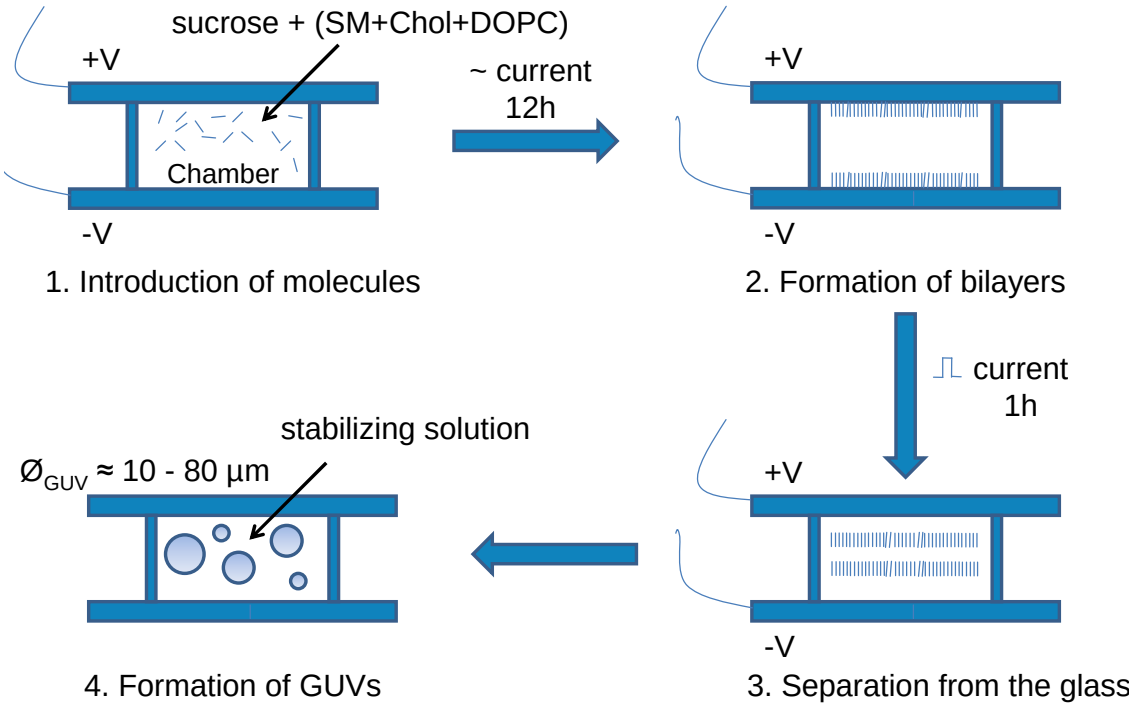

Figure 3.3: GUV sample preparation scheme.

One circular cover glass (Menzel-glaser, 25mm diameter) was heated to stick to a ring of parafilm. This cover glass together with another cover glass, were previously oxydized with ozone, generated by UV surface decontamination system (PDS-UV Novascan Tech.), for 3 minutes. GUVs were then injected inside the parafilm ring and diluted in an arbitrary ratio with a stabilizing solution (HEPES 10mM, NaCl 150mM, CaCl2 2mM, NaN3 2mM), the GUVs swell up to a round shape because of the difference of osmotic pressure between interior of sphere and the environment. Oxidization provided by ozone on the cover glass lead to generation of SiO- that can form chemical link with lipids through the mediation of Calcium in the buffer, thus reducing the lateral movement of GUVs. With this approach, we have obtained GUVs with diameter ranging from 10 to 80 μm.

DOPC and cholesterol were obtained from Avanti Polar Lipids, and chicken egg yolk sphingomyelin from Sigma Aldrich. Lipids were used without further purification and were stored in chloroform/methanol (9:1) at -20°C until use.

3.1.2 Cell membrane

The COS-7 cell line was derived by Yakov Gluzman in the early 1980s from the previously established CV-1 African green monkey kidney line. The cells exhibit fibroblast morphology are thus often called COS-7 monkey fibroblast or COS-7 fibroblast-like cells and are mostly utilized in transfection experiments. In this work the COS-7 cell line was chosen due to their facility in cultivation, replicative capacity and low fragility. Moreover the adherent nature of this cell makes it an ideal model for the membrane investigation studies. The cell preparation and study were performed in collaboration with Tsai Jung Han, master student.

Cell lines preparation

COS-7 cells (American Type Culture Collection No. CRL-1657) were maintained in 37°C with DMEM medium (Lonza, Belgium)completed by 5% FBS, and penicillin-streptomycin (50 units/ml). Before measurement, cells were transferred onto glass coverslips, incubated for 3.5 hour, washed twice with insertion buffer (NaCl 130mM, KCl 5mM, CaCl2 10mM, glucose 5mM, and HEPES 10 mM (pH 7.4)) and then stained with 5μ M di-8-ANEPPQ (dissolved by absolute ethanol to 1mM for preservation and usage) for 5 minutes. The cells were then washed twice again and kept at room temperature in the insertion buffer for the whole imaging process. 2PEF polarimetry on cell membranes was performed at room temperature (this work being a feasibility study).

Sample preparation and labelling

Before measurement, trypsin detached cells were transferred onto glass coverslips located in a metal chamber (attocell, invitrogen) and incubated in the same condition than these of routine maintenance. After 3.5 -7 hours, the cells were taken out from incubator, the DMEM complete medium was removed, then the cells were washed twice with insertion buffer (NaCl 130mM, KCl 5mM, $CaCl_2$ 10mM, glucose 5mM, and HEPES 10mM (pH 7.4), stored in 4°C) and then stained for 5 minutes by adding di-8-ANEPPQ solution (as mentioned before) at a final concentration of 5μM. Cells were washed twice again to remove the excessive fluorescence probe remaining in the buffer and then kept in insertion buffer for the whole imaging process. The insertion buffer is used rather than culture medium because it contains HEPES that keep the appropriate pH for cells and it lacks of phenol red which is an undesired source of fluorescence. All measurements were done at room temperature and finished within 3.5h from each preparation. In this condition, the cells are mainly partially attached to the cover glass, without too vigorous movement, and isolated from the other cells.

3.1.3 Fluorescent lipid probes

Fluorescent lipid probes can be divided into two classes : intrinsic and extrinsic. Intrinsic fluorescence occurs naturally whereas extrinsic fluorescence has to be added to the sample (such as from synthetised molecules). Since the lipid membrane does not exhibit any fluorescence and thereby has to be labeled with fluorophores in this chapter we will focus only on the extrinsic probes.

Membrane probes include fluorescent analogs of natural lipids, as well as lipophilic organic dyes. Fluorescent phospholipid analogs exhibit some structural resemblance to natural lipids : the fluorophore can be attached to one (or both) of the fatty acyl chains or to the polar head group. The attachment position of the fluorophore determines whether it is located in the hydrophobic interior or at the water/lipid interface. The depth of the probes in the bilayer can be adjusted by the length of the chain. On the other hand the fluorescent organic dyes are not analogs of any particular biological lipid class, but their general structure facilitates membrane labeling. These dyes are either amphiphilic (having both polar and nonpolar structural elements) or neutral (lacking charges and most soluble in very nonpolar environments). The amphiphilic dye contains a charged fluorophore that localizes the probe at the membrane's surface and lipophilic aliphatic "tails" that insert into the membrane.

Characteristics of the fluorophore (i.e. its size, the chain length and saturation or unsaturation of fluorescent lipid analogs) can have critical influence on the probe partitioning and lipid membrane properties. For instance fluorescent lipid probes with unsaturated chains are found to partition into the disordered liquid phase [117] whereas partitioning into ordered liquid phase is increased for fluorophores with saturated chains [118]. Therefore special care is needed for the selection of probes.

In this studies the general criteria of the selection of the fluorescent lipid probes is their high quantum yield and large nonlinear absorption cross section which makes this molecules suitable for two-photon excitation, as well as the orientation inside the lipid bilayer preferentially parallel to the lipid acyl chain axis and partitioning into both Lo and Ld phases.

In order to investigate the static orientational order of different fluorescent probes in GUV and cell membranes we chose the following fluorescent molecules (Fig. 3.5 and Fig. 3.6):

- DiI-C_{18} - 1,1'-dioctadecyl-3,3,3',3'-tetra methyl indo carbocyanine perchlorate
- di-8-ANEPPQ - 1-(3-sulfonatopropyl)-4-[beta [2-(di-n-octylamino)-6-naphtyl]vinyl] pyridinium betaine
- TMA-DPH - 1-(4-trimethyl ammonium-phenyl)-6-phenyl-1,3,5-hexatriene
- Laurdan - 6-dodecanoyl-2-dimethylamine-naphthalene
- C-Laurdan - 6-dodecanoyl-2-[N-methyl-N-(carboxymethyl)amino]naphthalene

The fluorescent lipid probes TMA-DPH, DiIC_{18}, di-8-ANEPPQ and Laurdan were purchased from Invitrogen molecular probes. C-Laurdan was synthesized by the group of Bong Rae Cho from Korea University in Seoul, South Korea [108].

All these probes excepted of DiI-C_{18} are present in both Lo and Ld phases of GUV build of DOPC/SM/Chol mixture and their transition dipole moment is parallel to the acyl chain.

DiI-C_{18} is known to locate in Ld phase in such lipid mixtures [119], is thus used as a preliminary control for the Lo and Ld domains identification. These domains are prepared in such conditions that they are of micrometric size and therefore well identificable. Indeed fluorescence signal detected from GUVs doped with DiI-C_{18} molecules shows the existence of liquid disorder domains in lipid membrane as illustrated in the Fig. 3.4. Further analysis of the molecular orientational is done without the DiI-C_{18} fluorophore in the membranes.

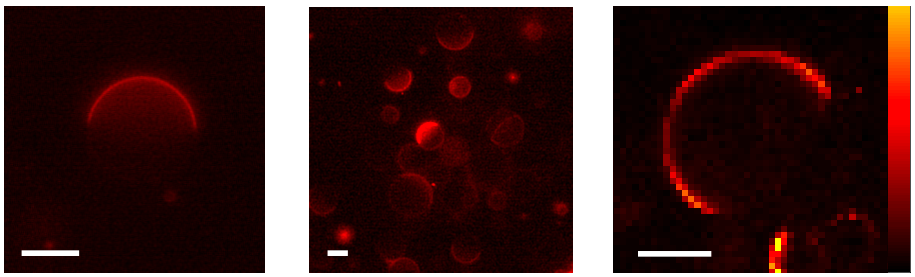

Figure 3.4: One photon fluorescence from a scanning confocal microscope (left and middle) and 2PEF image (right) obtained for GUVs doped with DiI-C_{18} fluorescent dyes reflecting Ld phase. Scale bars: 20μm.

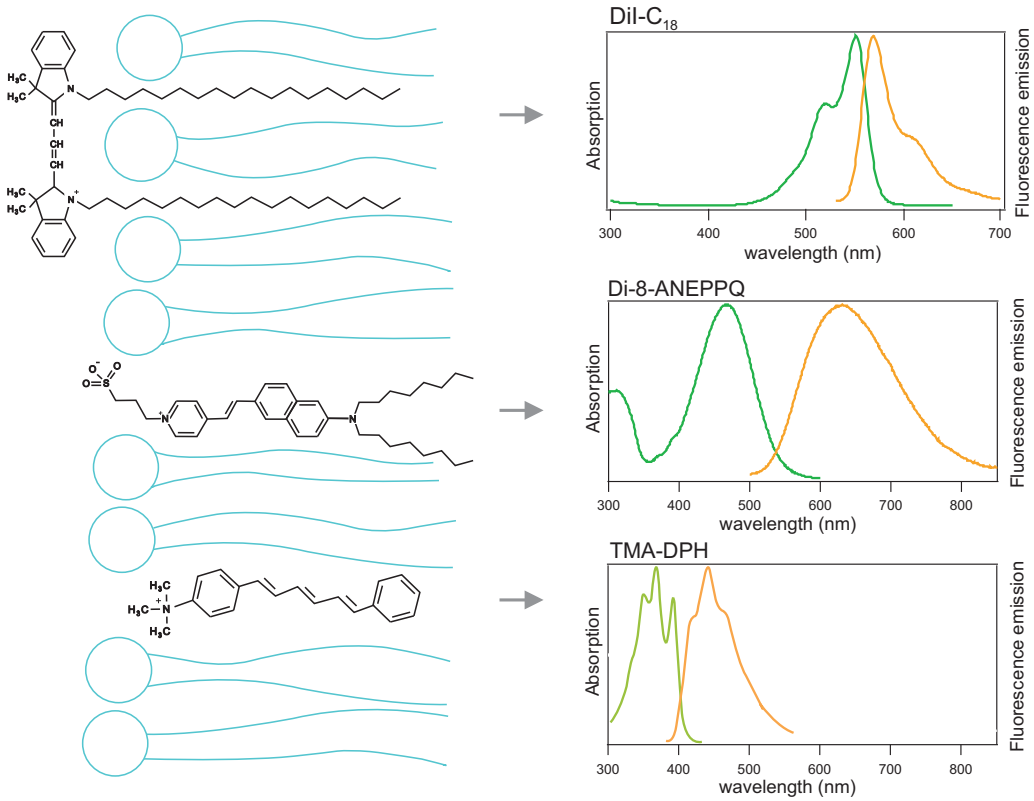

Figure 3.5: Structure of the fluorescent lipid probes and their schematic localization inside the membrane. Absorption and emission fluorescence spectra of di-8-ANEPPQ and DiI-C_{18} respectively in EtOH and MeOH solvent. Absorption and emission spectra of styryl dyes are at shorter wavelength in membrane environments than in reference solvents. The difference is typically 20nm for absorption and 80nm for emission, but varies considerably from one dye to another [120]. Absorption and emission spectra of TMA-DPH incorporated into lipid membrane. [121]

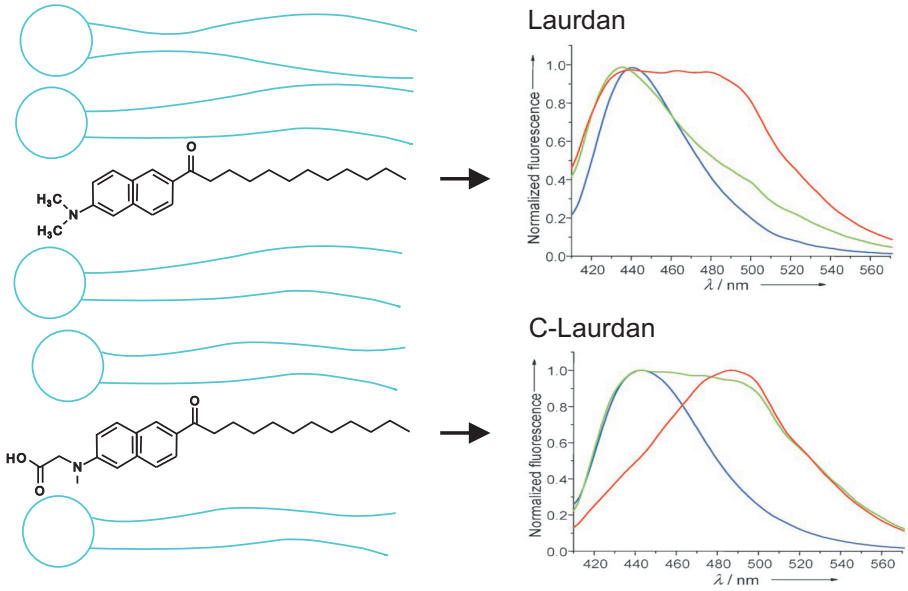

Figure 3.6: Structure of the fluorescent lipid probes and their schematic localization inside the membrane. Normalized emission spectra of Laurdan and C-Laurdan in the phospholipid vesicles exhibited liquid order phase (blue), liquid disorder phase (red) and composed of DOPC+SM+Chol mixture (green) [108]

.

di-8-ANEPPQ is well retained in the outer leaflet of cell plasma membrane due to its lipophilic nature and enter inside the cell after much longer time than for instance Laurdan. Therefore this fluorescent probe has been chosen in this work to label the cells.

TMA-DPH is one of the most common membrane fluorescent probe. The orientation of this dye within lipid bilayers is generally assumed to be oriented parallel to the lipid acyl chain axis as demonstrated by time-resolved fluorescence anisotropy and polarized fluorescence measurements of oriented samples [122, 123]. TMA-DPH has been used in this work to compare polarimetric data with results obtained from previous anisotropy fluorescence measurements.

Laurdan is a fluorescent organic dye that detects changes in membrane phase through its sensitivity to the polarity of its environment in the bilayer. It is known that variations in membrane water content and in lipids composition during phase transition cause shifts in the laurdan emission spectrum [12] (Fig. 3.6). This dye has been used to study lipid organization in membranes by detection and quantitation of coexisting lipid domains [124, 125] or for monitoring the effect of the cholesterol and temperature on the liquid phases [126, 115].

C-Laurdan is a recently synthesized dye (Korea University) which is also sensitive

to the lipid phase environment [108]. However its greater sensitivity to the membrane polarity allows to probe membrane environment more accurately. It has been shown that at 780nm excitation, C-Laurdan in raft mixtures made of both Lo and Ld phases exhibit broad emission spectra with two maxima depicted on the Fig. 3.6 [108]. The first one, around 440 nm, reflects the Lo phase (represented here in DPPC (1,2-dipalmitoyl- sn-glycero-3-phosphocholine) whereas the second one, around 490nm, is attributed to the Ld phase (DOPC). Laurdan and C-Laurdan are specifically chosen for their ability to provide a spectral identification (and thus a control measurement) of the Lo and Ld domains location on a GUV.

In two-photon fluorescence experiments the incident wavelength is set at 780nm for C-Laurdan, Laurdan, TMA-DPH and di-8-ANEPPQ, and 1040nm for $DiIC_{18}$. All the measurements given in this chapter are performed with a typical incident averaged power of 4 mW at the entrance of the microscope (which corresponds to about half a mW at the focal spot of the objectives).

3.2 Polarimetry in lipid membranes: theoretical model

In order to model the polarized two-photon excited fluorescence process in doped membranes in GUVs or cells we will employ the theoretical approach developed in chapter 1.

3.2.1 Molecular distribution model

The theoretical studies that allowed a qualitative interpretation of membrane lipid order were introduced in 1977 by K. Kinosita and coworkers [69]. The method is based on the fact that the polarization of emitted fluorescence, radiated by molecules excited by a pulse of polarized light, is maximal at the moment of excitation and decays to the stationary value after a certain period of time. For this reason the molecules in membrane exhibit wobbling motions rather than free rotation [127, 128, 129]. The rate of the polarization decay reflects the frequency of fluctuations of molecular orientation, while the stationary value reflects the orientational constraint imposed by neighboring molecules. The model that considers rod-shape molecules (with emission dipole moment parallel to the lipid acyl chain axis) freely diffusing in a constraint potential is called "wobbling-in-cone" (Fig. 3.7). In this model, the orientation of the emission and absorption transition dipole moment of the lipid probe $\boldsymbol{\mu}^{em}(\theta, \phi)$ are confined within a cone around the normal direction n of the membrane, corresponding to the molecular averaged orientation ρ introduced in chapter

1. $\boldsymbol{\mu}^{em}(\theta, \phi)$ fluctuates uniformly within the cone with a wobbling diffusion constant generally much faster than the integration time in polarimetric measurements. The maximum cone angle Ψ (Fig. 3.7) corresponds to the molecular distribution defined in chapter 1. This model was used in a study by D. Axelrod in 1979 which determined the orientation of fluorescence probes in lipid membranes under a high aperture focusing [34]. K. Florine-Casteel in 1990 further derived theoretical expressions of the fluorescence anisotropy dynamics and experimental results of the collected polarized fluorescence as a function of the observation position on rand-shape membrane surface as well as the degree of lipid order. As we could see in all these studies the orientational distribution in lipid membranes is defined as a cone shape with an abrupt change of the probe potential at a defined aperture angle $\theta = \Psi$. In this case

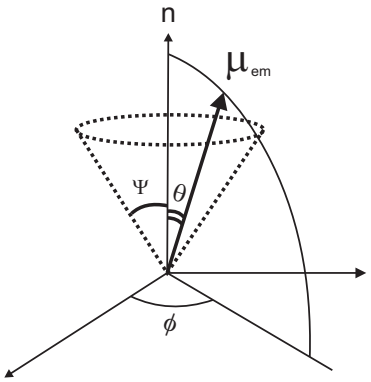

Figure 3.7: Wobbling-in-cone model [69].

$$f(\theta, \phi) = 1/(4\pi\Psi) \tag{3.1}$$

for $\theta \leq \Psi$ and $f(\theta, \phi) = 0$ otherwise. This corresponds to a very abrupt potential $U(\theta, \phi)$ in the more general thermal equilibrium T Boltzmann distribution $exp(-U(\Omega)/k_BT)$. Other functions have been proposed such as a normalized Gaussian distribution (which corresponds to a smoother potential) :

$$f(\theta, \phi) = (\sqrt{\ln 2}/\Psi) \exp(-\ln 2\theta^2/\Psi^2). \tag{3.2}$$

used by R. K. P. Benninger and coworkers in 2005 to study effect of the cholesterol on the molecular orientation in cell membranes [13] as well as Haluska and coworkers to model molecular order in liquid disorder domains in GUVs [80]. A cone contour function:

$$f(\theta, \phi) = \delta(\theta - \Psi) \tag{3.3}$$

was also seen to be appropriate to model molecular orientation in liquid ordered domains in GUV membranes [80].

The orientation of the angular distribution function in the macroscopic frame is defined by the orientation angle (ρ, η) of its symmetry axis, as illustrated in Fig. 3.8 a,b in the case of a cone distribution. Our first development assumes that the excitation and

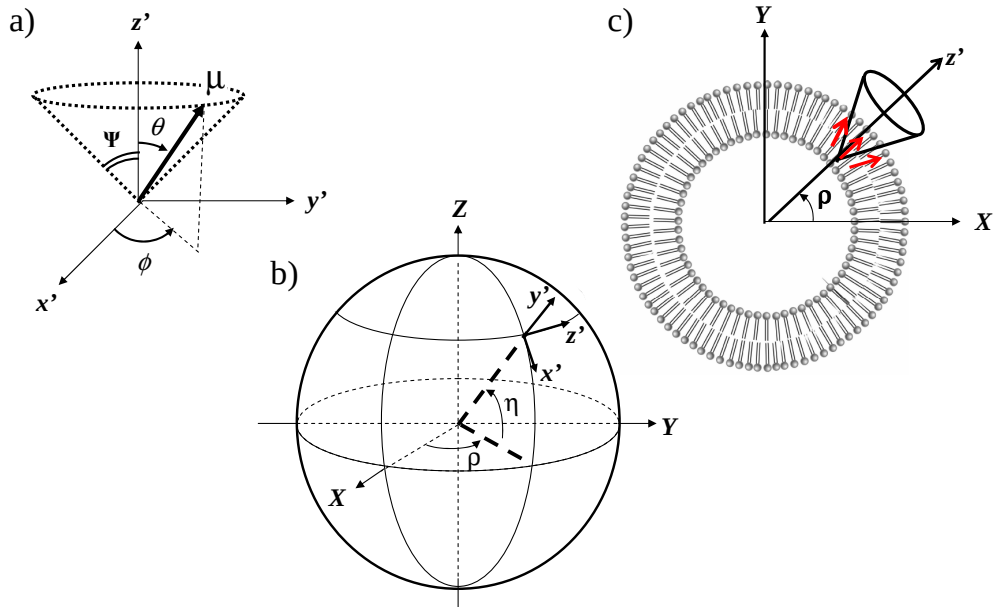

Figure 3.8: Definition of the coordinates used in the analysis. (a) In the microscopic frame, the Ψ parameter is the cone aperture of the distribution function. (θ, ϕ) defines the orientation of the molecular dipole in the cone frame. (b) In the laboratory frame, the Z axis is the optical axis, X and Y denote the sample plane in which the excitation polarization is defined. The angles ρ and η specify the cone orientation in the macroscopic frame. (c) Experimental configuration. The excitation light is focused on an equatorial point of the GUV where $\eta = 0$.

emission dipoles are parallel, the case of different orientations described in chapter 2 will be discussed later. The orientation of the excitation/emission dipole is given by the respective polar and azimuthal angles θ and ϕ in the membrane frame (x', y', z'), as described in Fig. 3.8 a. The components of the excitation dipole moment in the laboratory frame (X, Y, Z) are defined in the eq.1.37 given in chapter 1 :

$$\begin{bmatrix} \mu_X(\theta,\phi,\rho,\eta) \\ \mu_Y(\theta,\phi,\rho,\eta) \\ \mu_Z(\theta,\phi,\rho,\eta) \end{bmatrix} = \begin{bmatrix} -\sin\rho & -\cos\rho\sin\eta & \cos\rho\cos\eta \\ \cos\rho & -\sin\rho\sin\eta & \sin\rho\cos\eta \\ 0 & \cos\eta & \sin\eta \end{bmatrix} . \begin{bmatrix} \sin\theta\cos\phi \\ \sin\theta\sin\phi \\ \cos\theta \end{bmatrix} \tag{3.4}$$

Fig. 3.8 c, which illustrates the case where the distribution axis coincides with the membrane normal in a spherical GUV or cell, shows the experimental configuration where light is focused on an equatorial point ($\eta = 0$). In this situation the relevant parameters of the molecular distribution are Ψ and ρ. This is typically the situation used in existing works where the cell and GUV round shapes allow visualizing the ρ parameter with a reasonable accuracy. However the molecular orientation does not necessarily correspond

to the membrane normal direction. In many cases the membrane is in complex shape and its global orientation is difficult to visualize (Fig. 3.9). Here we present a more general point of view since the image can be misleading when trying to determine a "membrane normal direction".

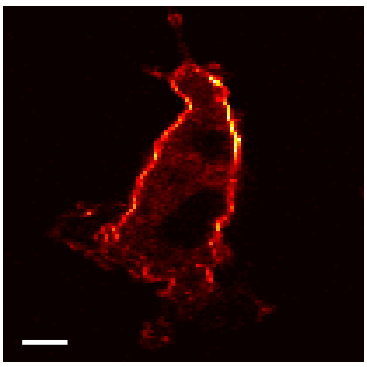

Figure 3.9: 2PEF image of a COS-7 cell doped with di-8-ANEPPQ. Scale bar $10\mu m$

3.2.2 Anisotropy analysis

As mentioned in chapter 1, anisotropy permits to retrieve an information on Ψ only if ρ is known. To adapt to this limitation, previous works have studied round shape membranes such as depicted in Fig. 3.10. To give an idea of a typical molecular disorder values Ψ observed in such cell membranes Fig. 3.10 depicts an example of the anisotropy analysis performed by Benninger *et all* [13] on round cells stained with three different fluorophores : BODIPY-GM1, BODIPY-PC and DiO (Fig. 3.10 a). Anisotropy images (Fig. 3.10 a) were analyzed by fitting the reduced linear dichroism LD^r defined by [13] :

$$LD^r(\Psi,\rho) = 3\frac{\langle I_{||}(\Psi,\rho)\rangle - \langle I_{\perp}(\Psi,\rho)\rangle}{\langle I_{||}(\Psi,\rho)\rangle + 2\langle I_{\perp}(\Psi,\rho)\rangle} \tag{3.5}$$

around the cell (here ρ is the variable). In this equation $I_{||}$ and $I_{\perp}$ are the 2PEF intensities measured in a parallel and perpendicular directions respectively, relative to the incident excitation polarization direction. This analysis requires a homogeneous Ψ values over the whole membrane contour as well as a known cell-contour shape (here a circle which provides a good knowledge of the ρ variable variations). The molecular cone aperture Ψ in the membrane where reported to be : BODIPY-GM1 $48 \pm 0.2°$, BODIPY-PC $49.5 \pm 0.2°$ and DiO $36.2 \pm 0.2°$. These values show that molecular orientations in membranes can span large cone aperture.

In order to better understand the feasibility of the fluorescence anisotropy analysis in round-shape membranes let us show an example how molecular distribution information

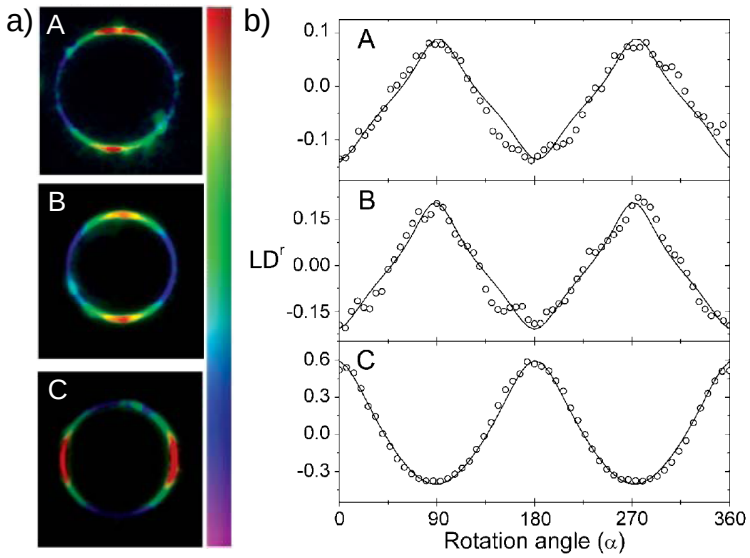

Figure 3.10: (a) 2PEF fluorescence anisotropy images of Daudi B-cells stained with : A-BODIPY-GM1, B-BODIPY-PC and C-DiO. (b) Measured LD^r (defined in text) as a function of the contour angle around the cell ρ (named angle α in the graphs). Theoretical fits for the data (solid lines) requires an homogeneous behavior of molecular order on the contour [13].

can be retrieved from lipid membrane using this technique. To do so, we use the polarization factor ratio $A = (I_Y - I_X)/(I_Y + I_X)$ measured for a circular incident excitation (as introduced in chapter 1), this quantity is similar to LD^r introduced in eq. 3.5. An image of the A factor is depicted in Fig. 3.11 a for a DOPC GUV doped with C-Laurdan molecules. Note that in all this work X is horizontal direction in the sample plane. Interpreting such image first requires the knowledge of the mean orientation of the molecules relative to the membrane normal direction. The A(ρ,Ψ) function (Fig. 3.11 c, calculated in chapter 1) can be used to determine Ψ assuming a known cone mean orientation ρ, as used in previous works [13, 80] where the membrane normal or tangential directions were assumed to coincide with the mean molecular orientation. The anisotropy image is however more complex in the case of lipid mixtures, as illustrated for C-Laurdan in a DOPC/Chol/SM GUV (Fig. 3.11 b). Figures 3.11 a,b can be analyzed assuming that the cone orientation and membrane normal direction coincide. As readily seen for C-Laurdan in a DOPC GUV (Fig. 3.11 a), anisotropy values at points A,C in Fig. 3.11 c do not surpass $A \pm 0.4$, for which $\Psi = 60° - 80°$. In a GUV formed by a (DOPC/Chol/SM) lipid mixture (Fig. 3.11 b), the Ψ parameter varies roughly from 30° to 80° (points D and E in Fig. 3.11 b are most probably in disordered regions). Measurement points around

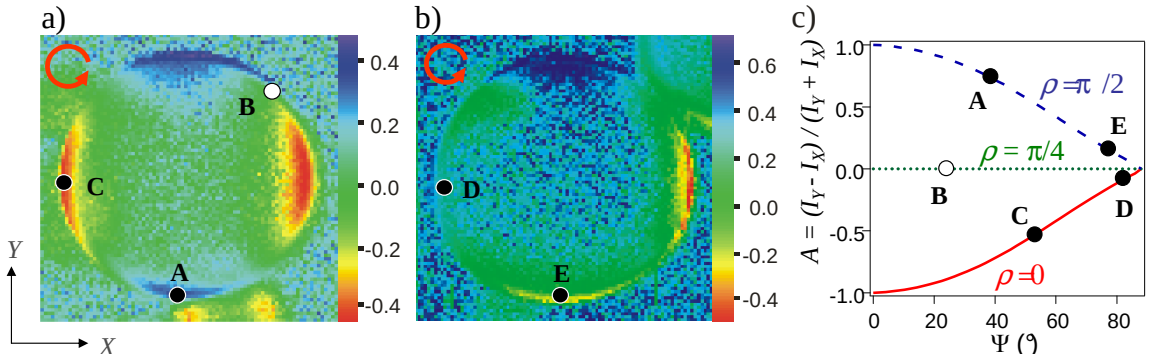

Figure 3.11: Images of the polarization factor ratio A, of C-Laurdan-labeled GUV formed by (a) DOPC and (b) DOPC/Chol/SM (1:1:1). (c) A factor calculated for a cone aperture model, at different cone mean orientations : $\rho = 90°$ (*dashed line*), $\rho = 45°$ (*dotted line*), $\rho = 0°$ (*solid line*). Measured points are indicated by letters A-E.

$\rho = \pi/4$ (point B) are not exploitable since A is insensitive to the molecular order in this case (Fig. 3.11 c). Therefore with this pure anisotropy measurement, it is not possible to distinguish the complete spatial localization of Lo and Ld phases.

3.2.3 Polarimetric 2PEF microscopy : influence of the distribution aperture, shape and average orientation.

The theoretical 2PEF polarization responses $I_X(\alpha)$ and $I_Y(\alpha)$ emitted by an assembly of fluorescent molecules are depicted in Fig. 3.12 for different distribution parameters Ψ and ρ, assuming $\eta = 0$ and a cone shape angular distribution. For relatively small aperture angles ($\Psi < \pi/6$), the molecules exhibit a quasi 1D order and thus very anisotropic I_X and I_Y polarization responses. For larger cone apertures, these two lobes are strongly deformed, due to the contribution of a broader range of dipole orientations. Fig. 3.12 shows that this polarimetric analysis is strongly sensitive to both width and mean orientation of the angular distribution of the molecules: whereas the mean orientation ρ is seen to predominantly affect the overall pointing direction of the polarization lobes responses, the cone aperture Ψ affects the relative deformation of these lobes. This approach shows that measurements with high angular accuracy can be obtained with no a priori knowledge of either ρ or Ψ values.

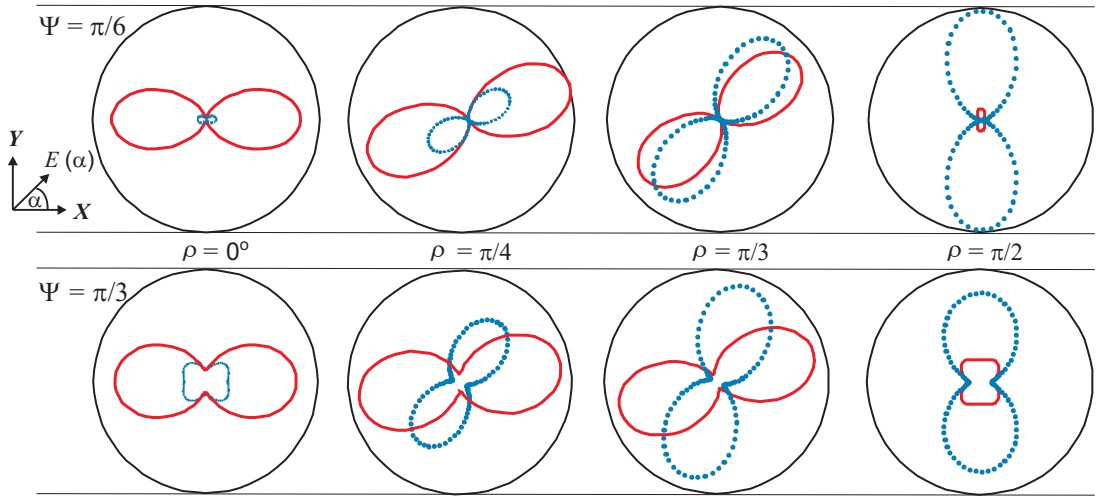

Figure 3.12: Influence of the ρ and Ψ parameters on 2PEF polarimetric responses calculated for I_X (*red solid line*) and I_Y (*blue dotted line*) analysis directions. The dichroic parameters $\delta = 0.26$rad and $\gamma = 0.005$ are used (as met in the experimental conditions).

The effect of the out-of plane orientation angle η of the cone aperture depicted in Fig. 3.13 shows that for η angles below 45°, the polarimetric responses are seen to be essentially independent on η (only minor deviations being seen in the curves amplitude). Above $\eta = 45°$, the polarimetric responses start deforming and tend towards a more "isotropic-like" response. At $\eta = 45°$, the response is totally isotropic ($I_X + I_Y$ is a circular response), as expected from a cone along Z projected in the (X, Y) plane. According to the experimental geometry the measured distributions are located on the equatorial perimeter of the membranes, therefore η is expected to lie close to 0° in this study.

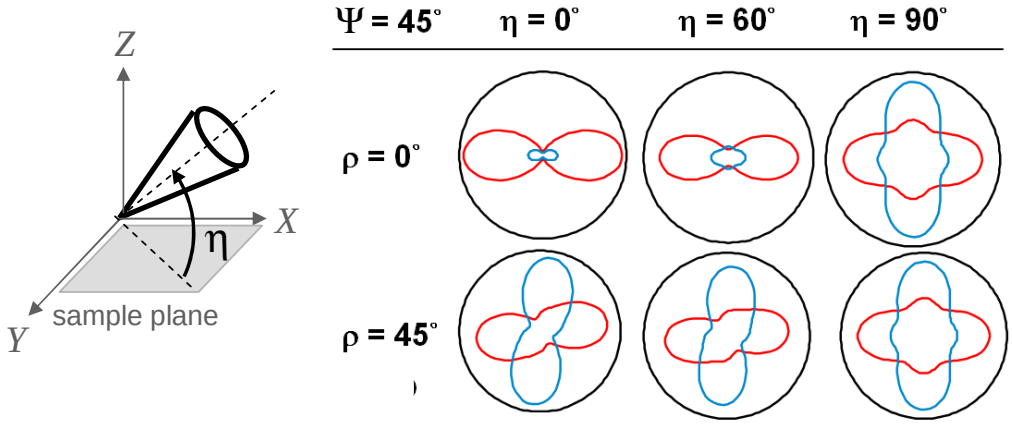

Figure 3.13: The influence of η parameter on the shape of polarimetric responses (the dichroic parameters introduced in Fig. 3.12 are accounted for in this analysis).

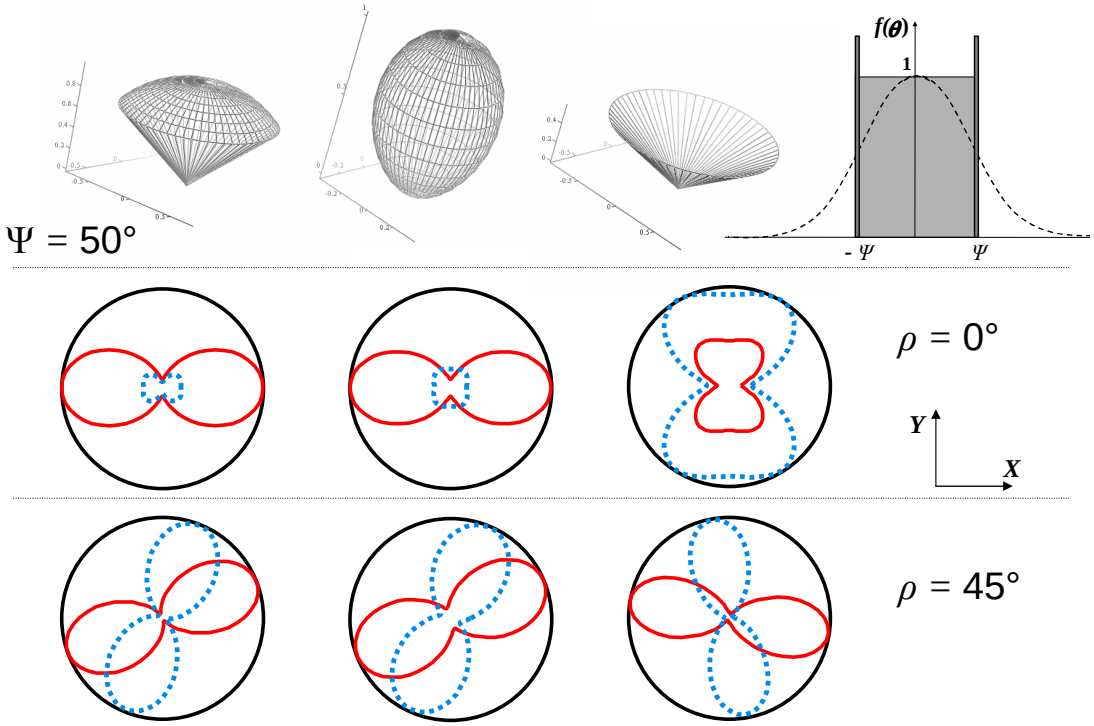

Figure 3.14: Two-photon polarimetric responses I_X (*solid line*) and I_Y (*dotted line*) as a function of the incident field rotation angle α for different angular distributions of the fluorescent molecules at fixed $\rho = 0, 45°$ and $\Psi = 50°$ parameters. From left to right: cone, Gaussian and cone-contour distributions, all of them having a FWHM equal to Ψ as represented on their θ-dependent section (far right graphic). The dichroic parameters $\delta = 0.26$rad and $\gamma = 0.005$ are used in this model.

Fig. 3.14 represents the influence of the angular distribution shapes discussed in 3.2.1 on the polarimetric responses $I_X(\alpha)$ and $I_Y(\alpha)$. I_X and I_Y polarization responses are plotted for three different $f(\theta, \phi)$ distributions described above : cone, Gaussian and cone-contour. The three functions have a FWHM (full width half maximum) equal to Ψ. Although of similar dependence with a two-lobes shape response, the cone and Gaussian models exhibit some differences in the opening of the lobes which can be explained by a smoother distribution shape for the Gaussian function case. The cone-contour model is very different and can be easily discriminated from filled-apertures models, which is not the case in traditional fluorescence anisotropy measurements [80]. In the data analysis we will discuss essentially the cone and Gaussian models, since the cone-contour model could not explain our observations.

3.3 Experimental results

In this section we will present the experimental results obtained form the investigation of the GUV lipide membranes doped with C-Laurdan, Laurdan, TMA-DPH and di-8-ANEPPQ fluorescent molecules, as well as cell membranes doped with di-8-ANEPPQ.

3.3.1 Investigation in two-phase lipid mixtures GUVs.

We studied at first the orientational behavior of Laurdan and C-Laurdan in GUVs exhibiting micrometric size domains. Without any specific spectral filtering, the GUV images look very homogeneous without clear indication of the presence of domains. This detection condition is kept for the polarimetric analysis. 2PEF polarimetric responses of C-Laurdan and Laurdan in DOPC/Chol/SM GUVs are depicted in Fig. 3.15 a,b for different points on the GUVs.

To determine the ρ, Ψ parameters, theoretical polarimetric responses for both intensities I_Y (α, ρ, Ψ) and I_X (α, ρ, Ψ) are calculated for (ρ,Ψ)-pairs with each parameter varying from 0° to 180° with a step of 1° (note that in this calculation the (δ, γ) dichroic parameters (see chapter 2) are entered in the field calculation and previously calibrated). The set of calculated polarimetric curves is then compared with experimental data, the sum of mean squares being used as an estimation of the fit quality:

$$\chi^2(\rho,\Psi) = \sum_{\alpha} \left(I_X^{exp}(\alpha) - I_X^{theo}(\alpha,\rho,\Psi)\right)^2 + \left(I_Y^{exp}(\alpha) - I_Y^{theo}(\alpha,\rho,\Psi)\right)^2 \qquad (3.6)$$

Here, both I_{exp} and I_{theo} are normalized by $max(I_X(\alpha) + I_Y(\alpha))$ to preserve the relative I_X versus I_Y amplitude information. The best fit solution (ρ, Ψ) in the least-squares method corresponds to the minimal value of $\chi^2(\rho,\Psi)$. The mean orientation angle of the distribution ρ is therefore not artificially introduced, but is deduced from the data fitting. In addition for a given position on the GUV, Ψ can be determined with a $\pm 0.5°$ precision, with a slight increase of this error margin to $\pm 2°$ at high cone apertures (in this situation the shape of the polarization responses is less sensitive to the ρ orientation, as can be expected from a large angular distribution of molecules).

Firstly, the data are seen to be consistent with models close to a cone or a Gaussian aperture. The cone-contour model can be discarded since it leads to very different polarimetric dependencies (Fig. 3.14). Next, the fits performed for a cone and a Gaussian model simultaneously over both Ψ and ρ parameters (both taken every 0.5°) results respectively in $\Psi = 36.5°$, $\rho = 69°$ (Fig. 3.16 a) and $\Psi = 38°$, $\rho = 69.5°$ (Fig. 3.16 b). A thorough analysis of this fitting accuracy shows that a Gaussian model seems slightly

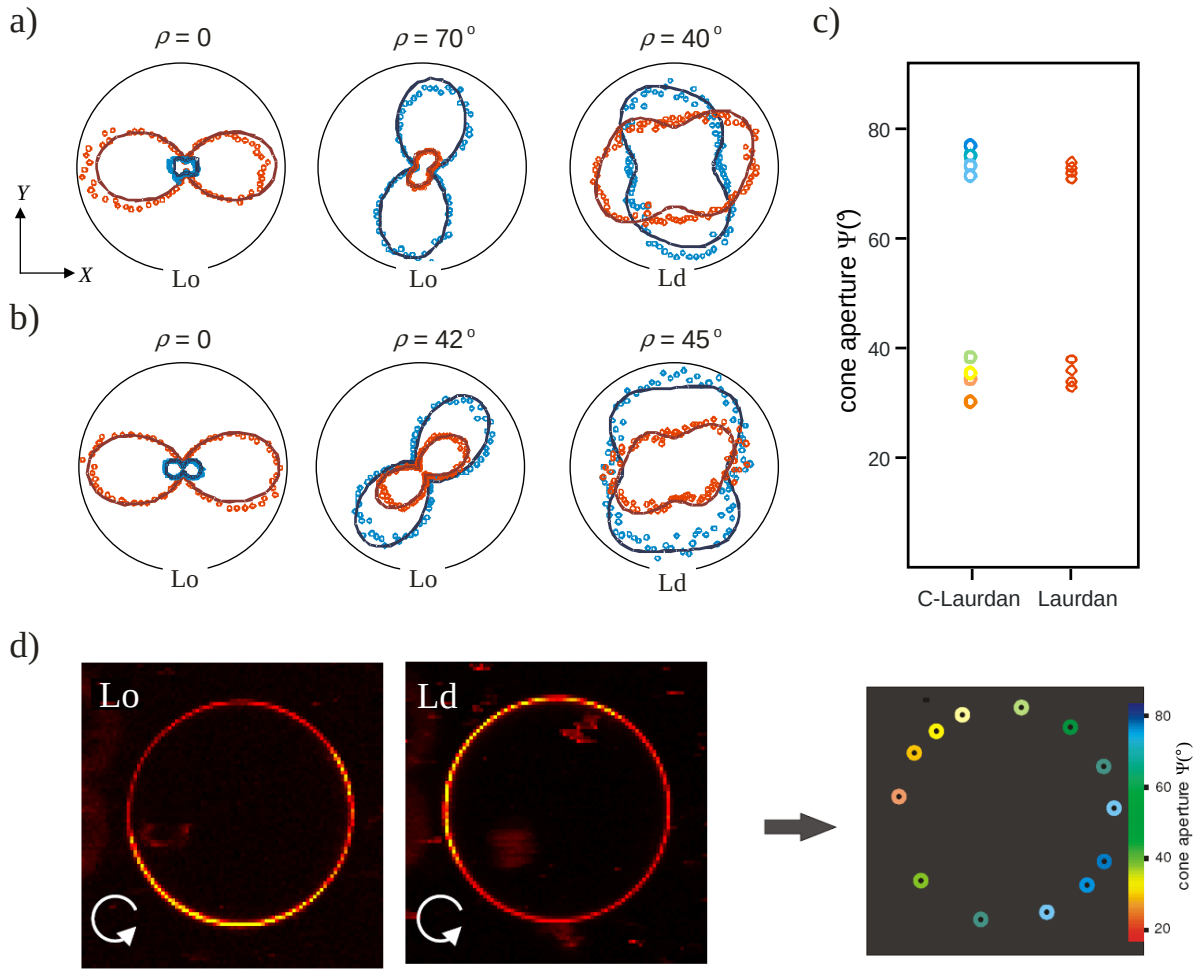

Figure 3.15: Experimental polarimetric responses I_X (*red dots*) and I_Y (*blue dots*) of (a) C-Laurdan (b) Laurdan measured at several locations on the GUVs contour. The Lo and Ld phases assignment is related to the Ψ cone aperture values obtained from the fit. (c) Distribution of the angular aperture Ψ obtained from polarimetric measurements performed for each fluorophore. (d) Color-coded spatial representation of the Lo and Ld phases on a C-Laurdan labeled GUV, compared to a similar image obtained with spectral filtering (left, detection 400 nm ± 20 nm and right, detection 560 nm ± 20 nm). 2PEF images are obtained at 780nm excitation with an incident circular polarization to avoid any photoselection effect in the image. The signals from the X and Y sensitive APDs are added to remove the analysis polarization effects. Diameter of the GUV ∼50 μm.

more adapted than a cone shape to the observed phenomenon. This is consistent with a statistically-driven orientational behavior, measured at equilibrium. Nevertheless, from the fitting of the polarimetric angular dependencies, both cone and Gaussian models lead

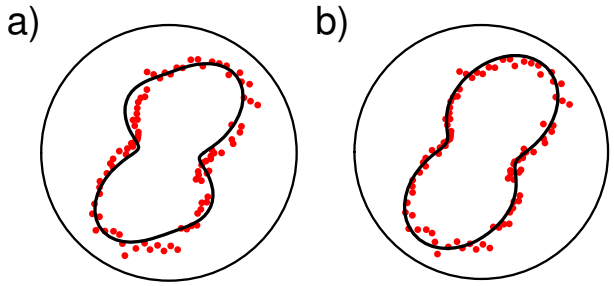

Figure 3.16: Experimental polarimetric responses I_X (*red dots*) from C-Laurdan located in a Lo phase region, fit by (a) a cone model and (b) a Gaussian model. The fits (*continuous lines*) are performed simultaneously over both Ψ and ρ parameters, both taken every 0.5°. Results of the fits are (a) $\Psi = 36.5°$ and $\rho = 69°$ and (b) $\Psi = 38°$ and $\rho = 69.5°$.

to similar ρ and Ψ values.

Secondly, the deduced mean orientation ρ of the molecular distribution is seen to also correspond to the measured normal direction of the membrane in the studied location.

At last in the microdomains-type GUV preparation, the measured distribution aperture angles Ψ can be clearly discriminated in two populations associated with respectively high and low aperture angles (Fig. 3.15c). By comparing the spatial location of the observed populations on the GUVs using a spectral filtering imaging (Fig. 3.15 d), we could deduce that these two populations can be assigned to the Lo and Ld lipid environments. The angles found in the Ld phase are also very close to the ones found in homogeneous GUVs made of pure DOPC, which is consistent with what is expected [Haluska 67]. Note also that these results do not depend on the size of the GUVs.

Fig. 3.15 d right is finally a "pure order information" figure that does not require any a priori knowledge on the sample apart from the out of plane η which is less determining. This kind of analysis seems to open to interesting studies towards more general molecule order imaging, as we will see later in cells for instance.

Cone aperture values obtained for both C-Laurdan and Laurdan show that their orientational behavior deviates substantially from a perfect orientational order. In the Ld phase, where the lipid acyl chains are highly disordered, the aperture angle is significantly increased. The reason for the relatively high disorder in both Lo and Ld phases might occur from the fact that these molecules locate in the hydrophobic part of the membrane due to Van der Walls interaction between their Lauric chains and the lipid chains [130, 108], as also observed in DPH-derivative fluorophores embedded in the membrane [80]. Although C-Laurdan seems to explore a larger range of cone apertures than other fluorophores

(Fig. 3.15), superimposing aperture angles and lipid phase images shows also a large spatial variation between ordered and disordered regions. In particular C-Laurdan is overall seen to be a more sensitive probe of local orientational order, as also observed in previous works [108].

A similar study was performed for the TMA-DPH and di-8-ANEPPQ fluorescent probes, which do not significantly modify their spectral emission behavior in Ld and Lo phases. The 2PEF polarimetric responses for these probes in DOPC/Chol/SM GUVs are depicted in Fig. 3.17 a,b.

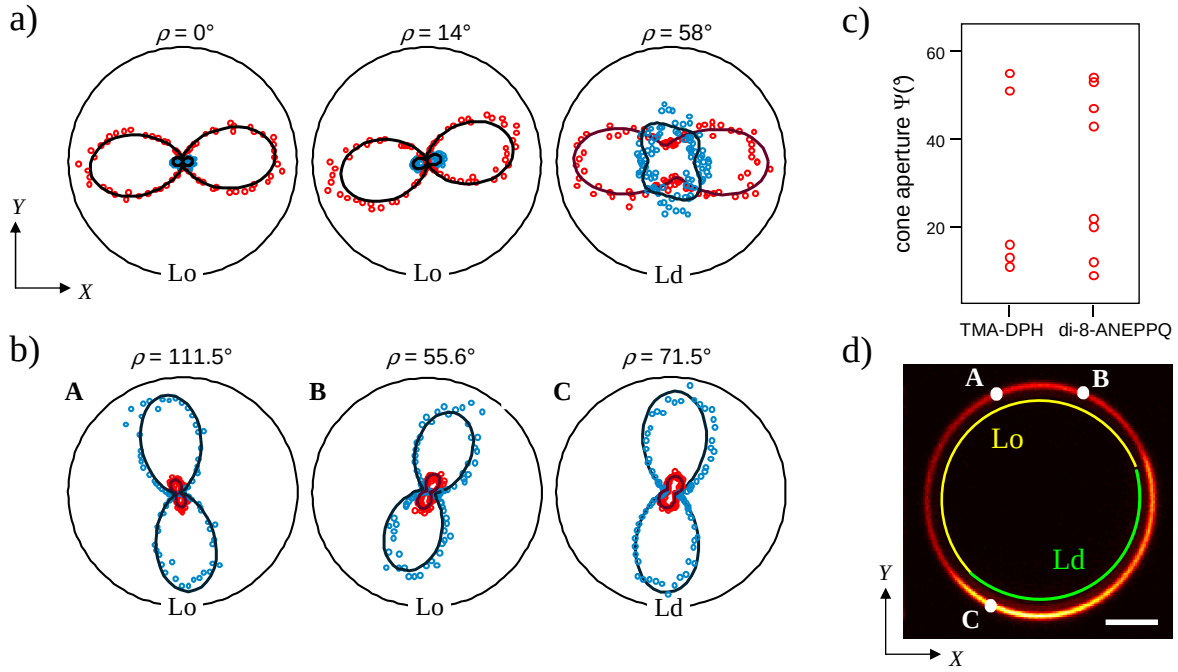

Figure 3.17: Experimental polarimetric responses I_X (*red dots*) and I_Y (*blue dots*) emitted by an assembly of (a) TMA-DPH and (b) di-8-ANEPPQ molecules, measured at several locations on GUVs contours. A large spectral band is detected around 500nm, with no specific spectral filtering. The indicated ρ values are obtained from the fit (*continuous lines*) from the cone model. The Lo and Ld phases assignment is related to the Ψ cone aperture values obtained from the fit. (c) Distribution of the angular aperture Ψ obtained from polarimetric measurements performed for each fluorophore. (d) 2PEF image of a di-8-ANEPPQ labeled GUV for a circular input polarization. GUV size : 17 μm. The color lines superimposed illustrate the spatial location of the Lo and Ld phases deduced from the following Ψ values : $\Psi < 37°$ (Lo) and $\Psi > 37°$ (Ld). Represented points : A : $\Psi = 27.8°$, B : $\Psi = 12.3°$, C : $\Psi = 46.5°$.

Again as in the Laurdan probes, the fits obtained from different points of the GUVs clearly show two distinct populations (Fig. 3.17 c). The spatial location of these populations shows the existence of micrometric size domains, as illustrated on a di-8-ANEPPQ labeled GUV for which many points have been analyzed along the whole contour (Fig. 3.17 d). Fig. 3.17 d also shows that the di-8-ANEPPQ molecule seems to preferentially locate in the disordered phase, the higher global intensity in this region being a signature of a higher molecular density. This figure shows finally that the lipid environment local rigidity can be directly probed by an orientational polarization imaging.

In the case of TMA-DPH and di-8-ANEPPQ, although the Lo or Ld environments cannot be identified from a control spectral measurement, the 2PEF polarimetric analysis permitted to directly create an image of the spatial distribution of molecular order (Fig. 3.17 d). The cone aperture values obtained are globally lower than for the Laurdan type molecules, which is consistent with their inclusion localization in the periphery part of the membrane. TMA-DPH, located near the more ordered headgroup region, has been reported to exhibit quasi 1D order in gel phases with cone aperture angles below 20° [68], which is consistent with the values found here in Lo regions. A similar behavior is observed for di-8-ANEPPQ although with a slightly higher flexibility (Fig. 3.17 c). The values obtained for di-8-ANEPPQ in Ld phases are close to the ones found for the BODIPY-PC fluorescent lipid probe [13].

The obtained Ψ values for all the studied dyes in heterogeneous GUVs are summarized in Table 3.1, together with the corresponding order parameters $< P_{\mathbf{J}=2,4,6} >$ defined in chapter 1. The Lo phase is overall characterized by a lower distribution aperture than in the Ld phase, and by higher $< P_{\mathbf{J}=4,6} >$ order parameters (the high $\mathbf{J}$ orders are indeed signatures of a narrow angular distribution). The obtained order parameters are close to the ones obtained in other works in homogeneous phases [34, 68, 13]. These measurements show finally that molecular order is strongly dependent on the fluorescent probe structure, primarily because it is driven by lipid-fluorophore interactions which are influenced by the molecular head position. The fluorescence is therefore not a direct signature of the lipids orientational behaviors themselves but rather reporters of lipids order modifications. Nevertheless, once such a probe has been characterized in a model environment such as in GUVs, it can be easily used for reporting local cell membrane lipid order information upon different conditions (such as temperature, drug treatment, etc.).

Table 3.1: Distribution aperture angle Ψ obtained from the polarimetric analysis for the studied molecules in both Lo and Ld lipid phases. The values are obtained from the measurement of 10 points per GUV, measured on 5 different GUVs in each case. The corresponding order parameters $< P_{\mathbf{J}} >$ ($\mathbf{J} = 2, 4, 6$) (normalized to $< P_{\mathbf{J}=\mathbf{0}} >$) are given for the Gaussian distribution shape.

Phase	C-Laurdan	Laurdan	TMA-DPH	di-8-ANEPPQ
Lo	$(33 \pm 6)°$	$(36 \pm 5)°$	$(16 \pm 4)°$	$(17 \pm 6)°$
	$< P_2 >= 1.715$	$< P_2 >= 1.674$	$< P_2 >= 1.920$	$< P_2 >= 1.911$
	$< P_4 >= 0.415$	$< P_4 >= 0.373$	$< P_4 >= 0.769$	$< P_4 >= 0.745$
	$< P_6 >= 0.267$	$< P_6 >= 0.242$	$< P_6 >= 0.602$	$< P_6 >= 0.570$
Ld	$(73 \pm 6)°$	$(71 \pm 4)°$	$(52 \pm 4)°$	$(46 \pm 5)°$
	$< P_2 >= 1.320$	$< P_2 >= 1.330$	$< P_2 >= 1.479$	$< P_2 >= 1.546$
	$< P_4 >= 0.169$	$< P_4 >= 0.174$	$< P_4 >= 0.241$	$< P_4 >= 0.277$
	$< P_6 >= 0.116$	$< P_6 >= 0.119$	$< P_6 >= 0.162$	$< P_6 >= 0.185$

3.3.2 Investigation in cell membranes.

The orientational behavior of di-8-ANEPPQ molecules was finally investigated in COS-7 cell membranes using the 2PEF polarimetry technique. In general, adherent cells with non-spherical shape were voluntarily chosen to probe the local molecular order in regions were the local orientation of the cell membrane is not easily determined. Nevertheless as can be seen in Fig. 3.18 the irregular shape of the cells can introduce non zero values of η (Fig. 3.8 b). The effect of the departure from the equatorial plane is shown (theoretically)

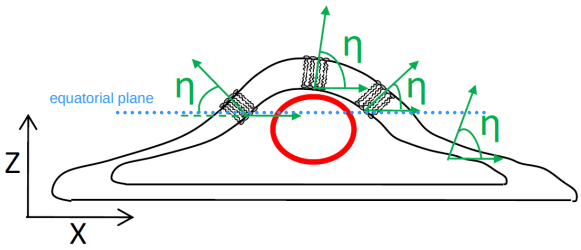

Figure 3.18: Schematic representation of the cell profile with out of plane angle [131].

in Fig. 3.13 and (experimentally) in Fig. 3.19 : the polarimetric data are seen to progressively resemble isotropic distributions when η increases, as expected from a tilted cone. Therefore to minimize the effect of the out-of plane angle of the molecular distribution the investigation plane was chosen at best the closest the equatorial plane represented

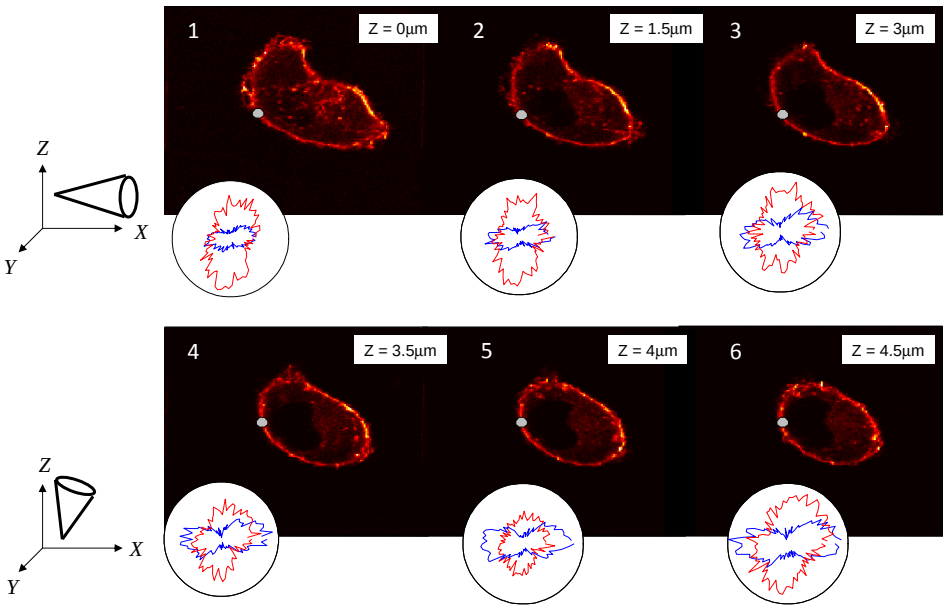

Figure 3.19: The influence of η parameter on the shape of polarimetric responses.

schematically in Fig. 3.18.

Fig. 3.20 illustrates examples together with the data for a few points investigated on the cells contours. This analysis was performed in the galvanometric scanning mode described in chapter 2, using a dwell time per pixel of 100μs and a stack of 180 images of different incident polar angles between 0° and 360°. In all the investigated cells, the ρ value obtained from the data fitting is roughly consistent with the membrane orientation visible on the cell image. 2PEF polarimetry measurements on COS-7 cells show that the molecules mean orientation roughly lies along the membrane normal direction. However in many points the membrane is of complex shape and its global orientation is difficult to visualize. The simultaneous fitting on both ρ and Ψ parameters makes it possible to avoid speculating on the local membrane contour as previously done [13, 29].

The corresponding Ψ value obtained from the data fitting is found to be larger than for DOPC GUV membranes. Opposite disorder properties have been previously found when comparing DOPC and cell membranes [109] in a solution of reconstructed vesicles. This high aperture angle in COS-7 cell membranes has nevertheless been found reproducibly on many cells over their whole membrane contours. Note however that in these measurements the noise level was somewhat higher than in GUV measurements leading to higher error margins for Ψ of about 5-10°. This noise is mostly due to the fact that the conditions of measurements are different : here the integration time per polarization angle is only 100μs (with respect to 50ms in GUVs) due to the fast scanning mode of measurement. In

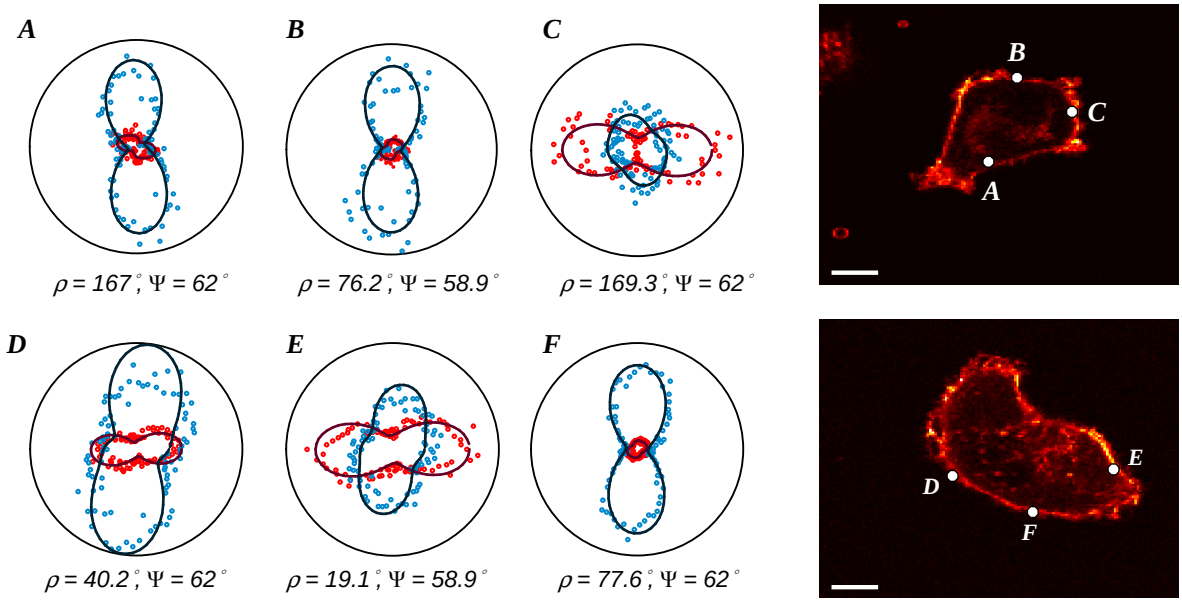

Figure 3.20: Experimental polarimetric responses I_X (*red dots*) and I_Y (*blue dots*) from di-8-ANEPPQ molecules labeling COS-7 cells membranes, measured at several locations (indicated by letters A-F) on two different cells contours. The indicated ρ and Ψ values are obtained from the fit (*continuous lines*) from the cone model described in the text. Scale bars : 10 μm. The images are the sum of all polarimetric images obtained in the fast galvanometric scan mode. The polarimetric data are obtained for a 3×3 pixel integration around the point of interest (corresponding to about 300nm integration area size).

addition the detectors (PMTs, see chapter 2) are less sensitive than the APDs previously used. Nevertheless this situation leads to a faster, parallel analysis over the whole image.

In order to understand the large cone aperture observed in the cell membranes, one could bring hypothesis of physical (morphology) or physical-chemistry (lipids compositions) nature. However before giving any possible explanation, one has to discard possible artefact effects that might lead to an overestimation of the deduced aperture angles. These effects mentioned in chapter 2 are discussed in what follows.

Influence the energy transfer on the polarimetric responses. The polarimetric response can be affected by homo-FRET especially at large cone apertures Ψ as shown in chapter 2. In our measurements, the mean distance between fluorescent molecules in GUVs is estimated to be about 10 nm accounting for their dilution (lipid:fluorophore = 1000:1) and a typical lipid cross section of around 50Å. This fluorophore interdistance is larger than the typical distances (a few nanometers) over which a 50 % FRET efficiency

occurs [89]. Nevertheless in cell membranes this distance cannot be calculated easily since the concentration of the dyes inserted into the plasma membrane is unknown. A Fluorescence Correlation Spectroscopy (FCS) [132] experiment performed by C. Favard (Institut Fresnel) allowed determining the averaged number of fluorophores within the beam diffraction-limited spot (of ∼300 nm diameter) which in GUVs and in COS-7 cells is found to be around 80 - 100 respectively. Therefore homo-FRET should not affected the polarimetric responses significantly in the present analysis.

In order to investigate this issue deeper, the effect of homo-FRET has been included in our analysis. Introducing homo-FRET in the analysis of the polarimetric experimental data in GUVs and cells tends to slightly improve the quality of the fit of both I_X and I_Y polarization dependence, however the final values obtained for both Ψ and ρ parameters do not change significantly. This shows in particular that the homo-FRET efficiency in the system is low (< 10 %).

Influence the emission/absorption dipoles directions on the polarimetric responses. The dependence of the 2PEF signals on the absorption-emission dipoles relative angle ξ study in chapter 2 shows that the polarimetric responses appears to be only slightly dependent on ξ for $\xi < 20°$. By inserting ξ as an additional fitting parameter in the analysis in all the polarimetric responses mentioned above, we have found that (i) the ξ angles for all the studied molecules cannot be higher than 20° (above this angle, the fitting quality is strongly affected), and (ii) inserting ξ in the model does not change the resulting angular apertures (Ψ, ρ) of more than a few %. The found ξ angles are furthermore consistent with the previously published values : $\xi = 19°$ in Prodan (6-propionyl-2-dimethylaminonaphthalene), a molecule similar to the Laurdan and C-Laurdan structures [133], $\xi = 7 - 16°$ in TMA-DPH [134].

Integration area over isotropic contributions. The presence of the rather small isotropic contribution of the intra-cellular partitioning of the fluorescent probe is seen to not affect the measurement, as ascertained by the evolution of the polarimetric data when decreasing the size of the integration area (below a few pixels, close to the diffraction limit, the polarimetric data remain identical).

A possible hypothesis of relatively high degree of disorder is the membrane local morphology. This disorder could be both dynamic and static. The first would occur from local membrane shape time fluctuations, the second from strong local changes in the membrane curvature at sub-wavelength scales. Indeed a preliminary study (performed

by Tsai Jung Han at Institut Fresnel) shows that when decreasing the osmotic pressure of the surrounding medium which makes the cells more spherical in particular because of cytoskeleton disruption, the aperture angle tends to decrease closer to the DOPC GUV values. This measurement seems finally to highlight the properties of the membrane sub-resolution scale structure: below the 300 nm optical limit, any disorder of the membrane at nanometer scales (ruffling, vesiculation...) will lead to an increase of the measured cone aperture of the probe molecules. In a more general context 2PEF polarimetry can be applied to the imaging of heterogeneous membranes organization occurring in endocytosis, exocytosis [135] and cell surface ruffling in which the treatment of the cell (cytoskeleton) can strongly modify the macroscopic membrane morphology [29] (Fig. 3.21).

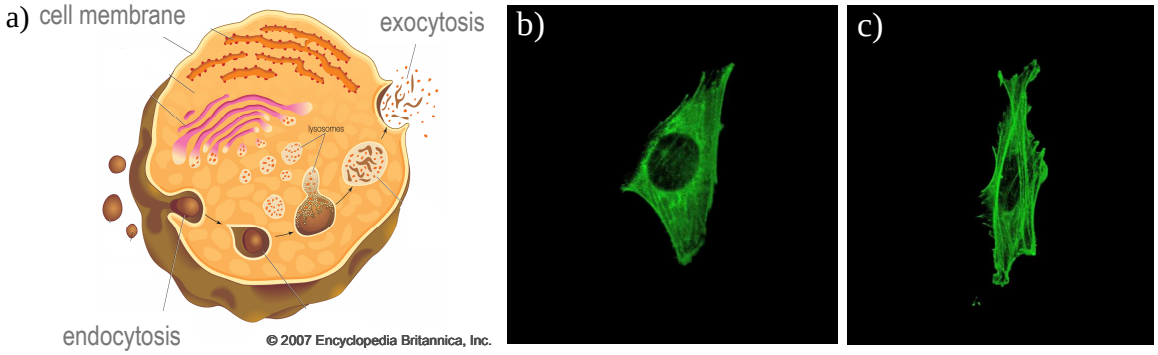

Figure 3.21: (a) The cell membrane itself undergoes concerted movements during which part of the fluid medium outside of the cell is internalized (endocytosis) or part of the cell's internal medium is externalized (exocytosis). These movements involve a fusion between membrane surfaces, followed by the re-formation of intact membranes. Membrane ruffling is the formation of a motile cell surface that contains a meshwork of newly polymerized actin filaments. (b) Cell transfected with GFP-actin: without ruffling, (c) cell exhibits extensive membrane ruffling [136]

3.4 Conclusion

The sensitivity of polarimetric 2PEF allows finally identifying quantitative features of the molecular angular distribution in local areas of a cell or GUV membrane without any *a priori* knowledge of its mean orientation. The spatial identification of molecular order behaviors in heterogeneous lipid and cell membranes can be used as a new type of probing technique of the lipid environment. This possibility opens the scope of structural studies to complex geometries of cells and biomolecular assemblies of a priori unknown nature.

This work has been recently applied to the analysis of the effect of drugs on the cell membrane local order : these studies show that both morphology and lipid composition effects are affecting molecular order.

Chapter 4

Molecular order in molecular inclusion compounds: "crystal-type" samples

In this Chapter we will apply polarimetric two-photon fluorescence microscopy to the investigation of the local static molecular orientational behavior in zeolite L inclusion compounds. First, we will report the origin of the host guest material compounds studies, in particular, we will describe the most common inclusion compound: zeolite L. Afterwards, we will demonstrate that the polarimetric microscopy imaging scheme permits a spatial investigation of possible molecular order heterogeneities in zeolite L channels doped with fluorophores, with a sub-micrometric resolution. We will show that the study performed on different fluorescent molecules inserted in zeolite L channels evidences a degree of disorder for either small or molecular flexible structures. Finally, we will introduce in the data analysis the effects of the birefringence and discuss the presence of fluorescence resonance energy transfer (homo-FRET) in zeolite L channels.

4.1 Host-guest material compounds: zeolite L

A zeolite is a crystalline aluminosilicate with a three dimensional framework structure that consists of uniformly sized pores of molecular nanometric dimensions. Fig. 4.1 a,b shows an example of micrometric size zeolite L crystal that consists of 1D nanochannels.

The structural, morphological and chemical variety of zeolites has lead to applications in different fields such as catalysis [138] and ion exchange in membranes [139]. In many cases zeolites serve as a host for supramolecular organization of molecules, ions, complexes and clusters. The obtained 1D molecular organization of the inserted dyes leads indeed to a variety of intriguing properties, such as light harvesting [140], high nonlinear optical

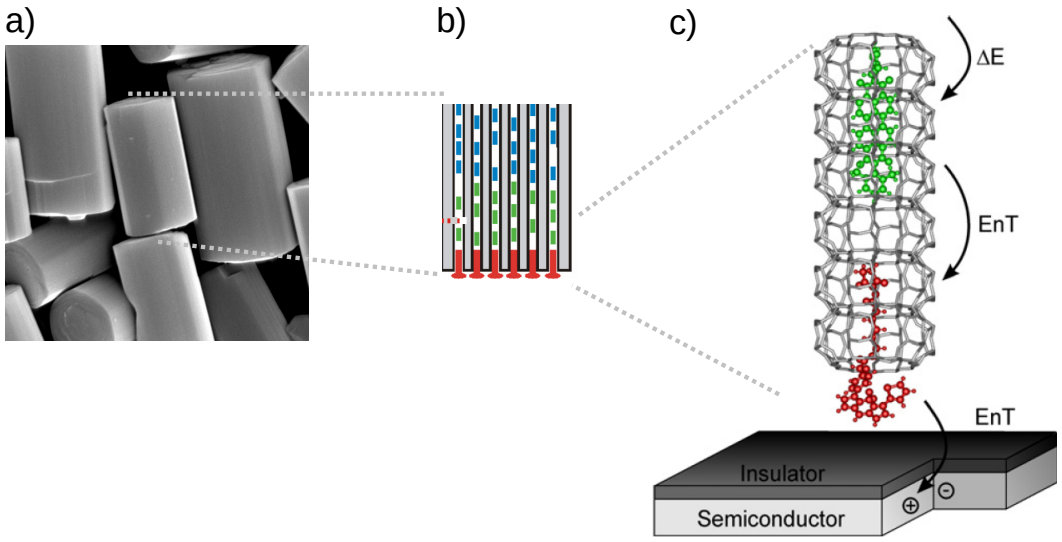

Figure 4.1: (a) Scanning electron microscopy image of zeolite L crystals [137]. b) Schematic representation of the 1D zeolite channels loaded with fluorophores: donor fluorescent molecules (green), stopcock molecules (red). (c) 1D energy transfer (EnT) from a photonic antenna to a semiconductor [137]. Typical size of a zeolite crystal: 300nm to 2 μm.

responses [141] or radiationless transport of electronic excitation energy to an external molecule attached to the entrance of the channels [142]. The functionalization of zeolite L crystals by inserting neutral or cationic dyes into the channels has been then the subject of a large amount of work aiming at highly ordered fluorescence active structures with micrometric size. For instance it has been demonstrated that by organizing cationic dyes in one dimensional channels of zeolite L crystals an artificial antenna for light harvesting and fast anisotropic energy transport can be realized [143, 144]. This idea is schematically represented in the Fig. 4.1 c. Fluorescent dyes inserted into the channels allow light harvesting and radiationless energy transport to an external acceptor or donor stopcock fluorophore which can than trap electronic excitation energy from donor molecules inside the crystals. The coupling a stopcock unit to an external device such as semiconductor results in energy transfer from the photonic antenna though an insulating layer and creating an electron-hole pair in the semiconductor. Favorable conditions for such a solar cell or photovoltaic device are a high concentration of monomeric dye molecules with high luminescence quantum yield and an ideal geometrical arrangement of the chromophores that favors energy transfer. Therefore quantifying the orientational and spatial organization of dyes in zeolite crystals is a key issue. Calculating orientational behaviors of dyes

in zeolite nanochannels environment using quantum chemistry could be an ideal way to predict which molecular structures are good candidates for this purpose. This is however a difficult task due to the highly constraint and charged environment probed by the molecules inside the channels. So far, very few theoretical studies therefore exist [145]. On the experimental side, imaging the orientation and organization of guest molecules in zeolites quantitatively has been performed so far using fluorescence anisotropy. These studies have shown that the molecules incorporated into the channels can adopt variety of positions from being parallel to the channel axis to the perpendicular orientations [140]. Modeling the molecular distribution in the channels has been essentially approached by assuming fixed orientations of molecules inside the channels (i.e. a "cone contour" model) [146, 141, 147]. In this situation, fluorescence anisotropy imaging can provide information on the molecular tilt angle, providing that the zeolite crystal is known. However recent study has shown that angular mobility is permitted even in very narrow channels [145] due to residual degrees of freedom in the steric position of the molecules. It is possible to extend the previous models to account for this molecular disorder, by introducing a more complete angular distribution accounting for three parameters: the mean orientation of the distribution (i.e. the zeolite crystal orientation), its aperture (i.e. the molecules tilt angle in the channels), and its width. This last parameter, which quantifies the degree of angular disorder in zeolite L channels, has never been measured and is nevertheless significant since a large amount of guest molecules that have been included into zeolite L are of a size that would permit various possible orientations in the channels. Deducing the three parameters of this more complete distribution is however impossible using fluorescence anisotropy imaging, since this technique allows only a single parameter measurement as shown in the previous chapter. For this reason a more refined analysis is required. We propose here to use a polarimetric approach where multiple polarization states are analyzed to study the zeolite L crystals similarly to the membrane study of chapter 3.

First we will introduce how to provide an indication of the disorder inside the crystal channels based on the "crystalline medium diagnostic" introduced in chapter 2. Next, we will explore to which extend polarimetry is able to quantify disorder in "almost crystalline samples" by also investigating possible birefringence and homo-FRET effects in the zeolite crystals. Finally we will investigate the spatial repartition of molecular order within the crystals for fluorescent molecules of different sizes and structures.

4.2 Zeolite L characteristics

Organic dyes have the tendency to form aggregates, causing fast thermal relaxation of electronic excitation energy which can be detrimental for photonic devices. Therefore the role of the host (nanochannels) is to prevent this aggregation and to superimpose a specific organization favorable for energy transfer. Zeolite L channels meet such a requirement: the diameter of the channels allows the formation of highly anisotropic dye assemblies where the molecules cannot glide past each other. Large amplitude motions of the dyes can be reduced because of the restricted lateral available space. An example of the zeolite L studied in this work is shown in Fig. 4.2.

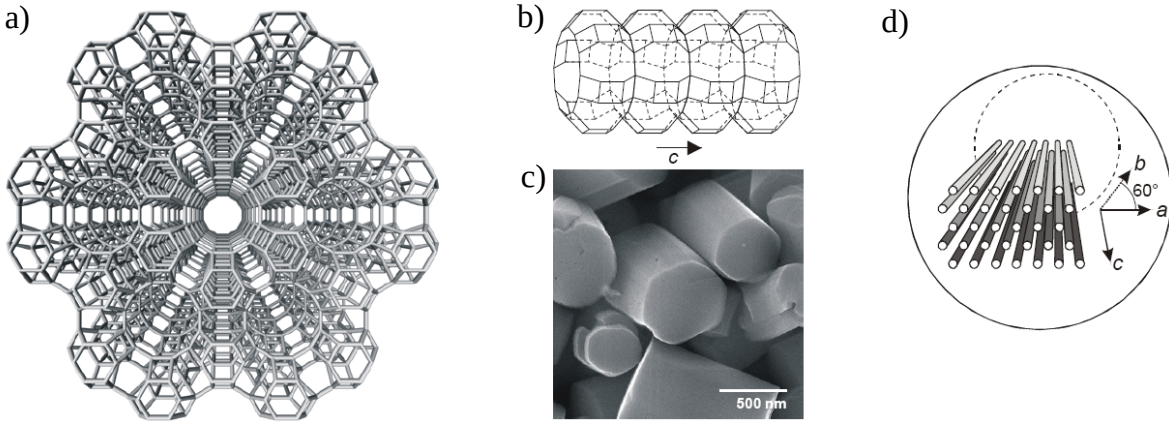

Figure 4.2: (a) Framework of zeolite L viewed along the c-axis. (b) Side view of a main channel. (c) Scanning electron microscopy image of zeolite L crystals. The channel entrances are located at the base surfaces of the cylindrical crystals. The channels run along the long axis (c-axis). (d) Schematic view of some channels assuming cylindrical morphology [137].

Zeolite L is a microporous aluminosilicate featuring hexagonally arranged 1D nanochannels and cylindrical symmetry [148, 149]. The stoichiometry of the zeolite is $M_9[Al_9Si_{27}O_{27}]\cdot nH_2O$, where the number of water molecules n per unit cell equals 21 in fully hydrated materials. Due to the aluminium atoms the crystal framework is charged negatively. This charge is compensated by M^+ cations. SiO_4 and AlO_4 give a rise to 1D channel system running along the c-axis (Fig. 4.2 b) [148, 150]. The lattice constants are: a=b=1,84 Å and c=0,75 Å. The primitive vector c correspond to channel axis while vectors a and b are perpendicular to it and make an angle of 60° (Fig. 4.2 d). The free diameter of the channels varies from 0.71 nm (narrowest part) to 1.26 nm (widest part).

The shape and the size of the crystals can be tuned during synthesis resulting in rod-like or disc-like crystals of a length from 30nm to 7μm of a diameter of around 500nm [151]. In this work we use rod-likes zeolite L crystals with a length varying between 3-5μm. These crystals were synthesized by L.-Q. Dieu at Institute of Inorganic Chemistry, University of Zürich (Switzerland).

4.3 Fluorescent doping dyes

We can distinguish between three types of molecules that can be inserted into the zeolite L channels. (i) Molecules which are so large that they have no other choice but to align along the c-axis (type 1 in Fig. 4.3) [146]. (ii) Molecules the size of which makes it hard to guess their position and orientation in the channel (type 2 in Fig. 4.3). (iii) Molecules which are small enough to fit into a unit cell but with a larger degree of freedom of orientation (type 3 and 4). Fig. 4.3 represents possible arrangements of fluorescent molecules inserted into the channels.

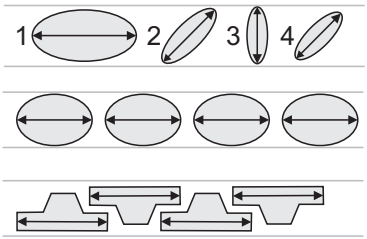

Figure 4.3: Four representative orientations of molecules and their transition dipole moments (double-headed arrow), top: 1: "large molecule" 2: "medium size molecule" 3 and 4: "small molecule", middle: orientation of large molecules parallel to the channel axis and which because of their size and shape have no electronic interaction, bottom: orientation of large molecules which align parallel to the channel axis and which have some electronic interaction because of their shape [137].

For our investigation we have chosen four fluorescent molecules depicted in the Fig. 4.4. First, DXP (N,N'-bis(2,6-dimethylphenyl)perylene-3,4,9,10-tetracarboxylic diimide) is a dye of the type (i) which orientation is *a priori* known due to its large size. Py(pyronine), Ox (oxonine) and DSM (4-(4-(dimethylamino)styryl)-N-methylpyridinium) belong to the type (ii). DXP and Ox have been already characterized using fluorescence anisotropy and are therefore used for comparison with previously obtained orientations inside the zeolite L channels [146]. The Py and DSM molecules are respectively structurally very

similar and very different compared to Ox, which allows us to probe the sensitivity of the polarimetric technique.

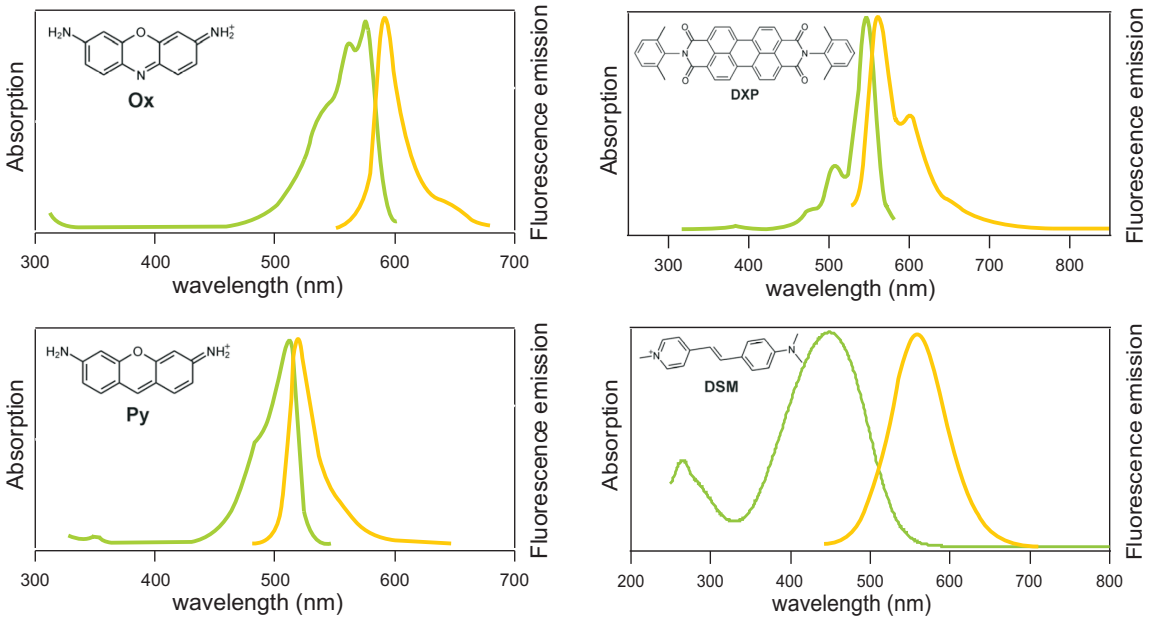

Figure 4.4: Structure of the dyes used in this study with their absorption/emission spectra when loaded into zeolite L.

The incident wavelength for 2PEF measurements is set at 850nm for DSM, 950nm Ox, and Py and 1000nm for DXP with a typical averaged power of a few mWs at the entrance of the microscope (which corresponds to less than half a mW at the focal spot of the objective).

Insertion of the molecules into zeolite channels

The two most common methods used for the insertion of dye molecules into zeolite channels are adsorption from the gas phase [152, 153] and ion exchange from solution [146]. The insertion from the gas phase was used for the neutral dye DXP whereas the cationic dye molecules DSM, Ox, Py were inserted by ion exchange. These samples fabrications were done in collaboration with D. Brühwiller and L.-Q. Dieu (Institute of Inorganic Chemistry, University of Zürich, Switzerland). Zeolite L crystals loaded with DSM, Ox and Py molecules were synthesized by dispersing 16 mg of zeolite L in 2 mL of bidistilled water. Different loading parameters p were obtained: p = 0.01 (DSM), p = 0.01 (Ox), and p = 0.05 (Py), where p is the number of occupied sites divided by the number of

total available sites in the zeolite L channels, determined quantitatively as in [144]. To obtain the desired loading p, the corresponding amount of dye is added to the zeolite L suspension while stirring. The suspension is then sonicated for 15 min and stirred for 1.5h at room temperature (DSM loaded crystals), 4 days at 80° C (Ox loaded crystals) and 12h at 100°C (Py loaded crystals). After centrifugation, the obtained dye-zeolite samples are washed with 2-methyl-1-propanol (DSM), ethanol and methanol (Ox), ethanol and 1-butanol (Py) to remove dye molecules adsorbed on the external surface of the zeolite crystals.

Fig. 4.5 depicts 2PEF microscopy images of two zeolites loaded with DSM and Ox molecules. DSM molecules are present in the channels of the crystal with the highest concentration in the middle. This effect is most likely a consequence of the washing procedure, as this tends to remove dyes adsorbed in the channels close to the entrances. The distribution of DSM molecules in the channels is also seen to be non-uniform, which is a signature of a possible heterogeneity of the molecular density within the crystals. We will investigate the orientation heterogeneous effect later in this chapter. The same behavior occurs for DXP (not shown). On the contrary the insertion of Ox and Py (which are structurally very similar) has not yet reached its equilibrium and the zeolite exhibits a typical sandwich structure with the molecules at the crystal ends and a dark zone in the middle. This effect has been already observed in variety of fluorescent dyes incorporated into zeolite crystals [140, 146, 137].

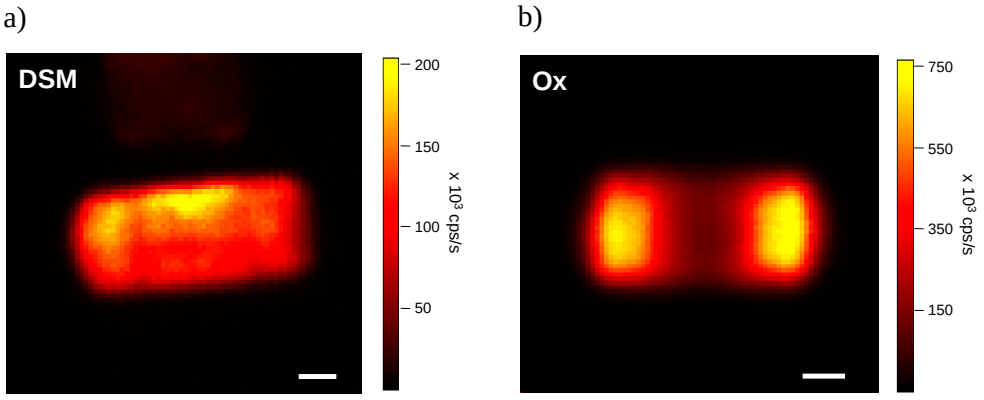

Figure 4.5: (a) 2PEF images $I_X + I_Y$ of zeolites L loaded with DSM and Ox molecules, excited with incident linear polarization $\mathbf{E}(\alpha = 0)$. Scale bars $1\mu m$. Note that in all this work X is the horizontal direction on the images in the sample plane.

4.4 Molecular distribution theoretical model

The polarized two-photon excited fluorescence (2PEF) process is modeled based on the approach developed in chapter 1. We will detail here more thoroughly the distribution function used in the model associated with zeolite doped compounds.

4.4.1 Historical model

So far, molecular orientation measurements in zeolite L inclusion compounds have been essentially approached by assuming that the molecules lie on a cone surface of which the aperture angle Θ can be measured by fluorescent anisotropy imaging, using the additional assumption that the cone axis is oriented along the channel axis *c*-axis (Fig. 4.6 a) [146, 154]. This model has proven to be useful for the rough description of a variety of dye-

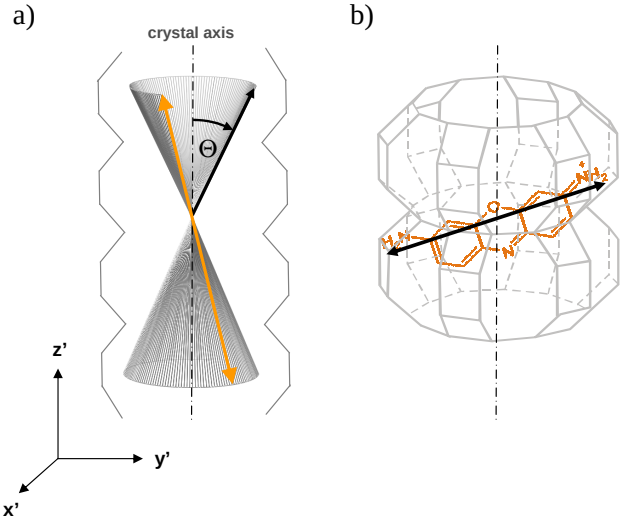

Figure 4.6: (a) Schematic view of the Ox molecule inserted into the channel. (b) The theoretical model based on the fluorescence anisotropy analysis. Similar fluorescent molecules orient along a cone aperture distribution within the zeolite channels. The angular distribution of the molecules lies on a cone surface.

zeolite composites [142, 146]. For instance the orientational distribution of Ox guest molecules has been found to be tilted of an angle $72° \pm 3°$ relative to the channel c-axis (Fig. 4.6 b). Nevertheless, this model does not include the possibility of a degree of disorder in the orientational behavior of the dyes, due to either time or spatial fluctuations. An alternative approach has been introduced considering that the molecules lie within

a filled cone distribution along the c-axis, to understand nonlinear optical properties of aligned zeolite crystals [141, 147]. This model however assumes a complete angular disorder within the cone angular aperture, which is unlikely to occur for a large variety of inserted molecules [137]. Moreover, both approaches require that the distribution exhibits a cylindrical symmetry along the crystal c-axis, which is not the case if possible local defects induce a mis-orientation of the cone axis. At last, the models described above show limitations such as the strong hypothesis of a homogeneous angular distribution of the molecules inserted in zeolite crystals channels. For these reasons these models, initially introduced for fluorescence anisotropy analysis, are refined in this work in order to account for a potential degree of disorder, either dynamic (within sub-millisecond time scale fluctuations) or spatial (within the nanometer scale).

4.4.2 Accounting for molecular disorder

Averaging over the fluctuations (in time and space) is expected to lead to an angular distribution represented by an enlarged cone surface, the width of which, is a bell-shaped function. The molecular angular distribution of the fluorescent dyes is defined by a normalized molecular orientational probability distribution function $f(\theta, \phi)$, with (θ, ϕ) the spherical angles denoting the molecular frame orientation (Fig. 4.7 a). In the laboratory frame the final distribution function depends on three parameters (Θ, Ψ, ρ) (Fig. 4.7 b), where Θ is the cone aperture, Ψ is the full width at half maximum of the cone width distribution (molecular disorder), and ρ the global orientation of the cone axis in the macroscopic frame (relative to the macroscopic X axis). This model is called "cone width" model in what follows. Although ρ is traditionally associated to the orientation of the zeolite c-axis in the macroscopic frame, this angle will be considered here as a free parameter in order to investigate potential defects in the crystals. The molecular orientational distribution function in the local frame of the symmetry axis is defined :

$$f(\theta, \phi, \Theta, \Psi) = exp\left[-\left(\frac{\theta - \Theta}{\frac{\Psi}{2\sqrt{ln(2)}}}\right)^2\right] \tag{4.1}$$

The angle differences between the excitation and emission dipoles are considered to lie below 20° for the studied molecules, which is a reasonable assumption for such systems since small differences between the dipoles angles have been measured in similar structures [155, 134]. In this situation, the effect of the relative absorption-emission dipole angles can be neglected in the polarimetric model (see chapter 2). The orientation of the excitation/emission dipole is therefore given by the respective polar and azimuthal angles

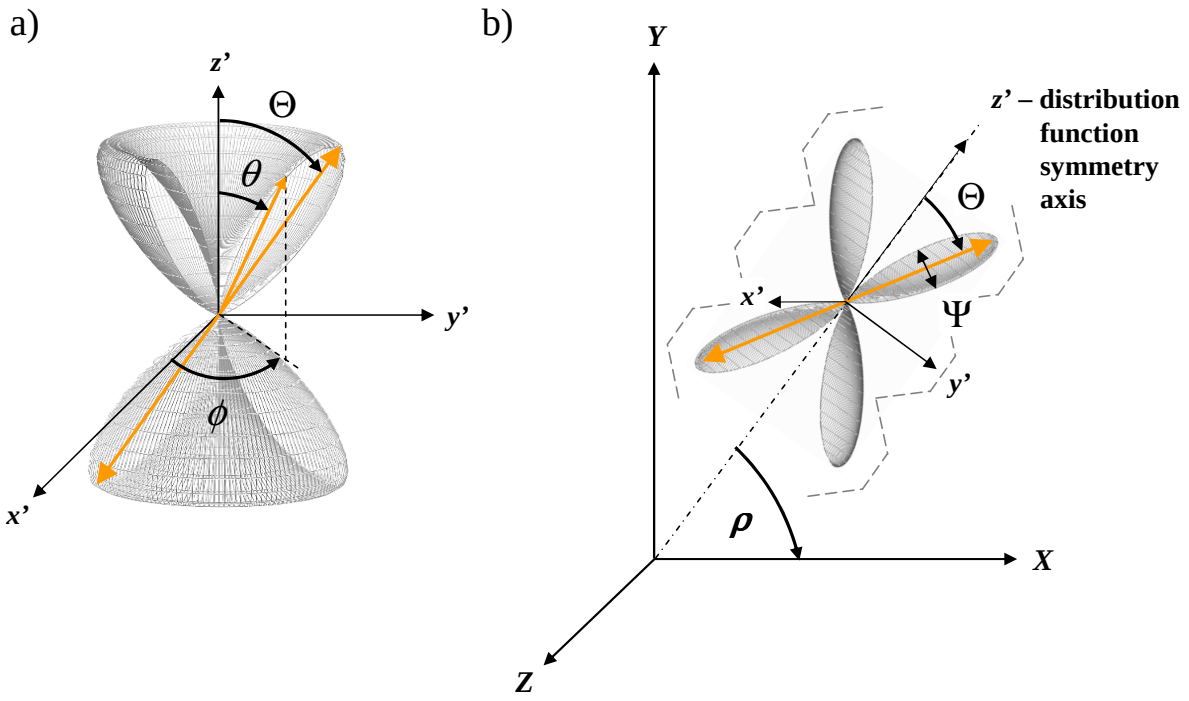

Figure 4.7: (a) Definition of the coordinates used in the analysis in the microscopic frame, the z' axis is related to the crystal c axis. (θ, ϕ) defines the orientation of the molecular dipole in the cone aperture frame. (b) In the laboratory frame, the Z axis is the optical axis, X and Y denote the sample plane in which the excitation polarization is defined. The angles Θ and Ψ specify respectively the aperture and the width of the molecular "cone-width" distribution. The parameter ρ defines its symmetry axis orientation in the macroscopic frame relative to X.

θ and ϕ in the crystal frame (x', y', z'), as described in Fig. 4.7 b. The time averaged fluorescence intensity of an ensemble of molecules within an orientational distribution is expressed in the chapter 1.

In principle the determination of the three parameters ρ, Θ and Ψ values would only require three input polarization angles measurement (given that these measurements are independent). However ambiguous determinations can occur using such approach (in particular for $\rho = 45°$ for which a ratiometric measurement cannot differentiate different cone apertures) and the accuracy of the measurement of these parameters can largely increase using the whole set of angle data as done in polarimetry. Along the same line as in the previous measurements performed in these systems, we modelled the expected

anisotropy A assuming that one of these parameters is known (for instance ρ). The $A(\Theta)$ dependence is shown in Fig. 4.8 for several Ψ and ρ value. Firstly, for any ρ value, assuming $\Psi \sim 0°$ is seen to lead to erroneous values for Θ, except around $\Theta \sim 45° - 50°$ where A depends weakly on Ψ. Secondly, different (ρ, Ψ) couples can lead to the same value of Θ for a given A measurement, which is therefore ambiguous. These observations justify the use of a full polarimetric approach to investigate molecular order in zeolite L compounds.

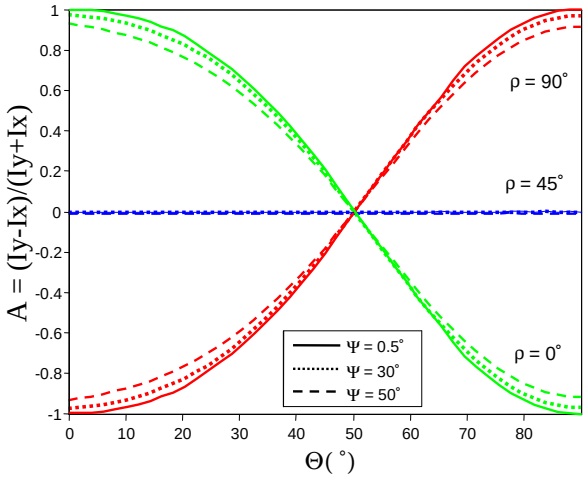

Figure 4.8: Anisotropy factor A calculated for the bell-shaped model as a function of Θ, at different cone mean orientations ρ and for several values of the width Ψ.

4.4.3 The effect of Θ and Ψ on the 2PEF polarimetric response: sensitivity of the technique

In order to better visualize the effect of both Θ and Ψ parameters on the 2PEF polarimetric responses as well as quantify the sensitivity of the technique to these angles, a few theoretical polarimetric responses are compared in Fig. 4.9 (assuming $\rho = 0°$). A closer look on the obtained lobes using the model detailed above shows that the Ψ disorder parameter affect the width and waist shape of these lobes. Different ρ values would also change the pointing direction of the whole lobes as well as their shape.

For small values of Ψ, the molecules exhibit a quasi 1D order and thus very anisotropic I_X and I_Y polarization responses, appearing as peaked two-lobes responses having the same shape. Increasing Ψ induces distortions on both $I_X(\alpha)$ and $I_Y(\alpha)$, with a more pronounced effect for I_Y. The I_Y lobes indeed undergo a larger shape and opening of their

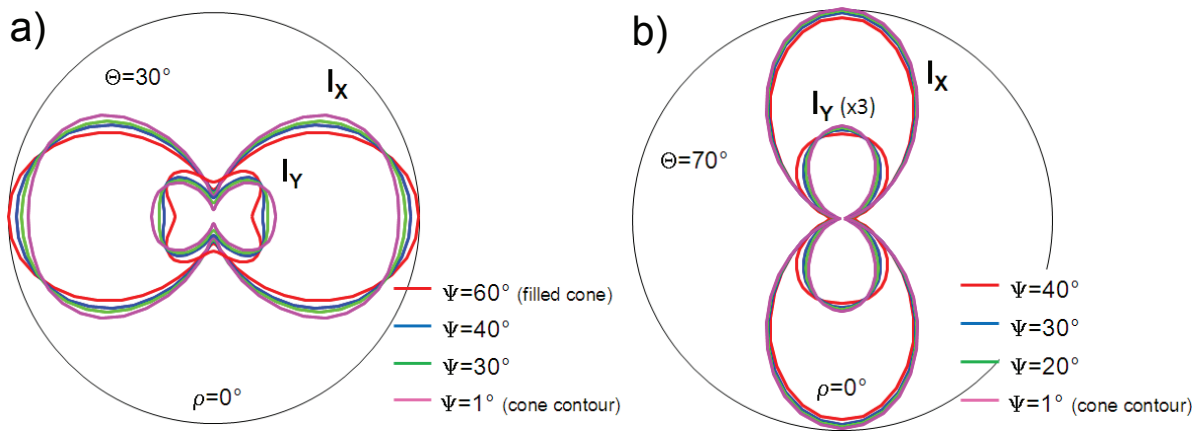

Figure 4.9: Two-photon polarimetric responses I_X and I_Y as a function of the incident field rotation angle α for different angular distributions of the fluorescent molecules at fixed $\rho = 0°$ angle.

waist, with a strong dependence on Ψ. Overall in the high molecular order ($\Psi = 5° - 25°$) range, the polarization response shape is less sensitive to the molecular distribution width, thus leading to lower accuracy ranges (about $\pm 5°$).

4.4.4 Possible distortion of the polarimetric responses due to the sample properties

As we mentioned in chapter 1, in a polarimetric measurement the sample can distort the responses for two reasons: the perturbation of the incident polarization state if propagating in an anisotropic environment (birefringence), and the perturbation of the light-matter interaction coupling due to energy transfer between molecules.

The birefringence effect is quantified by measuring the polarimetric dependence of the excitation laser passing through the zeolite L crystal, in the forward direction of the microscope using a collecting objective of numerical aperture NA = 0.6 (Fig. 4.10) as mentioned in chapter 2. However this effect induced by the crystal structure, is seen to be negligible as seen in the shape of the polarimetric I_Y^{ω} response, which resembles a response without any birefringent wave plate. Although this is surprising due to the crystalline nature of the sample, this might be due to the low loading content in molecules.

Note that in addition, emitted signal is collected in the epi detection set-up (see Fig. 2.1) and all measurements are performed close to the surface of the crystals, therefore minimizing birefringent effects (if any). We will therefore consider in what follows that the birefringence does not affect the observed polarimetric response [156, 157].

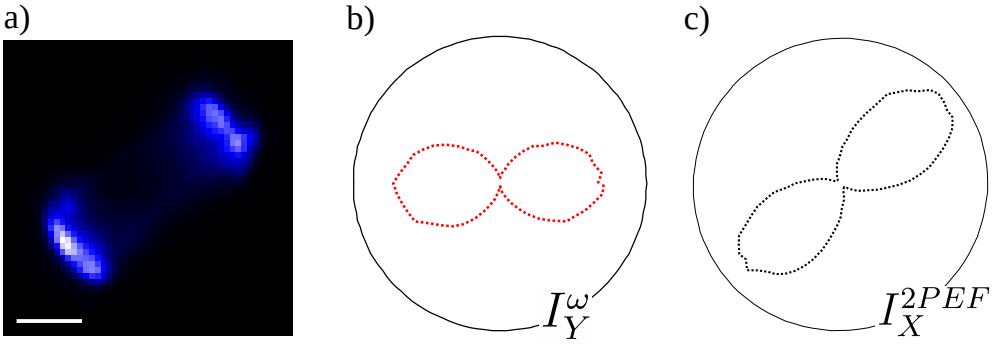

Figure 4.10: (a) 2PEF image of zeolite L crystal loaded with Ox molecules. (b) Laser polarimetric response through the crystal (c) 2PEF polarimetric response. Scale bar $2\mu m$.

Influence the energy transfer on the polarimetric responses. It is known that in such systems a degree of fluorescence resonant energy transfer (FRET) occurs between neighboring molecules [140]. The presence of homo-FRET can affect polarimetric data by introducing depolarization and therefore an overestimation of measured cone apertures. Following an identical approach as in chapter 2, we have modeled the effect of such transfer within a cone width distribution. It is seen that the polarimetric responses are not strongly affected by energy transfer for cone width values below $\Psi < 40°$, in geometries where $\rho = 0°$. Energy transfer in such structures has been furthermore shown to not reach higher values than 40% [145], which makes this effect quite negligible in our studies. This low value is probably partly due to the low molecular density in the investigated samples (comparing to a pure crystal).

4.5 Experimental results

Examples of 2PEF Polarimetric responses of DSM and Ox are depicted as polar graphs in Fig. 4.11b, for different points in the crystals (Fig. 4.11a). The fitting is performed for

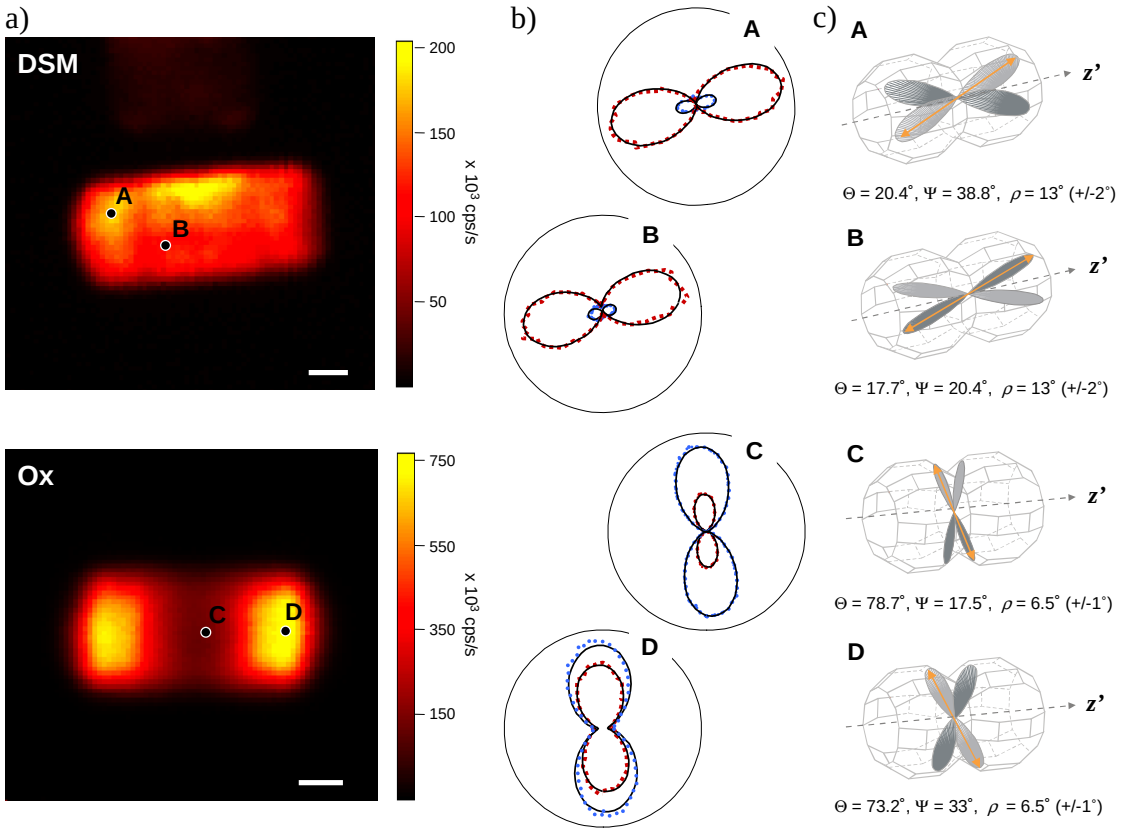

Figure 4.11: (a) 2PEF images $I_X + I_Y$ of zeolites L loaded with DSM and Ox molecules. Scale bars $1\mu m$. (b) Experimental polarimetric responses I_X (*green dots*) and I_Y (*red dots*) emitted by an assembly of molecules, as a function of the input polarization α angle, measured at several locations on the crystal (points A-D). The fit to the experimental data (*continuous black line*)follows the model described in the text. (c) Schematic representation of the molecular orientational distribution inside the zeolite channels, of which only a section is drawn for simplicity. The dichroic parameters $\delta = 0.12$ rad, $\gamma = 0.007$, at $\lambda_{exc} = 800$nm (DSM) and $\delta = 0.48$rad, $\gamma = 0.0098$, at $\lambda_{exc} = 1000$nm (Py) are used in the model.

both intensities I_X and I_Y, using all three angles ρ, Θ and Ψ as fitting parameters in the bell-shaped model described above (the quality of the fitting procedure will be discussed in the next section).

Fig. 4.11b shows that the experimental polarization responses agree well with the modeled polarimetry dependencies. For a given position on the crystal all parameters can be given with a $\pm 1°$ accuracy, with an increase of this margin error to $\pm 2°$ in the case of DSM, for which a slight photobleaching imposes to work at lower intensities resulting in more noisy signals.

The ρ, Θ, Ψ values obtained from the fit of the 2PEF polarimetric plots evidence key orientational behavior of the two molecules. First, the mean orientation ρ is seen to lie along the crystal axis c, as can be expected from the symmetry of the structure. Second, the cone aperture Θ is much smaller for DSM ($\Theta \simeq 20°$) than for Ox ($\Theta \simeq 75°$), which is in agreement with the size of these molecules relative to the dimensions of the zeolite channels (Fig. 4.12). The obtained value for Ox is furthermore consistent with the mean tilt orientation $= 72° \pm 3°$ of Ox in zeolite L compounds measured from fluorescence anisotropy in crystals of unknown orientations [146]. At last, both Θ and Ψ parameters vary from one place on the crystal to another giving an indication of orientational and distributional heterogeneity. This effect directed us to investigations of the spatial behaviors of the molecular distribution properties within zeolite crystals, as shown in the Fig. 4.13.

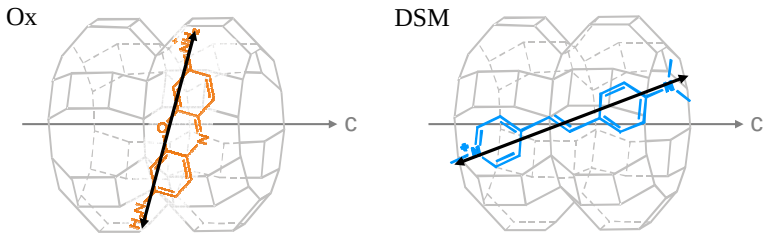

Figure 4.12: Schematic view of the Ox and DSM orientation inside the zeolite L channel, deducted from purely size-considerations.

The 2PEF polarimetric experiment performed on random positions on the crystals provides information on the spatial angular heterogeneity. First, the mean orientation of the distribution ρ is seen to be highly homogeneous within the crystals, and lies predominantly along the crystal axis c. For all the measured zeolites lying close to the X axis, the obtained ρ values range between 5° and 15° depending on the crystals studied, which is consistent with their orientation (crystals along the X axis were voluntarily chosen for polarimetric responses shapes comparison). In some rare cases, higher values have been observed such as in the squared area represented in Fig. 4.13a, where a value of $\rho = 35°$ is measured. This behavior is assigned to the presence of a defect in the crystal. Fig. 4.13 shows the spatial variation of the molecular cone aperture angle Θ, represented by black

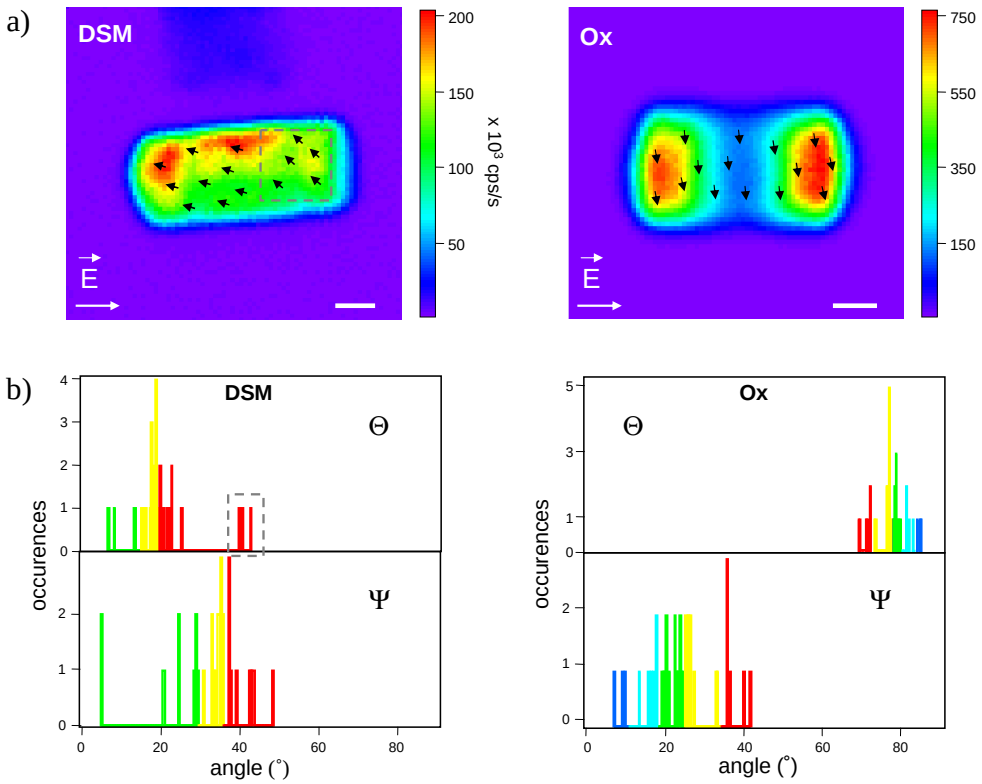

Figure 4.13: (a) 2PEF images $I_X + I_Y$ of zeolites L loaded with DSM and Ox molecules. The black arrows indicate the molecular aperture angle tilt Θ. Scale bars $1\mu m$. (b) Histograms of the Θ and Ψ values obtained from the fit to experimental data measured at several locations on the crystals loaded with DSM and Ox molecules. The color code is the same as in the signal intensity used in the images above. The squared regions in both (a) and (b) correspond to a specific region of high disorder.

arrows. Over several points measured on several crystals, the distribution of the Θ angles lies in the range of $15° - 20°$ for DSM (not accounting for the defect region for which $\Theta = 42°$) and $70° - 85°$ for Ox. The aperture angle distributions lie therefore within a quite narrow range of variations. Interestingly, the disorder parameter Ψ is seen to be correlated to the aperture angle: for Θ approaching the intermediate angle of 45°, a higher disorder is measured with Ψ approaching 40°. When the molecules lie closer to the c-axis (for DSM) or its perpendicular direction (for Ox), the order increases with $\Psi \simeq 20°$. Additional insights concerning the disorder behavior are provided by correlating the measured angles with the observed regions in the 2PEF images of Fig. 4.13a. A color code showing the low molecular concentration regions in green (low 2PEF intensity for all input polar-

ization angles) and the high molecular concentration regions in red (high 2PEF intensity) shows that overall, a high disorder is correlated with a high concentration. It is generally observed for both dyes that when the concentration increases, the angles of orientation tend to randomize (Θ approaches 45° and Ψ increases). Note that the measurement of such angles is performed by integrating the molecular information within a focal volume of about 300nm lateral diameter and 700nm longitudinal dimension, which corresponds to an average over a large number of molecules. The observation of a higher disorder could then correspond to a local perturbation of the molecular orientations due to increasing steric interactions between the dye molecules in regions where they are densely packed.

The experimental observations described above are seen to be generally similar for different zeolite crystals and different depths of investigation within a crystal. The averaged values of the Θ and Ψ parameters measured over a large population of different molecules are summarized in Table 4.1. Overall, the measured Ψ angles are lower for Ox compared

Table 4.1: Angular parameters of the distribution function obtained from 2PEF polarimetric data fitting from measurements performed for five different crystals for each investigated dye[a].

	DXP	DSM	Ox	Py
Θ	16°	16°	77°	80°
Ψ	19°	26°	24°	15°

[a]The angles given are averaged values. Typical margin errors are of a few degrees due to the large Θ and Ψ angular distribution over the entire crystal. The "out of range" values measured in some rare cases, as mentioned above, are not accounted for in this table.

to DSM (Fig. 4.13b), indicating that the higher flexibility of DSM gives rise to a greater variety of possible orientations. The other studied molecule Py shows a very similar cone aperture Θ as for Ox, as expected from its structure. Although still exhibiting a slight disorder, the Py and DXP molecules are seen to be the most ordered structures within the zeolite channels. This indicates that steric interactions provide some degree of freedom of insertion configurations within the channels, even for quite rigid molecules.

4.5.1 The quality of the fit

The general quality of the fit is shown for both DSM and Ox in Fig. 4.14, where the mean squared error $\chi^2(\rho, \Theta, \Psi)$ between typical experimental I_X and I_Y polarimetric responses and the expected theoretical responses:

$$\chi^2(\rho, \Psi) = \sum_{\alpha} \left(I_X^{exp}(\alpha) - I_X^{theo}(\alpha, \rho, \Theta, \Psi)\right)^2 + \left(I_Y^{exp}(\alpha) - I_Y^{theo}(\alpha, \rho, \Theta, \Psi)\right)^2 \qquad (4.2)$$

is depicted for a large span of (Θ, Ψ) values, assuming a fixed ρ and (Θ, ρ) assuming fixed Ψ. In all cases there is a clear minimum corresponding to the best fitting Θ, Ψ and ρ values. From the fits, it is clearly found that the measured molecular distribution width

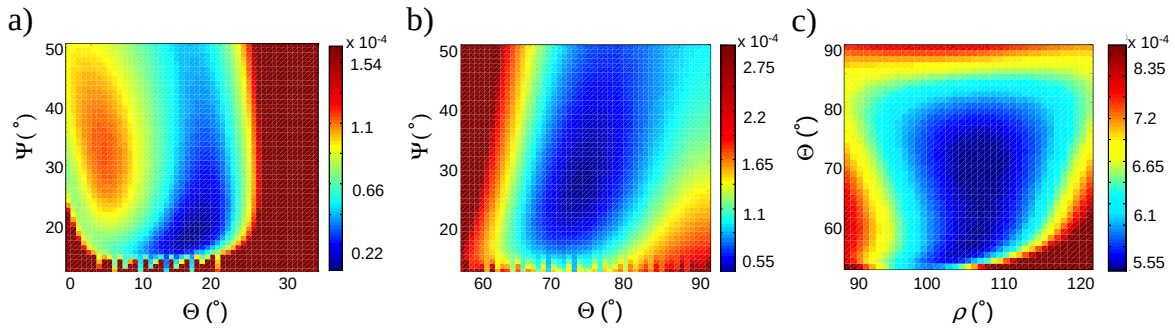

Figure 4.14: Typical mean squared error behavior between the measured I_X and I_Y intensities and the corresponding theoretical intensities, for Θ, Ψ and ρ values (in °) taken every 2° within a 40° range : (a) DSM and (b,c) Ox polarimetric responses.

Ψ differs from 0°, with on average $\Psi \simeq 20°$ for DSM and $\Psi \simeq 30°$ for Ox, while the region below $\Psi < 15°$ for DSM (Fig. 4.14 a) and $\Psi < 10°$ for Ox (Fig. 4.14 b) cannot be well fitted.

The relevance of introducing the Ψ width parameter in the fit of the polarimetric responses is illustrated in Fig. 4.15. In these figures two fitting procedures are depicted, one obtained from a fit over the three (ρ, Θ, Ψ) parameters (Fig. 4.15 a), the other one obtained from a fit on (ρ, Θ) with the cone width Ψ fixed to a very small value ($\Psi = 2°$) representing a pure cone surface model as previously proposed in the literature (Fig. 4.15 b). Obviously the cone surface model is of much poorer fitting quality compared to the cone width model. This is confirmed by the mean square error behavior where $\chi^2(\rho, \Theta)$ values are lower for the fitting procedure that includes the possibility of the disorder within crystal channels. Similar deviations can be found by trying to fit the data using a filled cone model.

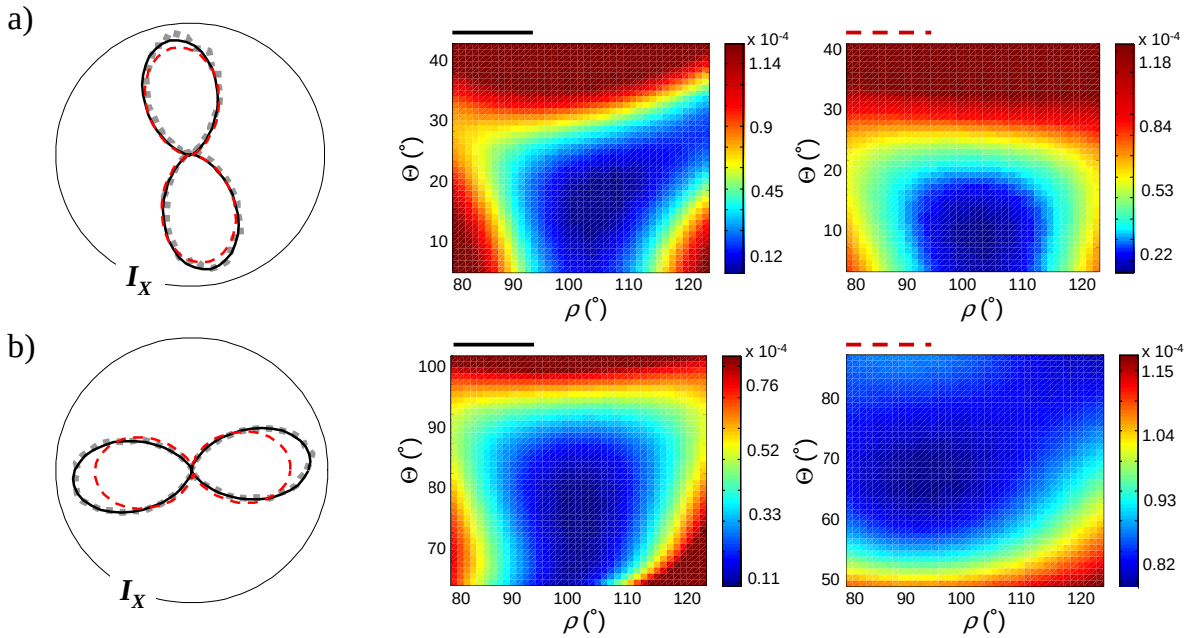

Figure 4.15: (a) Experimental polarimetric response I_X (dots) from DSM molecules and mean square error behavior, fit by ρ, Θ and Ψ (solid line) and ρ, Θ only ($\Psi = 2°$ is fixed - dashed line). The best fit is obtained for the follwing parameters : $\Theta = 17.2°$, $\Psi = 20.4°$ (solid line), $\Theta = 8°$ (dashed line).(b) Same procedure for the experimental polarimetric response I_X (dots) from Ox molecules, fit by $\Theta = 78.2°$, $\Psi = 22°$ (solid line) and $\Theta = 69°$ (dashed line).

4.6 Conclusion

In this chapter we applied the polarimetric TPEF technique to a "close to crystalline" sample. This analysis allows identifying quantitative features of the molecular angular distribution in zeolite L inclusion compounds, in particular the existence of molecular disorder at high molecular concentrations, the extent of which depends on the molecular structure. Extending this technique to microscopy permits to investigate the spatial heterogeneity of the molecular order information, thus providing both angular and spatial fluctuations mapping within the channels of zeolite L crystals. More extensively, this approach provides a tool to probe molecular organization of *a priori* unknown distributions with a sub-microscopic spatial resolution.

Chapter 5

Polarization resolved Three-photon fluorescence in crystals

Polarization resolved techniques in crystals have been so far mostly applied to coherent nonlinear optical processes such as Second Harmonic Generation (SHG) [91, 43] and more recently Coherent Anti Stokes Raman Scattering (CARS) [51]. A combined SHG and 2PEF analysis performed on nanometric size crystals showed that polarimetry is able to differentiate between single-crystals and polymorph structures, therefore providing an interesting crystallinity diagnostics at sizes that are not amenable by traditional X-ray diffraction techniques [41]. This analysis was based on a *a priori* knowledge of the crystal point-group of the investigated structures, thus defining the susceptibility tensors involved in the optical processes. In the various studies performed, a remarkable property arises : the fluorescence from pure crystals exhibits very similar polarization-responses shapes whatever the projection analysis direction of the signal [43]. Since this is not expected from a pure tensorial analysis (chapter 1), a possible explanation to this effect is a strong energy transfer between molecules as introduced in chapter **??**. This property could in particular be an interesting diagnostics for crystallinity. In the present study, our goal is to investigate the potentialities of polarized multiphoton fluorescence signals from protein crystals without any additional fluorescence staining [55]. Proteins are indeed naturally fluorescing at wavelengths in the UV range, due to the properties of their amino-acids. In particular tryptophan is the most efficient amino-acid with an absorption wavelength around 260nm and an emission around 300nm. The excitation of tryptophan would therefore be accessible using a three-photon excitation at wavelengths around 840nm, which is in the Ti-Sa laser range. We will therefore use this contrast to investigate polarization-resolved responses from pure protein crystals, using a model structure (Lysozyme) widely

studied.

Proteins, like many molecules, can form crystals when placed in the appropriate conditions. The goal of crystallization is usually to produce a well-ordered crystals and large enough (size of 0.3 -0.5mm is regarded as optimal [158]) to obtain useful X-ray diffraction data, which can then be analyzed to determine the protein's three-dimensional structure [159]. Knowledge of this structure is crucial in understanding the function of the protein from their amino acid sequences. Proteins crystallization remains however a challenge because of the difficulty to control the right initial nucleation conditions to produce a pure crystal. These conditions can affect properties such as crystal sizes, number of crystals and good enough quality for X-ray studies [160]. For instance an uncontrolled nucleation process (due to wrong medium conditions) prevents the growth of protein single crystals with sufficient size and qualities [161, 162]. The protein purity, temperature, pH, concentration can also have an influence on the final crystallization [162, 159]. At last, the average time to prepare protein crystals large enough for X-ray analysis is still very long (from a few days to few weeks) [158]. The most recent techniques of crystallinity investigation are now able to investigate micrometric size structure, which has motivated fast screening analysis platforms at these scales, such as Microcapillary Protein Crystallization Systems (with different pH buffers) [163] or Microfluidic Silicon Devices [164]. Combining such techniques with an optical diagnostics capable of investigating sub-micrometric scale structures would greatly improve the efficiency of protein crystals sorting, in particular by investigating the initial stage of the proteins crystallization.

In this chapter we describe the first investigations on three-photon fluorescence polarimetry on lysozyme protein crystals. To validate this technique before studying proteins, we first study a well known molecular crystal (p-terphenyl) active in the same excitation and emission wavelengths range. We will show that polarimetric 3PEF in crystals exhibits similar properties as already observed in other structures for 2PEF, indicating strong energy transfer between molecules.

5.1 Samples characteristics and preparation

5.1.1 P-terphenyl crystals

For the feasibility experiments we have chosen crystals that consist of 1,4-Diphenylbenzene (p-terphenyl) molecules due to their efficient fluorescence under three photon excitation. Moreover the structure of the p-terphenyl compounds has been widely studied by X-ray diffraction [165, 166, 167]. The crystals are monoclinic (C_{2h} point group) at room

temperature with two molecules per unit cell (Fig. 5.1 b) [168]. Molecules are placed in the unit cell frame (1,2,3) with their long molecular axis along the 3 direction. The central ring of the molecule is tilted alternately compared to the outer rings along in the (1,2) plane. Quantum chemical calculations reveal equilibrium inter-ring torsion in the range $40 - 50°$ (Fig. 5.1 c) [169]. The absorption and emission spectra of p-terphenyl

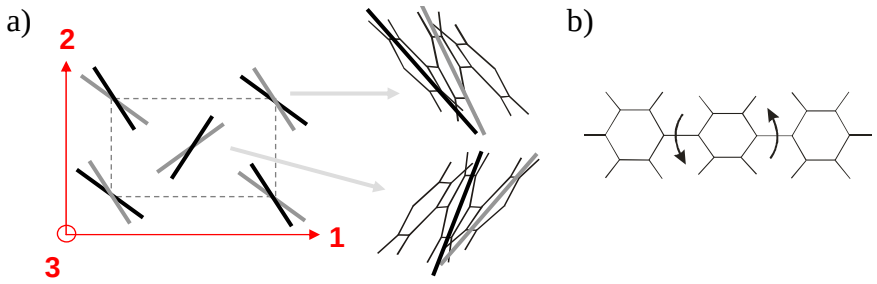

Figure 5.1: (a) P-terphenyl monoclinic unit cell indicated by a dashed line, outer rings of the p-terphenyl molecules (gray) and inner rings (black). Unit cell lengths : a = 8.119 Å, b = 5.615 Å, c = 13.618 Å. (b) Equilibrium interring torsion of the p-terphenyl inner ring [168].

molecules are depicted in Fig. 5.2. Although slight spectral shifts are expected in the crystalline form, these spectra are quite broad and therefore 3PEF signals from crystals are recorded using an excitation wavelength at 840nm. These measurements are performed with a typical average power of 1mW and an integration time of 50ms (for images) 0.1s (for polarization responses : this time is longer than in 2PEF conditions, due to the lower efficiency cross sections and detector sensitivity). To study 3PEF polarimetry in p-terphenyl crystalline structures, crystals of sub-millimetric size obtained from a powder were chosen for their good optical quality and directly placed on the microscope slide.

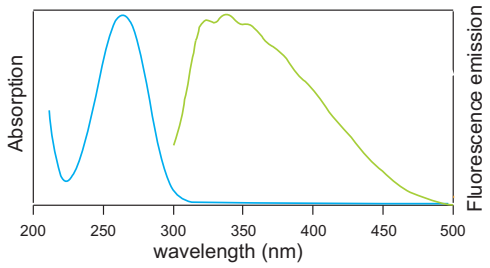

Figure 5.2: Normalized absorption and emission spectra of p-Terphenyl dissolved in cyclohexane [170].

5.1.2 Lysozyme

Lysozyme, also known as muramidase or N-acetylmuramide glycanhydrolase is a protein formed by amino acids that contains six tryptophan residues as indicated in Fig. 5.3 a. Each unit cell of $P4_32_12$ space group (D_4 point group of tetragonal-trapezohedral class, depicted in Fig. 5.3 c) is made of eight lysozyme molecules (Fig. 5.3 a). Lysozyme proteins crystallize in tetragonal crystals depicted in Fig. 5.3 d.

The absorption and emission spectra of tryptophan, the most efficient amino-acid for

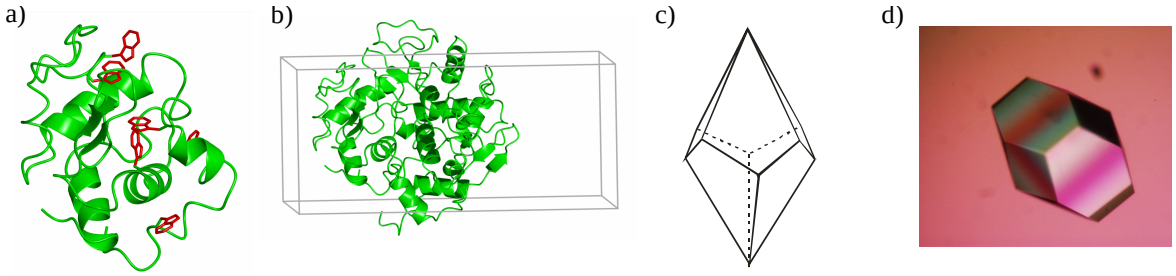

Figure 5.3: (a) Lysozyme protein structure with six tryptophan residues (depicted in red). (b) Lysozyme crystal unit cell containing eight molecules. Unit cell lengths : a = b = 79.1 Å, c = 37.9 Å. (c) Tetragonal-trapezohedral class of the tetragonal crystals system that correspond to $P4_32_12$ space group. (d) Tetragonal lysozyme crystal (reproduced from wikipedia).

fluorescence, are depicted in Fig. 5.4 in the natural folded state (N) of proteins. In protein crystals, the emission spectrum is entirely in the UV region below 400nm. In our three-photon fluorescence investigations, the most efficient excitation wavelength is seen to be around 810nm with an average power of 20mW and an integration time 50ms (for images) and 1s (for polarization responses). The signal from protein crystals was overall seen to be two orders of magnitude below the one obtained from p-terphenyl crystals, mostly due to the lower efficiency of the active molecules, which are also in much lower number.

Lysozyme crystallization

50 mg/ml of lysozyme from chicken egg white (purchased from Invitrogen molecular probes) was diluted in 0.1M sodium acetate buffer of pH 4.5 and next mixed in the same buffer 1:1 with 1M sodium chloride. Afterwards the mixture was put into a quartz chamber to allow for UV detection. Large crystals with volumes in the range from 5 μm to 1 mm grew overnight and were directly observed.

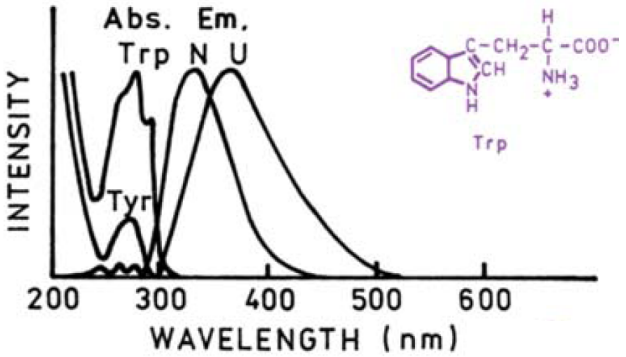

Figure 5.4: Normalized absorption and emission spectra of tryptophane (Trp) in an unfolded (U) and folded (N) protein. The absorption is compared to the less efficient Tyr (tyrosine) amino-acid [55].

All the measurements shown below were performed using the forward UV detection set-up, using a 1.2 NA focusing for the excitation and a 0.6 NA collection aperture in the UV range (chapter **??**). The dichroic mirror used was the FF720-SDiO1 mirror, which is expected to introduce a minimal polarization distortion in the range 800-850nm (typically $\delta = 0.2234$rad and $\gamma = 0.009$).

5.2 Modeling three-photon fluorescence responses from crystals

Fig. 5.5 shows typical 3PEF polarization responses detected along the two analyzed X and Y directions for both p-terphenyl and lysozyme crystals. In most of the investigated crystals these responses are seen to made of four lobes, with I_X and I_Y exhibiting similar shapes.

This behavior is typical of the previously investigated "pure" crystals [41, 91, 43], and strongly differs from polarimetric responses recorded for poly-crystalline [41] or disordered media [74] where I_X and I_Y would necessary have very different shapes (see Fig. 2.22). Therefore in the this analysis, we will follow a model introduced in chapter 2 which includes decoupled absorption and emission processes in the crystal : this model implies in particular that only the molecular three-photon excitation tensor ξ has an influence on the shape of a polarimetric response :

$$I_X^{3ph}(\Omega, \alpha) = \sum_{IJKLMN} \xi_{IJKLMN}(\Omega) \cdot E_I E_J E_K E_L^* E_M^* E_N^* \cdot \alpha_{XX}(\Omega) \tag{5.1}$$

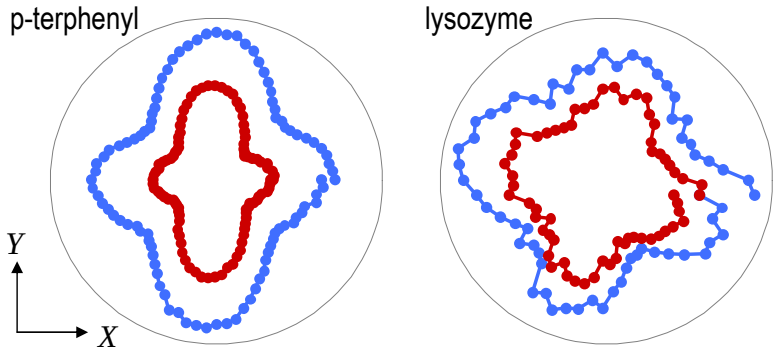

Figure 5.5: 3PEF polarimetric responses detected for two arbitrary chosen crystals in I_X (red dotted line) and I_Y (blue dotted line) polarization directions.

where $\Omega = (\theta, \phi, \psi)$ is the Euler set of angles defined in Fig. 5.6 a, α is the emission susceptibility tensor and $E_I, E_J...$ are the incident field polarization projections on each macroscopic axis. The three-photon absorption and emission susceptibility tensors are constructed relying on the different dipole orientations present in the unit cell frame. To built this tensors we will use the approach introduced in chapter 1.

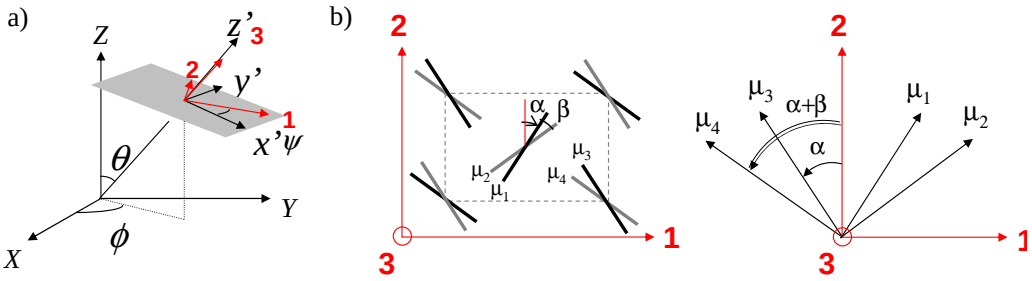

Figure 5.6: (a) Orientation of the unit cell frame (1,2,3) in the macroscopic frame (X,Y,Z). The z' direction is the axis of highest symmetry in the crystal unit cell structure. The (x',y') axes define therefore the plane containing the molecules (grey rectangle) in the crystal frame (x',y',z') (b) Orientation of transition dipole moments in the unit cell frame $1, 2, 3$: $\alpha \approx 33°$ and $\beta \approx 21°$.

As we have seen in the previous section the central ring of the p-terphenyl molecule is tilted (see Fig. 5.6 b), this results that each molecule of the unit-cell has two transition dipole moments oriented in the (1,2) plane with an angle β between them, and an additional one along the molecule axis (along the 3 direction). The molecules of the unit cell are furthermore oriented with an angle α relative to the 2 axis. In each unit cell, the

assembly of transition dipoles is therefore :

$$\begin{aligned}
\mu_1 &= [\sin\alpha, \cos\alpha, 0] \\
\mu_2 &= [\sin(\alpha+\beta), \cos(\alpha+\beta), 0] \\
\mu_3 &= [-\sin\alpha, \cos\alpha, 0] \\
\mu_4 &= [-\sin(\alpha+\beta), \cos(\alpha+\beta), 0] \\
\mu_5 &= [0, 0, 1]
\end{aligned} \tag{5.2}$$

where μ_5 is the transition dipole moment along the molecule parallel to the 3 axis which accounts on the out of plane absorption probability. Note that we choose transition dipole moments of equal amplitude (from the structure observations). Knowing an average values of both $\alpha \approx 33°$ and $\beta \approx 21°$ [168] we can construct the six order susceptibility tensor for the three-photon absorption tensor ξ, from the multiple dipoles $p = 1, .., 5$:

$$\xi_{ijklmn} = \sum_{p=1}^{5} \mu_p^i \mu_p^j \mu_p^k \mu_p^l \mu_p^m \mu_p^n \tag{5.3}$$

where *(i,j,k,l,m,n)* = (1,2,3).

The influence of the unit cell orientation on the three-photon fluorescence polarimetric response (either I_X, I_Y or $I_X + I_Y$) calculated using approach developed in chapter 1 is depicted on Fig. 5.7, in the case $\psi = 0°$. Theoretical 3PEF polarimetric responses from this model structure exhibit mostly four-lobe shapes, characteristic of the presence of at least two transition dipoles directions in the sample plane (see 1). These responses also show significant changes depending on the unit cell orientation in the (X,Y,Z) frame. Firstly, as expected the tilt of an angle ϕ relative to X results in a rotation of the polarimetric pattern. Secondly, this pattern is strongly sensitive to the tilt angle of the unit cell with respect to the sample plane (θ angle rotation). However the general property of a four-lobes shape is preserved.

Fig. 5.8 illustrates the dependence of these 3PEF polarization response on both the relative angle β between the dipoles in the (1,2) plane and the relative magnitude between these dipoles. In both cases, a part from extreme angle variations, the four-lobe shape is still preserved with a contrast which varies depending on the unit cell parameters. Overall, the polarimetric response pattern symmetry resembles the symmetry of the structure in the (1,2) plane.

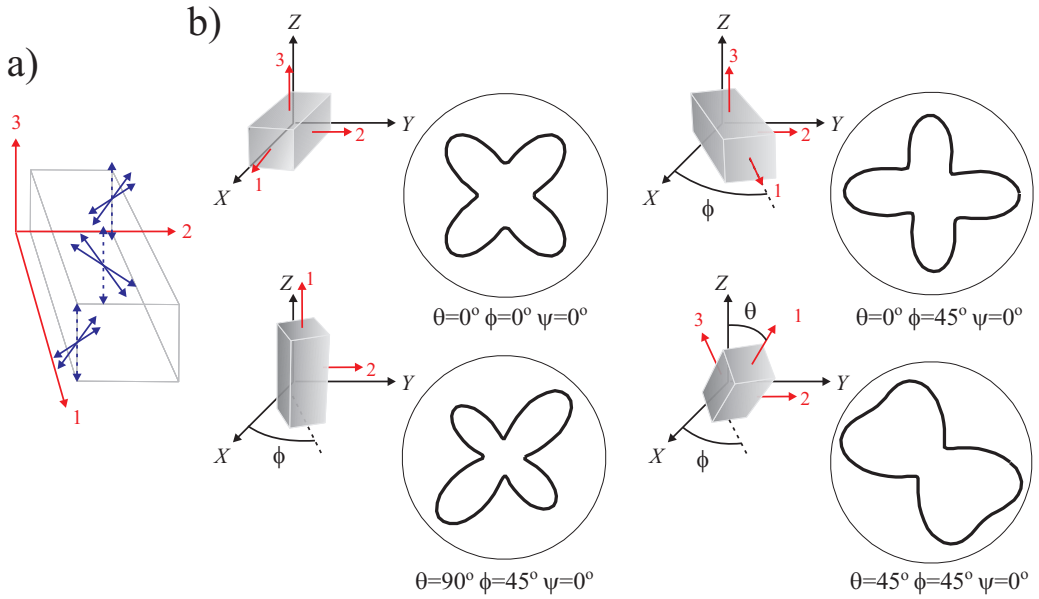

Figure 5.7: (a) Schematic representation orientation of transition dipole moments (blue arrows) in the unit cell : in the $(1,2)$ plane (solid arrows) and parallel to the (3) (along the molecule axis) (dashed arrows) (b) Three-photon fluorescence polarimetric response $I_X = I_Y = I_X + I_Y$ calculated for different unit cell orientation.

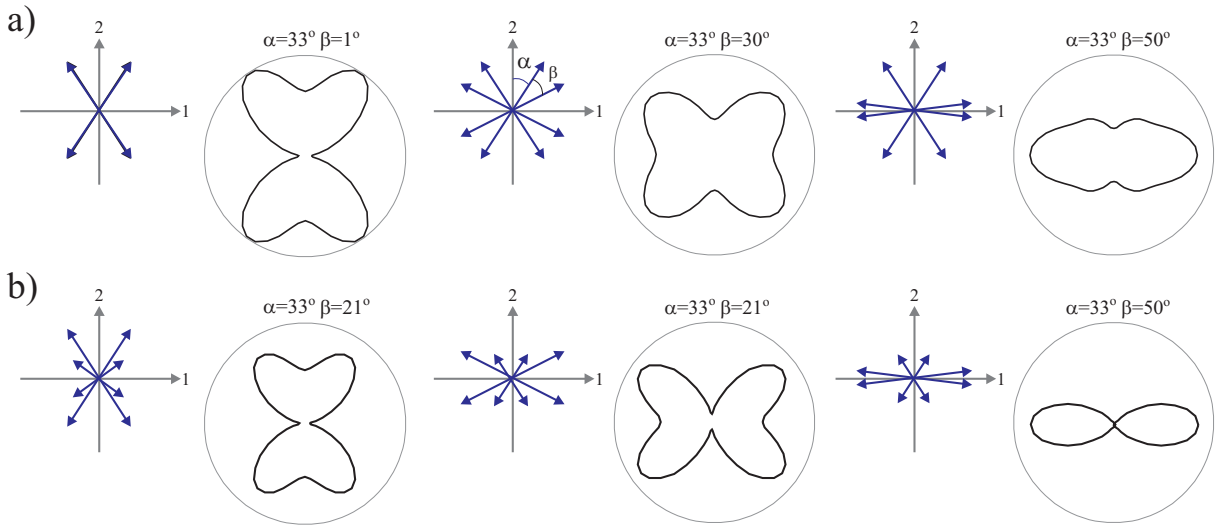

Figure 5.8: Three-photon fluorescence polarimetric responses $I_X = I_Y = I_X + I_Y$ calculated for different (a) angle β and (b) amplitude between transition dipole moments constituting the unit cell which orientation is $(\theta = 0°, \phi = 0°, \psi = 0°)$.

To illustrate the sensitivity of this analysis to the separation angle between the dipoles still preserving the same global symmetry, Fig. 5.9 depicts polarimetric patterns calculated when enlarging the angle β between the dipoles, while the global orientation $\alpha + \frac{\beta}{2}$ is kept constant. This figure shows that 3PEF is able to resolve four dipole directions when the relative angle separation is larger than 20°.This would not be accessible using two-photon fluorescence (see Fig.1.15).

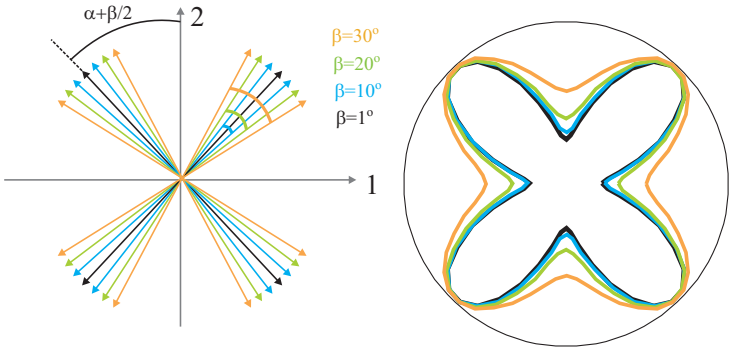

Figure 5.9: Three-photon fluorescence polarimetric responses $I_X = I_Y = I_X + I_Y$ calculated for different angle β between transition dipole moments but constant general orientation $\alpha + \frac{\beta}{2} = 43°$. Orientation of the unit cell : $(\theta = 0°, \phi = 0°, \psi = 0°)$.

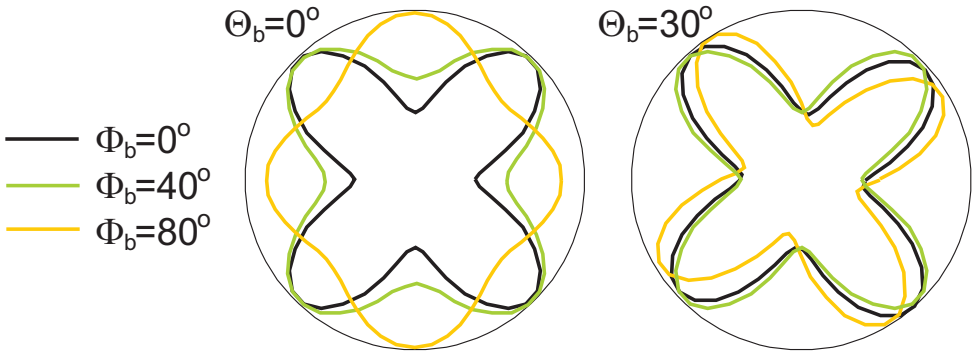

Figure 5.10: Influence of the birefringence effect on three-photon fluorescence polarimetric responses $I_X = I_Y = I_X + I_Y$ calculated for different values of Φ_b, for an optical axis Θ_b oriented parallel to X and tilt of $\Theta_b = 30°$. Orientation of the unit cell : $(\theta = 0°, \phi = 0°, \psi = 0°)$.

In chapter 2 we have shown that polarimetric responses can suffer from distortions introduced by optics or sample itself. In particular, the ellipticity occurring from the sample birefringence is expected to modify the polarimetric dependence of the measured

signal, especially when propagating through micrometric scale depths. We expect that this effect will not be negligible when focusing in the volume of molecular crystals such as in p-terphenyl. Fig. 5.10 illustrates possible distortions of polarimetric lobes appearing with increasing the phase shift Φ_b in the input field polarization. It can be seen that the birefringence affects polarimetric curves, however the global symmetry (represented by four dipoles) does not change.

5.3 Analysis of experimental results

In this section we will present three-photon fluorescence study performed on p-terphenyl crystals and preliminary results on Lysozyme protein crystals.

5.4 P-terphenyl crystals

Fig. 5.11 shows the 3PEF signal from typical p-terphenyl crystals whose size vary from sub-micrometric to a few millimeters. It can be seen that 3PEF microscopy permits to detect the fluorescence signal from crystals of subwavelength size (∼200nm) (Fig. 5.11 b). Typical polarimetric responses are depicted in Fig. 5.12 for a few observed crystals.

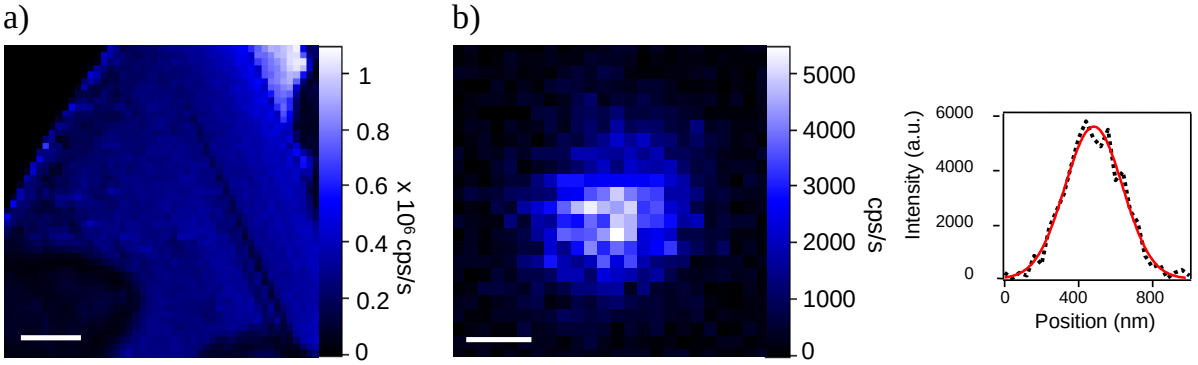

Figure 5.11: 3PEF images of p-terphenyl crystals. (a) Crystal size $\sim 500 \times 500\mu$m. Scale bar 20μm. (b) Observation of a single sub-micrometric size crystal. Scale bar 200nm. Gaussian fit of the signal intensity : FWHM 220nm±10nm.

Obviously the shape of the polarimetric patterns exhibits most often four lobes shapes characteristic of the four-dipoles symmetry detailed in the previous section. The I_X and I_Y responses exhibit in addition similar shapes, representative of a strong energy transfer

effect within this structure. This would be expected from the inter-molecular distance of a few nanometers.

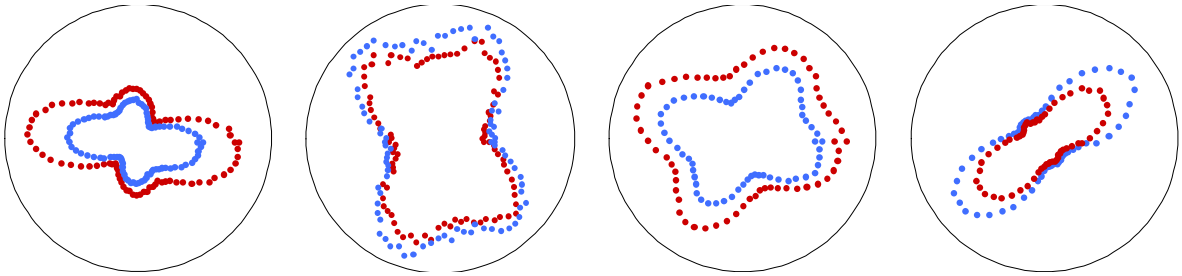

Figure 5.12: Experimental polarimetric responses of I_X (red dotted line) and I_Y (blue dotted line) detected for different p-terphenyl crystals.

In order to investigate the birefringence effect in p-terphenyl crystals, the polarimetric dependence of the excitation laser passing through a millimetric size crystal was measured, using the method developed in **??**. To account for this effect in a systematic way, for each 3PEF measurement we chose to detect simultaneously two responses : I_Y^{ω} along the Y analysis direction, representative of the birefringence affecting the incident beam averaged over the whole crystal thickness, and I_X^{3ph}, the 3PEF fluorescence signal along the X analysis direction (the 3PEF responses along the Y analysis direction, being of the same shape, were not recorded). The birefringence effect illustrated in Fig. 5.13 is clearly non-negligible. Indeed, the laser intensity I_Y^{ω} polarimetric dependence when passing through the crystal (Fig. 5.13 b) is tilted and more open comparing to I_Y^{ω} from the non-birefringent glass substrate (Fig. 5.13 a). To determine the Θ_b (the birefringence slow axis direction) and Φ_b (phase shift of the incident field polarization when passing through the sample, see Fig. 2.23) parameters, theoretical polarimetric response for the $I_Y^{\omega}(\Theta_b, \Phi_b)$ intensity is calculated for (Θ_b, Φ_b)-pairs with each parameter varying from 0° to 360° with a step of 2° (note that in this calculation the (δ, γ) dichroic parameters (see chapter 2) are entered in the field calculation and previously calibrated). The set of calculated polarimetric curves is then compared with the experimental data, the sum of mean squares being used as an estimation of the fit quality:

$$\chi^2(\Theta_b, \Phi_b) = \sum_{\alpha} \left(I_Y^{exp}(\alpha) - I_Y^{theo}(\alpha, \Theta_b, \Phi_b) \right)^2 \tag{5.4}$$

The values Θ_b and Φ_b found from this fitting procedure show that these parameters remains similar for different depths in the crystal (from 1μm, which correspond to the sample plane, to 20μm Fig. 5.13 b) as expected. Since this measurement is made of the

whole interaction volume through the crystal thickness. The general quality of the fit is depicted in Fig. 5.13 c for two experimental responses. It can be seen that the minimum of the fitting error is unique and can be found for Θ_b with $\pi/2$ periodicity and Φ_b with π periodicity. Note that only one global minimum is found accounting for the (δ, γ) dichroic parameters due to minimal polarization distortions introduced by the dichroic mirror used in this experiment. The 3PEF intensity I_X^{3ph} detected simultaneously along X analysis direction, decrease progressively with the depth penetration (Fig. 5.13 d) due to the possible three-photon absorption of the incident illumination in the crystal. The four-lobe shape is also seen to be progressively lost at the larger depth, possibly due to birefringence deformations (Fig. 5.10). Therefore for the further analysis we will use the polarimetric responses detected close to the crystal surface.

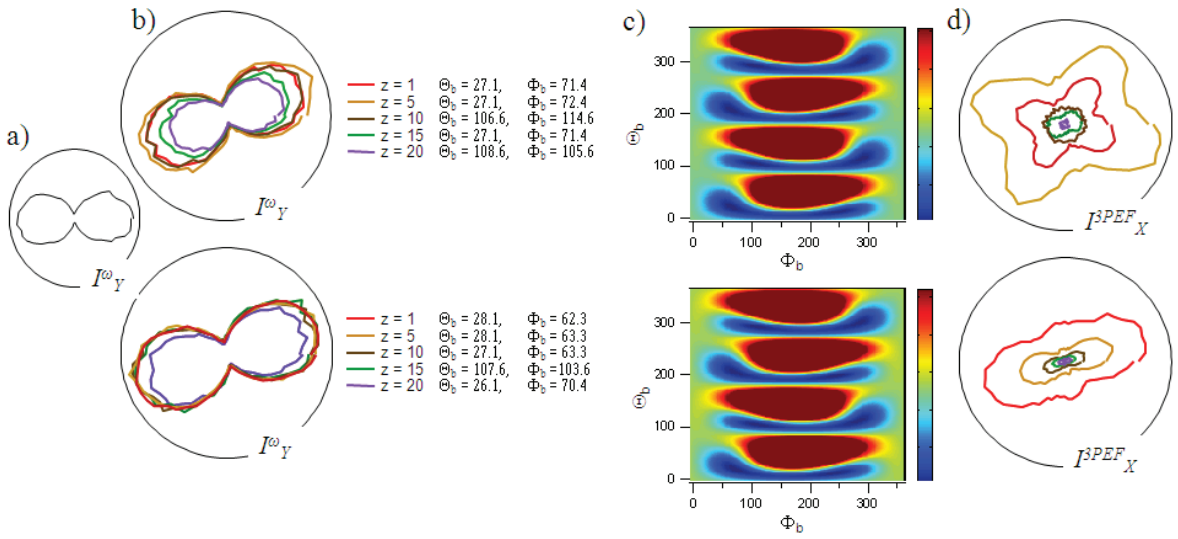

Figure 5.13: Experimental birefringence measurement in a p-terphenyl crystal. (a) Laser polarimetric response I_Y^{ω} from the non-birefringence glass substrate (no crystal). (b) Laser polarimetric response I_Y^{ω} passing through the crystal detected for different depth in the crystal (Z in μm) with Θ_b and Φ_b parameters obtained from the fitting procedure. (c) Typical mean squared error behavior between the measured I_Y^{ω} intensity and the corresponding theoretical intensities, for Θ_b and Φ_b values (in °) taken every 2° in the range from 0° to 360°. (d) 3PEF polarimetric responses detected simultaneously with I_Y^{ω} responses.

The obtained Θ_b and Φ_b parameters were introduced in the 3PEF polarimetric analysis

accounting for the depth of penetration of the incident versus emission beams, as well as for their different wavelengths in the expression of the associated Φ_b (see chapter 2). Once these parameters are identified, they are introduced in the 3PEF model and a fit is performed on the Euler angles defining the macroscopic orientation of the crystal, using the crystal symmetry defined in the previous section. Fig. 5.14, which shows the result of such fits, illustrate the better quality obtained when introducing the birefringence factors.

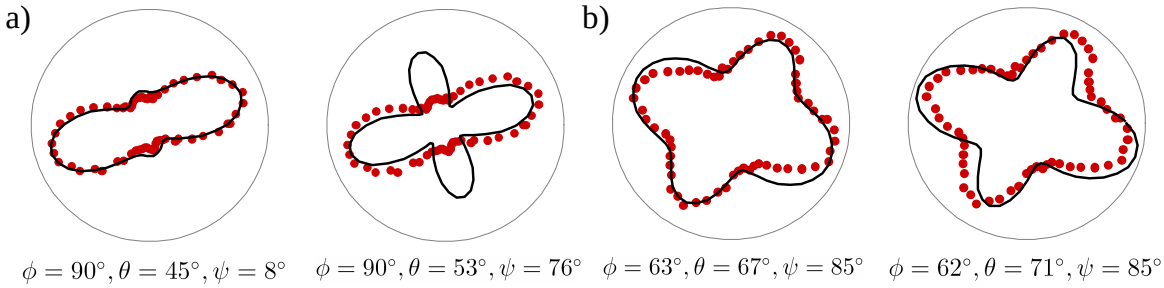

Figure 5.14: Experimental polarimetric responses I_X (red dotted lines) of p-terphenyl crystals fit (black solid line) by ϕ, θ, ψ. (a) The fit (black solid line) performed for birefringence parameters $\Theta_b = 28°$, $\Phi_b = 63°$ (right curve) and the fit does not account on the birefringence effect $\Theta_b = 0°$, $\Phi_b = 0°$ (left curve). (b) $\Theta_b = 27°$, $\Phi_b = 72°$ (right curve) and $\Theta_b = 0°$, $\Phi_b = 0°$ (left curve).

5.5 Lysozyme crystals

In the previous section we have seen that polarization resolved three-photon fluorescence is a probe of some relevant information in molecular crystals : the possible energy transfer between molecules (and thereby the degree of crystallinity in a crystal), as well as an indication of the minimum numbers of dipoles orientations in the unit cell structure. We will attempt to use this analysis as a probe of the crystal quality in proteins crystals.

Fig. 5.15 illustrate 3PEF microscopy images of lysozyme protein crystals after about 12 hours of crystallization. The excitation wavelength is set such as the Tryptophan molecules are excited (see previous section). Both the transmission picture and the 3PEF scanning image resemble the expected crystal shape from the structure symmetry. Although protein crystals are much more fragile samples than molecular crystals (they have to be kept in aqueous environment at precise pH, they are quite sensitive to

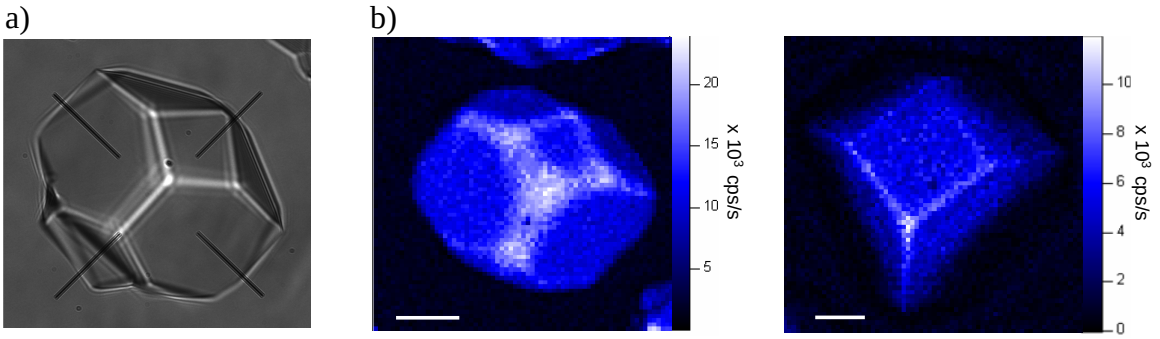

Figure 5.15: (a) Wide field and (b) 3PEF images of lysozyme crystals. Scale bars : 10μm.

photodamage and their fluorescence signal is overall weaker, as mentioned above), we could find correct intensity and integration time conditions to be able to measure polarimetric signatures from such crystals. Typical 3PEF polarimetric responses are depicted in Fig. 5.16. As it was the case in p-terphenyl crystals, the I_X and I_Y polarimetric patterns exhibit similar shapes, which was also observed in measurements performed on ten arbitrarily chosen crystals. We can thus affirm that the approach developed previously is applicable and that the crystalline nature of this sample is confirmed.

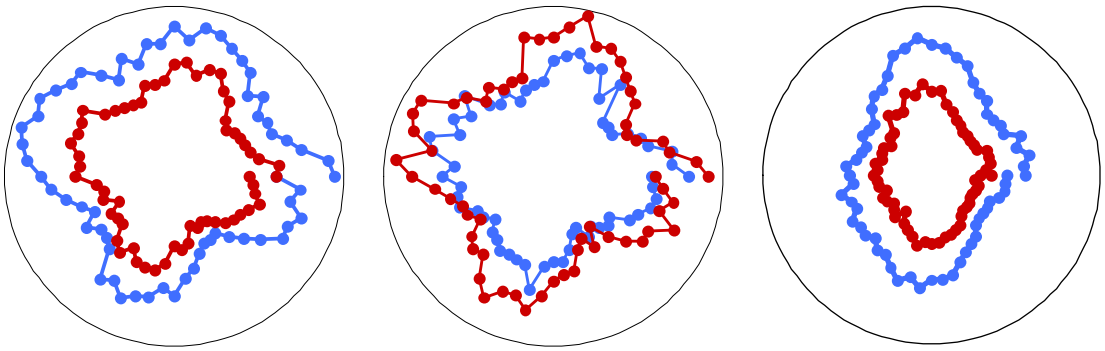

Figure 5.16: 3PEF polarimetric responses I_X (red dotted lines) and I_Y (blue dotted lines) of lysozyme crystals.

This observation seems therefore to support the relevance of such a crystallinity diagnostic in protein crystals. In addition, the 3PEF polarimetric responses detected from tryptophan residues in protein crystals resembles the four lobe patterns observed in the polarimetric responses for p-terphenyl. Since these lobes are also quite open, the structure

most likely exhibits at least four transition dipoles orientations (see Fig. 5.9). For this reason, in a first approximation we adapt a four-dipoles model to lysozyme crystals, even though the structure is known to possess six tryptophane molecules. Note however that three-photon fluorescence process will not be able to distinguish between four and more dipole moments due to limited access of this process in terms of orders of symmetry, as shown in Chapter 1. For the fitting procedure we chose polarimetric patterns (left and middle in Fig. 5.16) that look like four-dipoles structures in a plane, therefore we can assume $\theta = 90$ and $\psi = 0$, and we look for the global orientation ϕ and possible angles between the dipoles. These lobes are symmetric, we thus keep the angle $\alpha + \frac{\beta}{2} \propto 45°$ and increase the angle β between the dipoles such as in Fig. 5.9. This fitting procedure, shown in Fig. 5.17, confirm the crystalline nature of this sample and that the structure is built from a minimum of four dipoles.

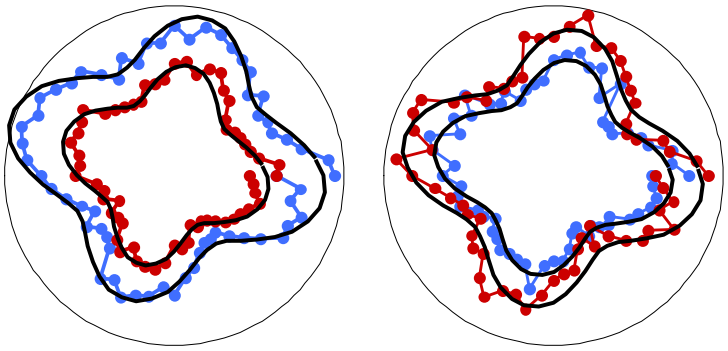

Figure 5.17: Fit (black solid line) of 3PEF polarimetric responses I_X (red dotted lines) and I_Y (blue dotted lines) of lysozyme crystals.

5.6 Conclusion

In this chapter we have shown that the polarization resolved 3PEF microscopy gives access to important information in molecular and protein crystals : there is visibly a strong inter-molecular energy transfer in the structure, illustrated by similar polarimetric shapes whatever the analysis direction. This seems to indicate a possible crystalline diagnostic of such samples, which is of valuable interest for future protein crystallization investigations. Knowing the crystal structure, this technique is furthermore able to provide information on the 3D unit cell orientation. This technique however suffers from some weaknesses : it is not able to provide a readout of the symmetry order in the structure, even though the

knowledge of a lower limit of the number of dipoles is possible. Moreover a more sensitive detection scheme would be required to investigate small size protein crystals, in which the number of available Tryptophan residues is small. The application to crystallinity diagnostics in protein crystals is therefore not straightforward. This is however the first application, to the best of our knowledge, of three-photon polarization resolved microscopy on biological and molecular ordered media investigation without any additional staining.

Conclusion and perspectives

In this thesis we presented the potential and feasibility of polarization resolved multiphoton microscopy for the readout of the static molecular organization at sub-microscopic scales in complex media. This approach, based on a tuneable excitation polarization state complemented by a polarized read-out, is easily implementable and does not require hypotheses on the molecular angular distribution such as its mean orientation, which is a main limitation in traditional fluorescence anisotropy measurements.

This analysis first requires that the excitation polarization state at the focal spot of the objective can be reliably controlled. We have shown that possible distortions originating from the instrument or from the sample itself can be characterized by linear and two photon fluorescence polarimetry measurements. We have shown that this preliminary study is crucial for any future analysis of polarimetric data.

We first applied the polarimetric two-photon fluorescence microscopy technique to the quantitative imaging the local static molecular orientational behavior in model lipids and cell membranes. The results show the possibility to retrieve membrane order information in membranes of complex shapes, which should be of great interest to the biological community for the imaging a molecular order and orientation. This information is indeed a key component in the understanding of molecular interactions that drive the morphology of biomolecular assemblies. In particular, this study can be extended to the determination of the presence of external factors influencing changes in molecular organization inside the cell membrane. For instance, membrane ruffling processes in cell trafficking (endocytosis and exocytosis) is not entirely understood. Investigation of the molecular distribution at cell junctions under tension during embryo development,would be also an interesting possibility.

All these future studies necessitate however a fast analysis since dynamical processes are involved with sub-second time scale. Several improvements of the present technique

could be implemented along this direction : first, the analysis of the polarimetric data can in principle be performed using less incident polarization angles of measurement. Providing that the signal to noise ratio is sufficient, only a few angles are necessary. Second, a parallel polarimetric analysis can be performed using a faster imaging technique. The galvanometric scanning recently developed in our laboratory permits to acquire polarimetric data as a stack of images for different polarization directions at a high rate. This configuration is more adapted to *in vivo* samples investigation, whose morphology is continuously altering in response of the physiological events at various time and spatial scales.

We demonstrated that the polarimetric microscopy imaging scheme permits a spatial investigation of possible heterogeneities of the molecular distribution in inclusion material compounds. This study performed on different fluorescent molecules inserted in zeolite L channels evidenced a degree of disorder for either small or flexible molecular structures. This is an important information for the development of host-guest composites with photonic antenna properties, since molecular organization has a direct influence on the 1D energy and electron transfer properties within the channels of the structure.

Finally, the polarization resolved analysis was implemented in three-photon fluorescence microscopy for the structural analysis of biological environments without staining. 3PEF polarimetric analysis, applied to the investigation of the structure of protein crystals of lysozyme, evidenced signatures that are characteristics of typical multipolar crystals, including energy transfer between molecules. This property could be used as a crystallinity diagnostic at sizes below the optical diffraction limit, that are often not amenable by traditional crystallography techniques. This application could provide a new tool for the preliminary control of the crystallization state of an unknown protein crystal before any X-ray structure analysis. The sensitivity of the three-photon fluorescence to high order of symmetries could furthermore permit the investigation of complex media with a more refined analysis of the structure than from lower order processes.

Overall, this PhD was dedicated to modeling and experimental investigation of molecular organization in biological and molecular media, including the construction of an experimental set-up for multiphoton polarization resolved studies. Since this approach can be extended to general structures such as cells and tissues, and other contrasts such as second harmonic generation (SHG) or higher order processes, more work will be definitely required to take advantage of polarization resolved analysis in biological media. Future investigations have already started in cell membranes under different drug treat-

ments (actin depolymerization, cholesterol depletion), and fibrous tissues analysis (2PEF of elastin and SHG in collagen in thick tissues).

Bibliography

[1] J. Pawley, *Handbook of Biological Confocal Microscopy*. Springer, 2006.

[2] R. Pepperkok and J. Ellenberg, "High-throughput fluorescence microscopy for systems biology.," *Nat Rev Mol Cell Biol*, vol. 7, pp. 690–696, Sep 2006.

[3] R. M. Hoffman, "The multiple uses of fluorescent proteins to visualize cancer in vivo.," *Nat Rev Cancer*, vol. 5, pp. 796–806, Oct 2005.

[4] T. Misgeld and M. Kerschensteiner, "In vivo imaging of the diseased nervous system.," *Nat Rev Neurosci*, vol. 7, pp. 449–463, Jun 2006.

[5] W. R. Zipfel, R. M. Williams, and W. W. Webb, "Nonlinear magic: multiphoton microscopy in the biosciences.," *Nat Biotechnol*, vol. 21, pp. 1369–1377, Nov 2003.

[6] W. Denk, J. H. Strickler, and W. W. Webb, "Two-photon laser scanning fluorescence microscopy.," *Science*, vol. 248, pp. 73–76, Apr 1990.

[7] M. Goeppert-Mayer, "Über elementarakte mit zwei quantensprüngen," *Annalen der Physik*, vol. 401, p. 273, 1931.

[8] I. D. Abella, "Optical double-photon absorption in cesium vapor," *Phys. Rev. Letters*, vol. 9, p. 453, 1962.

[9] S. Singh and L. T. Bradley, "Three-photon absorption in napthalene crystals by laser excitation," *Phys. Rev. Lett.*, vol. 12, p. 612, 1964.

[10] S. W. Hell, K. Bahlmann, M. Schrader, A. Soini, H. Malak, I. Gryczynski, and J. R. Lakowicz, "Three-photon excitation in fluorescence microscopy," *J. Biomed. Opt.*, vol. 1, p. 71, 1996.

[11] C. Xu, E. Soin, W. Zipfel, J. B. Shear, R. M. Williams, and W. W. Webb, "Multiphoton fluorescence excitation: new spectral windows for biological nonlinear microscopy," *Proc. Natl. Acad. Sci. USA*, vol. 93, p. 10763, 1996.

[12] L. A. Bagatolli and E. Gratton, "Two-photon fluorescence microscopy observation of shape changes at the phase transition in phospholipid giant unilamellar vesicles.," *Biophys J*, vol. 77, pp. 2090–2101, Oct 1999.

[13] R. K. P. Benninger, B. Onfelt, M. A. A. Neil, D. M. Davis, and P. M. W. French, "Fluorescence imaging of two-photon linear dichroism: cholesterol depletion disrupts molecular orientation in cell membranes.," *Biophys J*, vol. 88, pp. 609–622, Jan 2005.

[14] L. Moreaux, T. Pons, V. Dambrin, M. Blanchard-Desce, and J. Mertz, "Electro-optic response of second harmonic generation membrane potential sensors," *Opt. Lett.*, vol. 28, p. 625, 2003.

[15] J. E. Aubin, "Autofluorescence of viable cultured mammalian cells.," *J Histochem Cytochem*, vol. 27, pp. 36–43, Jan 1979.

[16] M. Dellinger, M. Geze, R. Santus, E. Kohen, C. Kohen, J. G. Hirschberg, and M. Monti, "Imaging of cells by autofluorescence: a new tool in the probing of biopharmaceutical effects at the intracellular level.," *Biotechnol Appl Biochem*, vol. 28 (Pt 1), pp. 25–32, Aug 1998.

[17] S. Zhuo, J. Chen, S. Xie, Z. Hong, and X. Jiang, "Extracting diagnostic stromal organization features based on intrinsic two-photon excited fluorescence and second-harmonic generation signals.," *J Biomed Opt*, vol. 14, no. 2, p. 020503, 2009.

[18] I. Freund, M. Deutsch, and A. Sprecher, "Connective tissue polarity. optical second-harmonic microscopy, crossed-beam summation, and small-angle scattering in rat-tail tendon.," *Biophys J*, vol. 50, pp. 693–712, Oct 1986.

[19] P. J. Campagnola, A. Millard, M. Terasaki, P. Hoppe, C. J. Malone, and W. Mohler, "3-dimesional high-resolution second harmonic generation imaging of endogenous structural proteins in biological tissues," *Biophys J*, vol. 81, p. 496, 2002.

[20] E. Ralston, B. Swaim, M. Czapiga, W.-L. Hwu, Y.-H. Chien, M. G. Pittis, B. Bembi, O. Schwartz, P. Plotz, and N. Raben, "Detection and imaging of non-contractile inclusions and sarcomeric anomalies in skeletal muscle by second harmonic generation combined with two-photon excited fluorescence.," *J. Struct. Biol.*, vol. 162, pp. 500–508, 2008.

[21] D. Débarre, W. Supatto, A.-M. Pena, A. Fabre, T. Tordjmann, L. Combettes, M.-C. Schanne-Klein, and E. Beaurepaire, "Imaging lipid bodies in cells and tissues using third-harmonic generation microscopy.," *Nat Methods*, vol. 3, pp. 47–53, Jan 2006.

[22] N. Olivier, M. Luengo-Oroz, L. Duloquin, E. Faure, T. Savy, I. Veilleux, X. Solinas, D. Débarre, P. Bourgine, A. Santos, N. Peyriéras, and E. Beaurepaire, "Cell lineage reconstruction of early zebrafish embryos using label-free nonlinear microscopy," *Science*, vol. 339, p. 967, 2010.

[23] C. L. Evans, E. O. Potma, M. Puoris'haag, D. Cote, C. P. Lin, and X. S. Xie, "Chemical imaging of tissue in vivo with video-rate coherent anti-stokes raman scattering microscopy," *Proc. Natl. Aca. Sci.*, vol. 102, p. 16807, 2005.

[24] A. Zumbusch, G. R. Holtom, and X. S. Xie, "Vibrational mircoscopy using coherent anti-stokes raman scattering," *Phys Rev Lett*, vol. 82, p. 4014, 1999.

[25] D. L. Wokosin, V. E. Centonze, S. Crittenden, and J. White, "Three-photon excitation fluorescence imaging of biological specimens using an all-solid-state laser," *Bioimaging*, vol. 4, p. 208, 1996.

[26] S.-W. Chu, S.-P. Tai, C.-L. Ho, C.-H. Lin, and C.-K. Sun, "High-resolution simultaneous three-photon fluorescence and third-harmonic-generation microscopy," *Microscopy Research and Technique*, vol. 66, p. 193, 2005.

[27] T. Pentcheva and M. Edidin, "Clustering of peptide-loaded mhc class i molecules for endoplasmic reticulum export imaged by fluorescence resonance energy transfer.," *J Immunol*, vol. 166, pp. 6625–6632, Jun 2001.

[28] D. R. Fooksman, G. K. Grönvall, Q. Tang, and M. Edidin, "Clustering class i mhc modulates sensitivity of t cell recognition.," *J Immunol*, vol. 176, pp. 6673–6680, Jun 2006.

[29] R. K. P. Benninger, B. Vanherberghen, S. Young, S. B. Taner, F. J. Culley, T. Schnyder, M. A. A. Neil, D. Wüstner, P. M. W. French, D. M. Davis, and B. Onfelt, "Live cell linear dichroism imaging reveals extensive membrane ruffling within the docking structure of natural killer cell immune synapses.," *Biophys J*, vol. 96, pp. L13–L15, Jan 2009.

[30] D. Cheresh, J.Leng, and R. Klemke, "Regulation of cell contraction and membrane ruffling by distinct signals in migratory cells," *J. Cell Biol*, vol. 146, p. 1107, 1999.

[31] A. Anantharam, B. Onoa, R. H. Edwards, R. W. Holz, and D. Axelrod, "Localized topological changes of the plasma membrane upon exocytosis visualized by polarized tirfm.," *J Cell Biol*, vol. 188, pp. 415–428, Feb 2010.

[32] J. A. Dix and A. S. Verkman, "Mapping of fluorescence anisotropy in living cells by ratio imaging. application to cytoplasmic viscosity.," *Biophys J*, vol. 57, pp. 231–240, Feb 1990.

[33] T. H. Foster, B. D. Pearson, S. Mitra, and C. E. Bigelow, "Fluorescence anisotropy imaging reveals localization of meso-tetrahydroxyphenyl chlorin in the nuclear envelope.," *Photochem Photobiol*, vol. 81, no. 6, pp. 1544–1547, 2005.

[34] D. Axelrod, "Carbocyanine dye orientation in red cell membrane studied by microscopic fluorescence polarization.," *Biophys J*, vol. 26, pp. 557–573, Jun 1979.

[35] J. Borejdo and S. Burlacu, "Measuring orientation of actin filaments within a cell: orientation of actin in intestinal microvilli.," *Biophys J*, vol. 65, pp. 300–309, Jul 1993.

[36] M. Vincent, J. Gallay, J. de Bony, and J. F. Tocanne, "Steady-state and time-resolved fluorescence anisotropy study of phospholipid molecular motion in the gel phase using 1-palmitoyl-2-[9-(2-anthryl)-nonanoyl] -sn-glycero-3-phosphocholine as probe.," *Eur J Biochem*, vol. 150, pp. 341–347, Jul 1985.

[37] J. V. Rocheleau, M. Edidin, and D. W. Piston, "Intrasequence gfp in class i mhc molecules, a rigid probe for fluorescence anisotropy measurements of the membrane environment.," *Biophys J*, vol. 84, pp. 4078–4086, Jun 2003.

[38] A. M. Vrabioiu and T. J. Mitchison, "Structural insights into yeast septin organization from polarized fluorescence microscopy.," *Nature*, vol. 443, pp. 466–469, Sep 2006.

[39] D. Lara and C. Dainty, "Axially resolved complete mueller matrix confocal microscopy," *Appl. Opt*, vol. 45, p. 1917, 2006.

[40] V. L. Floc'h, S. Brasselet, J. Roch, and J. Zyss, "Two-photon fluorescence and second-harmonic generation microscopy applied to orientational monitoring of molecules," *J. Phys. Chem. B*, vol. 107, p. 12403, 2003.

[41] S. Brasselet, V. L. Floc'h, F. Treussart, J.-F. Roch, J. Zyss, E. Botzung-Appert, and A. Ibanez, "In situ diagnostics of the crystalline nature of single organic nanocrystals by nonlinear microscopy.," *Phys Rev Lett*, vol. 92, p. 207401, May 2004.

[42] C. Anceau, S. Brasselet, and J. Zyss, "Local orientational distribution of molecular monolayers probed by nonlinear microscopy," *Chem. Phys. Lett.*, vol. 411, p. 98, 2005.

[43] S. Brasselet and J. Zyss, "Nonlinear polarimetry of molecular crystals down to the nanoscale," *C. R. Physique*, vol. 8, p. 165, 2007.

[44] R. M. Williams, W. R. Zipfel, and W. W. Webb, "Interpreting second-harmonic generation images of collagen i fibrils.," *Biophys J*, vol. 88, pp. 1377–1386, Feb 2005.

[45] A. Pena, T. Boulesteix, T. Dartigalongue, M. Strupler, E. Beaurepaire, and M. C. Schanne-Klein, "Chiroptical effects in the second harmonic signal of collagens i and iv: applications in nonlinear microscopy.," *Nonlinear Opt., Quantum Opt.*, vol. 35, 2006.

[46] C. Odin, Y. L. Grand, A. Renault, L. Gailhouste, and G. Baffet, "Orientation fields of nonlinear biological fibrils by second harmonic generation microscopy," *J. Microsc.*, vol. 229, p. 32, 2008.

[47] S. Psilodimitrakopoulos, S. I. C. O. Santos, I. Amat-Roldan, A. K. N. Thayil, D. Artigas, and P. Loza-Alvarez, "In vivo, pixel-resolution mapping of thick filaments' orientation in nonfibrilar muscle using polarization-sensitive second harmonic generation microscopy.," *J Biomed Opt*, vol. 14, no. 1, p. 014001, 2009.

[48] D. Oron, D. Yelin, E. Tal, S. Raz, R. Fachima, and Y. Silberberg, "Depth-resolved structural imaging by third harmonic generation microscopy," *J. Struct. Biol.*, vol. 147, p. 3, 2004.

[49] N. Olivier, F. Aptel, K. Plamann, M.-C. Schanne-Klein, and E. Beaurepaire, "Harmonic microscopy of isotropic and anisotropic microstructure of the human cornea," *Opt Express*, vol. 18, p. 5028, 2010.

[50] H. Wang, Y. Fu, P. Zickmund, R. Shi, and J.-X. Cheng, "Coherent anti-stokes raman scattering imaging of axonal myelin in live spinal tissues.," *Biophys J*, vol. 89, pp. 581–591, Jul 2005.

[51] F. Munhoz, H. Rigneault, and S. Brasselet, "High order symmetry structural properties of vibrational resonances using multiple-field polarization coherent anti-stokes raman spectroscopy microscopy.," *Phys Rev Lett*, vol. 105, p. 123903, Sep 2010.

[52] J. F. W. Herschel, "On a case of superficial colour prsented by a homogeneous liquid inernally colourless.," *Philosophical Translation of the Royal Society of London*, vol. 135, p. 143, 1845.

[53] G. G. Stokes, "On the change of rafrangibility of light," *Philosophical Translation of the Royal Society of London*, p. 463, 1852.

[54] A. Jabłoński, "Uber den mechanismus der photolumineszenz von farbstoffphosphoren," *Zeitschrift fur Physik*, vol. 94, p. 38, 1935.

[55] J. R. Lakowicz, *Principles of Fluorescence Spectroscopy*. Springer, 1999.

[56] J. Franck and E. G. Dymond, "Elementary processes of photochemical reactions.," *Trans. Faraday Soc.*, vol. 21, p. 536, 1926.

[57] E. Condon, "A theory of intensity distribution in band systems.," *Phys. Rev.*, vol. 28, p. 1182, 1926.

[58] M. Kasha, "Characterization of electronic tansitions in complex molecules.," *Discuss. Faraday Soc.*, vol. 9, p. 14, 1950.

[59] R. W. Boyd, *Principles of Nonlinear Optics*. Academic press, Wiley.

[60] S. Bidault, *Manipulation optique de l'organisation de chromophores non-lineaires et luminescents*. PhD thesis, École normale supérieure de Cachan, 2004.

[61] P. E. Hänninen, E. Soini, and S. W. Hell, "Continuous wave excitation two-photon flourescence microscopy," *Bioimaging*, vol. 2, p. 117, 1994.

[62] C. Sheppard and M. Gu, "Image formation in two-photon fluorescence microscopy," *Optik*, vol. 86, p. 104, 1990.

[63] O. Nakamura, "Three-dimensional imaging characteristics of laser scan fluorescence microscopy: two-photon excitation vs. one-photon excitation," *Optik*, vol. 93, p. 93, 1992.

[64] M. Gu and C. R. J. Sheppard, "Comparison of three-dimensional imaging properties between two-photon and single-photon fluorescence microscopy," *J. Microsc*, vol. 177, p. 128, 1995.

[65] P. T. C. So, T. French, W. M. Yu, K. M. Berland, C. Y. Dong, and E. Gratton, "Time-resolved fluorescence microscopy using two-photon excitation," *Bioimaging*, vol. 3, p. 49, 1995.

[66] P. So, H. Kim, and I. Kochevar, "Two-photon deep tissue ex vivo imaging of mouse dermal and subcutaneous structures," *Opt Express*, vol. 3, p. 339, 1998.

[67] W. R. Zipfel, R. M. Williams, R.Christie, A. Y. Nikitin, B. T. Hyman, and W. W. Webb, "Live tissue intrinsic emission microscopy using multiphoton-excited native fluorescence and second harmonic generation," *PNAS*, vol. 100, p. 7075, 2003.

[68] K. Florine-Casteel, "Phospholipid order in gel- and fluid-phase cell-size liposomes measured by digitized video fluorescence polarization microscopy.," *Biophys J*, vol. 57, pp. 1199–1215, Jun 1990.

[69] K. Kinosita, S. Kawato, and A. Ikegami, "A theory of fluorescence polarization decay in membranes.," *Biophys J*, vol. 20, pp. 289–305, Dec 1977.

[70] M. V. Gurp, "The use of rotation matrices in the mathematical description of molecular orientations in polymers," *Colloid and polymer science*, vol. 273, p. 607, 1995.

[71] F. Perrin, "Polarisation de la lumičre de fluorescence. vie moyenne des molécules dans l'etat excité," *Journal de Physique et le Radium*, vol. 7, p. 390, 1926.

[72] G. Weber, "Rotational brownian motion and polarization of the fluorescence of solutions," *Adv. Protein Chem.*, vol. 8, p. 415, 1953.

[73] R. E. Dale, S. C. Hopkins, U. A. an der Heide, T. Marszałek, M. Irving, and Y. E. Goldman, "Model-independent analysis of the orientation of fluorescent probes with restricted mobility in muscle fibers," *Biophys J*, vol. 78, p. 1606, 1999.

[74] A. Gasecka, T.-J. Han, C. Favard, B. R. Cho, and S. Brasselet, "Quantitative imaging of molecular order in lipid membranes using two-photon fluorescence polarimetry.," *Biophys J*, vol. 97, pp. 2854–2862, Nov 2009.

[75] B. Corry, D. Jayatilaka, B. Martinac, and P. Rigby, "Determination of the orientational distribution and orientation factor for transfer between membrane-bound fluorophores using a confocal microscope.," *Biophys J*, vol. 91, pp. 1032–1045, Aug 2006.

[76] T. Ha, T. Enderle, D. S. Chemla, P. R. Selvin, and S. Weiss, "Single molecule dynamics studied by polarization modulation," *Phys Rev Lett*, vol. 77, p. 19, 1996.

[77] T. J. Gould, M. S. Gunewardene, M. V. Gudheti, V. V. Verkhusha, S.-R. Yin, J. A. Gosse, and S. T. Hess, "Nanoscale imaging of molecular positions and anisotropies.," *Nat Methods*, vol. 5, pp. 1027–1030, Dec 2008.

[78] C. Dietrich, L. A. Bagatolli, Z. N. Volovyk, N. L. Thompson, M. Levi, K. Jacobson, and E. Gratton, "Lipid rafts reconstituted in model membranes.," *Biophys J*, vol. 80, pp. 1417–1428, Mar 2001.

[79] D. Scherfeld, N. Kahya, and P. Schwille, "Lipid dynamics and domain formation in model membranes composed of ternary mixtures of unsaturated and saturated phosphatidylcholines and cholesterol.," *Biophys J*, vol. 85, pp. 3758–3768, Dec 2003.

[80] C. K. Haluska, A. P. Schröder, P. Didier, D. Heissler, G. Duportail, Y. Mély, and C. M. Marques, "Combining fluorescence lifetime and polarization microscopy to discriminate phase separated domains in giant unilamellar vesicles.," *Biophys J*, vol. 95, pp. 5737–5747, Dec 2008.

[81] T. E. Schaus, E. W. Taylor, and G. G. Borisy, "Self-organization of actin filament orientation in the dendritic-nucleation/array-treadmilling model," *Proc. Natl. Acad. Sci. U. S. A.*, vol. 104, p. 7086, 2007.

[82] B. Richards and E. Wolf, "Electromagnetic diffraction in optical systems. ii. structure of the image field in an aplanatic system," *Proc. R. Soc. Lond. A*, vol. 253, p. 358, 1959.

[83] I. Ledoux, C. Lepers, A. Peigaud, J. Badan, and J. Zyss, "Linear and nonlinear optical properties of n-4-nitrophenyl l-prolinol single crystals," *Opt. Commun*, vol. 80, p. 149, 1990.

[84] R. C. T. Frank P. Bolin, Luther E. Preuss and R. J. Ference, "Refractive index of some mammalian tissues using a fiber optic cladding method," *Appl. Opt*, vol. 28, p. 2297, 1989.

[85] D. T. Poh, "Examination of refractive index of human epidermis in-vitro and in-vivo," *Proc. Inter. Conf. Lasers*, vol. 96, p. 118, 1996.

[86] P. Schön, F. Munhoz, A. Gasecka, S. Brustlein, and S. Brasselet, "Polarization distortion effects in polarimetric two-photon microscopy.," *Opt Express*, vol. 16, pp. 20891–20901, Dec 2008.

[87] K. Komorowska, S. Brasselet, J. Zyss, L. Pourlsen, M. Jazdzyk, H. J. Egelhaaf, J. Gierschnera, and M. Hanack, "Nanometric scale investigation of the nonlinear efficiency of perhydrotriphynylene inclusion compounds," *Chem. Phys*, vol. 318, p. 12, 2005.

[88] E. Y. S. Yew and C. J. R. Sheppard, "Effects of axial field components on second harmonic generation microscopy.," *Opt. Express*, vol. 14, p. 1167, 2006.

[89] T. Förster, "Zwischenmolekulare energiewanderung und fluoreszenz," *Ann. Physik*, vol. 437, p. 55, 1948.

[90] R. Clegg, *Fluorescence resonance energy transfer (FRET) in Fluorescence Imaging.* John Wiley & Sons, 1996.

[91] V. L. Floc'h, S. Brasselet, J. Zyss, B. R. Cho, S. H. Lee, S. J. Jeon, M. Cho, K. S. Min, and M. P. Suh, "High efficiency and quadratic nonlinear optical properties of a fully optimized 2-dhigh efficiency and quadratic nonlinear optical properties of a fully optimized 2-d octupolar crystal characterized by nonlinear microscopy," *Adv. Mater.*, vol. 17, p. 2, 2005.

[92] C. Botta, G. Bongiovanni, A. Mura, G. D. Silvestro, and R. Tubino, "Energy transfers in weakly interacting oligothiophenes," *Synth. Met*, vol. 116, p. 175, 2001.

[93] J. R. Salcedo, A. E. Siegman, D. D. Dlott, and M. D. Fayer, "Dynamics of energy transport in molecular crystals : the picosecond transient-grating method," *Phys. Rev. Lett.*, vol. 41, p. 131, 1978.

[94] P. Moens, M. Helms, and D. Jameson, "Detection of tryptophan to tryptophan energy transfer in proteins," *The Protein Journal*, vol. 23, p. 79, 2004.

[95] D. Ait-Belkacem, A. Gasecka, F. Munhoz, S. Brustlein, and S. Brasselet, "Influence of birefringence on polarization resolved nonlinear microscopy and collagen shg structural imaging.," *Opt Express*, vol. 18, pp. 14859–14870, Jul 2010.

[96] S. J. Singer and G. L. Nicolson, "The fluid mosaic model of the structure of cell membranes.," *Science*, vol. 175, pp. 720–731, Feb 1972.

[97] L. Pike, "The challenge of lipid rafts," *Journal of Lipid Research*, p. 1, 2008.

[98] Z. Korade and A. K. Kenworthy, "Lipid rafts, cholesterol, and the brain," *Neuropharmacology*, vol. 55, p. 1265, 2008.

[99] B. Kholodenko, J. Hoek, and H. Westerhoff, "Why cytoplasmic signaling proteins should be recruited to cell membrane," *Trends Cell Biol*, vol. 10, p. 173, 2000.

[100] R. Kolesnick, "The therapeutic potential of modulating the ceramide/sphingomyelin pathway," *J Clin Invest*, vol. 110, p. 3, 2002.

[101] F. G. van der Goot and T. Harder, "Raft membrane domains: from a liquid-ordered membrane phase to a site of pathogen attack," *Semin Immuno*, vol. 13, p. 89, 2001.

[102] M. Simons, P. Keller, J. Dichgans, and J. B. Schulz, "Cholesterol and alzheimer's disease: is there a link?," *Neurology*, vol. 57, p. 1089, 2001.

[103] L. A. Bagatolli, "To see or not to see: lateral organization of biological membranes and fluorescence microscopy.," *Biochim Biophys Acta*, vol. 1758, pp. 1541–1556, Oct 2006.

[104] F. M. Menger and J. S. Keiper, "Chemistry and physics of giant vesicles as biomembrane models.," *Curr Opin Chem Biol*, vol. 2, pp. 726–732, Dec 1998.

[105] S. L. Veatch and S. L. Keller, "Seeing spots: Complex phase behavior in simple membranes," *Biochimica et Biophysica Acta*, vol. 1746, p. 172, 2005.

[106] A. V. Samsonov, I. Mihalyov, and F. S. Cohen, "Characterization of cholesterol-sphingomyelin domains and their dynamics in bilayer membranes.," *Biophys J*, vol. 81, pp. 1486–1500, Sep 2001.

[107] T. Baumgart, S. T. Hess, and W. W. Webb, "Imaging coexisting fluid domains in biomembrane models coupling curvature and line tension.," *Nature*, vol. 425, pp. 821–824, Oct 2003.

[108] H. M. Kim, H.-J. Choo, S.-Y. Jung, Y.-G. Ko, W.-H. Park, S.-J. Jeon, C. H. Kim, T. Joo, and B. R. Cho, "A two-photon fluorescent probe for lipid raft imaging: C-laurdan.," *Chembiochem*, vol. 8, pp. 553–559, Mar 2007.

[109] A. Gidwani, D. Holowka, and B. Baird, "Fluorescence anisotropy measurements of lipid order in plasma membranes and lipid rafts from rbl-2h3 mast cells.," *Biochemistry*, vol. 40, pp. 12422–12429, Oct 2001.

[110] D. A. Brown and E. London, "Functions of lipid rafts in biological membranes.," *Annu Rev Cell Dev Biol*, vol. 14, pp. 111–136, 1998.

[111] K. Simons and D. Toomre, "Lipid rafts and signal transduction.," *Nat Rev Mol Cell Biol*, vol. 1, pp. 31–39, Oct 2000.

[112] H. W. Meyer, K. Semmler, and P. J. Quinn, "The effect of sterols on structures formed in the gel/subgel phase state of dipalmitoylphosphatidylcholine bilayers.," *Mol Membr Biol*, vol. 14, no. 4, pp. 187–193, 1997.

[113] M. R. Vist and J. H. Davis, "Phase equilibria of cholesterol/dipalmitoylphosphatidylcholine mixtures: 2h nuclear magnetic resonance and differential scanning calorimetry.," *Biochemistry*, vol. 29, pp. 451–464, Jan 1990.

[114] N. Kahya, D. Scherfeld, K. Bacia, B. Poolman, and P. Schwille, "Probing lipid mobility of raft-exhibiting model membranes by fluorescence correlation spectroscopy.," *J Biol Chem*, vol. 278, pp. 28109–28115, Jul 2003.

[115] L. A. Bagatolli and E. Gratton, "Two photon fluorescence microscopy of coexisting lipid domains in giant unilamellar vesicles of binary phospholipid mixtures.," *Biophys J*, vol. 78, pp. 290–305, Jan 2000.

[116] M. Angelova and D. Dimitrov, "Liposome electroformation," *Faraday Discuss. Chem. Soc.*, vol. 81, p. 303, 1986.

[117] R. M. Mesquita, E. Melo, T. E. Thompson, and W. L. Vaz, "Partitioning of amphiphiles between coexisting ordered and disordered phases in two-phase lipid bilayer membranes.," *Biophys J*, vol. 78, pp. 3019–3025, Jun 2000.

[118] A. Beck, D. Heissler, and G. Duportail, "Influence of the length of the spacer on the partitioning properties of amphiphilic fluorescent membrane probes.," *Chem Phys Lipids*, vol. 66, pp. 135–142, Nov 1993.

[119] T. Baumgart, G. Hunt, E. R. Farkas, W. W. Webb, and G. W. Feigenson, "Fluorescence probe partitioning between lo/ld phases in lipid membranes.," *Biochim Biophys Acta*, vol. 1768, pp. 2182–2194, Sep 2007.

[120] *Molecular Probes Handbook, A Guide to Fluorescent Probes and Labeling Technologies (Invitrogen life science).*

[121] D. Illinger, G. Duportail, Y. Mely, N. Poirel-Morales, D. Gerard, and J. G. Kuhry, "A comparison of the fluorescence properties of tma-dph as a probe for plasma membrane and for endocytic membrane.," *Biochim Biophys Acta*, vol. 1239, pp. 58–66, Oct 1995.

[122] F. Mulders, van H. van Langen, G. van Ginkel, and Y. K. Levine, "The static and dynamic behavior of fluorescent probe molecules in lipid bilayers," *Biochim Biophys Acta*, vol. 859, p. 209, 1986.

[123] S. Wang, J. M. Beechem, E. Gratton, and M. Glaser, "Orientational distribution of 1,6-diphenyl-1,3,5-hexatriene in phospholipid vesicles as determined by global analysis of frequency domain fluorimetry data.," *Biochemistry*, vol. 30, pp. 5565–5572, Jun 1991.

[124] T. Parasassi, F. Conti, and E. Gratton, "Time-resolved fluorescence emission spectra of laurdan in phospholipid vesicles by multifrequency phase and modulation fluorometry.," *Cell Mol Biol*, vol. 32, no. 1, pp. 103–108, 1986.

[125] T. Parasassi, G. D. Stasio, A. d'Ubaldo, and E. Gratton, "Phase fluctuation in phospholipid membranes revealed by laurdan fluorescence.," *Biophys J*, vol. 57, pp. 1179–1186, Jun 1990.

[126] T. Parasassi, M. D. Stefano, M. Loiero, G. Ravagnan, and E. Gratton, "Influence of cholesterol on phospholipid bilayers phase domains as detected by laurdan fluorescence.," *Biophys J*, vol. 66, pp. 120–132, Jan 1994.

[127] P. Wahl, M. K. an J. P. Changeux, and J. C. Auchet, "A study on the motion of protenis in excitable membrane fragments by nanosecond fluorescence polarization microscopy.," *Eur. J. Biochem*, vol. 18, p. 335, 1971.

[128] L. A. Chen, R. E. Dale, S. Roth, and L. Brand, "Nanosecond time-dependent fluorescence depolarization of diphenylhexatriene in dimyristoyllecithin vesicles and the determination of "microviscosity".," *J Biol Chem*, vol. 252, pp. 2163–2169, Apr 1977.

[129] S. Kawato, K. Kinosita, and A. Ikegami, "Dynamic structure of lipid bilayers studied by nanosecond fluorescence techniques.," *Biochemistry*, vol. 16, pp. 2319–2324, May 1977.

[130] P. L. Chong and P. T. Wong, "Interactions of laurdan with phosphatidylcholine liposomes: a high pressure ftir study.," *Biochim Biophys Acta*, vol. 1149, pp. 260–266, Jul 1993.

[131] H. Ranchon, "Corrections des distortions de polarization en microscopie de fluorescence pour la mesure d'ordres moleculaires," tech. rep., Institut Fresnel, MOSAIC group, 2010.

[132] D. Magde, B. E. L. Elson, and W. W. Webb, "Thermodynamic fluctuations in a reacting system: Measurement by fluorescence correlation spectroscopy," *Phys Rev Lett*, vol. 29, p. 705, 1972.

[133] F. Moyano, M. A. Biasutt, J. J. Silber, and N. M. Correa, "New insights on the behavior of prodan in homogeneous media and in large unilamellar vesicles," *J. Phys. Chem. B*, vol. 110, p. 11838, 2006.

[134] J. M. Muller, D. H. Harryvan, J. C. D. Verhagen, G. van Ginkel, and E. E. van Faasen, "The orientation of the transition dipole moments of tma-dph embedded in a poly(vinylalcohol) film," *Chem. Phys.*, vol. 211, p. 413, 1996.

[135] S. Sund, J. Swanson, and D. Axelrod, "Cell membrane orientation visualized by polarized total internal reflection fluorescence," *Biophys J*, vol. 77, p. 2266, 1999.

[136] A. Sharma and B. J. Mayer, "Phosphorylation of p130cas initiates rac activation and membrane ruffling.," *BMC Cell Biol*, vol. 9, p. 50, 2008.

[137] G. Calzaferri, S. Huber, H. Maas, and C. Minkowski, "Host-guest antenna materials.," *Angew. Chem. Int. Ed.*, vol. 42, p. 3732, 2003.

[138] J. M. Thomas, "Uniform heterogeneous catalysts: The role of solid-state chemistry in their development and design," *Angew. Chem. Int. Ed.*, vol. 27, p. 1673, 1988.

[139] T. Bein, "Synthesis and applications of molecular sieve layers and membranes," *Chem. Mater.*, vol. 8, p. 1636, 1996.

[140] S. Megelski and G. Calzaferri, "Tuning the size and shape of zeolite l based inorganic/organic host/guest composites for optical antenna systems," *Adv. Funct. Mater*, vol. 11, p. 277, 2001.

[141] H. S. Kim, S. M. Lee, K. Ha, . S. C Jung, Y.-J. Lee, Y. S. Chun, D. S. Kim, B. K. Rhee, and K. Yoon, "Micropatterns of spores displaying heterologous proteins," *J. Am. Chem. Soc.*, vol. 126, p. 673, 2004.

[142] D. Brühwiler, G. Calzaferri, T. Torres, J. H. Ramm, N. Gartmann, L.-Q. Dieu, I. López-Duarte, and M. V. Martínez-Díaz, "Nanochannels for supramolecular organization of luminescent guests," *J. Mater. Chem.*, vol. 19, p. 8040, 2009.

[143] G. C. N. Gfeller, "Energy migration in dye-loaded hexagonal microporous crystals," *J. Phys. Chem. B*, vol. 101, p. 1396, 1997.

[144] N. Gfeller, S. Megelski, and G. Calzaferri, "Transfer of electronic excitation energy between dye molecules in the channels of zeolite l," *J. Phys. Chem. B*, vol. 102, p. 2433, 1998.

[145] J. Tsuwi, E. Soin, R. Berger, G. Labat, G. Couderc, N.-R. Behrnd, P. Ottiger, F. Cucinotta, K. Schürmann, M. Bertoni, L. Viani, J. Gierschner, J. Cornil, A. Prodi-Schwab, L. D. Cola, M. Wübbenhorst, and J. Hulliger, "Alignment and relaxation dynamics of dye molecules in host-guest inclusion compounds as probed by dielectric spectroscopy.," *J. Phys. Chem. A*, vol. 114, p. 5956, 2010.

[146] S. Megelski, A. Lieb, M. Pauchard, A. Drechsler, S. Glaus, C. Debus, A. J. Meixner, , and G. Calzaferri, "Orientation of fluorescent dyes in the nano channels of zeolite l," *J. Phys. Chem. B*, vol. 105, p. 25, 2001.

[147] T. Shim, D. Kim, M. H. Lee, B. K. Rhee, H. M. Cheong, H. S. Kim, and K. B. Yoon, "Determination of the hyperpolarizability components of hemicyanine dyes by measuring the anisotropic fluorescence and second harmonic of the dyes uniformly aligned within zeolite channels.," *J. Phys. Chem. B*, vol. 110, p. 16874, 2006.

[148] D. W. Breck, *Zeolite Molecular Sieves.* John Wiley & Sons Inc, 1974.

[149] R. Barrer, *Zeolites and clay minerals as sorbents and molecular sieves.* Academic Press: London, 1978.

[150] C. Baerlocher, W. Meier, and D. Olson, *Atlas of Zeolite Framework Types.* Elsevier Science, 2001.

[151] A. Z. Ruiz, D. Brühwiler, T. Ban, and G. Calzaferri, "Oriented zeolite material and method for producing the same," *Monatsh. Chem.*, vol. 136, p. 77, 2005.

[152] M. Pauchard, A. Devaux, and G. Calzaferri, "Dye-loaded zeolite l sandwiches," *Chem. Eur. J.*, vol. 6, p. 3456, 2000.

[153] S. Hashimoto, M. Hagiri, N. Matsubara, and S. Tobita, "Photophysical studies of neutral aromatic species confined in zeolite l: Comparison with cationic dyes," *Phys. Chem. Chem. Phys.*, vol. 3, p. 5043, 2001.

[154] B. Hennessy, S. Megelski, C. Marcolli, V. Shklover, C. Bärlocher, and G. C. ferri, "Characterization of methyl viologen in the channels of zeolite l," *J. Phys. Chem. B*, vol. 103, p. 3340, 1999.

[155] N. Nemkovich, H. Reis, and W. Baumann, "Ground and excited state dipole moments of coumarin laser dyes: Investigation by electro-optical absorption and emission methods," *J. Lumin.*, vol. 71, p. 255, 1997.

[156] C. Striebel, K. Hoffmann, and F. Marlow, "The microcrystal prism method for refractive index measurements on zeolite-based nanocomposites," *Microporous Mater*, vol. 9, p. 43, 1997.

[157] K. Hoffmann, F. Marlow, and J. Caro, "Photoinduced switching in nanocomposites of azobenzene and molecular sieves," *Adv. Mat.*, vol. 9, p. 567, 1997.

[158] J. Drenth, *Principles of protein x-ray crystallography.* Springer Advanced Texts in Chemistry, 1999.

[159] R. Gale, *Crystallography Made Crystal Clear.* San Diego: Academic Press, 1993.

[160] A. Sanjoh and T. Tsukihara, "Spatiotemporal protein crystal growth studies using microfluidic silicon devices," *J. Crystal Growth*, vol. 196, p. 691, 1999.

[161] R. Boistelle and J. P. Astier, "Crystallization mechanisms in solution," *Journal of Crystal Growth*, vol. 90, p. 14, 1988.

[162] A. McPherson and P. Shlichta, "Facilitation of the growth of protein crystals by heterogeneous/epitaxial nucleation," *J. Crystal Growth*, vol. 90, p. 47, 1988.

[163] C. J. Gerdts, M. Elliott, S. Lovell, M. B. Mixon, A. J. Napuli, B. L. Staker, P. Nollertc, and L. Stewart, "The plug-based nanovolume microcapillary protein crystallization system (mpcs)," *Acta Cryst*, vol. D64, p. 1116, 2008.

[164] A. Sanjoh, T. Tsukihara, and S. Gorti, "Surface-potential controlled si-microarray devices for heterogeneous protein crystallization screening," *J. Cryst. Growth*, vol. 232, p. 618, 2001.

[165] J. Baudour, Y. Delugeard, and H. Cailleau, "Transition structurale dans les polyphényles. i. structure cristalline de la phase basse température du p-terphényle à 113 k," *Acta. Cryst. B*, vol. 32, p. 150, 1976.

[166] G. P. Charbonneau and Y. Delugeard *Acta. Cryst. B*, vol. B32, p. 1420, 1976.

[167] J. Baudour and H. Cailleau, "Structural phase transition in polyphenyls. iv. double-well potential in the disordered phase of p-terphenyl from neutron (200 k) and x-ray (room-temperature) diffraction data," *Acta. Cryst. B*, vol. 33, p. 1773, 1977.

[168] P. Bordat and R. Brown, "Correspondence between electronic origins and substitution sites in pentacene/p-terphenyl mixed crystals by molecular modeling," *Chem. Phys.*, vol. 246, p. 323, 1999.

[169] H. Kobayashi *Bull. Chem. Soc. Jpn.*, vol. 56, p. 3224, 1983.

[170] H. Dua, R. A. Fuh, J. Li, A. Corkan, and J. S. Lindsey, "Photochemcad: A computer-aided design and research tool in photochemistry," *Photochemistry and Photobiology*, vol. 68, p. 141, 1998.